

ulm university universität ulm



BOSCH
Technik fürs Leben

Integrated quantum magnetometers based on colour centres in diamond

DISSERTATION

zur Erlangung des Doktorgrades Dr. rer. nat.
der Fakultät für Naturwissenschaften der Universität Ulm

vorgelegt von

Felix Michael Stürner

aus Ulm

2023

Amtierender Dekan: Prof. Dr. Thorsten Bernhardt

Erstgutachter: Prof. Dr. Fedor Jelezko
Zweitgutachter: PD Dr. Boris Naydenov

Tag der mündlichen Prüfung: 21. Februar 2023

Diese Dissertation ist am Zentralbereich Forschung und Vorausentwicklung der Robert Bosch GmbH, D-71272 Renningen, Deutschland, in Zusammenarbeit mit dem Institut für Quantenoptik der Universität Ulm, D-89081 Ulm, erstellt worden.

Version: 1. Juli 2023
Copyright (2023) Felix M. Stürner

Für meine Familie.

Abstract

This work addresses the progress of diamond-based magnetic field sensing using negatively charged nitrogen vacancy (NV) centres. NV centres are stable colour centres in diamond consisting of nitrogen atoms and adjacent vacancies. NV-based magnetometers can offer a disruptive potential over classical magnetic field sensors due to their extraordinary properties, such as ultra-high sensitivity in combination with a large dynamic range. These characteristics can path the way for new areas of application.

Transferring this technology developed in basic research to commercial products requires a high degree of sensor integration and miniaturisation in order to enable precise measurements of magnetic fields outside of laboratory environments. In addition to compactness and portability, the assembled NV magnetometers must above all meet the desired performance characteristics desired for the intended application. Factors, such as manufacturability and product cost, also play a non-negligible role in the sensor development. This is especially true if the application is intended for the mass market or is to be sold there.

Subject of this work are advances in the development and miniaturisation of NV magnetometers. This progress is discussed on the basis of two assembled prototypes. These demonstrators can be seen as one of the first attempts to bring the NV technology to product application.

The first prototype presented in this thesis uses a light-emitting diode (LED) as light source. Main focus in the development of the sensor is the compact arrangement of the necessary components to minimise the construction volume of the sensor head. However, additional bulky laboratory equipment is still required for operation, which limits the sugar cube sized sensor head to laboratory environments. A magnetic field resolution in the microtesla range has been achieved with this NV sensor.

While the achieved performance of the first prototype is mainly limited by a low optical pumping rate provided by the LED, a fibre-based approach is chosen for the second prototype. In addition, a balanced detection scheme composed of two photodiodes is implemented to tackle fluctuations in the optical excitation path. The design of this NV sensor is based on commercially available components for all functional sensor parts, which are compactly integrated. This allows portable measurements of magnetic fields with sub-pT $\mathrm{Hz}^{-1/2}$ sensitivity.

In addition to the integrated NV magnetometers, a proof-of-principle of a novel sensing technique using the excited-state fluorescence lifetime is shown. This method can be used when technical noise of the optical excitation path limits the performance of an NV sensor.

Published Thesis Content

Large parts of this thesis are based on and taken from the following publications, which were published before the completion of this work:

[1] F. M. Stürner, A. Brenneis, J. Kassel, U. Wostradowski, R. Rölver, T. Fuchs, K. Nakamura, H. Sumiya, S. Onoda, J. Isoya, and F. Jelezko, *Compact integrated magnetometer based on nitrogen-vacancy centres in diamond*, Diamond and Related Materials 93, 59 (2019),
URL: https://dx.doi.org/10.1016/j.diamond.2019.01.008
Copyright (2019) Elsevier B.V. All rights reserved. Reuse permitted according to author rights.

[2] F. M. Stürner, A. Brenneis, T. Buck, J. Kassel, R. Rölver, T. Fuchs, A. Savitsky, D. Suter, J. Grimmel, S. Hengesbach, M. Förtsch, K. Nakamura, H. Sumiya, S. Onoda, J. Isoya, and F. Jelezko, *Integrated and Portable Magnetometer Based on Nitrogen-Vacancy Ensembles in Diamond*, Advanced Quantum Technologies 4, 2000111 (2021),
URL: https://dx.doi.org/10.1002/qute.202000111
Copyright (2021) The Authors. Published under a Creative Commons Attribution-NonCommercial-NoDerivatives License 4.0 (CC BY-NC-ND 4.0, https://creativecommons.org/licenses/by-nc-nd/4.0/).

[3] F. M. Stürner†, Y. Liu†, P.-O. Colard, M. Markham, and F. Jelezko, *Magnetometry based on the excited-state lifetimes of a single nitrogen-vacancy center in diamond*, Applied Physics Letters 119, 134001 (2021),
URL: https://dx.doi.org/10.1063/5.0070639
Copyright (2021) The Authors. Published under an exclusive license by AIP Publishing.

† These authors contributed equally to the work.

Contents

List of Figures **xiii**

List Of Tables **xvii**

1 Introduction **1**

2 The Nitrogen-Vacancy Centre In Diamond **7**

2.1 The Diamond 8

2.1.1 Diamond Synthesis 8

2.2 The Nitrogen-Vacancy Centre 11

2.2.1 NV Physical Structure 11

2.2.2 NV Formation 11

2.2.3 NV Electronic Properties 12

2.2.4 NV Optical Properties 14

2.2.5 NV Spin Hamiltonian 16

2.2.6 NV Spin Resonance 19

3 Magnetometry Using Nitrogen-Vacancy Centres **23**

3.1 Magnetic Field Sensitivity 24

3.2 Sensitivity Optimisation 26

3.2.1 Diamond Material 31

3.2.2 Optical Spin Excitation 36

3.2.3 Static Bias Magnetic Field 37

3.2.4 Spin Manipulation 39

3.2.5 Optical Spin Readout 41

3.2.6 Conclusion 44

4 LED-Based NV Magnetometer **47**
4.1 Introduction . . . 48
4.2 Sensor Assembly . . . 48
4.2.1 Diamond Sample . . . 51
4.2.2 Optical Excitation . . . 51
4.2.3 Spin Manipulation . . . 53
4.2.4 Optical Spin Readout . . . 53
4.3 Experimental Results And Discussion . . . 54
4.3.1 ODMR Measurement . . . 54
4.3.2 Sensitivity Measurement . . . 64
4.4 Conclusion . . . 67

5 Fibre-Based NV Magnetometer **71**
5.1 Introduction . . . 72
5.2 Sensor Assembly . . . 73
5.2.1 Optical Excitation . . . 73
5.2.2 Diamond Sample . . . 76
5.2.3 Spin Manipulation . . . 76
5.2.4 Optical Spin Readout . . . 77
5.2.5 Signal Processing . . . 79
5.2.6 Offset Magnetic Field . . . 79
5.3 Experimental Results . . . 80
5.4 Discussion And Outlook . . . 88
5.5 Conclusion . . . 94

6 Fluorescence Lifetime-Based NV Magnetometry **95**
6.1 Introduction . . . 95
6.2 Materials And Methods . . . 96
6.2.1 Experimental Setup . . . 96
6.2.2 Diamond Sample . . . 97
6.3 Experimental Results And Discussion . . . 98
6.4 Conclusion And Outlook . . . 104

7 Conclusion And Outlook **107**
7.1 Conclusion . . . 107

7.2 Outlook . . . 109

A Supplementary Information **111**
A.1 Introduction . . . 111
A.2 The Nitrogen-Vacancy Centre In Diamond . . . 112
A.2.1 NV Spin Hamiltonian . . . 112
A.3 Magnetometry Using NV Centres . . . 113
A.3.1 Sensitivity Optimisation . . . 113
A.4 LED-Based NV Magnetometer . . . 113
A.4.1 Optical Spin Readout . . . 114
A.4.2 Experimental Results . . . 115
A.4.3 Power Consumption . . . 116
A.5 Fibre-Based NV Magnetometer . . . 117
A.5.1 Sensor Assembly . . . 117
A.5.2 Spin Manipulation . . . 118
A.5.3 Signal Recording And Processing . . . 126
A.5.4 Experimental Results . . . 129
A.5.5 Laser Power Stability . . . 134
A.5.6 Power Consumption . . . 136
A.6 Fluorescence Lifetime-Based NV Magnetometry . . . 137
A.6.1 Experimental Setup . . . 137

B Abbreviations And Symbols **141**
B.1 List Of Abbreviations . . . 141
B.2 List Of Symbols . . . 143

Bibliography **147**

Acknowledgements **199**

List Of Publications **203**

Curriculum Vitae **207**

Erklärung **209**

List of Figures

1.1 Magnetometer technologies and high sensitivity applications. 3
1.2 Number of published articles and intellectual property disclosures related to NV centres. 4

2.1 Structure of the diamond and the NV centre. 9
2.2 Absorption and emission spectra of the NV centre. 14
2.3 Energy level scheme of the NV centre's electron spin. 15
2.4 NV energy level scheme with corresponding ODMR spectra. 18

3.1 Electron spin resonance of the NV centre. 25
3.2 Simulative analysis of the achievable sensitivity for an NV ensemble magnetometer. 28
3.3 Simulative analysis of the achievable linewidth and contrast for an NV ensemble magnetometer. 30
3.4 Broadening of the ensemble linewidth. 32
3.5 Optical excitation and spin manipulation of NV centres. 38
3.6 Total internal reflection of the NV fluorescence. 43

4.1 Miniaturised and integrated magnetometer. 49
4.2 Transmission spectrum of the short and long pass filter. 50
4.3 Optical excitation of the LED-based NV sensor. 52
4.4 Microwave structure with transmission line for spin manipulation. . . 54
4.5 Results of optical ray tracing simulations for fluorescence collection. . 55
4.6 Optically detected magnetic resonance. 56
4.7 Results of ODMR measurements. 58

4.8 Magnetic field simulations of the LED bond wire. 62
4.9 Dependence of the linewidth and the contrast on the microwave power. 63
4.10 Calculation of the Allan deviation. 66
4.11 Minimum detectable magnetic field derived from the noise analysis. . 67
4.12 Minimum detectable magnetic field derived from the noise analysis. . 68

5.1 Sensor head of the fully integrated NV magnetometer. 73
5.2 Schematic of the complete NV sensor setup. 74
5.3 Optical ray tracing simulations for the optical excitation of the NV centres. 75
5.4 Experimental evaluation of the measured signal dependent on the photodiode position. 78
5.5 Demodulated and integrated signal of an ODMR spectrum. 80
5.6 Simulative evaluation of the offset magnetic field generated by a pair of tapered Helmholtz coils. 81
5.7 Optically detected magnetic resonance. 82
5.8 Evaluation of the magnetic field sensitivity with respect to sensor parameters. 84
5.9 Sensitivity determination with square-wave test field using the Allan deviation. 87
5.10 Measurement of the change in the magnetic field due to the movement of an elevator. 89

6.1 Schematic of the pulsed setup. 97
6.2 Confocal images of single NV centres. 98
6.3 Spin-selective fluorescence decay curves. 99
6.4 ODMR spectra of three different analysis methods and resulting $B_{\min}$. 101

7.1 Images of the NV magnetometers assembled at Robert Bosch GmbH. 108

A.1 Simulative analysis of the achievable linewidth and contrast for an NV ensemble magnetometer. 113

A.2 Simulative analysis of the collection efficiency along the optical axis of the GRIN lens. 114
A.3 Image of the portable setup of the fibre-based NV magnetometer. . . 117
A.4 Images of the integrated fibre-based NV magnetometer. 118
A.5 Design and simulation of the double split-ring resonator. 119
A.6 Scanning electron microscope images of the double split-ring resonator. 120
A.7 Adjustments of the properties of the double split-ring resonator. . . . 121
A.8 Simulative result of the field distribution of the double split-ring resonator. 122
A.9 Microwave double-split ring resonator. 123
A.10 Measured spectral power output of the spin manipulation equipment. 125
A.11 Spin manipulation and ODMR spectrum for one NV orientation. . . . 126
A.12 Slope and noise dependence on the applied hyperfine splitting frequency and on the modulation frequency. 127
A.13 Simulative analysis of the logarithmic transimpedance amplification circuit. 129
A.14 Optically detected magnetic resonance with simultaneous spin manipulation. 130
A.15 Variation of the microwave power to optimise the magnetic field sensitivity. 131
A.16 Variation of the microwave power to optimise the magnetic field sensitivity. 132
A.17 Variation of the integration time to optimise the magnetic field sensitivity. 133
A.18 Variation of the modulation frequency to optimise the magnetic field sensitivity. 134
A.19 Analysis of the laser stability on the performance of the magnetic field detection. 136
A.20 Schematic of the confocal microscope setup. 138

List of Tables

2.1 Comparison of the interaction parameters of the nitrogen isotopes ^{14}N and ^{15}N. 19

3.1 Overview of recorded diamond parameters with corresponding NV properties. 34
3.2 Overview of used microwave structures with corresponding properties. 40

5.1 Comparison of magnetometer technologies. 93

A.1 Overview of magnetometer technologies in terms of sensing capabilities. 111
A.2 Refractive indices of different materials used in optical ray tracing simulations. 115
A.3 Temperature estimation of the diamond. 116
A.4 Power consumption of the LED-based sensor. 116
A.5 Geometrical parameters of the double split-ring resonator. 120
A.6 Power consumption of the fibre-based NV sensor. 136

1 Introduction

The development of quantum physics by scientists such as Erwin Schrödinger, Werner Heisenberg and Max Planck at the beginning of the 20th century and the subsequent scientific discussions about quantum mechanical effects that could not be explained by the then prevailing classical physics enabled numerous technical inventions and advances. Examples are the development of lasers, transistors, atomic clocks, the method of magnetic resonance tomography and navigation using satellites. These so-called 'first-generation' quantum technologies can be traced back to the research successes of quantum physics.

Progress in basic research in recent decades showed that new areas of applications can be opened up and existing technologies could be further improved by exploiting quantum mechanical principles, such as superposition, entanglement, uncertainty relations or many-body effects. Interests in the 'second-generation' quantum technologies, including quantum computers, quantum encryption and quantum sensors are no longer limited to academic research institutions, but are also in importance for companies and politics. In recent years, numerous start-ups and spin-offs have been founded worldwide in the fields of quantum technologies. Many countries, such as the USA, China, Japan and the EU, have launched funding programmes for activities in this technology field[1]. However, main challenges for a successful transfer of 'second generation' quantum technologies into mature and commercially available products lie in the integration of the specialized components into compact and robust systems that allow cost-efficient operation outside laboratory environments.

While the number of available quantum computers is currently still limited with restricted rights of use for research and development institutions, there are already a few quantum sensor technologies as products available on the market, *e.g.* optic-

[1] https://qureca.com/overview-on-quantum-initiatives-worldwide/ (2021/07/04)

ally pumped magnetometers (OPMs) based on vapour cells[2]. Due to their unique properties, quantum sensors aim to outperform existing sensor technologies in terms of sensitivity and accuracy in certain cases. This could enable completely new application possibilities that would not be feasible with the current state of the art.

Regarding magnetometers, new fields of application arise in the areas of material analysis, position sensing and navigation as well as in the field of medical diagnostics, see figure 1.1a. State of the art magnetometers include Hall sensors [1–3], fluxgate sensors [4, 5], magnetoresistance magnetometers with executions of anisotropic magnetoresistance (AMR) [6], giant magnetoresistance (GMR) [7,8] and tunnel magnetoresistance (TMR) [9, 10] magnetometers, induction coil magnetometers [11], superconducting interference devices (SQUIDs) [12–14], OPMs [15, 16] and spin-exchange relaxation free (SERF) magnetometers [17, 18]. A comparison of the different magnetometer technologies in terms of their performance characteristics are summarised in figure 1.1b and table A.1. In particular, SQUIDs and OPMs have already successfully demonstrated their capability to precisely detect relatively small magnetic fields [19–21].

Another promising candidate in the field of quantum magnetometers is the negatively charged nitrogen-vacancy (NV) centre in diamond due to its excellent sensing properties, including optically accessible spin state information [46], long coherence times even at room temperature [47] and large dynamic operation range [48]. A steadily growing number of new NV-related publications, see figure 1.2, and numerous recently founded start-ups technologically dealing with these colour centres, *e.g.* NVision Imaging Technologies GmbH[3], Diatope GmbH[4], Quantum Diamond Technologies Inc.[5] and ODMR Technologies Inc.[6], reflect the increased interest. In addition, existing companies, like Robert Bosch GmbH[3], Carl Zeiss AG[7] and Thales SA[3], see possibilities and opportunities for new products and applications using NV centres, such that development activities have been started on individual levels.

[2] https://quspin.com (2020/06/02)
[3] https://asteriqs.eu/consortium/ (2020/06/02)
[4] https://diatope.com/ (2021/12/18)
[5] https://quantumdiamondtech.com/ (2020/06/02)
[6] http://odmrtechnologies.com/ (2020/06/02)
[7] https://quantentechnologien.de/forschung/foerderung/schluesselkomponenten-fuer-quantentechnologien/miliquant.html (2020/06/02)

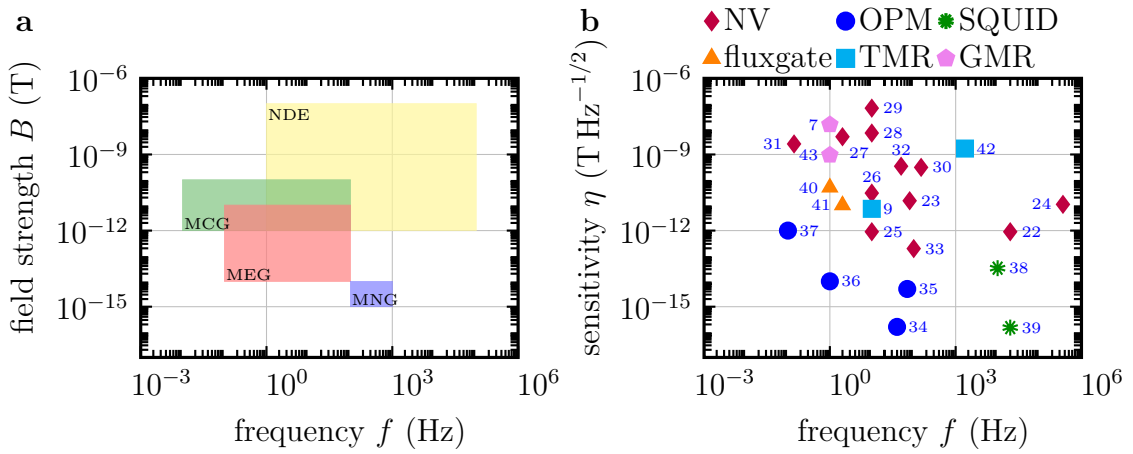

Figure 1.1: Magnetometer technologies and high sensitivity applications. a) Potential applications for high sensitivity magnetometers with required magnetic field resolution and corresponding frequency range [44, 45] including non-destructive evaluation (NDE), magnetocardiography (MCG), magnetoencephalography (MEG) and magnetoneurography (MNG). This subfigure is based on [45]. **b)** Selection of reported sensitivities η_B for different magnetometer technologies from recently published articles or data sheets of commercially available sensors. The achievements of NV magnetometers [22–33], OPMs [34–37], SQUIDs [38, 39], fluxgate sensors [40, 41], TMR sensors [9, 42] and GMR sensors [7, 43] are added to this graph dependent on the measurement frequency f. Further characteristics of these sensing technologies are summarised in table A.1.

NV centres consist of substitutional nitrogen atoms and adjacent vacancies in the crystal lattice of a diamond and possess optically accessible electron spins, which can be both optically initialised and read out. These colour centres show long coherence times at room temperatures [47] and enable the detection of static and oscillating magnetic fields [22, 49, 50] with a high dynamic range [48]. In addition to the detection of magnetic fields, NV centres are able to measure electric fields [51–53], temperature [54, 55], pressure [56], strain [57, 58] and pH (potential of hydrogen) scale [59]. Single spin detection [60], nuclear magnetic resonance (NMR) spectroscopy [61–63], non-destructive material analysis [64] and rotation measurements [65–69] have been successfully demonstrated by NV centres. Further fields are related to condensed and dark matter physics [70, 71], quantum computing [72], simulation [73, 74], information processing [75, 76], aerospace [77] and geology [78, 79].

For an industrial use of the NV sensing technology, two applications have significant potential to create new business cases and markets due their sensing capabilities

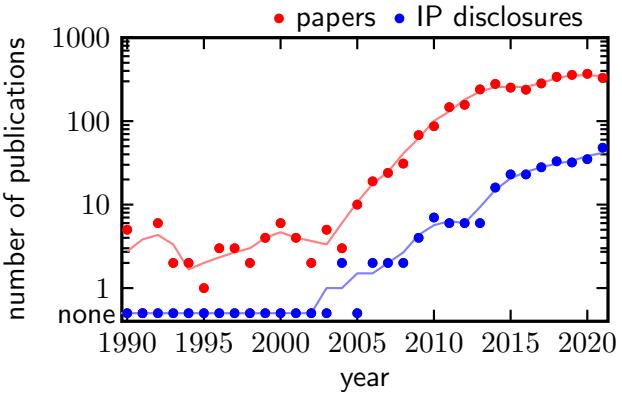

Figure 1.2: Number of published papers in scientific journals and intellectual property (IP) disclosures related to NV centres during the past decades. A literature search on scientific articles[1] (red data) based on the database Scopus® and a search on IP disclosures[2] (blue data) based PatBase Express® related to NV centres were conducted using the following keywords: *"nitrogen-vacancy cent*" OR "nitrogen vacancy cent*" OR "NV cent*" OR "NV diamond"*. Both search studies were conducted on 2nd January 2022. Lines of moving mean (of three neighbouring data points) are added to the graph.

combining high spatial resolution, high dynamic range and high sensitivity.

First, current imaging using NV centres offers a wide range of applications in the field of diagnostic technique for electronic components [80], *e.g.* graphene structures [81], integrated circuits [82,83], field-programmable gate arrays [82], hard disk drives [84] and batteries [85, 86]. Second, bio-imaging of magnetic signals [87], especially magnetic signals by neuronal brain activity [20, 23, 88], could offer new promising applications. It includes tools that enable less intrusive and more accurate diagnoses of diseases. Recently demonstrated experiments for bio-imaging using NV centres are the non-invasively magnetic imaging of magnetotactic bacteria in living cells [89], imaging of action potentials of large axons [23], imaging of magneto-cardiac signals of a living rat [90], imaging of superparamagnetic particles to identify sentinel lymph nodes in breast cancer patients [91–93] and detection of hemoglobin [94] and ferritin [95].

Combining NV sensing with artificial intelligence (AI) methods, *e.g.* machine learning and artificial neural networks, may further improve the sensor's performance as well as widen the potential fields of applications. First NV experiments combined with AI methods have been recently demonstrated [96–100].

[8] https://scopus.com/ (2022/01/02)
[9] https://patbase.com/express/search_basic.asp (2022/01/02)

In order to transfer this NV sensing technology into industrial products, it must be ensured that the necessary components of NV sensors can be integrated into a compact system that is affordable, mass-producible and reliably functional under real-life conditions. Setting up such sensors, challenges are highly related to the development and manufacturability of the single sensor components as well as assembly and packaging aspects. Approaches and concepts for sensor miniaturisation [25,26,101–103] and first prototypes of integrated NV magnetometers have been recently demonstrated [28,30,31,104–106].

This work shows possible approaches to address the challenges of building NV magnetometers for a precise detection of magnetic fields with sub-nanotesla sensitivity in a compact and portable way. This paves the way for commercial use of the NV sensor technology for mass production with the possibility of new fields of applications.

Thesis Outline

This thesis is divided into three main parts: a theoretical description of the NV centre and its usage as magnetic field sensor followed by experimental sections, which include the design and experimental results of two integrated NV magnetometers, and a proof-of-principle of a new sensing approach and the appendices.

The theoretical part of this thesis starts with a fundamental description of NV centres in diamond, see chapter 2. This includes details about diamonds as their host material, the physical NV properties, the methods how to create them in the crystal lattice and the quantum effects needed for the magnetic field detection. This fundamental part about NV centres is followed by a chapter, which focuses on the design and development of high-sensitive NV magnetometers, see chapter 3. The fundamental limits to detect magnetic fields as well as how the performance of NV magnetometers can be optimised with respect to the relevant sensor elements are addressed in this chapter.

The following two chapters report on the progress of transferring this sensing technology from bulky laboratory setups into integrated and miniaturised sensor devices. A detailed description about the sensor designs, simulative considerations on relevant parameters affecting the performance of the sensors, as well as the achieved

results are given for the compact NV magnetometers. Chapter 4 presents a LED-based NV magnetometer with primary goal of minimising the construction volume of the sensor device. The performance of this LED-based sensor is mainly limited by the optical excitation power provided by the LED. Therefore, the sensor concept presented in chapter 5 uses an optical system composed of laser and fibre for the optical illumination of the NV centres to overcome this limitation. Further features, such as a balanced detection scheme referencing laser fluctuations, improved the magnetic field sensitivity. Whereas the sensor described in chapter 4 still uses bulky laboratory equipment of laser and microwave sources to optically excite and manipulate the NV spins, the integrated NV magnetometer in chapter 5 allows a portable measurement of magnetic fields by a sensor head featuring a complete integration of all functional components and achieving sub-nT $\mathrm{Hz}^{-1/2}$ magnetic field sensitivity.

One limiting factor for the detection of magnetic field by NV centres is the stability of the recorded fluorescence rate. This rate is typically affected by instabilities of the optical excitation, *e.g.* fluctuations of the laser output power. A novel sensing method is presented in chapter 6, which makes use of the excited-state lifetimes of a single NV centre to measure the electron spin resonance. This proof-of-principle demonstrates that the lifetime-based analysis can have advantages over the conventional intensity-based sensing technique.

The thesis is summarised in chapter 7 and an outlook about potential applications of NV centres follows this conclusion.

Appendix A provides supplementary information going beyond the chapters 2 to 5 and appendix B lists the abbreviations and symbols used in this dissertation.

2 The Nitrogen-Vacancy Centre In Diamond

Diamond is a host for more than 500 luminescent colour centres [107] including the NV centre [108, 109], the negatively charged silicon-vacancy (SiV) centre [110, 111], the negatively charged germanium-vacancy (GeV) centre [112,113] and the tin-vacancy (SnV) centre [114]. Due to its physical properties, diamond is an interesting platform for a wide range of scientific research activities. Especially the NV centre in diamond has proven to be a promising quantum sensing technology combining high magnetic sensitivity [22] and high spatial resolution [50]. This thesis therefore focuses on this point defect in diamond.

One important achievement in the research and development towards a sensitive magnetometry platform associated with the NV centre is the theoretical consideration of the optically detected magnetic resonance (ODMR) measurement, which was elaborated in 1949 [115]. Further milestones were the investigations of the optical pumping process by Loubser *et al.* in 1978 [116] and the observation of ODMR spectra in diamond with NV ensembles by Reddy *et al.* in 1987 and by van Oort *et al.* in 1988 [117,118]. Gruber *et al.* demonstrated the first spin manipulation of a single NV centre in 1997 [119]. The work of Wolf *et al.* in 2015 showed a magnetic field detection in the sub-picotesla range [22].

The following chapter covers the fundamental physics of the NV centre. Its first section gives an overview of the diamond (section 2.1). The second part of this chapter (section 2.2) addresses the physical structure of the NV centre, its generation in diamond, its electronic and optical properties, as well as its spin dynamics including spin Hamiltonian and spin resonance behaviour.

2.1 The Diamond

Diamond is a common host material for NV centres [120, 121]. Diamond not only evokes associations with gemstones and jewellery, but also finds great favour due to its material properties in a variety of industrial applications due to its material properties, such as grinding and polishing tools, optical elements and use in high-powered electronic and acoustic devices [122].

As diamond is a stable allotrope of carbon with sp^3 orbital hybridisation, carbon atoms are tetrahedrally arranged in the crystal lattice, see figure 2.1a. The crystal structure of diamond can be described by a unit cell with a two-atomic basis of a face-centred cubic (fcc) lattice with an atom-to-atom distance of 1.54 Å. Each of the carbon atoms in the crystal has four valence electrons forming covalent bonds with high binding energies to the nearest neighbours under an angle of 109.5° [123], see figure 2.1b.

These strong covalent bonds make the lattice extremely rigid such that diamond is the hardest naturally existing material with hardness values of (56 to 102) GPa [124]. Due to its large band gap between valence and conducting band of around 5.47 eV [125], diamond is an efficient thermal conductor and electrical insulator. Diamond is characterised by a high thermal conductivity of (0.9 to 2.3) $\mathrm{kW\,m^{-1}\,K^{-1}}$ [126] and a relatively low electrical conductivity with a resistivity at room temperature of $(10^{13}$ to $10^{16})\,\Omega\,\mathrm{m}$ [127]. Additionally, it has a high refractive index of $n = 2.426$ for a wavelength of 532 nm [128] and is optically transparent for light in the ultraviolet to the infrared wavelength range [129]. Biocompatibility, inertness [130] and an extremely low thermal expansion coefficient are further characteristics [131]. All these properties enable the material diamond for a variety of engineering and research applications.

2.1.1 Diamond Synthesis

The need of synthetically fabricated diamonds is not only linked to the increased demand of diamond material, but also associated to the required reproducible material properties for specific applications [122]. Besides the shock wave synthesis [132], two

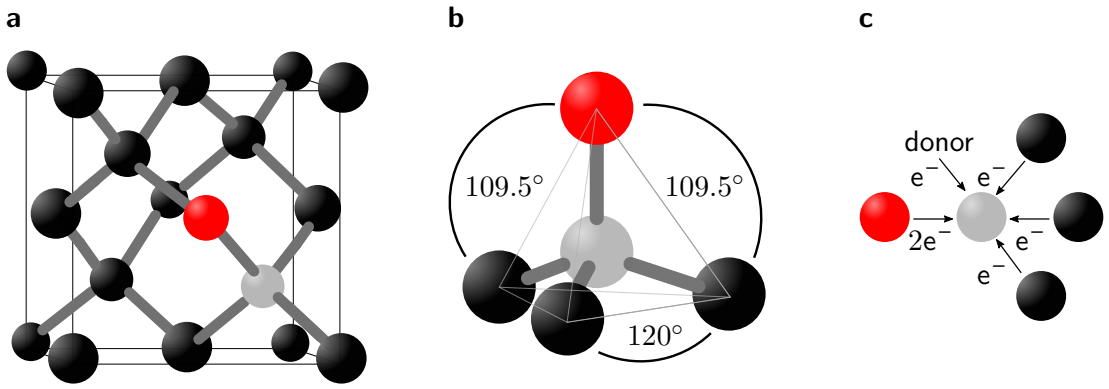

Figure 2.1: Structure of the diamond and the NV centre. a) Schematic drawing of the diamond lattice consisting of carbon atoms (black), a nitrogen atom (red) and a vacancy spot (grey). The neighbouring atoms have a distance of 1.54 Å between neighbouring atoms and the lattice constant is 3.57 Å [123]. **b)** Schematic drawing of the NV centre showing the tetrahedral arrangement of the atoms with a bonding angle of 109.5° [123]. The carbon atoms have a rotational symmetry of 120° [123]. **c)** Schematic drawing of the electronic configuration of the negatively charged NV centre, which possesses six electrons. The surrounding three carbon atoms provide one electron each, two electrons are from the nitrogen atom and one electron from a donor of the diamond lattice.

main synthesis methods have emerged: the method of high pressure high temperature (HPHT) [133] and the method of chemical vapour deposition (CVD) [122, 134].

The method of HPHT, as already indicated in its naming, imitates the growth conditions under which diamonds are formed in nature [133]. A source of pure carbon, typically graphite or diamond seed, is heated at temperatures above 1300 K and put mechanically under pressure with typical values above 5 GPa [135]. Under these conditions, carbon melts and thermodynamically transfers into diamond. By adding a solvent metal to the carbon source, such as nickel, cobalt or iron, the growth rate can be increased resulting in a faster synthesis [136].

Whereas HPHT diamonds can be grown on large-scales and at relatively low production costs [128], it is difficult to control the impurity concentration of these grown diamonds [137]. HPHT grown diamonds typically contain a non-negligible number of impurities, especially nitrogen, which are incorporated into the diamond lattice [120]. In recent years, several advances have been achieved to address this issue and improve the level of crystal purity for HPHT grown diamonds [138, 139].

The technique of CVD is the other prominent synthesis method. Several CVD methods have been developed that enable a growth of diamonds at lower pressure with values of (10-300) mbar [135] and lower temperatures with values of (700-1200) °C [140] compared to the conditions required for HPHT synthesis. This includes microwave-assisted plasma-enhanced CVD [135], plasma-enhanced CVD [141] and hot filament CVD [132].

For CVD in general, a diamond seed (for homoepitaxial growth) and a non-diamond substrate (for heteroepitaxial growth) is placed inside a CVD chamber. A gas mixture is added to the chamber, which typically contains hydrogen and a small percentage of carbon ($< 5\%$), mostly methane [122, 135]. In order to start the deposition of carbon atoms on the provided seed/substrate, the gas mixture needs to be activated either thermally using hot filaments or using a plasma [142]. In recent years, CVD synthesis using plasma and microwave (MW) irradiation has become the most popular CVD method [142]. Under the applied conditions of temperature and pressure in the CVD chamber, radicalised carbon atoms bond to the surface of the provided material forming both sp^2 and sp^3 orbitals [120]. The highly activated hydrogen atoms stabilise the deposited carbon layers, as these atoms are more likely to etch away the sp^2 carbon bonds than the sp^3 bonds [120]. This enables the growth of diamonds layer by layer [135].

In general, CVD synthesis allows to grow diamonds with a fine control of incorporated impurities in the crystal lattice, whereas the impurity control can be more challenging for the HPHT synthesis [120, 143]. This is mainly linked to the fact that the resulting diamond quality originates from the purity of the given gas source and solid precursor material [120, 122].

To sum up, the challenges of CVD and HPHT synthesis of diamonds are related to the purity and quality of the grown material described by the concentration of impurities and lattice defects. Additional factors are strain properties, the size and orientation of the grown material. Whereas the HPHT synthesis is favourable to produce diamonds with lower strain and fewer lattice defects than CVD grown diamonds [120], the CVD synthesis has the advantage of easily controlling the concentration of incorporated impurities in the crystal [122], which can be more difficult to achieve for the HPHT method [137].

2.2 The Nitrogen-Vacancy Centre

2.2.1 NV Physical Structure

The NV centre is a stable colour defect consisting of a substitutional nitrogen atom and an adjacent vacancy spot in the crystal of a diamond [109], see figure 2.1b. In the tetrahedral arrangement of the lattice points in the crystal with a bonding angle of 109.5° [123], the sp^3 hybridised orbitals of the nitrogen atom and the three neighbouring carbon atoms dangling in the vacancy form a C_{3v} symmetry [109,144]. The bonding line between the nitrogen atom and the vacancy is the rotation axis of the colour centre with rotation invariance for the three carbon atoms around 120°, see figure 2.1b. This line is called the 'NV axis'. As a consequence of the rotation invariance, the NV centre can take four equivalent orientations along the $\langle 111 \rangle$ crystallographic axes: $[111]$, $[1\bar{1}\bar{1}]$, $[\bar{1}\bar{1}1]$ and $[\bar{1}1\bar{1}]$ [145,146].

2.2.2 NV Formation

The NV centre can be either created during the synthesis of diamonds or after the growth process [132]. Forming the negative charged state of an this colour centre requires a substitutional nitrogen atom that traps a diffusing vacancy to occupy an adjacent lattice spot. In addition, an electron is required for the negative charge state provided by a donor from the lattice.

For the NV formation during the growth process, a nitrogen-containing precursor material is added to the synthesis chamber, such that the introduced nitrogen can occupy lattice positions in the grown layers. However, the NV formation during the synthesis process can be quite challenging, as typically only a small fraction of the substitutional nitrogen atoms is converted into NV centres [120]. Another method during the synthesis process is the combination of CVD synthesis and δ-doping [147,148]. This typically creates thin layers of NV centres.

Forming an NV centre directly during the growth process has the advantage that it can be preferentially aligned along one specific crystallographic axis of the diamond, see section 2.2.1. This is in contrast to post-growth methods, which typically result in a random distribution of NV centres along all four crystallographic dir-

ections [132]. Recent reports demonstrated alignment ratios along a single [111] crystallographic orientation of up to 99% [146, 149, 150]. As of today, the preferential alignment of NV centres is mainly limited to diamonds containing a relatively low NV concentration [120].

The growth of diamonds is typically accompanied by forming a relatively low number of NV centres. To overcome this limitation and thus increase the NV concentration, several recipes of post-growth methods have been established [132, 135, 151]. The typical steps of post-growth NV formation comprise the introduction of nitrogen impurities, the creation of vacancies and annealing steps. One of the most common methods to introduce nitrogen atoms is ion implantation [152, 153] with energies ranging from keV to MeV [135]. Methods to create vacancies are *i.a.* electron irradiation [154–156], neutron irradiation [157], hot irradiation [151, 157] and laser processing [151, 158]. These techniques to create impurities and vacancies are usually combined with post-annealing steps with temperatures above 600 °C - either at conditions of low pressure or of high pressure [120] - making vacancies mobile and repairing some of the lattice damages caused by the ion bombardment [159].

Detailed information about the NV formation in artificially grown diamonds are summarised by Radtke *et al.* [132] and Achard *et al.* [135].

2.2.3 NV Electronic Properties

The NV centre can exist in different charge states being primarily present as neutrally charged NV^0 centre [160, 161] and negatively charged NV^- centre [108, 121]. The positively charged NV^+ centre has only recently been observed in experiments [162]. Unbound electrons from the nitrogen and carbon atoms, which are adjacent to the vacancy, determines the electronic configuration of the NV centre.

The NV^0 centre is formed by five electrons, where two of them are from the nitrogen atom and three are from the dangling bonds of the carbon atoms adjacent to the vacancy [161]. Capturing an additional electron from a donor in the lattice results in the NV^- centre [163]. These two electronic configurations differ significantly in their optical properties and magnetic characteristics. The NV^0 centre is paramagnetic and possesses an electron spin of $S = 1/2$ [108], since one of its five electrons remains unpaired without forming covalent bonds. The NV^- centre

is characterised by an electron spin of $S = 1$ resulting from the two unpaired electrons [164], see figure 2.1c. Besides the differences in electron spin properties, the NV^0 and NV^- centres are optically active and can be clearly distinguished by their emission spectra with corresponding photon side bands [165], see figure 2.2. NV^0 shows a zero-phonon line (ZPL) at 2.15 eV corresponding to a wavelength λ_{ZPL} of 575 nm [166], whereas the ZPL of NV^- is at 1.945 eV with $\lambda_{ZPL} = 637$ nm [167].

In contrast to NV^0 and NV^- centres, the understanding of the NV^+ centre is still limited due to a lack of clear optical and magnetic signatures [165].

Since the focus of this thesis is on the negatively charged NV centre in diamond, the abbreviation 'NV' stands for the colour centre with this charge state in the following.

The unique sensing capabilities of the NV centre rely on the physics of its intrinsic electron spin. To understand the spin dynamics, the electronic structure and the spin levels need to be taken into account. Considering the C_{3v} symmetry of an NV centre, the electronic structure can be modelled by theoretical group theory within the band gap of a diamond [144, 168]. The energy scheme consists of a spin triplet in the ground state with $^3A_2$ symmetry and a spin triplet in the excited state with ^3E symmetry [169], see figure 2.3. In addition to these triplets, the group theory reveals two intermediate singlets states $^1A_1$ and ^1E between ground and excited states [169]. Coulomb interactions split the ground and excited states by an energy of 1.945 eV [167, 170] resulting in an optical transition of 637 nm [171].

As the NV centre's electron spin is a $S = 1$ system [164], three electron spin sublevels exist. These sublevels are denoted by the spin quantum numbers $m_s = 0$ and $m_s = \pm 1$ [172]. Spin-spin interactions between the two unpaired electrons of the NV centre lift the degeneracy of the sublevels ($m_s = 0$ and $m_s = \pm 1$) in the ground state resulting in a zero-field splitting (ZFS) of $D_{gs} = 2.87$ GHz [173], see figure 2.3. At ambient conditions, a similar zero-field splitting can be observed for the sublevels of the excited state with a splitting parameter of $D_{es} = 1.42$ GHz [174] caused by the dynamic Jahn-Teller effect [175].

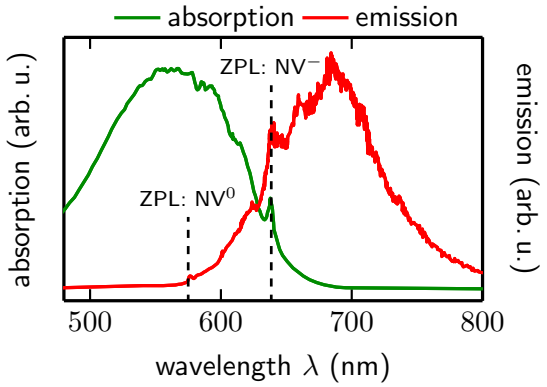

Figure 2.2: Absorption and emission of the NV centre. Sketch of the absorption and emission spectra of the NV centre with a ZPL at 575 nm for the NV^0 centre [166] and a ZPL at 637 nm for the negatively charged NV centre [167]. This figure is based on [176].

2.2.4 NV Optical Properties

As mentioned in section 2.2.3, the NV centre's optical transition from the ground to the excited level is characterised by a ZPL of 637 nm [167]. This ZPL is accompanied by broad phonon sidebands with partially overlapping emission and absorption spectra at room temperature conditions, see figure 2.2. Whereas the absorption spectrum covers wavelengths down to approximately 450 nm [177], the broad emission band ranges up to roughly 800 nm [108] with a peak at around 680 nm [178].

The energy level scheme shown in figure 2.3 may help to understand the spin dynamics and fluorescing properties of the NV centre. Spin population can be off-resonantly excited from the $^3A_2$ to the ^3E levels by optical illumination [179], *e.g.* using a laser with a wavelength of 532 nm. This population transfer is spin-conserving due to a weak spin-orbit interaction [180], which means that $\Delta m_s = 0$ is fulfilled. After a non-radiative de-excitation process of less than 0.1 ps [181], the spin population relaxes back to the ground level.

From the ^3E level, two decay paths exist, see figure 2.3. The direct decay path is spin-conserving with a decay time of roughly 12 ns [182] accompanied by the emission of a photon in the red spectral wavelength range [180]. For NV centres in nanodiamonds, this excited-state lifetime is approximately 25 ns long due to a different refractive index of the environment affecting the lifetime compared to NV centres in bulk diamond [121].

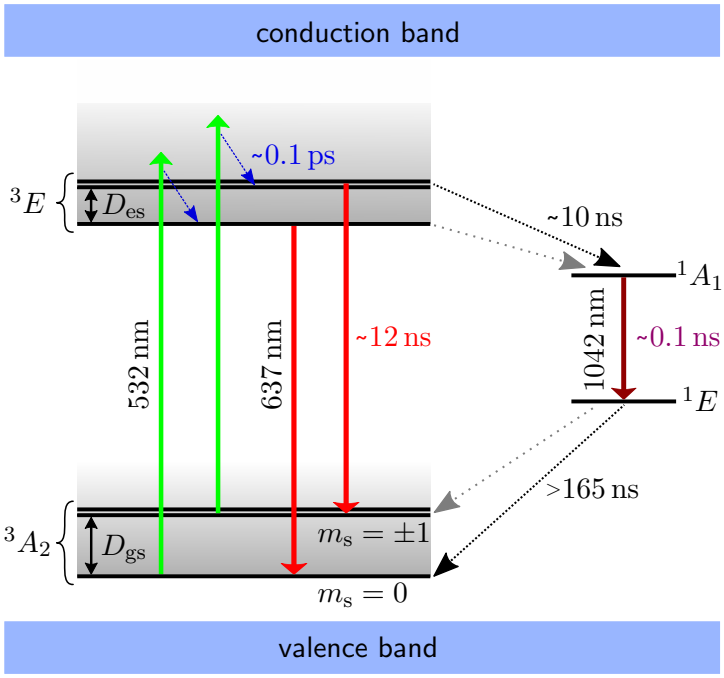

Figure 2.3: Energy level scheme of the NV centre's electron spin. The electron spin triplets of the ground state $^3A_2$ and excited state ^3E are located within diamond's band gap between the valence and conduction bands. The spin sublevels in the ground state are exemplarily labelled with the corresponding spin quantum number m_s. Optical excitation using green light, *e.g.* a laser with a wavelength of 532 nm, pumps spin population from the ground to the excited states (represented by solid green arrows). After a non-radiative, photonic decay process (dashed blue arrows), direct decay to the ground states is spin-conserving under the emission of fluorescence (solid red arrows) with wavelengths of (637 to 800) nm [108]. In contrast, the decay path via the ISC through the metastable singlet states $^1A_1$ and ^1E changes the spin state. This state change is accompanied with an infrared photon emission between the singlet spin levels (solid purple arrow). Strong (weak) non-radiative spin transitions are shown with dotted black (grey) arrows. The corresponding timescales of the decay paths [182–185] as well as the zero-field splittings in the ground and excited states are added to the schematic.

Besides the direct relaxation, spin population can also decay via the metastable singlet states $^1\mathrm{A}_1$ and ^1E to the ground level. In this case, the population transfer into the ground level with $m_s = 0$ is more likely than for states with $m_s = \pm 1$ [186], see figure 2.3. This decay path is called intersystem crossing (ISC) and includes the emission of an infrared photon with a wavelength of 1042 nm between $^1\mathrm{A}_1$ and ^1E [172, 187]. The infrared emission intensity is about four orders of magnitude weaker than the red fluorescence emission from the direct decay [188]. Regarding

the time constants of the ISC, relaxation between the ^3E to the $^1\mathrm{A}_1$ level takes place within roughly 10 ns [184]. The observed lifetime for the $^1A_1$ state [184] is about 100 ps, while the decay time from the ^1E to the ground level is temperature-dependent and varies between (165 to 371) ns [183, 185].

Probabilities for the decay path selection - either the direct radiative decay or the relaxation via the ISC - are correlated to the initial spin state before optical excitation. Spins with a quantum number of $m_\mathrm{s} = \pm 1$ show a higher probability to choose the decay path via the ISC compared to spins with $m_\mathrm{s} = 0$ [128, 189]. Due to the resulting differences in decay times between the two decay paths [184, 188], roughly 30% less photons are emitted by spins with $m_\mathrm{s} = \pm 1$ compared to spins with $m_\mathrm{s} = 0$ [190]. The coexistence of the different fluorescence intensities and the pronounced population transfer into the $m_\mathrm{s} = 0$ ground state after the ISC enables optical pumping into the $m_\mathrm{s} = 0$ state and therefore a proper spin preparation after several excitation cycles [191]. Optical initialisation and spin readout are key features for the spin resonance detection enabling NV centres to measure magnetic fields [192]. Details about the sensing principles are summarised in section 2.2.6.

2.2.5 NV Spin Hamiltonian

As the NV centre is embedded in the crystal lattice and surrounded by other defects, its electron spin interacts not only with the nuclear spin of the intrinsic nitrogen atom (either ^{14}N or ^{15}N), but also couples to other spins being present in the crystal lattice, *e.g.* ^{13}C nuclear spins. As the focus of this thesis is on the NV centre's electron spin, the electron's ground state Hamiltonian $\mathcal{H}_\mathrm{gs}$ will be discussed in the following. Main contributions to $\mathcal{H}_\mathrm{gs}$ in the absence of an external magnetic field are electron spin-spin interactions causing the ZFS, hyperfine couplings with nearby nuclear spins and quadrupole interactions with nuclear spins. If an external magnetic field is present, electron and nuclear spin Zeeman interaction further contribute to $\mathcal{H}_\mathrm{gs}$. The resulting Hamiltonian can be expressed by the sum of the contributing components [109, 193, 194]:

$$\mathcal{H}_\mathrm{gs} = \underbrace{\mathcal{H}_\mathrm{fine}}_{\substack{\text{fine}\\\text{interaction}}} + \underbrace{\mathcal{H}_\mathrm{hf}}_{\substack{\text{hyperfine}\\\text{interaction}}} + \underbrace{\mathcal{H}_\mathrm{quad}}_{\substack{\text{quadrupole}\\\text{interaction}}} + \underbrace{\mathcal{H}_\mathrm{eZ}}_{\substack{\text{electron Zeeman}\\\text{interaction}}} + \underbrace{\mathcal{H}_\mathrm{nZ}}_{\substack{\text{nuclear Zeeman}\\\text{interaction}}} \tag{2.1}$$

As stated in section 2.2.3, electron spin-spin interactions due to the NV centre's two unpaired electrons lead to a fine structure with a degeneracy of the $m_\mathrm{s} = 0$ and $m_\mathrm{s} = \pm 1$ sublevels, see figure 2.4. The corresponding Hamiltonian can be expressed by [116]

$$\mathcal{H}_\mathrm{fine} = \hat{\boldsymbol{S}}^\dagger \, \mathbb{D} \, \hat{\boldsymbol{S}} = h\, D \left[\hat{\boldsymbol{S}}_{\boldsymbol{z}}^2 - \frac{1}{3} S(S+1) \right] + E \left(\hat{\boldsymbol{S}}_{\boldsymbol{x}}^2 - \hat{\boldsymbol{S}}_{\boldsymbol{y}}^2 \right), \tag{2.2}$$

where h is the Planck constant, $\hat{\boldsymbol{S}}$ the electronic spin operator with $\hat{\boldsymbol{S}}^\dagger = \left(\hat{\boldsymbol{S}}_{\boldsymbol{x}}, \hat{\boldsymbol{S}}_{\boldsymbol{y}}, \hat{\boldsymbol{S}}_{\boldsymbol{z}} \right)$ and $\mathbb{D}$ the electron interaction tensor. D and E are the axial and off-axial ZFS parameters. Whereas D is temperature-dependent and characterised by D_gs at room temperature [173] with a dependence of $\mathrm{d}D/\mathrm{d}T \approx -74.2\,\mathrm{kHz\,K^{-1}}$ [195], E depends on the strain condition of the used diamond sample [193]. Typically, the effect of strain on the splitting is much smaller than the ZFS, *i.e.* $E \ll D$ [109, 193].

The NV electron spin can further couple to the spin bath generated by nuclear spins, which are in close proximity to the NV centre. The interactions of electron and nuclear magnetic moments lead to a hyperfine energetic splitting, see figure 2.4. As the NV centre is composed of a nitrogen atom containing a nuclear spin (either ^{14}N or ^{15}N), a hyperfine interaction is intrinsically included. The contribution of additional couplings to other nuclear spins, *e.g.* nearby ^{13}C spins, strongly depends on the distance between the NV centre and the nuclear spin [196]. The Hamiltonian describing this hyperfine interaction can be expressed by

$$\mathcal{H}_\mathrm{hf} = \hat{\boldsymbol{S}}^\dagger \, \mathbb{A} \, \hat{\boldsymbol{I}} = A_\mathrm{gs}^\parallel \, \hat{\boldsymbol{S}}_{\boldsymbol{z}} \, \hat{\boldsymbol{I}}_{\boldsymbol{z}} + A_\mathrm{gs}^\perp \left(\hat{\boldsymbol{S}}_{\boldsymbol{x}} \, \hat{\boldsymbol{I}}_{\boldsymbol{x}} + \hat{\boldsymbol{S}}_{\boldsymbol{y}} \, \hat{\boldsymbol{I}}_{\boldsymbol{y}} \right), \tag{2.3}$$

where $\hat{\boldsymbol{I}}$ is the nuclear spin operator with $\hat{\boldsymbol{I}}^\dagger = \left(\hat{\boldsymbol{I}}_{\boldsymbol{x}}, \hat{\boldsymbol{I}}_{\boldsymbol{y}}, \hat{\boldsymbol{I}}_{\boldsymbol{z}} \right)$ and $\mathbb{A}$ the hyperfine interaction tensor. $A_\mathrm{gs}^\parallel$ and $A_\mathrm{gs}^\perp$ are the axial and transverse hyperfine coupling constants with $A_\mathrm{gs}^\perp$ with corresponding values given in table 2.1 [197].

In addition to the hyperfine coupling, quadrupole interaction occurs for nuclear spins with $I > 1/2$ [198], *e.g.* ^{14}N. The corresponding Hamiltonian can be expressed by [194]

$$\mathcal{H}_\mathrm{quad} = \hat{\boldsymbol{I}}^\dagger \, \mathbb{Q} \, \hat{\boldsymbol{I}} = Q \left[\hat{\boldsymbol{I}}_{\boldsymbol{z}}^2 - \frac{1}{3} I(I+1) \right], \tag{2.4}$$

where $\mathbb{Q}$ is the quadrupole interaction tensor with Q as the nuclear quadrupole splitting parameter with corresponding value given in table 2.1 [199].

The application of an external magnetic field $\boldsymbol{B}$ with $\boldsymbol{B}^\dagger = (B_x, B_y, B_z)$ lifts the

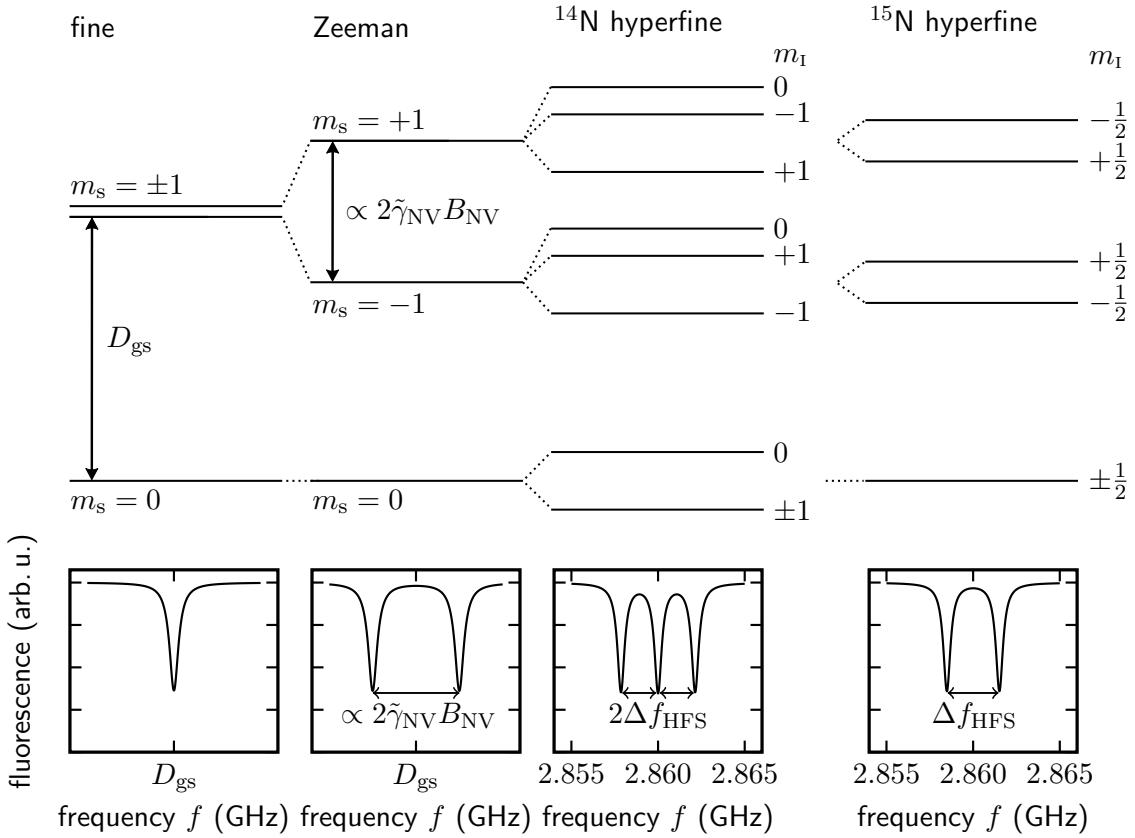

Figure 2.4: NV energy level scheme with corresponding ODMR spectra. The ground state configuration of the NV centre in this level scheme includes the fine interaction, the electron Zeeman interaction and the hyperfine interaction with the intrinsic nitrogen nuclear spin of the isotopes ^{14}N and ^{15}N. The corresponding ODMR spectra for these interactions are shown below, respectively. This figure is based on [200–202].

degeneracy of the electron spin levels corresponding to $m_\mathrm{s} = \pm 1$. It introduces an additional splitting of the nuclear spin levels with quantum numbers $m_\mathrm{I} = \{0; \pm 1\}$ for ^{14}N and $m_\mathrm{I} = \{\pm 1/2\}$ for ^{15}N, see figure 2.4. These interactions due the Zeeman effect are summarised by $\mathcal{H}_\mathrm{eZ}$ and $\mathcal{H}_\mathrm{nZ}$ with

$$\mathcal{H}_\mathrm{Z} = \mathcal{H}_\mathrm{eZ} + \mathcal{H}_\mathrm{nZ} = \tilde{\gamma}_\mathrm{NV}\, \boldsymbol{B}^\dagger\, \hat{\boldsymbol{S}} + \tilde{\gamma}_\mathrm{n}\, \boldsymbol{B}^\dagger\, \hat{\boldsymbol{I}}, \tag{2.5}$$

where $\tilde{\gamma}_\mathrm{NV} = \gamma_\mathrm{NV}/2\pi = g_\mathrm{e}\mu_\mathrm{B}/h \approx 28.024\,\mathrm{GHz\,T^{-1}}$ is the gyromagnetic ratio of the electron spin divided by 2π [204] with the Landé factor $g_\mathrm{e} = 2.0028$ [116] and the Bohr magneton μ_B. The reduced gyromagnetic ratio of the nuclear spin is described by $\tilde{\gamma}_\mathrm{n}$ with corresponding values given in table 2.1.

Table 2.1: Comparison of the interaction parameters of the nitrogen isotopes. The values of the reduced nuclear gyromagnetic ratio $\tilde{\gamma}_\mathrm{n}$, the axial hyperfine parameter $A_\mathrm{gs}^\parallel$, the transverse hyperfine parameter $A_\mathrm{gs}^\perp$ and the nuclear quadrupole splitting parameter Q are listed for ^{14}N and ^{15}N in this table. Note that the quadrupole splitting exists only for ^{14}N [198].

Coefficient	Nitrogen isotope	Value	Reference
$\tilde{\gamma}_\mathrm{n}$	^{14}N	$3.077\,\mathrm{MHz\,T^{-1}}$	[203]
	^{15}N	$-4.316\,\mathrm{MHz\,T^{-1}}$	[203]
$A_\mathrm{gs}^\perp$	^{14}N	2.70 MHz	[197]
	^{15}N	3.65 MHz	[197]
$A_\mathrm{gs}^\parallel$	^{14}N	−2.14 MHz	[197]
	^{15}N	3.03 MHz	[197]
Q	^{14}N	−4.945 MHz	[199]

The contributions of the spin interactions from equations 2.2 to 2.5 result in the total ground state Hamiltonian $\mathcal{H}_\mathrm{gs}$ described by

$$\mathcal{H}_\mathrm{gs} = \hat{\boldsymbol{S}}^\dagger\,\mathbb{D}\,\hat{\boldsymbol{S}} + \hat{\boldsymbol{S}}^\dagger\,\mathbb{A}\,\hat{\boldsymbol{I}} + \hat{\boldsymbol{I}}^\dagger\,\mathbb{Q}\,\hat{\boldsymbol{I}} + \tilde{\gamma}_\mathrm{NV}\,\boldsymbol{B}^\dagger\,\hat{\boldsymbol{S}} + \tilde{\gamma}_\mathrm{n}\,\boldsymbol{B}^\dagger\,\hat{\boldsymbol{I}}. \tag{2.6}$$

2.2.6 NV Spin Resonance

Computing the eigenenergies of the spin Hamiltonian from equation 2.6 reveals information about the transition frequencies of the NV centre's electron spin, see figure 2.4. These electron spin resonance (ESR) frequencies can be experimentally recorded due to the spin-dependent fluorescing property and the ability to transfer spin population between the m_s sublevels using microwave pulses, see section 2.2.4.

The simplest method to detect these resonances is the technique of continuous-wave optically detected magnetic resonance (CW-ODMR) [119]. The electron spin is optically pumped into the $m_\mathrm{s} = 0$ state resulting in the emission of red fluorescence. In addition to the continuous illumination, an oscillating microwave field is simultaneously applied and its frequency is varied. The $m_\mathrm{s} = 0$ state, characterized by a high level of emitted fluorescence intensity, remains unaffected until the irradiated energy of the microwave field matches the energy of the spin transition between the $m_\mathrm{s} = 0$ and $m_\mathrm{s} = \pm 1$ sublevels. In the resonant case, the spin flips, changes its state and the emitted fluorescence intensity is reduced by up to 30%

compared to the level of $m_s = 0$ [190], see figure 2.4. From the position of the dip in the ODMR fluorescence spectrum, the ZFS parameter D of the fine interaction can be determined [173]. At room temperature condition, it is described by D_{gs}.

Any externally applied magnetic field $\boldsymbol{B}$ changes the eigenenergies of $\mathcal{H}_{gs}$ resulting in two ESR frequencies $f_\pm$ of the selected spin [193]. This field lifts the degeneracy of the $m_s = \pm 1$ sublevels and two resonance dips can be observed in the recorded ODMR spectrum due to the induced electron Zeeman splitting, see figure 2.4. The projection of $\boldsymbol{B}$ onto the NV axis (defined as B_{NV}) has strong impact on the ESR frequencies. For magnetic fields with a weak field projection onto the NV axis with $B_{NV} < 5\,\mathrm{mT}$, the resonance frequencies of the spin transitions between the $m_s = 0$ and $m_s = \pm 1$ states are given by [193]

$$f_\pm = D_{gs} \pm \sqrt{(\tilde{\gamma}_{NV} B_{NV})^2 + E^2}. \tag{2.7}$$

This formula describes the ESR frequencies of an ODMR measurement at room temperature, where the temperature dependence of D is not taken into account. Additionally, the hyperfine interaction is neglected. For a sample with relatively low strain, equation 2.7 follows to

$$f_\pm \approx D_{gs} \pm \tilde{\gamma}_{NV} B_{NV}. \tag{2.8}$$

This linear dependence of the ESR frequencies enables an NV centre to precisely measure magnetic fields [49, 193]. By including the temperature dependence of D, a measurement of both magnetic field and temperature can be carried out simultaneously with an NV centre [54, 55].

Since the crystal structure of a diamond allows four possible orientations of the NV centre along the crystallographic axes, see section 2.2.1, the projection strength of the external magnetic field B_{NV} onto the four NV axes may differ for each NV orientation. This results in up to eight ESR frequencies that can be measured in an ODMR spectrum for an NV ensemble. By measuring all ESR frequencies, the magnetic field vector can be fully reconstructed [205, 206]. A detailed description of how field extraction is performed is summarized by Balasubramanian *et al.* [207].

In addition to the fine and Zeeman interactions, the technique of CW-ODMR is

capable to resolve the hyperfine interactions between the electron and nuclear spins. For this purpose, the interplay between optical pumping and spin manipulation needs to be optimised [120, 200, 208]. Three resonance dips for each NV orientation and spin transition can be observed in the spectrum, if ^{14}N is the present nitrogen isotope, whereas two dips are visible for ^{15}N [201], see figure 2.4.

Going beyond the method of CW-ODMR, further sensing techniques have been developed to measure the NV spin state information, from which the magnetic field information can in turn be derived. These include pulsed ODMR [200, 208, 209] and Ramsey measurements [120, 200, 210]. Since this thesis is limited to the use of CW-ODMR measurements in the experimental results shown (sections 4.3, 5.3 and 6.3), reference is made to the work of Barry *et al.* [120] and Levine *et al.* [200] for the other measurement techniques.

3 Magnetometry Using Nitrogen-Vacancy Centres

Magnetic field sensing experiments using NV centres in diamond can be divided into experiments with a single NV centre or NV ensembles hosted either in bulk diamond or in nanodiamonds. According to Webb *et al.* [211], the experimental scope is another classification factor distinguishing between bulk magnetometry, wide-field imaging magnetometry and scanning magnetometry. NV magnetometry experiments can be further split by detected type of magnetic field, *i.e.* direct current (DC) and alternating current (AC) fields [22, 202], how the spin state information is obtained, *i.e.* by optical or electrical readout [50, 212], and about the gathered field information, *i.e.* scalar or vector magnetometry [27, 213].

Achievements in measuring magnetic fields using NV centres include the detection of AC signals with a sensitivity of $0.9\,\mathrm{pT\,Hz^{-1/2}}$ measured by Wolf *et al.* [22], resolving action potentials of neurons in a worm with $15\,\mathrm{pT\,Hz^{-1/2}}$ by Barry *et al.* [23] and the demonstration of a vector field detection with $50\,\mathrm{pT\,Hz^{-1/2}}$ performed by Schloss *et al.* [213]. A DC gradiometer with $2.6\,\mathrm{pT\,Hz^{-1/2}}$ has been recently demonstrated by Zhang *et al.* [31], whereas novel approaches using cavities [26] and flux concentrators [25, 31, 33] enable new possibilities for measurements. Kim *et al.* demonstrated an integrated solution for an NV magnetometer using the complementary metal-oxide-semiconductor (CMOS) technology [103, 214].

The following chapter addresses the magnetic field sensitivity, which can be achieved by NV centres (section 3.1), and discusses how to set up a high sensitive NV magnetometer (section 3.2). In this detailed analysis, the key elements for an NV magnetometer, *i.e.* diamond material, optical spin excitation, offset magnetic field, spin manipulation and optical spin readout, are discussed and a short conclusion is given.

3.1 Magnetic Field Sensitivity

One important figure of merit for magnetometers is the magnetic field sensitivity η_B characterised by

$$\eta_B = \delta B_{\min} \sqrt{t}, \tag{3.1}$$

which describes the minimal magnetic field strength $\delta B_{\min}$ that still can be resolved within a measurement time t with a signal-to-noise ratio of 1. This quantity enables a classification of magnetic field sensors in terms of absolute precision with respect to the needed sensing time, see figure 1.1b.

The fundamental sensitivity limit for NV centres is given by spin projection-noise [15, 120]. Since the spin state of the NV centre is usually not determined directly, but via the emitted fluorescence, *e.g.* in CW-ODMR measurements, photon shot noise must be added to the noise consideration [120, 200]. Especially for conventional readout techniques, where the number of detected photons is relatively low, photon shot-noise is the dominating noise quantity [215]. Under these circumstances, projection-noise can be neglected [215].

The intensity profile $\mathcal{I}(\nu)$ of an ESR depends on the applied microwave frequency ν, see section 2.2.6, and can be described by [208]

$$\mathcal{I}(\nu) = \mathcal{R}\left[1 - C\mathcal{F}\left(\frac{\nu - \nu_{\text{res}}}{\Delta\nu}\right)\right], \tag{3.2}$$

where $\mathcal{R}$ is the photon rate, C the measurement contrast, $\mathcal{F}$ the function of the lineshape, ν_{res} the resonance frequency and $\Delta\nu$ the linewidth of the curve characterised by the full width at half maximum. For CW-ODMR, the ESR curve can be typically characterised by a Lorentzian function [208].

Any change in the local magnetic field leads to a shift in the resonance frequency according to the Zeeman splitting [193]. The accuracy δB determining a change in the local magnetic field can be detected by an NV magnetometer. It depends on the noise of the measured signal $\delta\mathcal{S}(t)$ during the recording time t as well as on the amplitude of the sensor's response $\partial\mathcal{S}(t)/\partial B$, *i.e.*

$$\delta B = \frac{\delta\mathcal{S}(t)}{\partial\mathcal{S}(t)/\partial B}. \tag{3.3}$$

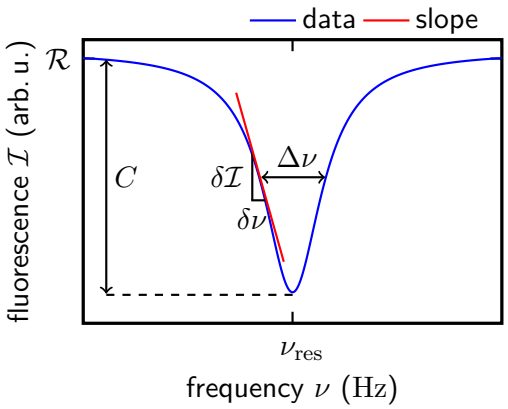

Figure 3.1: Electron spin resonance of the NV centre. The Lorentzian shape of the ESR for the detected fluorescence intensity $\mathcal{I}$ (blue curve) is characterised by the resonance frequency ν_{res}, the fluorescence rate $\mathcal{R}$, the contrast C and the linewidth $\Delta\nu$. NV centres are most sensitive to detect changes in the magnetic field at an applied microwave frequency, which corresponds to the position of maximum slope (red curve) of the ESR curve. This slope is described by the parameters $\delta\mathcal{I}$ and $\delta\nu$. This figure is based on [216].

For a photon shot-noise scaling, the uncertainty of the signal $\delta\mathcal{S}(t)$ behaves as follows

$$\delta\mathcal{S}(t) \propto \sqrt{\mathcal{I}\cdot t}, \tag{3.4}$$

which can be further approximated to $\delta\mathcal{S}(t) \approx \sqrt{\mathcal{R}\,t}$. The sensor's response $\partial\mathcal{S}(t)/\partial B$ describes the slope of the resonance curve shown in figure 3.1 and has the following relationship

$$\frac{\partial\mathcal{S}(t)}{\partial B} \propto \frac{\partial\mathcal{I}(\nu)}{\partial\nu}. \tag{3.5}$$

NV centres are most sensitive to small changes of the magnetic field at the position of maximum slope of the ESR curve leading to a δB_{min}, where

$$\left|\left(\frac{\partial\mathcal{I}(\nu)}{\partial\nu}\right)\right|_{\mathrm{max}} = \frac{C\mathcal{R}}{\Delta\nu\mathcal{P}_{\mathcal{F}}} \tag{3.6}$$

is valid [208]. Here, $\mathcal{P}_{\mathcal{F}}$ is a numerical parameter related to the specific profile $\mathcal{F}$ of the spin resonance and scales as $4/\left(3\sqrt{3}\right)$ for a Lorentzian profile [208]. Based on the equations 3.3 to 3.6, the photon shot-noise limited sensitivity results in [23]

$$\eta_{\mathrm{PSN}} \approx \frac{\mathcal{P}_{\mathcal{F}}}{\tilde{\gamma}_{\mathrm{NV}}}\frac{\Delta\nu}{C\sqrt{\mathcal{R}}}. \tag{3.7}$$

Whereas η_{PSN} from equation 3.7 represents the achievable sensitivity limit of an NV magnetometer in the photon shot-noise limit, additional sources of noise may worsen the sensor's performance [217]. Noise sources can be associated to the sensing operation like fluctuations in the optical pumping and spin manipulation processes, instabilities in the electronic circuits and temperature drifts, but disturbances in the surrounding magnetic field, *e.g.* induced by nearby power lines or moving objects like elevators and trains [217].

Taking into account the existing interactions between the NV diamond material used, the sensor elements and the operating parameters, a holistic view of the sensor system with regard to the desired application area is required for overall performance optimisation.

3.2 Sensitivity Optimisation

The capability to detect magnetic fields, which are in the nanotesla range and below, using NV ensembles is primarily determined by the setup characteristics of the used NV magnetometer. This includes the physical properties of the addressed NV centres and their host material diamond, such that parameters like NV concentration, NV orientation, coherence properties and strain impacting on the achievable sensitivity (section 3.2.1). Further limitations are associated with the operating parameters of the NV sensor, *i.e.* the optical excitation (section 3.2.2), the spin manipulation (section 3.2.4) and the optical spin readout (section 3.2.5). In order to use the NV sensing properties as optimally as possible, the applied processes of optical pumping and spin manipulation must ideally fit to the given properties of the NV centres. For many sensing applications, it is advisable to externally apply a static bias magnetic field (section 3.2.3). This enables a clear spectral separation of the spin resonances associated with the different NV orientations, such that the vector information of a measurable magnetic field can be extracted [207]. External factors, such as temperature fluctuations or interfering magnetic fields, may deteriorate the sensor performance and need to be minimised as good as possible.

In order to evaluate the sensing capabilities of an NV magnetometer, a simulative analysis of the photon shot-noise limited magnetic field sensitivity using equation 3.7 was carried out for different operating parameters of optical excitation and spin manipulation, which will be described in the following. The results of this simulation are shown in the figures 3.2 and 3.3.

In this simulation, a diamond is modelled as a rectangular body with a thickness z_{dia} of 0.5 mm and an NV concentration $[\mathrm{NV}^-]$ of 1 ppm. The NV centres are characterised by the specific spin times of T_1 being the spin-lattice relaxation time and T_2 the homogeneous decoherence time. Modelling the diamond used in the assembled prototypes from chapters 4 and 5, T_1 is set to 5 ms and T_2 to 100 µs.

A 532 nm laser with a beam diameter of d_{laser} and an optical power density of I_{opt} at the entering surface of the diamond excites the NV centres. For simplicity, a beam expansion inside the diamond due to Snell's law of refraction is neglected, such that inside the diamond a cylindrical volume of

$$V_{\mathrm{laser}} = \pi \left(\frac{d_{\mathrm{laser}}}{2} \right)^2 z_{\mathrm{dia}} \tag{3.8}$$

is excited. The power of the excitation light propagating through the diamond is attenuated due to the absorbing property of the NV centres according to the Beer-Lambert law. The power progression inside the diamond can be described by [218]

$$I(z) = I_{\mathrm{opt}} \exp\left(-\sigma [\mathrm{NV}^-] z \right), \tag{3.9}$$

where σ is the absorption cross-section with a value of $3.1 \times 10^{-17}\,\mathrm{cm}^2$ [219]. The fraction of light being absorbed by the NV centres is described by

$$p_{\mathrm{absorb}} = 1 - \frac{I\left(z = z_{\mathrm{dia}}\right)}{I_{\mathrm{opt}}}. \tag{3.10}$$

Considering the 0.5 mm thick diamond with 1 ppm NV centres, approximately 23.9% of the initial power is absorbed by the NV centres, if assuming that each NV centre in the illuminated volume is excited only once and reflections inside the diamond are neglected. The absorbed light is though not fully transferred into red fluorescence as ionisation processes switch between the negative and neutral charge states of

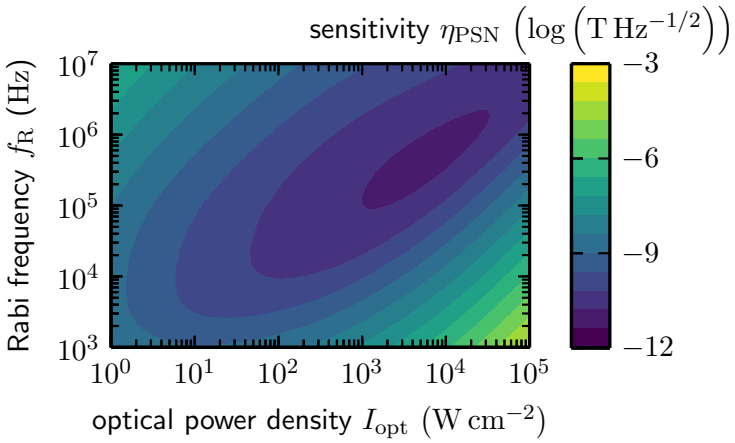

Figure 3.2: Simulative analysis of the achievable sensitivity for an NV ensemble magnetometer depending on the applied processes of optical pumping and spin manipulation. The achievable photon shot-noise limited sensitivity η_{PSN} of an NV magnetometer with specific properties is analysed according to equation 3.7 dependent on the applied optical power density I_{opt} and the resulting Rabi frequency f_{R}, which correlates to the applied spin manipulation. The detected photon rate, linewidth and contrast of measured spin resonance are modelled according to equations 3.12, 3.14 and 3.15, respectively. The corresponding 2D plots for $\Delta\nu$ and C are shown in figure A.1. Input values for this simulative analysis are a diamond thickness z_{dia} of $0.5\,\mathrm{mm}$ and an NV concentration of $1\,\mathrm{ppm}$. Spin times of $T_1 = 5\,\mathrm{ms}$ and $T_2 = 100\,\mu\mathrm{s}$ as well as an inhomogeneously broadened linewidth of $\Delta\nu_{\mathrm{inh}} = 100\,\mathrm{kHz}$ corresponding to $T_2^* \approx 3.18\,\mu\mathrm{s}$ are applied. For the spin resonance, a constant contrast factor of $\theta = 0.2$ is assumed [208]. Input parameters for the optical excitation are a laser diameter at the entering surface of the diamond of $50\,\mu\mathrm{m}$, an absorption coefficient of $3.1 \times 10^{-17}\,\mathrm{cm^2}$ [219] and a photon energy of $E_{\mathrm{ph}}^{532\,\mathrm{nm}} \approx 1.057 \times 10^{-13}\,\mathrm{J}$. The detected fluorescence rate $\mathcal{R}$ is calculated using equation 3.12 with input parameters of $p_{\mathrm{absorb}} \approx 23.9\%$, $\chi_{\mathrm{NV_0}} = 0.3$, $\xi_{\mathrm{col}} = 1.5\%$ and $\xi_{\mathrm{det}} = 50\%$.

the NV centres [177, 220]. Further details can be found in section 2.2.3. For the simulation, a dwell probability for the $\mathrm{NV^0}$ state of $\chi_{\mathrm{NV_0}} \approx 0.3$ is assumed, which is in good agreement to the findings of Waldherr *et al.* [221] and the reported quantum efficiency by Radko *et al.* [222]. The re-polarisation rate Γ_{P} is based on the optical excitation parameter and is therefore reduced by $\chi_{\mathrm{NV_0}}$, such that it can be expressed by

$$\Gamma_{\mathrm{P}} = \sigma \frac{I_{\mathrm{av}}}{E_{\mathrm{ph}}^{532\,\mathrm{nm}}} \left(1 - \chi_{\mathrm{NV_0}}\right), \tag{3.11}$$

where $E_{\mathrm{ph}}^{532\,\mathrm{nm}}$ is the energy of the excitation light with $E_{\mathrm{ph}}^{532\,\mathrm{nm}} \approx 1.057 \times 10^{-13}\,\mathrm{J}$ and I_{av} represents the mean value of the optical excitation derived from equation 3.9 along the optical axis inside the used diamond.

The detectable fluorescence rate $\mathcal{R}$ can be approximated with respect to the optical excitation energy absorbed by the NV centres located in a volume V_{laser}. This absorbed energy is then converted into red fluorescence by considering χ_{NV_0}. However, optical constraints, like total internal reflections inside the diamond and surface roughness of the diamond, limit the outcoupling of the emitted NV fluorescence, see section 3.2.5. This reduces the collection efficiency, which is taken into account by the collection efficiency factor ξ_{col}. The collected fluorescence intensity can be further reduced by any imperfections of the detection unit, *e.g.* detection dead times or a low internal quantum efficiency, summarised by the detection efficiency factor ξ_{det}. The fluorescence rate is therefore calculated by

$$\mathcal{R} = I_{\text{opt}} \frac{A_{\text{laser}}}{E_{\text{ph}}^{532\,\text{nm}}} p_{\text{absorb}} \left(1 - \chi_{\text{NV}_0}\right) \xi_{\text{col}} \xi_{\text{det}}. \tag{3.12}$$

Besides $\mathcal{R}$, linewidth and contrast are further important parameters describing the spin resonance. As derived in the equation of the photon shot-noise limited sensitivity from figure 3.1, $\Delta\nu$ and C impact the resulting slope of the ESR and therefore the achievable sensitivity. Sample-specific contributions, *e.g.* decoherence effects due to spin-spin interactions and optical effects from other diamond defects overlapping with the NV properties, as well as measurement-specific effects contribute the overall linewidth of an NV ensemble and may lead to a broadening of the intrinsic linewidth [120, 200, 208]. The resulting ESR linewidth can be regarded as the sum of the inhomogeneously broadened linewidth $\Delta\nu_{\text{inh}}$ and the measurement-specific part $\Delta\nu_{\text{power}}$ such that [203, 223]

$$\Delta\nu = \Delta\nu_{\text{inh}} + \Delta\nu_{\text{power}}. \tag{3.13}$$

Typically, microwave power broadening is one of the major contributions to $\Delta\nu$. Further details about the NV linewidth and the specific contributions are discussed in sections 3.2.1 and 3.2.3. Jensen *et al.* reported a model describing the ESR of an NV ensemble, which approximates the linewidth by [223]

$$\Delta\nu \approx \frac{\gamma_2^*}{\pi} + \sqrt{\left(\frac{\gamma_2^{\text{eff}}}{\pi}\right)^2 + \frac{4\gamma_1^{\text{eff}}}{\gamma_2^{\text{eff}}} f_{\text{R}}^2}, \tag{3.14}$$

where γ_i^{eff} are the effective relaxation rates ($i \in \{1, 2\}$) with $\gamma_1^{\text{eff}} = 1/T_1 + \Gamma_{\text{P}}$ and

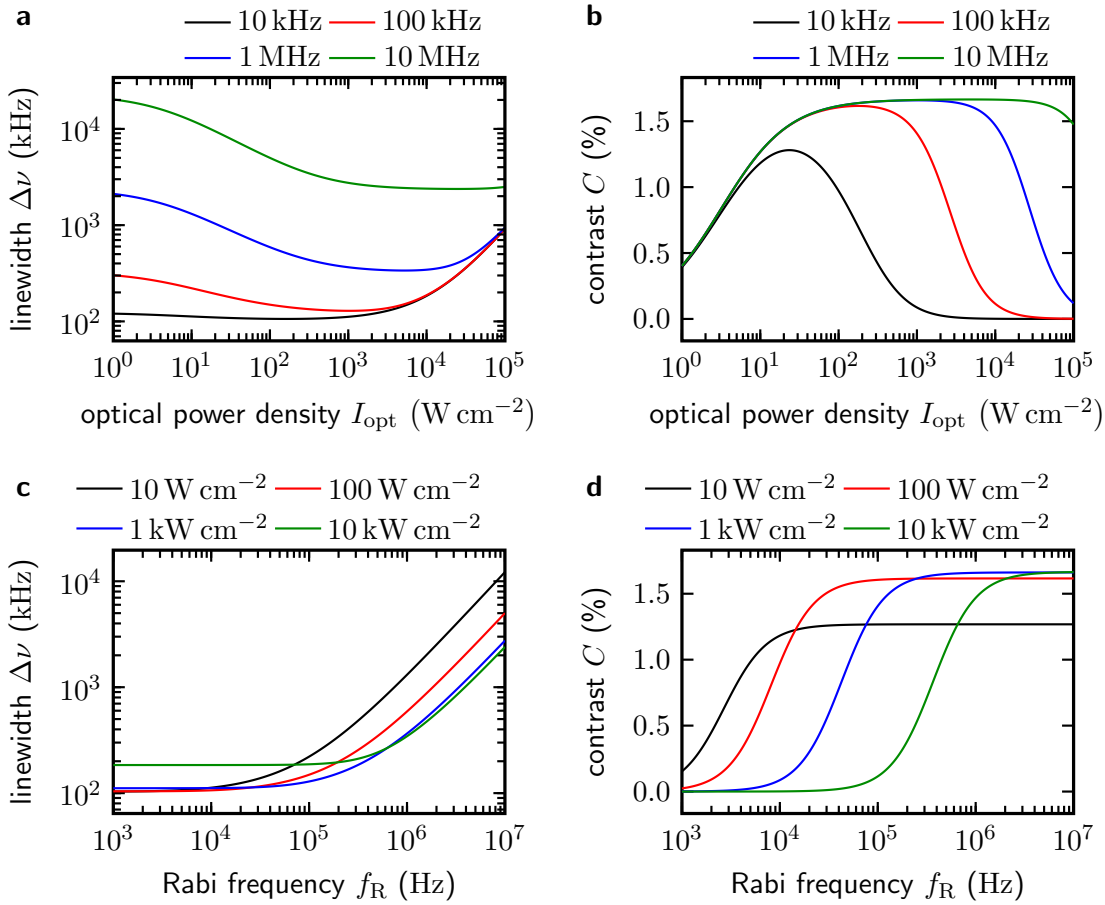

Figure 3.3: Simulative analysis of the achievable linewidth and contrast for an NV ensemble magnetometer. Exemplary plots of the analysed linewidth $\Delta\nu$ and contrast C depending on the parameters of optical power density I_{opt} and Rabi frequency f_R. The input parameters of the simulation are summarised in the caption of figure 3.2. **a)** Linewidth dependency on the optical excitation for four Rabi frequencies. **b)** Contrast dependency on the optical excitation for four Rabi frequencies. **c)** Linewidth dependency on the spin manipulation for four optical excitation values. **d)** Contrast dependency on the spin manipulation for four optical excitation values.

$\gamma_2^{\text{eff}} = 1/T_2 + \Gamma_P/2$ and f_R the Rabi frequency in Hz.

Based on the model by Jensen *et al.*, the resonance contrast can be analogously expressed in terms of physical properties of the NV ensembles and of the measurement parameters such that [223]

$$C \approx \frac{1}{4}\frac{1}{3}\theta \frac{\Gamma_P}{\Gamma_P + \Gamma_1(1-\theta)} \frac{(2\pi f_R)^2}{(2\pi f_R)^2 + \Gamma_2(\Gamma_1 + \Gamma_P)}, \tag{3.15}$$

where θ represents an overall contrast constant [208, 223].

The simulation results of the photon shot-noise limited η_B for the modelled NV magnetometer setup are shown in figure 3.2. The described model reveals a minimal sensitivity η_{PSN} of 12.5 pT Hz$^{-1/2}$, which can be obtained for I_{opt} of 6.0 kW cm^{-2} and for f_{R} of 409.5 kHz. An upper limit of η_{PSN} with 135.0 µT Hz$^{-1/2}$ is calculated for I_{opt} of 100.0 kW cm^{-2} and for f_{R} of 1.0 kHz.

3.2.1 Diamond Material

Diamonds with NV centres form the basis of NV magnetometers. These samples can be artificially grown by HPHT and CVD methods, see section 2.1.1. Subsequent steps of electron or iron irradiation with annealing and post-treatment processes are required to create and activate the NV centres in the lattice structure, see section 2.2.2. The material quality of these artificially grown diamonds determines to a large extent the achievable sensitivity, as the resulting spin resonance behaviour is strongly correlated with the diamond quality and the properties of the NV centres, see figure 3.4. This influence is described by equation 3.2 using the parameters of linewidth $\Delta\nu$, contrast C and photon rate $\mathcal{R}$.

The growth of diamonds and the incorporation of NV centres into the lattice structure with certain requirements for NV properties is quite challenging, as several technical parameters have to be accurately selected and applied to achieve the desired quality of NV samples [135]. While diamonds with high NV density usually emit a larger number of fluorescence photons compared to low density samples, thus improving photon shot-noise [200], these samples usually contain a larger number of other defects and impurities. This devotes as a source of dephasing for the NV ensembles due to dipolar magnetic coupling [120, 208]. Any source of decoherence arising from other lattice defects or stresses in the diamond degrades the ability of NV centres to accurately detect magnetic fields. This is associated with a decrease in the inhomogeneously broadened transverse spin relaxation time T_2^*, corresponding to a broadening of the measured linewidth via the relation $\Delta\nu \propto 1/T_2^*$ [217], see figure 3.4a. Reported values of $\Delta\nu$ for samples with different growth conditions and NV properties are summarised in table 3.1.

Main dephasing contributions are interactions of the NV electron spin with ^{13}C

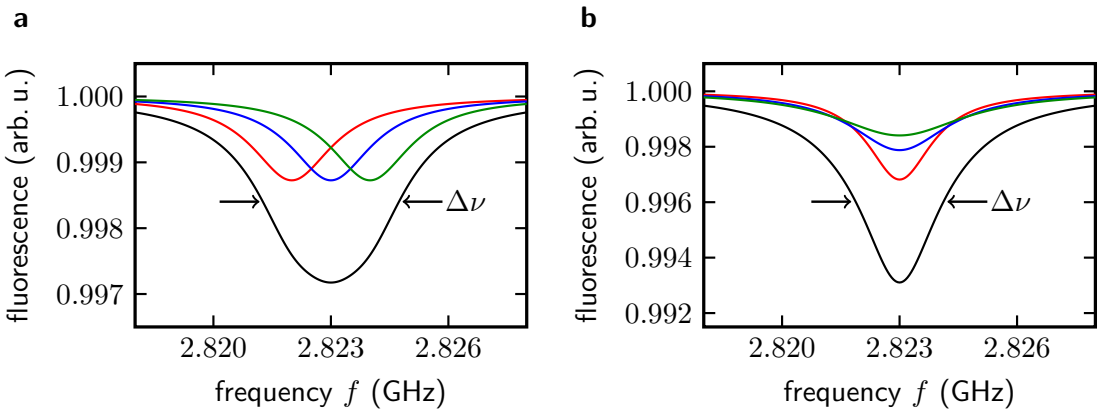

Figure 3.4: Broadening of the ensemble linewidth. Each single NV centre, which is located in the illuminated volume of the diamond, contributes to the signal. However, the physical properties of these NV centres and the experimental conditions of the optical pumping and spin manipulation processes may vary between different locations inside the diamond leading to a different spin resonance behaviour. The recorded signal is therefore a superposition of the individual contributions of the addressed NV centre (different colours represent the spin resonance of different NV centres) resulting in the overall resonance spectrum (drawn in black). **a)** shows the broadening of the linewidth resulting from different resonance frequencies of the NV ensembles due to variations in the local environment. This includes magnetic field gradients over the diamond volume (*e.g.* from the applied offset magnetic field) and/or strain inhomogeneities. **b)** Broadening of the linewidth may also occur due to differences in the local microwave field at the NV centres, *e.g.* power broadening and/or variations in dephasing times T_2^*. This figure is based on [200].

nuclear spins due to dipolar coupling [190], interactions with substitutional nitrogen impurities (also called P_1-centres) with an electron spin of $S = 1/2$ [116] and interactions with paramagnetic NV^0 centres [160]. Strain inhomogeneities and gradients across the diamond can further affect the coherence of the NV ensembles. As shown in figure 3.4a, strain inhomogeneities can shift the resonance frequencies of individual NV centres such that the overall $\Delta\nu$ is broadened [51, 224].

Considering the main dephasing contributions, T_2^* can be qualitatively approximated in terms of material-related aspects by [120, 225]

$$\frac{1}{T_2^*(\text{ensembles})} \approx \frac{1}{T_2^*(^{13}\text{C})} + \frac{1}{T_2^*(\text{P}_1)} + \frac{1}{T_2^*(\text{NV}^-)} + \frac{1}{T_2^*(\text{NV}^0)} + \frac{1}{T_2^*(\text{strain})}. \quad (3.16)$$

Temperature variations [195], gradients and inhomogeneities in electric and external magnetic fields [120, 226] and other spin dephasing mechanisms are not in-

cluded in this T_2^* expression. In addition, optically illuminated NV^0 centres in the diamond also emit photons after excitation. This fluorescence overlaps with the emission spectrum of the negatively charged NV centres, see figure 2.2. It therefore contributes to the detected background and reduces the achievable contrast, which in turn affects the sensitivity [225].

From a diamond engineering perspective, it is important to solve and optimise the problems related to other spins, unwanted impurities and induced strain in order to set up a highly sensitive NV magnetometer. This includes a high conversion efficiency of the initial nitrogen concentration, resulting in a sufficiently large NV concentration with good coherence properties of the grown diamond sample. The choice of synthesis method should be made carefully, as each method may have limitations and disadvantages compared to the others, see section 2.1.1. CVD grown diamonds typically have a higher mechanical stress level than HPHT grown diamonds [120, 227]. With the HPHT method, control and reproducibility of impurity concentration is usually more difficult than with CVD synthesis [120, 143]. Single crystal diamonds grown by HPHT can have sectors with different crystal orientations, which often requires a cutting of the samples into individual sectors.

The use of an isotopically purified carbon source during diamond growth can dramatically reduce the concentration of unwanted nuclear spins associated with ^{13}C (with a nuclear spin of $I = 1/2$ and a natural abundance of about 1.1% [228]), thus extending T_2^* [47, 120]. The use of ^{12}C enriched gas containing a nuclear spin of $I = 0$ is a mitigation method that can be applied during CVD growth as well as when using a ^{12}C enriched solid medium during HPHT synthesis. This isotopic enrichment can determine the predominant nitrogen isotope of the NV centres, *i.e.* whether ^{14}N or ^{15}N is present, which affects the achievable resonance contrast due to the different splitting properties of the two nitrogen isotopes.

Strain inhomogeneities in the diamond due to dislocations and interstitial nitrogen/carbon atoms in the crystal structure can affect the spin transitions and lead to frequency shifts, which could then widen the overall linewidth of the NV ensembles [232], see figure 3.4a. High-temperature annealing at low or high pressure above 600 °C can help to reduce stresses inside the diamond, as lattice damage caused by the irradiation process, for example, can be repaired to some extent by

Table 3.1: Overview of recorded diamond parameters with corresponding NV properties of dephasing time or linewidth. This overview classifies diamond samples used in recently published articles into the growth method, the ratio between ^{13}C and ^{12}C isotopes, the concentrations of nitrogen atoms [N] and of NV centres [NV^-], the measured linewidth $\Delta\nu$ and the addressed type of NV centres, *i.e.* single centres or NV ensembles. This list is sorted by the reported linewidth in ascending order.

Synthesis method	C isotope ratio ^{13}C	^{12}C	[N]	[NV^-]	$\Delta\nu$	Type of NV centres	Reference
CVD	0.3%	99.7%	0.05 ppb	0.06 ppt	55 kHz	single	[47]
HPHT	0.03%	99.97%	N/A	0.4 ppm	81.8 kHz	ensembles	[32]
HPHT	0.03%	99.97%	0.6 ppm	0.4 ppm	200 kHz	ensembles	[229]
CVD	N/A	N/A	$<$ 1 ppm	25 ppb	400 kHz	ensembles	[230]
HPHT	1.1%	98.9%	50 ppm	(1 − 10) ppm	1.2 MHz	ensembles	[231]
CVD	1.1%	98.9%	1 ppm	0.01 ppm	1.2 MHz	ensembles	[231]

these methods. Furthermore, annealing promotes the movement of vacancies and interstitial nitrogen atoms [120, 132], which could improve the NV conversion efficiency with potentially positive side effects on the parameters of equation 3.7.

The influence of nitrogen-related defects, such as P_1 and NV^0 centres, especially on T_2^* and $\mathcal{R}$ depends on the initial nitrogen concentration and on the NV conversion efficiency. The initial nitrogen concentration represents the upper NV density limit. In order to create an NV centre, a substitution nitrogen atom must receive an electron from a donor and a vacancy must move to the neighbouring lattice site, see section 2.2.3. This means that the N-to-NV conversion efficiency strongly depends on the physical positions of the nitrogen atoms and the vacancies and on their mobility to occupy two adjacent lattice sites [120].

Typical approaches used after diamond growth are irradiation [155], implantation [152, 153] and subsequent annealing steps under high pressure or temperature to initiate and enhance the NV generation process [132, 233]. However, determining the optimal value for the conversion efficiency is not straightforward and a complete conversion of nitrogen atoms to NV centres is not necessarily desirable [120]. This is related to the fact that if the NV centres are packed too densely in the diamond matrix, interactions with other NV centres become a serious problem leading to decoherence and thus to a reduction of T_2^* [190, 232]. Moreover, the control of the charge state depends on the local conditions inside the diamond and can be affected

by external fields as well as by the optical pumping process [177]. A detailed analysis on the selection of the optimal initial nitrogen concentration for the growth and NV formation processes is summarised by Kleinsasser *et al.* [234] and Edmonds *et al.* [225].

The resulting shape of the diamond after growth and cutting, the orientation of the NV centres inside the diamond and the condition of the surfaces are other characteristics that must be considered when selecting the diamond material with respect to the achievable sensitivity and the specific sensing application. Besides a rectangular shape of the diamond, diamonds can also be cut in special shapes, as shown for example by Clevenson *et al.* [235]. This can improve the optical excitation by trapping the excitation light inside the diamond and thus utilising the remaining light intensity compared to a 'single-pass' approach, where only a fraction of the light intensity would be absorbed by the NV centres.

In addition to sculpturing the shape of the diamond by cutting or etching processes [236], surface conditions, such as roughness or contamination, may impact the outcoupling of the emitted fluorescence from the diamond and need to be considered [237, 238].

Typically, NV centres are aligned uniformly along the four crystallographic axes of the diamond lattice [145, 146], see section 2.2.1. Preferential alignment of the NV axes could be beneficial for certain sensing applications as the contrast is increased for the selected orientation due to a reduced background signal from NV spins of the three other NV orientations [135]. An almost perfect alignment for $\geq 99\%$ of the NV centres inside a diamond has recently been demonstrated for CVD grown diamonds [239, 240].

Setting up a highly sensitive NV magnetometer requires a diamond sample with good coherence properties and a sufficiently high density of NV centres is needed. The main parameters and challenges for diamond growth and NV formation are to keep the number of unwanted spins and impurities, as well as strain on the sample as low as possible. This is necessary to achieve a high NV conversion efficiency and to optimise the charge state ratio between negatively and neutrally charged NV centres.

3.2.2 Optical Spin Excitation

Optical illumination of the diamond is essential to transfer spin population from the ground to the excited state, as described in section 2.2.4. This pumping process forms the basis for NV magnetometry. To make the best use of NV sensing properties, the interplay between optical pumping and spin manipulation must be considered. Relevant parameters for the optical excitation are the light power, the wavelength, the polarisation and the stability of the applied optical excitation.

It is obvious that the sensitivity of equation 3.7 can be improved by increasing the excitation power P_{opt}, since there is a strong correlation between P_{opt} and the emitted fluorescence power P_{fl}, which can be described as follows [223]

$$P_{\text{fl}} \propto P_{\text{opt}}/P_{\text{sat}}, \tag{3.17}$$

where P_{sat} is the NV saturation intensity. An increased fluorescence rate $\mathcal{R}$ improves the sensitivity in the photon shot-noise limit by the square root of the fluorescence intensity according to equation 3.7. Experiments by Jensen *et al.* have shown that a higher light intensity can decrease the measured linewidth improving the sensitivity [223]. However, an increase in P_{opt} is also accompanied by an increased heating of the diamond due to a partial transfer of the illumination energy into phonons [241]. For high powers, solutions must be developed for dissipating the induced heat and controlling the temperature of the diamond [211].

In addition, it may be advantageous to optimise the light paths through the diamond so that the excitation light is used more efficiently compared to a 'single-pass' design due to the relatively low NV absorption property [242]. This could improve the optical pumping without requiring higher light powers and therefore may reduce the light source and thermal management requirements of the NV sensor. Suggestions for an efficient use of the excitation light include anti-reflection coatings on the light-entering surface of the diamond and more advanced sensor designs, such as the light-capturing waveguide approach recently demonstrated by Clevenson *et al.* [235].

The second crucial parameter for the optical excitation is the wavelength used, since two NV charge states exist with different absorption cross-sections [243]. Normally, the fluorescence emission of the diamond is a superposition of NV^- and NV^0

centres [177]. Considering the photon sidebands of these two charge states, an optimal excitation wavelength should be set between (510 to 540) nm according to the findings of Aslam *et al.* [161]. Such excitation settings ensure that the rate for charge state switches between NV^- and NV^0 are relatively small and a relatively high NV^- fluorescence rate can be obtained.

The light polarisation is an additional parameter that affects the spin transfer from the ground to the excited state through its projection onto the NV dipoles, see figure 3.5a. In particular, for vector magnetometry applications, at least three of the four possible NV orientations must be significantly addressed by the excitation light in order to extract vector information from the driven NV orientations [200].

The stability of the optical excitation in terms of output power, wavelength and polarisation can usually be observed in the recorded fluorescence signal and affects the performance of the sensor. Methods to circumvent such instabilities must be thoroughly considered and implemented in the experimental setup, if the used light source is not able to meet the requirements. An example is common mode suppression used in a balanced detection scheme [28, 244].

Due to the interaction of optical initialisation and spin manipulation, sensitivity optimisation that is only subject to optical excitation can be incomplete and therefore deviate from the optimal working point.

3.2.3 Static Bias Magnetic Field

For most magnetic field measurements with NV centres, it is helpful to apply a static bias field $\boldsymbol{B_0}$ to resolve the resonance features of the four NV orientations, see figure 2.4. Otherwise, these resonances may overlap [193]. In order to obtain the complete field information of a measurable magnetic field, at least three of the four NV orientations must be measured distinguishably, *i.e.* the resonance frequencies for the different spin orientations must differ from each other. A detailed description of how to extract the vector field information from an ODMR measurement is summarised by Balasubramanian *et al.* [47].

Offset magnetic fields can be applied by permanent magnets [26, 218], electromagnets [245] or current carrying coils [205, 246]. For a sensitive NV magnetometer, it is

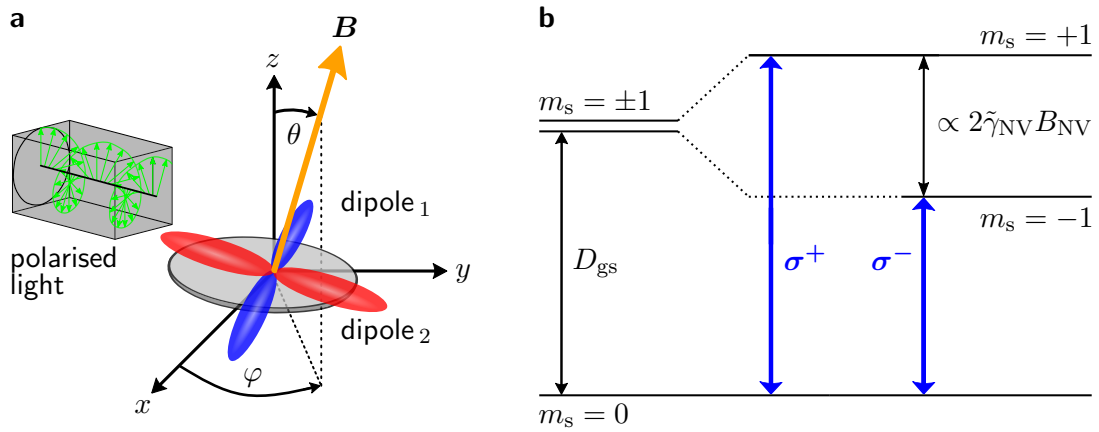

Figure 3.5: Optical excitation and spin manipulation of NV centres. a) The schematic drawing shows optical NV dipoles oriented in the xy-plane, the NV axis oriented along the z-axis and an applied magnetic field vector $\boldsymbol{B}$, which is tilted by angle θ from the z-axis. The coupling of the optically polarised light and the orientation of the optical NV dipoles is essential for the initialisation of the NV system. **b)** Detailed view on the energy level scheme of the NV centre from figure 2.4 with focus on the spin population transfer between the $m_s = 0$ to $m_s = \pm 1$ states by applying a microwave field (blue arrows). σ^+ circularly polarised microwaves invert spin population between the $m_s = 0$ to $m_s = +1$ sublevels, whereas σ^- polarised waves transfer population between the $m_s = 0$ and $m_s = -1$ sublevels.

crucial that the applied bias field at the location of the optically excited NV centres in the diamond is as homogeneous as possible. Inhomogeneities in the $\boldsymbol{B_0}$ field can contribute to a broadening of the linewidth $\Delta\nu$ of the NV ensembles, see figure 3.4a.

Examples of generating homogeneous magnetic fields are permanent magnets arranged in an Halbach geometry [247, 248] and current carrying Helmholtz coils [202, 246, 249], see section 5.2.6. The sole use of permanent magnets can be disadvantageous, as permanent magnets typically show a temperature-dependent magnetisation behaviour with potential magnetisation drifts over lifetime [250].

Recently, a new sensing technique has been presented by Zheng *et al.* [202] that eliminates the need for a bias magnetic field by selectively driving the hyperfine transitions with frequency-modulated circularly polarised microwaves. This technique enables NV centres for quantum sensing applications at zero-field and reduces the complexity of the sensor design to implement an external magnetic field.

3.2.4 Spin Manipulation

An oscillating microwave field $\boldsymbol{B_1}$ is necessary to perform ESR measurements using NV centres to transfer population between the spin levels. The spin transfer between the $m_s = 0$ and $m_s = \pm 1$ states is polarisation-dependent on the applied microwave field [251, 252]. If the field is σ^+ (σ^-) circularly polarised, population is transferred between the $m_s = 0$ to $m_s = +1$ ($m_s = -1$) levels, see figure 3.5b.

A broadband, strong, circularly polarised and uniformly distributed microwave field is favourable for a highly sensitive NV magnetometer [253]. The coupling strength of the applied microwave field with the NV centres is crucial for sensing experiments and has a direct influence on the resulting spin resonance behaviour. A stronger field usually leads to increased values of contrast and linewidth [223]. However, contrast enhancement and linewidth power broadening are opposite effects to improve the magnetic field sensitivity, as graphically shown in figure 3.4b. Optimisation of the spin manipulation should therefore be considered with respect to the optical pumping process to maximise the slope of the spin resonance, which in turn improves detection capabilities.

Besides the strength of $\boldsymbol{B_1}$, another challenge is the uniformity of the field over the illuminated diamond volume, since the total signal results from all optically addressed NV centres at different locations. In addition, the structure generating the microwave field must allow optical access to the diamond. For the chosen application, the bandwidth of the microwave structure must fit the required dynamic range, *e.g.* by using specially designed structures [209, 254, 255]. Losses in the electronic circuit and impedance mismatches affect the efficiency of the power-field conversion and thus the power consumption of the NV magnetometer. Fluctuations and instabilities in the amplitude and frequency of the oscillating field are mainly related to the microwave source and must be minimised. An overview of recently published microwave structures with corresponding characteristics and properties is summarised in table 3.2.

The simplest technique to generate an oscillating field is to use a thin (copper) wire fed by an external microwave source [60, 261]. This is a widely used and powerful technique to generate strong fields of arbitrary frequency for single NV centres, as the

Table 3.2: Overview of used microwave structures for NV experiments with corresponding properties reported in recent publications. This overview classifies a selection of microwave structures used in recently published articles [255–260] according to their electronic and geometrical structure, the achievable field amplitude for a given power input, the provided field uniformity in areal and lateral dimensions, the bandwidth f_{BW} and the measured reflection parameter S_{11}.

Microwave structure	Field amplitude	Field uniformity areal	Field uniformity lateral	f_{BW}	S_{11}	Reference
3D loop gap resonator	5 G @ 42 dBm	$> 50\,\mathrm{mm}^2$	5 mm	80 MHz	−10 dBm	[256]
Double split-ring resonator	5.96 G @ 0.5 W	$(0.95 \times 1.12)\,\mathrm{mm}^2$	N/A	80 MHz	−25 dBm	[257]
Open dielectric resonator	10 MHz @ 5.2 W	$(2.4 \times 2.4)\,\mathrm{mm}^2$	1.7 mm	N/A	N/A	[255]
Coplanar waveguide	6.64 G @ 1.0 W	N/A	N/A	15.8 MHz	−10 dBm	[258]
Planar ring resonator	3 G @ 1.0 W	$1\,\mathrm{mm}^2$	N/A	437 MHz	N/A	[259]
Square split-ring resonator	N/A	$(1.5 \times 1.5)\,\mathrm{mm}^2$	N/A	15 MHz	−16.3 dBm	[260]

wire can be positioned close to a selected defects. However, a uniform field distribution over a larger area/volume is quite difficult to achieve, since the radiated power of such a wire decreases strongly with increasing distance according to Ampère's law [259]. Strip line waveguides fabricated on printed circuit boards (PCBs) have been demonstrated in various designs, such as microstrip waveguides [252, 261, 262] and coplanar waveguides [246, 258, 263], which enable broadband transmission of an oscillating field [256, 258]. These structures typically exhibit a low conversion efficiency of the applied input power to the delivered field as well as field inhomogeneities across the waveguide [256]. Resonator structures, such as planar ring resonators [259, 264], square split-ring resonators [260, 265] and double split-ring resonators [28, 257, 261], square split-ring resonators [265] and omega resonators [266–269] are a preferred choice to efficiently generate strong and homogeneously distributed microwave fields. Nonetheless, the homogeneous field distribution is mainly limited

to the in-plane region of the fabricated structure and the achievable bandwidth is relatively low [255]. Recently presented approaches for a 3D uniform spin manipulation include open dielectric resonators [255, 270] and loop-gap resonators [256].

A simultaneous manipulation of the hyperfine interactions - associated with the intrinsic isotopes ^{14}N and ^{15}N - can be achieved by mixing the applied microwaves with a frequency corresponding to the axial hyperfine constant $A^{\parallel}$, leading to an improvement in contrast [28, 271].

An alternative technique for ESR measurements with NV centres without the need of an oscillating microwave field is the method of microwave-free magnetometry described by Wickenbrock *et al.* [245, 272]. Exploiting the NV properties at the ground state level anti-crossing (LAC), magnetic field sensing is based on the fluorescence intensity, which drops if the LAC condition is pertubated by any additional magnetic field. Although no microwave field is required, high demands are placed on the magnetic field strength in order to fulfil the LAC condition [205].

3.2.5 Optical Spin Readout

The emitted fluorescence is the key element for gaining knowledge about the NV electron spin states for magnetometry. The emission patterns of an NV centre with portions of s- and p-polarised light are determined by its two orthogonal NV optical dipoles, which are perpendicular to the NV axis [273]. Inside the diamond, the exact orientation of the dipoles for each NV centre may vary due to inhomogeneous non-axial strain [274]. For an ensemble magnetometer, the fluorescence emission though can be regarded to be isotropic with an emission, which is averaged over all orientations and dipoles, such that the fluorescence intensity can be described by [274]

$$I_{\mathrm{fl}} = \frac{1}{2}\left(I_{\mathrm{dipole}_1} + I_{\mathrm{dipole}_2}\right), \tag{3.18}$$

where I_{dipole_i} is the fluorescence intensity emitted by the specific dipole i with $i \in \{1; 2\}$.

According to equation 3.7, the detected fluorescence intensity has direct impact on

the achievable magnetic sensitivity. An increased fluorescence detection improves the photon shot-noise limited sensitivity η_{PSN} by the inverse square root of the fluorescence rate $\mathcal{R}$. Due to diamond's high refractive index of $n_{\mathrm{dia}} = 2.42$ at visible light [128], total internal reflection (TIR) is a major challenge to obtain high fluorescence rates as the majority of the emitted fluorescence remains inside the diamond, as shown in figure 3.6. According to Snellius's law, only light rays with angles θ relative to the surface normal that are smaller than critical angle θ_{TIR} with

$$\theta_{\mathrm{TIR}} = \arcsin\left(\frac{n_{\mathrm{air}}}{n_{\mathrm{dia}}}\right) \approx 24.6^{\circ} \tag{3.19}$$

are able to pass the diamond-air interface with $n_{\mathrm{air}} = 1$. The fraction f_{TIR} of the isotropically emitted NV fluorescence I_{fl} exiting the diamond can be approximated to [274]

$$f_{\mathrm{TIR}} \approx \int_0^{2\pi} \int_0^{\theta_{\mathrm{TIR}}} \mathrm{d}\phi\, \mathrm{d}\theta\, \sin(\theta)\, I_{\mathrm{fl}}. \tag{3.20}$$

The potentially detectable light, which is not affected by TIR, is further reduced as the transmission at the diamond exiting interface depends on its polarisation according the Fresnel's transmission coefficients $T_{\mathrm{fresnel}}(\theta)$, which is angle-dependent. Neglecting the polarisation of the light, an average value of the transmission coefficient with $T_{\mathrm{fresnel,av}} \approx 0.83$ is obtained for the regarded angle window of $0 \leq \theta \leq \theta_{\mathrm{TIR}}$. The fraction of fluorescence ξ_{col} that can be detected within a cone of θ_{TIR} can be approximated to [220]

$$\xi_{\mathrm{col}} \approx \frac{1}{4\pi} \int_0^{2\pi} \int_0^{\theta_{\mathrm{TIR}}} \mathrm{d}\phi\, \mathrm{d}\theta\, \sin(\theta)\, I_{\mathrm{fl}} T_{\mathrm{fresnel,av}} \tag{3.21}$$

$$= \frac{1}{2}\left[1 - \cos(\theta_{\mathrm{TIR}})\right] I_{\mathrm{fl}} T_{\mathrm{fresnel,av}}. \tag{3.22}$$

Based on this calculation, less than 1.5% of the isotropically emitted NV fluorescence can be detected by an ideal detector. This includes the simplification of parallel diamond surfaces without having any optical imperfections, *e.g.* a rough diamond surface. Note that these assumptions are usually not valid.

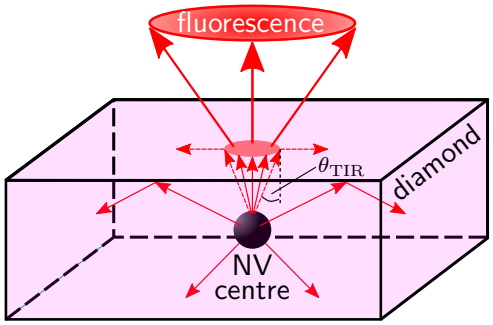

Figure 3.6: Total internal reflection of the NV fluorescence. The majority of the emitted fluorescence of an NV centre is internally reflected at a diamond-air interface and can thus not be detected outside the diamond. Only rays with an incident angle of θ_{TIR} leave the diamond. A small number of arrows indicating the emission direction are shown in this image.

A more precise calculation of the collection efficiency compared to equation 3.21 considers the numerical aperture NA of the detector. This leads to an acceptance angle of $\theta_{\mathrm{max}} = \arcsin\left(NA/n_{\mathrm{dia}}\right)$. The polarisation of the emitted light is taken into account by $I_{\mathrm{fl,s}}$ and $I_{\mathrm{fl,p}}$ with angle-dependences on ϕ and θ [274], as described by Le Sage *et al.* [274]. ξ_{col} is then described by

$$\xi_{\mathrm{col}} = \int_0^{2\pi} \int_0^{\theta_{\mathrm{max}}} \mathrm{d}\phi\, \mathrm{d}\theta\, \sin\left(\theta\right) \left[I_{\mathrm{fl,s}}\left(\theta,\phi\right) T_{\mathrm{s}} + I_{\mathrm{fl,p}}\left(\theta,\phi\right) T_{\mathrm{p}}\right]. \tag{3.23}$$

This theoretical formula may further deviate from experimental results. Filters in the optical path may reduce the light intensities, detectors may deviate from a perfect detection arising due to quantum limits and dead times and quality imperfections in the surface of the diamond may introduce additional reflections affecting the light to couple out of the diamond [274].

To overcome the limitations of TIR, several techniques have recently been developed to circumvent this challenge for diamonds and thus improve collection efficiency. This includes tapered fibres [275], metallic mirrors placed in proximity to NV centres [276], nanofabricated solid immersion lenses [277, 278], parabolic mirrors [279, 280], dielectric optical antennas [281], anti-reflection coatings [282], hybrid waveguide structures [283], plasmonic gratings [284], circular grating structures [220, 285], TIR lenses [286], pyramidal tips [287] and other advanced photon collection methods [22, 235, 274].

In addition to optimising fluorescence collection efficiency through optical geometries or sensor design in general, it is also necessary to prevent a detection of the excitation light. Optical filters [32] and gratings [103], which absorb the excitation light before being collected by the detection unit, can be introduced in the optical setup.

Besides the conventional readout of the emitted fluorescence, new techniques to extract the spin state information of the NV centres include spin-to-charge conversion [288, 289], photoelectric readout [212, 290, 291], repetitive readout comprising single shot readout [292, 293], level anti-crossing readout [199], near infrared absorption readout [26, 294, 295], green absorption readout [120], spin readout based on maximum likelihood estimation [296] and laser threshold magnetometry [297–299].

3.2.6 Conclusion

For the development and construction of an NV magnetometer, the so-called modular principle can be used. The most important components to be selected are a diamond sample with NV centres, a light source, a detection unit and equipment for generating an oscillating field. Other elements are connected with an offset magnetic field or with a magnetic shielding, which can be optionally installed or used depending on the application of the NV sensor.

While a random assemblage of components likely enables a magnetic field measurement, the construction of a highly sensitive magnetometer is not straightforward and may be therefore unlikely with this approach. In order to select from the pool of possibilities, which are described and discussed in sections 3.2.1 to 3.2.5, those that lead to a compact and sensitive magnetometer, the following consideration is necessary: these components as well as their operating parameters must match to each other and harmonise with the properties of the NV ensembles.

In addition, the intended sensor application may influence the choice of sensor elements, making one option more advantageous than others. This is for example linked to distribution property of the NV orientations (uniform distribution versus preferential orientation) inside the diamond, which can favourable for either scalar or vector magnetometry. In general, the interplay between optical pumping and spin manipulation strongly impacts the achievable sensitivity. For example, if the

optical pumping is too strong compared to the applied spin manipulation, the spins are pumped back to their initial state relatively quickly, which reduces the magnetic response and thus worsens the sensitivity.

To sum up, a general statement about which elements should be selected and preferred to others for the assembly of an NV magnetometer is not trivial. The subsections of section 3.2 are intended to give an insight into already published concepts and approaches for the individual sensor functions and components. In addition to the pure sensor design, disturbance variables inside and outside the sensor, such as temperature drift and technical noise, also play a non-negligible role in influencing the measurement performance.

Another degree of freedom for the sensor design is the choice of the measuring principle, whereby there is also a strong connection to the application. It is important that the installed components meet the requirements of the chosen measuring principle.

For a commercial application of the NV technology, the sensor performance is an essential aspect to enable new applications, to replace existing technology and to achieve new sales markets. However, the availability and the costs of the sensor components as well as the patent situation for the designed sensor must be decisively examined.

4 LED-Based NV Magnetometer

This chapter is based on [218] with minor edits. Parts of the former appendix are now included in the main text. The taken text passages are marked by marginal notes, whereas the taken captions are not additionally highlighted. Reprinted under author rights from [218]. Copyright (2019) Elsevier B.V. All rights reserved.

The development of an LED-based NV magnetometer was conceived by Tino Fuchs, Robert Rölver, Andreas Brenneis and Felix M. Stürner in cooperation with Fedor Jelezko. The design of the 3D-printed construction and the assembly of the NV sensor were performed by Julian Kassel and Felix M. Stürner. The filter structures were created and analysed by Robert Rölver. The design of the microwave transmission line structure was performed by Uwe Wostradowski in discussion with Andreas Brenneis and Felix M. Stürner. Optical considerations of the sensor, including optical ray trace simulations, were performed by Felix M. Stürner in discussion with Andreas Brenneis. Simulations of the induced magnetic field by the bond wire of the LED were performed by Tino Fuchs and Felix M. Stürner in discussion with Andreas Brenneis. The diamond sample was supplied by Junichi Isoya, Shinobu Onoda, Hitoshi Sumiya and Kazuo Nakamura. The experiments were performed by Felix M. Stürner and the measurement data were analysed by Felix M. Stürner in discussion with Andreas Brenneis and Fedor Jelezko. Fruitful discussions with Jakob Steiner, Julia Michl, Jörg Wrachtrup and Thomas Buck helped with to advance the development of the NV sensor.

4.1 Introduction

[218] In this chapter, we demonstrate a prototype of a compact and integrated magnetic field sensor with a construction volume of about 2.9 cm^3. The integrated sensor device consists of an LED as a light source, a diamond sample, a structure for guiding microwaves, optical components for the collection of the emitted fluorescence, a photodetector and electronic components such as a constant current source for driving the LED and an amplification circuit for the optical detection. In contrast to the mentioned fibre-based systems, the focus of this approach is to put all essential components in one housing, which could make the sensor device suitable for a portable application. In the current stage, the microwave generation and the control of the sensor are performed externally.

4.2 Sensor Assembly

[218] A schematic overview of the sensor assembly is depicted in figure 4.1a, whose components are arranged in a multilayer design. The main elements from bottom to top were an LED as the light source, a diamond sample containing NV centres, a microwave transmission circuit, a lens and a photodiode. Three printed PCBs included the electronic components for driving the LED and for sensing the photocurrent of the photodiode (PCB 1 & 3) as well as for guiding microwaves to the diamond (PCB 2). The top and bottom PCBs (PCB 1 & 3) were electrically connected by pogo pins and two 3D-printed spacers were used to precisely assemble all optoelectronic components of the sensor. The construction volume of the sensor was 2.9 cm^3, see figure 4.1b.

In detail, a bare die of a high power LED (Cree C527EZ500), which was glued on PCB 1, was used for optical excitation of the NV centres, see figure 4.3a. This LED has an emitting area of $(450 \times 450)\,\mu m^2$ and a maximum optical power of 70 mW. The anode of the LED was connected by a gold bond wire with PCB 1. On top of this board a 3D-printed spacer was placed, which has a cylindrical opening hole necessary for the optical path of the excitation light

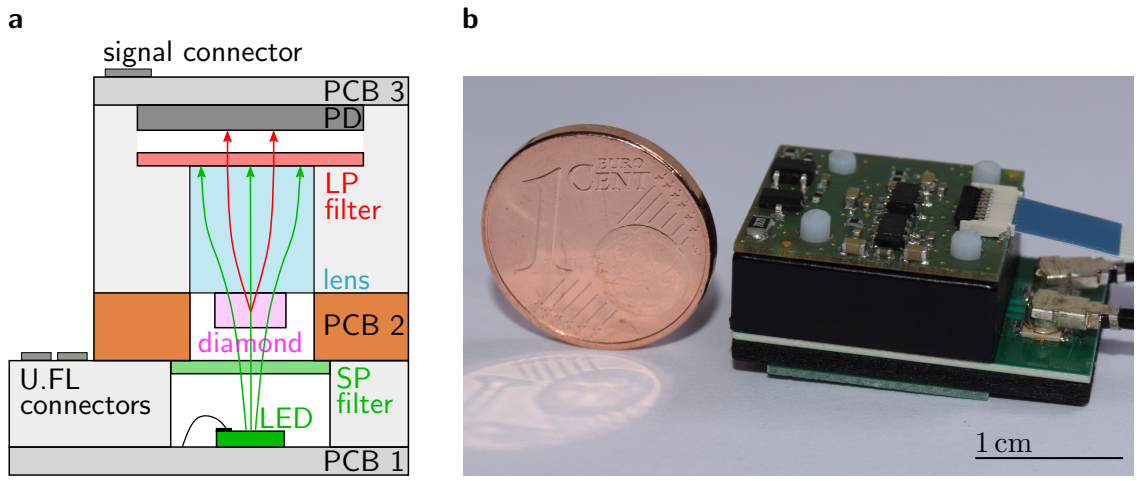

Figure 4.1: Miniaturised and integrated magnetometer. **a)** Schematic of the sensor assembly with a construction volume of $2.9\,\mathrm{cm}^3$. **b)** Image of the sensor device placed next to an Euro cent coin. The ribbon cable is used for the power supply of the integrated electronics and for the readout of the photodetector. This figure is modified from [218] with the permission of the publisher. Copyright (2019) Elsevier B.V. All rights reserved.

from the LED to the diamond. A microwave transmission line on PCB 2 followed the multilayer assembly and was connected via two U.FL connectors to an external microwave source (Anritsu MG3692A), see figure 4.4a. The diamond was located inside a hole of PCB 2 with a diameter = 2 mm and was attached to a gradient refractive index (GRIN) lens by a 30 µm thick layer of polydimethylsiloxane (PDMS), see figure 4.1a.

The GRIN lens (GRINTECH GT-LFRL-180-025-50-NC (670)) with a numerical aperture of 0.5, a diameter of 1.8 mm and a length of 4.3 mm is clamped inside a second 3D-printed spacer, which is located above PCB 2. This lens was used to increase the outcoupling efficiency of the NV centre's fluorescence from the diamond, see section 4.2.4. A photodiode (Hamamatsu S1226-5BQ) with an active area of $(2.4 \times 2.4)\,\mathrm{mm}^2$ was used to detect the emitted fluorescence of the NV centres and was connected to PCB 3, see figure 4.1a. This photodiode had an average responsivity of $Q \approx 0.34\,\mathrm{A\,W}^{-1}$ in the spectral range of (630 to 800) nm and was bonded with a gold wire to PCB 3. A transimpedance amplification circuit using two operational amplifiers (Texas Instruments OPA657) amplified the photocurrent by a gain factor of $G = 27\,\mathrm{kV\,A}^{-1}$ and a 14-bit

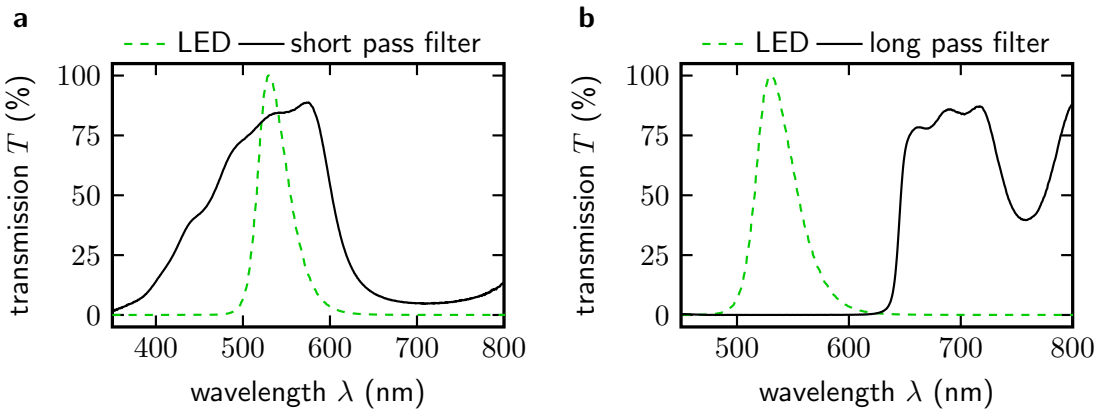

Figure 4.2: Transmission spectrum of the short and long pass filter. a) The spectral transmission coefficient T was measured by a spectrometer (OceanOptics NIRQuest512) recording the transmitted light intensity of a white-light lamp (Energetiq EQ99X-FC) through the short pass filter (black solid line). The cut-off wavelength, which corresponds to 50% of the maximum transmission value, is $\lambda_{\mathrm{cut-off}} \approx 605.3\,\mathrm{nm}$. A spectral curve of the emitted light of the LED is added to this plot (green dotted line). **b)** Analogous measurement of the spectral transmission coefficient T of the long pass filter. The majority of the emitted light by the LED is suppressed by the DBR but allows the transmission of the fluorescences as the NV centres mainly emit in the spectral range between 630 and 800 nm. This figure is based on [218].

analogue-to-digital converter (National Instruments NI PXI-5122) digitised the analogue voltage S.

In addition to the described assembly, a distributed Bragg reflector (DBR) was placed between the LED and the diamond. This filter fulfils two functions. First, it cuts off the long-wave emission spectrum of the LED ($\lambda_{\mathrm{cut-off}} \approx 605.3\,\mathrm{nm}$), which would overlap with the emission spectrum of the NV- centres, see figure 4.2a. Secondly, it reflects the fluorescence light (mainly wavelengths between 630 and 800 nm [121]) towards the photodiode, which would otherwise be lost. This filter was grown by chemical vapour deposition of several layers of amorphous silicon carbide (aSiC, $n \approx 2.6$) and silicon oxide (SiO_2, $n \approx 1.45$). A second DBR (long pass filter) was placed between the lens and the photodiode in order to block the excitation light in the detection channel. The cut-off wavelength is $\approx 644.7\,\mathrm{nm}$, see figure 4.2b.

4.2.1 Diamond Sample

> For the experiments we used a (111) diamond plate of $(0.8 \times 0.8 \times 0.5)\,\mathrm{mm}^3$, which was obtained by laser-cutting and polishing from a 99.97% ^{12}C-enriched diamond single crystal grown by the temperature gradient method at high pressure and high temperature using a carbon powder source prepared by pyrolysis of ^{12}C-enriched methane. The concentrations of the original crystal measured by electron spin resonance were $[\mathrm{NV}] \sim 0.4\,\mathrm{ppm}$ and $[\mathrm{P1}] \sim 2.0\,\mathrm{ppm}$ after 2 MeV electron irradiation ($2 \times 10^{18}\,\mathrm{cm}^{-2}$) followed by annealing at 1000°C for 2 h.
>
> The resulting NV centres were homogeneously distributed over the entire diamond and orientated randomly along all four crystallographic axes of the diamond lattice. The paramagnetic defect density of this diamond was chosen such that the intrinsic ESR linewidth ($\Delta\nu \approx 0.1\,\mathrm{MHz}$ [300]) shows no limitation to the sensor performance [301], but guarantees a sufficient number of colour centres contributing to the measured signal. [218]

4.2.2 Optical Excitation

> For the optical excitation of the NV centres we used an LED with an emitting area of $(450 \times 450)\,\mu\mathrm{m}^2$ and a maximum optical output power of $P_{\mathrm{opt}} \leq 64\,\mathrm{mW}$. [218]

For obtaining information about the achievable optical polarisation rate Γ_{P} using this LED, we considered our light source to behave as a Lambertian emitter. This means that the emitted light intensity I strongly depends on the emission angle θ relative to the surface normal such that the LED's light emission can be approximated to $I(\theta) \sim \cos(\theta)$ [302]. The Lambertian emitting characteristic and the maximum optical output power of the LED P_{opt} were used in optical ray tracing simulations using Zemax OpticStudio® in order to evaluate the light density on the surface of the diamond, see figure 4.3. From the simulation result, we estimated an optical power density on the diamond of $I_0 \approx 0.37\,\mathrm{W\,cm}^{-2}$ for a distance d of 1.8 mm between the surfaces of LED and diamond, see figure 4.3b.

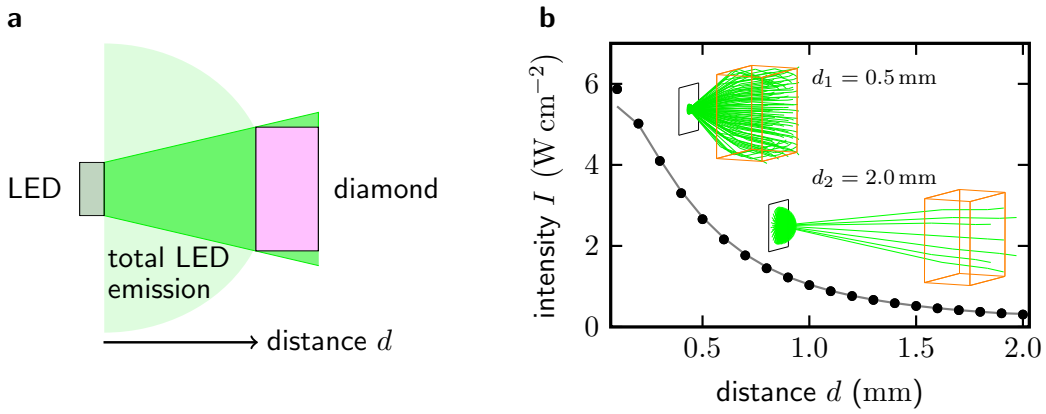

Figure 4.3: Optical excitation of the LED-based NV sensor. **a)** Schematic drawing shows the optical illumination of the diamond using a LED. As LEDs emit light diffusely, the light intensity I on the diamond surface strongly depends on the distance d between the surfaces of LED and diamond. **b)** Result of optical ray trace simulations using Zemax OpticStudio® showing this light-distance dependency for an LED illumination. The light intensity I is evaluated with a detector corresponding to the size of the diamond, which is located directly below the diamond surface. A line of moving mean (of three neighboring data points) is added to the graph. For the simulation, the emitting area of the LED is set to $(450 \times 450)\,\mu\text{m}^2$ and the optical power at the LED surface to $P_{\text{opt}} = 64\,\text{mW}$ corresponding to the experimental settings. A visualisation of the simulation is added to this graph for two distances, *i.e.* $d_{1,2} = (0.5, 2.0)\,\text{mm}$.

This value is further reduced by the absorption of the NV centres, see section 3.2, along the optical path. We considered this absorption by applying the Beer-Lambert law for the intensity progression $I(z)$ inside the diamond

$$I(z) = I_0 \exp\left(-z/l_{\text{abs}}\right) \tag{4.1}$$

with an absorption length $l_{\text{abs}} = ([\text{NV}]\,\sigma)^{-1}$, which is given by the concentration of the NV centres with $[\text{NV}] \sim 0.4\,\text{ppm}$ for our sample, and the absorption cross-section $\sigma \approx 0.95 \times 10^{-16}\,\text{cm}^2$ [303].

For our diamond with a thickness of 0.5 mm, we therefore assumed an average intensity of $I \approx 0.84 \cdot I_0 \approx 0.31\,\text{W}\,\text{cm}^{-2}$. For a photon energy of $E_{\text{ph}} \approx (1240\,\text{eV}\,\text{nm})/(530\,\text{nm})$ this results in a polarisation rate of

$$\Gamma_{\text{P}} = \sigma \frac{I}{E_{\text{ph}}} \approx 79\,\text{Hz}. \tag{4.2}$$

4.2.3 Spin Manipulation

A design of two parallel microwave striplines fabricated on a PCB is used to provide an oscillating magnetic field, which is necessary for manipulating the NV spin states, see figure 4.4a. These lines are terminated by a 50 Ω resistor and connected by a U.FL connector, respectively. The diamond, which is connected to the GRIN rod lens, is positioned in the cylindrical hole of the PCB. In the experimental frame, we supplied only one of the two transmissions lines by the external microwave source. Technical details of the transmission line using simulations are summarised in figure 4.4b. For the analysis of the measurement data, the microwave power P_{MW} is the power, which is transmitted through the microwave circuity. We further considered a line loss of 3 dB included in the presented data sets, which is mainly caused by losses of the U.FL connectors. [218]

4.2.4 Optical Spin Readout

Guiding the emitted fluorescence light from the diamond to the photodiode, we used a GRIN rod lens attached to the diamond by a 30 µm thin layer of PDMS, [218]
see figure 4.5a. This lens ensures a separation of the diamond and the electronics of the photodiode such that interfering influences of the photodiode on the dynamics of the diamond can be reduced, *e.g.* induced magnetic field gradients by the bond wire of the photodiode. Regarding the assembly of the sensor, a spatial gap between GRIN lens and photodiode is additionally necessary to bond the electrical conduction of the photodiode.

Analysing the optical detection path, we performed optical ray tracing simulations modelling the fluorescence emission by a radial emitter located inside the diamond, see figure 4.5. For the simulations, we applied the optical properties of the GRIN rod lens according to the data sheet of the manufacturer and we assumed an ideal detector. Comparing the detection efficiency of our setup with the simple situation, where the diamond is completely surrounded by air and the fluorescence is collected in a free beam (figure 4.5b), the simulations showed that the efficiency is slightly improved for spatial distances d larger than 400 µm, see figure 4.5c.

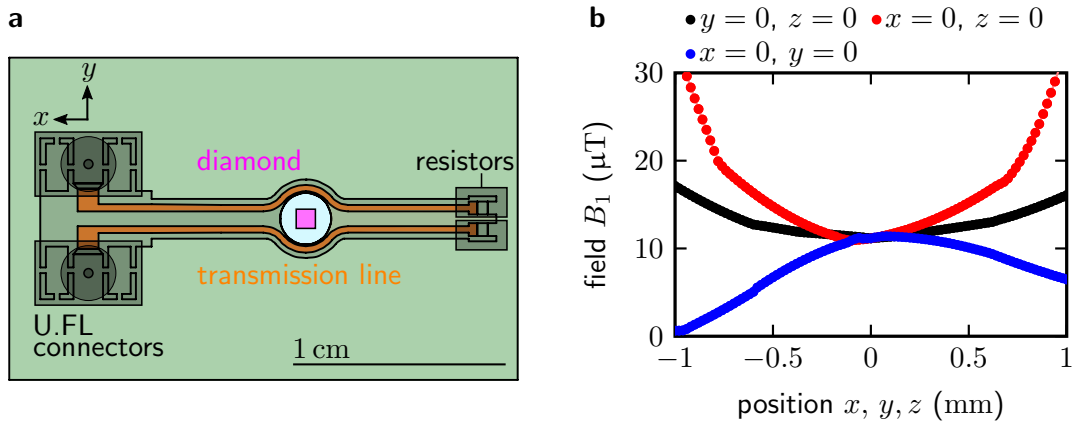

Figure 4.4: Microwave structure with a transmission line for the spin manipulation. **a)** Schematic drawing of the microwave board (PCB 2 shown in figure 4.1a), on which the transmission line (orange) is fabricated for guiding the microwaves. U.FL connectors are used for the supply of externally generated microwaves (by a laboratory microwave source). The grey area on the board represents the ground of the PCB and the diamond sample (purple) is located inside the cylindrical hole of the PCB (light blue). **b)** Simulated result of the microwave field magnitude B_1 distribution using CST Microwave Studio®. The magnitude is shown as a function of the coordinates x, y, z with the origin of the coordinate system located at the surface and in the centre of cylindrical hole of PCB 2. The results of the field strength distribution were simulated at a frequency of $f \approx 2.85\,\mathrm{GHz}$ for an input power level of $P_{\mathrm{ref}} = 1\,\mathrm{W}$. Lines of moving mean (of three neighbouring data points) are added to the graphs. This figure is modified from [218] with the permission of the publisher. Copyright (2019) Elsevier B.V. All rights reserved.

4.3 Experimental Results And Discussion

4.3.1 ODMR Measurement

[218]

The magnetic resonance of the NV centres was optically detected to measure the projection of an externally applied magnetic field onto the four crystallographic orientation axes. For this purpose, we used the technique of optically detected magnetic resonance [119]. The magnetic resonance can be detected as a drop in fluorescence intensity if the applied microwave frequency matches the resonance transition, see figure 4.6. In this case, the spin flip leads to a drop of the fluorescence. For a magnetic field along the NV centre axis, the resonance

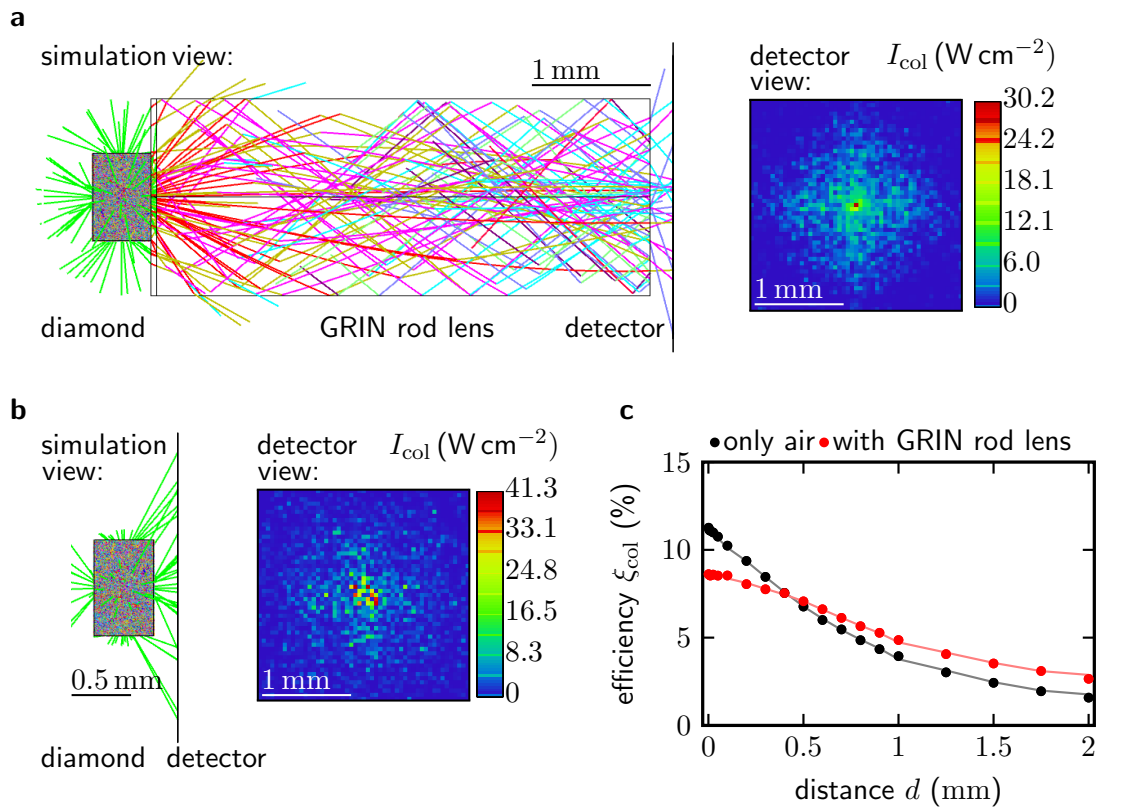

Figure 4.5: Simulative comparison of the fluorescence collection efficiency between a diamond-air and a diamond-GRIN interface. Optical ray trace simulations are performed using Zemax OpticStudio®. A radial emitter with emitting power of $P_{\mathrm{out}} = 1\,\mathrm{W}$ represents a single NV centre and is located in the centre of the diamond with dimensions of $(0.8 \times 0.8 \times 0.5)\,\mathrm{mm}^3$. The light rays are collected by a detector with an active area of $(2.4 \times 2.4)\,\mathrm{mm}^2$. 10k rays are used to run the simulations, the used refractive indices are summarised in table A.2 and 300 rays are displayed in the graphical 2D views. The colouring of the displayed rays results from the number of interfaces interactions. **a)** Graphical display and 2D detector view of the simulation settings corresponding to the LED-based magnetometer. **b)** 2D and detector view of the setting without using a GRIN rod lens. Here, the diamond is only surrounded by air and the fluorescence directly collected by the detector. **c)** Resulting plot of the collection efficiency $\xi_{\mathrm{col}} = P_{\mathrm{col}}/P_{\mathrm{out}}$ for the two simulation cases: diamond-GRIN interface (dia-GRIN) described in a) and diamond-air interfaces (dia-air) in b). P_{col} is the collected light power of the detector and d the distance between GRIN lens and detector in a) and the distance between diamond and detector in b). Lines of moving mean (of three neighbouring data points) are added to the graphs.

frequencies $\nu_\pm$ of the $m_\mathrm{s} = 0 \rightarrow m_\mathrm{s} = \pm 1$ transition are given by [193]

$$\nu_\pm \approx D_{\mathrm{gs}} + \beta \Delta T \pm \tilde{\gamma}_{\mathrm{NV}} B_0, \tag{4.3}$$

where $D_{\mathrm{gs}} \approx 2.87\,\mathrm{GHz}$ is the zero-field splitting due to the spin-spin interaction,

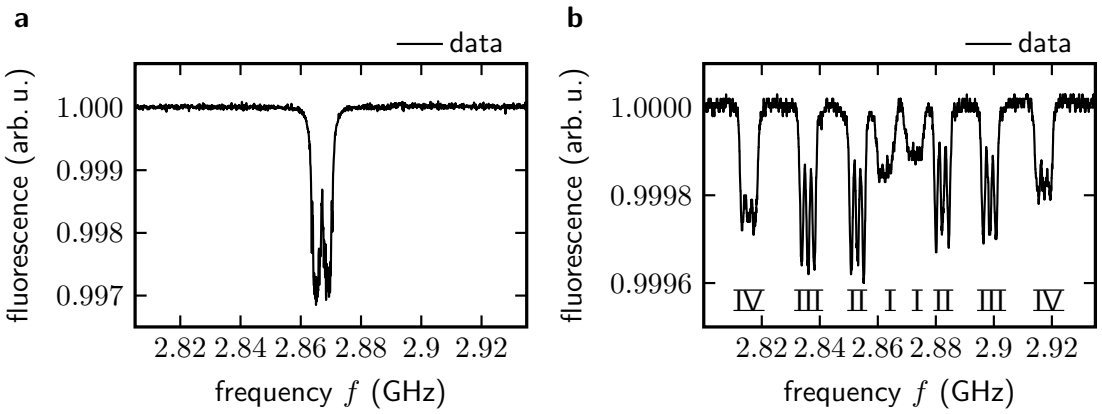

Figure 4.6: Optically detected magnetic resonance. **a)** ODMR spectrum showing the fluorescence signal of an ensemble of NV centres without an externally applied magnetic field. **b)** The application of a constant magnetic field splits the resonances according their geometric projection (equation 4.3) and the ODMR spectrum comprises the resonances corresponding to the four crystallographic orientations of the NV centres (I–IV). This figure is modified from [218] with the permission of the publisher. Copyright (2019) Elsevier B.V. All rights reserved.

$\beta = \mathrm{d}D_{\mathrm{gs}}/\mathrm{d}T \approx -74.2\,\mathrm{kHz\,K^{-1}}$ the temperature dependence of the zero-field splitting [195], $\tilde{\gamma}_{\mathrm{NV}} = \mu_{\mathrm{B}} g_e/h \approx 28.024\,\mathrm{GHz\,T^{-1}}$ the gyromagnetic ratio divided by 2π with μ_{B} the Bohr magneton, $g_e \approx 2$ the Landé factor, h the Planck constant and B_0 the magnetic field strength along the respective NV axis [204].

We performed the ODMR measurement in a continuous mode, both for optical and microwave excitation. ODMR spectra were recorded by systematically increasing the microwave frequency f and integrating the analogue voltage S of the photodetector for 70 ms for each microwave frequency. To reduce long-term drifts, each measurement was followed by a measurement of the fluorescence where the microwaves were turned off. The ratio of the values was plotted in the ODMR spectra.

Figure 4.6 shows ODMR spectra without and with an externally applied magnetic field using a permanent magnet. A splitting of resonance features around the zero-field splitting ($D_{\mathrm{gs}} \approx 2.87\,\mathrm{GHz}$) can be observed in the ODMR spectrum recorded without the external magnetic field, see figure 4.6a. These two features have a linewidth $\Delta\nu$ with a full width at half maximum of 3.82 MHz, respectively. This Zeeman shift of the $m_{\mathrm{s}} = \pm 1$ energy levels could be explained

by a magnetic field, which was mainly induced by current flow through the LED bond wire, see figure 4.1a. This bond was roughly 1.6 mm away from the surface of the diamond.

In the presence of the external magnetic field $\boldsymbol{B_0}$, the resonance transitions shift according to equation 4.3 and the projection of the external field along the orientation axes of the NV centres. Hence, four pairs of resonances are observable in the spectrum shown in figure 4.6b. These resonance features correspond to the $m_\mathrm{s} = 0 \rightarrow m_\mathrm{s} = \pm 1$ ground state transitions of the four crystallographic orientations of the NV centres in the diamond lattice. We measured a projection of $\boldsymbol{B_0}$ on the NV orientation Ⅳ largest frequency shift of $\approx 1.82\,\mathrm{mT}$. Each of these four resonances (marked Ⅰ–Ⅳ) comprises a hyperfine structure consisting of three narrow peaks shown in figure 4.7a. This hyperfine structure is associated with the coupling of the NV centre's electron spin to the nitrogen nuclear spins.

The hyperfine splitting of the electron spin resonance was fitted using a sum of three physical Lorentzian

$$f(x) = \sum_{i=1}^{3} A_i \frac{\sigma_i^2}{(x - x_{0,i})^2 + \sigma_i^2}, \tag{4.4}$$

where A is an amplitude, σ the scale parameter specified to the full width at half maximum $\Delta\nu$ with $\Delta\nu = 2\sigma$ and i the number of the hyperfine splitting transition.

Unless otherwise stated, the following discussion and analysis will refer to resonance Ⅲ of figure 4.6b. Fitting the data with a triple Lorentzian function we found that these resonances are split by $\approx 2.14\,\mathrm{MHz}$, which corresponds to hyperfine splitting caused by the $^{14}\mathrm{N}$ isotope [197]. A full width at half maximum of $\Delta\nu = 1.11\,\mathrm{MHz}$ and a contrast $C = 0.051\%$ is derived for this resonance from the fit in figure 4.7a.

A temperature of the diamond of $\approx 69°\mathrm{C}$ was estimated from the spectrum in figure 4.6b shown in table A.3. This rather high value is in agreement with numerical simulations conducted with COMSOL Multiphysics®, which show that the LED reaches a temperature above 110°C at its surface. Therefore, it

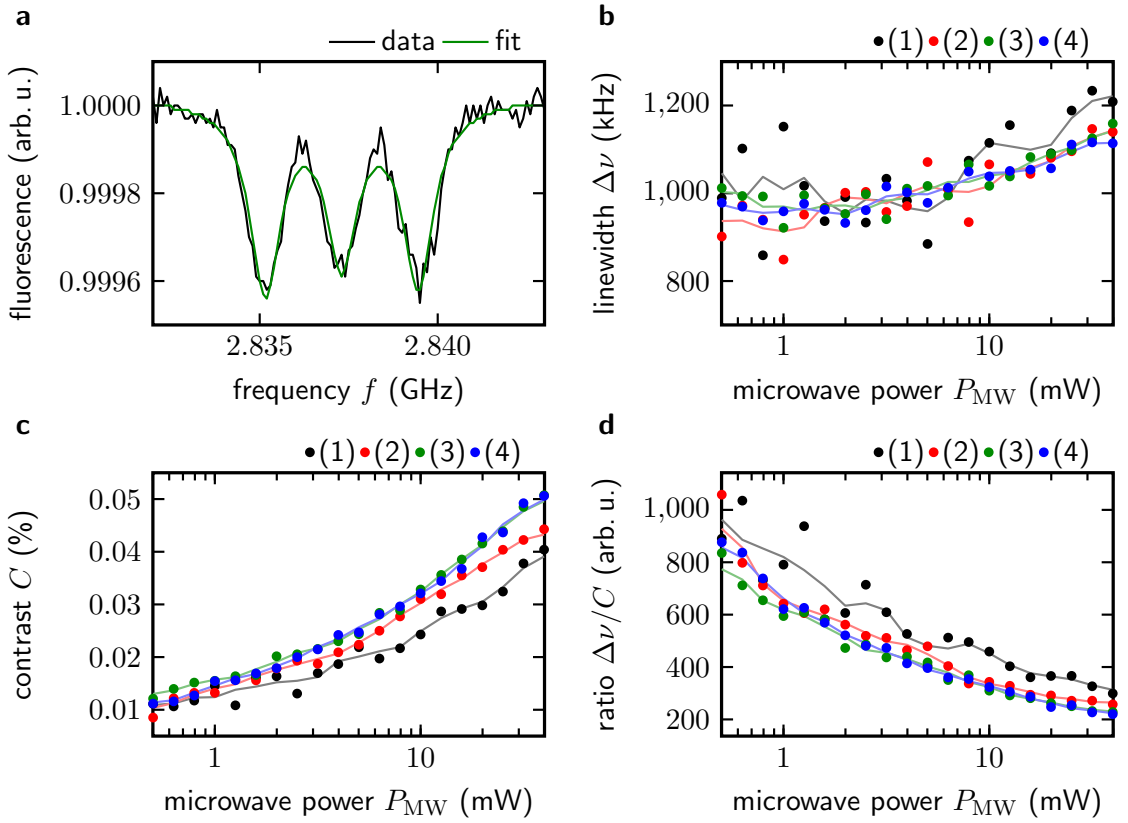

Figure 4.7: Results of ODMR measurements. a) Zoom-in of the fine structure shown in figure 4.6b with a hyperfine splitting of $\Delta f_{\mathrm{HFS}} \approx 2.14\,\mathrm{MHz}$. The solid red line is a triple Lorentzian fit to the data. **b)** Dependence of linewidth $\Delta\nu$ on the applied microwave power P_{MW} for four different optical powers of the LED (1)-(4): $P_{\mathrm{opt}} = (27.1, 42.6, 54.4, 64.0)\,\mathrm{mW}$. **c)** Corresponding dependence of the measured contrast C. **d)** Corresponding plot of the ratio $\Delta\nu/C$. This figure is based on [218].

is plausible that the main effect of temperature increase inside the diamond was explainable due to heat flow of the LED. Likewise, the influence of the applied microwave field is though not negligible as the microwave structure on the PCB were closely located to the diamond.

For sensing applications, a heating of the diamond might be a problem as temperature fluctuations shift the resonance frequencies (*e.g.* a temperature change of 1 K shifts the resonance frequency by $\approx -74.2\,\mathrm{kHz}$ [195], which corresponds to a magnetic field variation of $\approx 2.65\,\mu\mathrm{T}$). Monitoring both $m_{\mathrm{s}} = \pm 1$ resonances allows magnetometer protocols, which are insensitive to temperature drifts.

Nevertheless, the high temperature of the diamond and consequently of the housing of the sensor device is a crucial issue for a wide range of applications, especially for biological and medical applications. Actively cooling components, *e.g.* Peltier elements, could help to decrease the created heat inside the device. However, integrating such elements would make the assembly more complex and probably make the device less compact. Separating the light source, which is one of the main heating sources, from the diamond could be also an option.

In the limit of photon shot-noise, the sensitivity η_B and the minimal detectable magnetic field $B_{\min}$ of the ODMR based magnetometer are given by [208]

$$B_{\min} = \frac{\eta_B}{\sqrt{\tau}} = NF \frac{1}{\tilde{\gamma}_{\mathrm{NV}}} \frac{\Delta\nu}{C} \frac{1}{\sqrt{\mathcal{R}\tau}}. \tag{4.5}$$

Here, NF is a numerical factor related to the profile of the spin resonance (for a Lorentzian profile: $NF = 4/3/\sqrt{3} \approx 0.77$ [208]), τ the measurement time, $\mathcal{R}$ the photon rate, C the contrast and $\Delta\nu$ the linewidth of the optically detected magnetic resonance.

In order to find the optimum operation point of the sensor device, we next investigated the dependence of C and $\Delta\nu$ on the excitation intensity of the light and the microwave field.

ODMR Analysis

Figure 4.7 shows the linewidth $\Delta\nu$ and the contrast C as a function of the applied microwave power P_{MW}. The data were obtained by fitting the ^{14}N hyperfine split resonances for the chosen NV orientation axis Ⅱ shown in the ODMR spectrum of figure 4.7b. The dependence of the applied microwave power on the linewidth is depicted in figure 4.7a. A minimal linewidth of $\Delta\nu \approx (0.95 \pm 0.05)\,\mathrm{MHz}$ was found for $P_{\mathrm{MW}} < 5\,\mathrm{mW}$. Increasing the applied microwave power leads to a broadening of the measured linewidth. Figure 4.7b shows the dependence of the contrast C on the applied microwave field. The contrast increases from 0.02% to 0.05% with the applied microwave power. In contrast to the observed microwave induced increase of the linewidth and the [218]

contrast, no significant influence of the optical excitation intensity on the linewidth and the contrast was observed within the feasible optical power range, *i.e.* $P_{\mathrm{opt}} \leq 64\,\mathrm{mW}$, see figure 4.7b,c. This finding is in agreement with the rather low value of the optical polarisation rate Γ_{P} from equation 4.2.

In the following, we apply an analytic model according to Dréau *et al.* in order to describe the linewidth and contrast measured in the experiments [208] . For this purpose, we consider the power dependency of linewidth and contrast only for the highest accessible optical excitation power by the LED, *i.e.* $P_{\mathrm{opt}} = 64.0\,\mathrm{mW}$.

ODMR Linewidth

[218] According to Dréau *et al.* the linewidth of NV ensembles can be analytically modelled by the following equation [208]

$$\Delta\nu = \frac{1}{\pi}\sqrt{\Gamma_2^{*2} + \frac{\Omega_{\mathrm{R}}^2\Gamma_2^*}{2\Gamma_1 + \Gamma_{\mathrm{P}}}} \tag{4.6}$$

as a function of the Rabi frequency Ω_{R}, the spin-lattice relaxation rate Γ_1, the inhomogeneous spin relaxation rate Γ_2^* and the optical pumping rate Γ_{P}. For this model, we consider the regime where $\Gamma_{\mathrm{P}} < \Gamma_1,\Gamma_2^*$ because of the low optical excitation intensity of the LED. Otherwise, equation 4.6 would simplify to $\Delta\nu = \frac{1}{\pi}\sqrt{\Gamma_2^{*2} + \Omega_{\mathrm{R}}^2}$. The Rabi frequency was calculated by [304]

$$\Omega_{\mathrm{R}} = \frac{\gamma_{\mathrm{NV}} B_1 \sin(\alpha)}{\sqrt{2}}. \tag{4.7}$$

Here, the microwave field strength B_1 was derived from a reference power level P_{ref} and an amplitude B_{ref}, which were taken from numerical simulations using CST Microwave Studio® of the microwave transmission line using the following equation

$$B_1 = B_{\mathrm{ref}}\sqrt{P_{\mathrm{MW}}/P_{\mathrm{ref}}}. \tag{4.8}$$

The simulation yields an amplitude of $B_{\mathrm{ref}} \approx 11.5\,\mu\mathrm{T}$ at the position of the diamond for $P_{\mathrm{ref}} = 1\,\mathrm{W}$, as shown in figure 4.4b. In the experimental setup, the oscillating magnetic field $\boldsymbol{B_1}$ was tilted with respect to the preferred direction of the NV centres by $\alpha \approx (52 \pm 16)°$. We therefore assumed a geometric

coupling factor of $\sin(\alpha) \approx 0.8$ in equation 4.7 for the analysis of the magnetic resonance. The calculated value of $\Gamma_P \approx 79\,\text{Hz}$ and equation 4.6 were used to fit the data in figure 4.9a. The resulting fit parameters are $\Gamma_1 \approx (0.47 \pm 0.06)\,\text{Hz}$ and $\Gamma_2^* \approx (3.04 \pm 0.02)\,\text{MHz}$.

The latter figure corresponds to an inhomogeneously broadened linewidth of $\Delta\nu = \Gamma_2^*/\pi \approx 0.97\,\text{MHz}$. We explain the increase of the linewidth compared to the intrinsic linewidth of the diamond of $\approx 0.1\,\text{MHz}$ by magnetic field gradient, which originates from a current flow through the bond wire of the LED, see figure 4.8.

The fit in figure 4.9a results in a spin-lattice relaxation time of $T_1 = 1/\Gamma_1 \approx 2.1\,\text{ms}$. This rather short relaxation time is in contrast to 5.9 ms for this diamond, which has been measured on a confocal setup using a pulsed experiment to directly measure the longitudinal relaxation time T_1. We explain the discrepancy by two effects. First, the diamond in the miniaturised sensor reaches a temperature of $\approx 69°\text{C}$ because of the dissipated Joule heating of the integrated electronic components (LED, current source and microwave transmission lines). This temperature increase deteriorates T_1 [305]. Secondly, the model from equation 4.6, which we used, is a rather indirect method compared to the pulsed measurement of the T_1 time, because it relies on several fit parameters.

ODMR Contrast

Analogously to the linewidth measurement data, we applied the model from Dréau *et al.* to the measured contrast data shown in figure 4.9b. The model of the contrast is given by [208] [218]

$$C = \frac{\theta\Gamma_P}{2(1-\theta)\Gamma_1 + \Gamma_P} \frac{\Omega_R^2}{\Omega_R^2 + \Gamma_2^*(2\Gamma_1 + \Gamma_P)} \tag{4.9}$$

as a function of the Rabi frequency Ω_R, the spin-lattice relaxation rate Γ_1, the inhomogeneous transversal spin relaxation rate Γ_2^* and the optical pumping rate Γ_P. $\theta \approx 0.2$ is a weighting factor of the fluorescence rates of the different spin polarisations [208].

We used the fitting results of $\Gamma_1 \approx (0.48 \pm 0.06)\,\text{kHz}$ and $\Gamma_2^* \approx 3.04 \pm 0.02\,\text{MHz}$ from equation 4.6 and figure 4.9a in order to fit the data of the contrast (blue

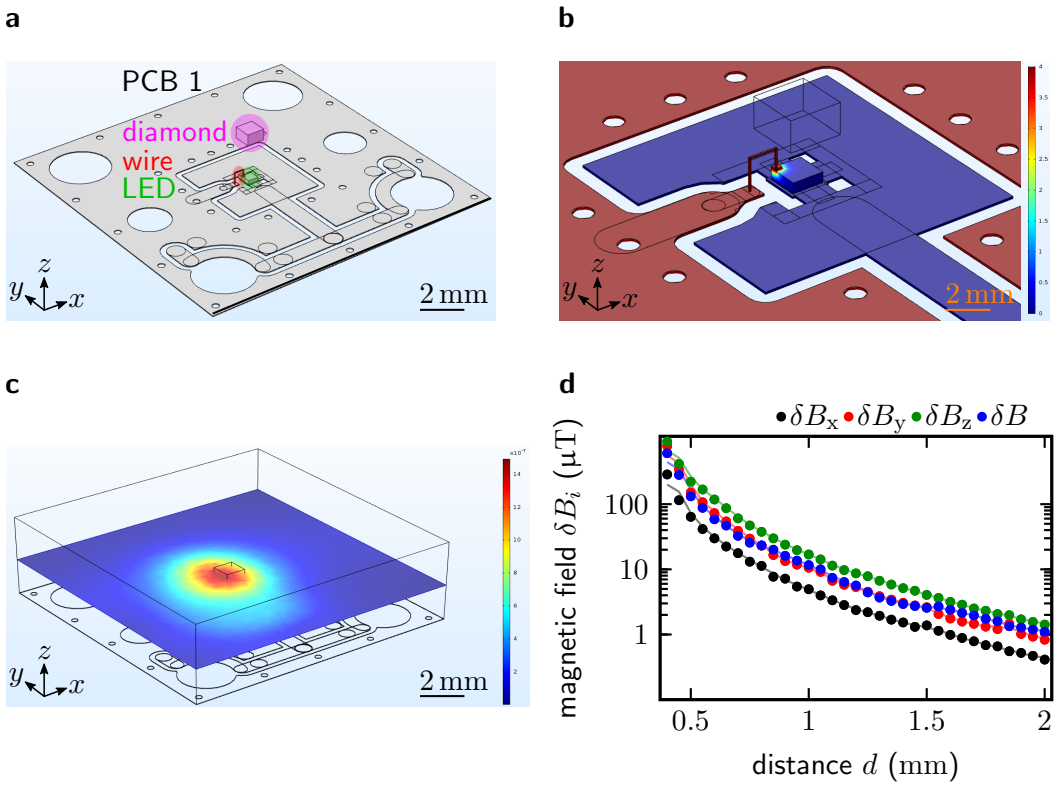

Figure 4.8: Simulation results of the induced magnetic field on the diamond by the LED bond wire. a) Graphical view on the simulation settings for evaluating the influence of the magnetic field induced by the LED bond wire on the diamond using COMSOL Multiphysics®. The LED bond is modelled as a rectangular wire made of silicon with an electrical conductivity of $\sigma_{\mathrm{el}} = 300\,\mathrm{S\,m^{-1}}$. The surrounding PCB is based on the computed-aided design (CAD) file of PCB1 (figure 4.1a) with dimensions of $10\,\mathrm{mm} \times 40\,\mathrm{mm}$ and the electric lines are made of copper. The position of the diamond is aligned to the centre of the LED surface with a distance d between surface of the LED and backside of the diamond (along the optical axis, z-axis). **b)** Simulated distribution of the electrical potential for an applied current of $I = 175\,\mathrm{mA}$ through the bond wire. The LED is supplied by a bias voltage of $U_{\mathrm{bias}} = 4.0\,\mathrm{V}$. **c)** Simulated distribution of the induced magnetic field $\boldsymbol{B}$ with $B = \sqrt{B_{\mathrm{x}}^2 + B_{\mathrm{y}}^2 + B_{\mathrm{z}}^2}$ induced by current flow through the LED bond wire. The field distribution is shown for the central plane through the diamond for $d = 1.8\,\mathrm{mm}$ corresponding to the assembly of the NV sensor. **d)** Simulated results of the deviations of the magnetic field components B_{x}, B_{y}, B_{z} and the absolute deviation of δB within the diamond volume for different distances d. Lines of moving mean (of three neighbouring data points) are added to the graphs.

solid line). Especially, for larger values of P_{MW} the model deviates from the data (blue line, fit_1). We therefore considered the heating of the applied microwave and consequently a deterioration of T_1 with increasing microwave power (red

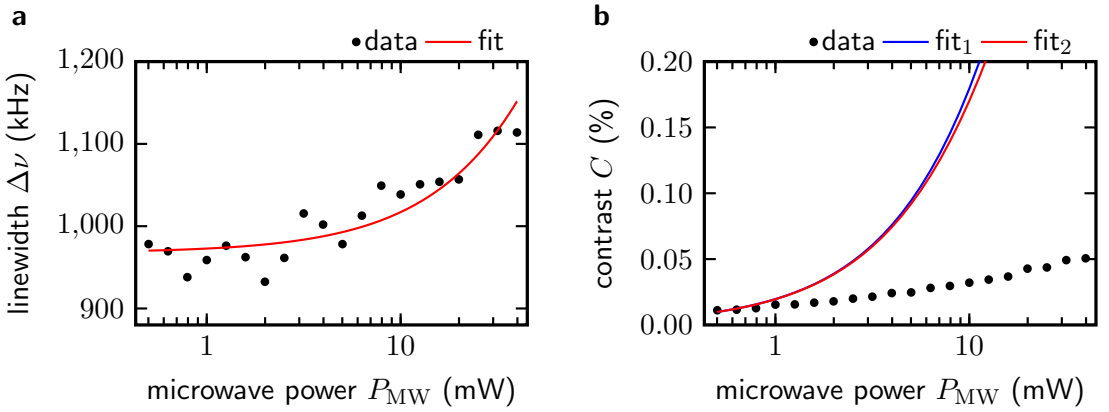

Figure 4.9: Dependence of the linewidth and the contrast on the spin manipulation. **a)** Resonance linewidth $\Delta\nu$ depending on the applied microwave power P_{MW} with an optical power P_{opt} of 64 mW from the LED. The solid line is a fit to the data points according to equation 4.6. **b)** Corresponding dependence of the contrast on the microwave power P_{MW}. The solid lines are two fits to the data points according to equation 4.9 with slight differences (detailed description in main text). However, the conformity of the model to the measured data is poor. This figure is based on [218].

line, fit$_2$) [305]. For this purpose, we assumed that the Joule heating of the microwaves is mainly dissipated by convection. We calculated the temperature increase ΔT by

$$\Delta T = 2\kappa A P_{\mathrm{MW}} \tag{4.10}$$

using a temperature coefficient of $\kappa = 10\,\mathrm{W\,m^{-2}\,K^{-1}}$, a total surface of the sensor $A \approx 10.7\,\mathrm{cm^2}$ and the assumption that the temperature difference ΔT of the diamond (to the ambient temperature) is roughly twice the value of the temperature difference of the surface (to the ambient temperature). From the work of Jarmola *et al.* we extracted $T_1' = \partial T_1/\partial T \approx -(34 \pm 6)\,\mu\mathrm{s\,K^{-1}}$ in the range of $0°\mathrm{C} < T < 100°\mathrm{C}$ [305]. We modelled T_1 as

$$T_1\,(\Delta T) \approx T_1^{\mathrm{model}} - T_1'\Delta T, \tag{4.11}$$

where $T_1^{\mathrm{model}} \approx 2.13\,\mathrm{ms}$ and ΔT the induced temperature due to Joule heating. This results in a slightly smaller difference between the model and the data (red solid line, fit$_2$). This could indicate that Joule heating can deteriorate the sensor performance for the given excitation conditions.

However, the deviation remains for larger values of P_{MW}. An explanation for this deviation might be due to the different experimental settings compared to the work by Dréau *et al.* [208]. In our system, a large ensemble of NV centres was illuminated by a rather low excitation intensity (section 4.2.2), whereas Dréau *et al.* performed experiments with a single NV centre and a light intensity, which was more than three orders of magnitude larger than in our experiments [208].

4.3.2 Sensitivity Measurement

[218] The parameters of linewidth and contrast are part of the photon shot-noise limited sensitivity for a DC magnetic field measurement of equation 4.5. Typically, counteracting effects between light and microwave excitation need to be considered in order to find the optimum working parameters for an NV based magnetometer [208].

Figure 4.9a shows a power induced broadening of the linewidth due to the applied microwave power, while the contrast increases with the applied microwave power as shown in figure 4.9b. This finding differs from the behaviour of a single NV centre, where a saturation of the contrast would be expected when the linewidth broadens. The reason for the increase of the contrast in our ensemble magnetometer can be explained by the inhomogeneous distribution of resonance frequencies in the diamond. The inhomogeneous distribution is due to a magnetic field gradient. In this case, increasing the microwave power leads an excitation of additional NV centres, which are detuned to the applied microwave. This leads a broadening of the observed linewidth and simultaneously to an increase of the contrast as these detuned NV centres contribute to the signal.

Linked to equation 4.5, calculating the ratio of linewidth and contrast reveals information about the sensor performance within the possible ranges of optical and microwave power for the sensor device. As the ratio $\Delta\nu/C$ shown in figure 4.7d for different settings (P_{MW} and P_{opt}) shows no minimal turning

point, we can conclude that the achievable light intensities and microwave fields of our device does not exploit the full sensor potential. It is plausible that our sensor would perform better if higher values both for P_{MW} and P_{opt} are applied to the diamond.

The values of the linewidth and contrast will be used in the next paragraph in order to determine the sensitivity of the sensor device. For this purpose, we used the Allan deviation σ_{adev} to characterise the noise level of the sensor [271]. In contrast to calculation of the standard deviation, the Allan deviation determines the deviations only within a given averaging time τ. The sampled data was binned to intervals of length τ so that $\sigma_{\mathrm{adev}}(\tau)$ can be calculated by [22]

$$\sigma^2_{\mathrm{adev}}(\tau) = \frac{1}{2}\left\langle(\overline{y}_{n+1} - \overline{y}_n)^2\right\rangle . \tag{4.12}$$

The Allan deviation compares the average of each bin $\overline{y}_n$ to the average of the next bin $\overline{y}_{n+1}$, see figure 4.10. Instead of calculating the overall standard deviation of a sampled data set, the Allan deviation determines the standard deviation as a function of the binning time [306]. This approach allows to identify the optimal integration time where the resolution of the sensor is best.

Figure 4.11 shows the minimal detectable magnetic field B_{min}, which can be measured within a certain averaging time τ by the NV sensor. To calculate B_{min} we used equation 4.5 and replaced the noise-to-signal ratio $1/\sqrt{R\tau}$ by the experimentally quantified ratio $\Delta S/S$

$$B_{\mathrm{min}}(\tau) = NF\frac{1}{\tilde{\gamma}_{\mathrm{NV}}}\frac{\Delta\nu}{C}\frac{\Delta S(\tau)}{S}. \tag{4.13}$$

Here, ΔS is the noise level that was derived by the Allan deviation of the measured signal shown in equation 4.12. The measured average signal level of $S \approx 1.85\,\mathrm{V}$ corresponds to a detected fluorescence power of $P_{\mathrm{fl}} = S/(QG) \approx 0.20\,\mathrm{mW}$. We recorded the fluorescence for 100 ms with a sampling rate of 100 MHz to calculate B_{min} (green line in figure 4.11) while exciting with a microwave frequency of $f \approx 2859.84\,\mathrm{MHz}$ being resonant to the selected hyperfine transition. For reference, we recorded the noise of the used sampling card analogously (orange line in figure 4.11). For this measurement, the signal cable

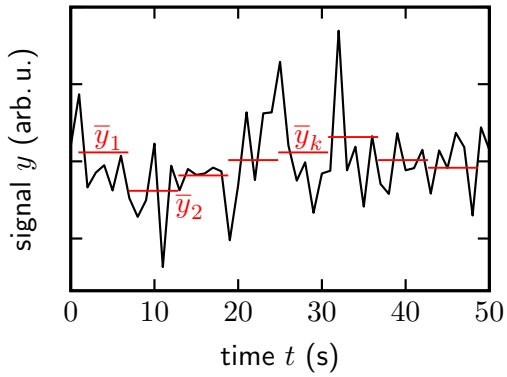

Figure 4.10: Calculation of the Allan deviation. $\sigma_{\mathrm{adev}}(\tau)$ determines the deviation of recorded data y over time t by comparing the mean values $\overline{y}_k$ for a given averaging time τ with each other.

of the sensor was unplugged from the input of the ADC and the input was terminated with a 50 Ω resistor. The black curve in figure 4.11 corresponds to the photon shot-noise limit and thus scales with as $1/\sqrt{\tau}$, see equation 4.5.

For short averaging times $\tau \leq 1\,\mu s$ we observed a $1/\sqrt{\tau}$-scaling in the data for both measurements (sensor operation and sampling card), which show a nearly parallel behaviour to the $1/\sqrt{\tau}$-scaling of the photon shot-noise curve. However, a difference in the noise level between these two measurements is observed, which becomes smaller with increasing τ. For $1\,\mu s < \tau < 1\,ms$, the data show no significant difference in B_{min} and for times τ larger than 1 ms the curves become approximately horizontal.

This indicates that the sensitivity of our sensor is mainly limited by the sampling card for $\tau > 1\,\mu s$ as the two curves (sensor performance and limit of the sampling card) show similar progression. For $\tau \leq 1\,\mu s$, we found that the increase of the noise was due to the switching on the electronics of the photodiode and transimpedance amplification circuit, see figure 4.12. No additional noise level due to switching on the microwaves and the LED was observed, see figure 4.12. An improvement in terms of magnetic field sensitivity could be achieved if the noise level of the sampling card is further reduced or if a differential amplifier is used, which allows a higher transimpedance.

The photon shot-noise limit corresponds to a sensitivity of $\eta_B \approx 2.95\,\mathrm{nT\,Hz^{-1/2}}$, *i.e.* $B_{\mathrm{min}} \approx 2.95\,\mathrm{nT}$ for an averaging time of $\tau = 1\,s$. The minimal detectable

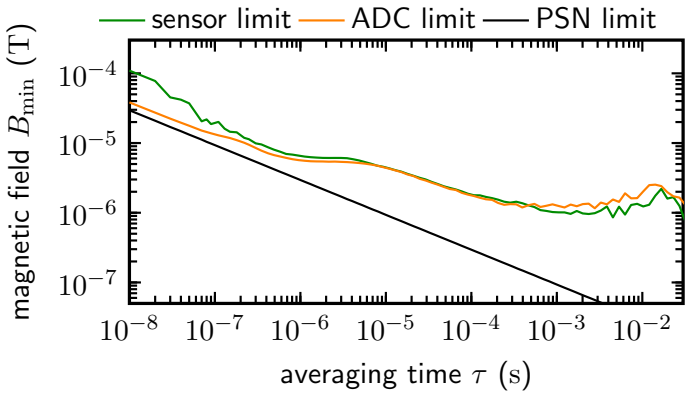

Figure 4.11: Minimum detectable magnetic field derived from the noise analysis. The dependency of the minimum detectable magnetic field B_{min} on the averaging time τ was derived from the measured Allan deviation σ_{adev} of the signal of the photodetector. B_{min} was calculated with equation 4.13 using the fitted results of the contrast $C = 0.051\%$, the linewidth $\Delta\nu = 1.11\,\mathrm{MHz}$, an average signal level $S = 1.845\,\mathrm{V}$, a responsivity $Q = 0.34\,\mathrm{A\,W^{-1}}$ and a gain factor $G = 27\,\mathrm{kV\,A^{-1}}$. The noise of the sensor (green line) was recorded while exciting with a microwave frequency that was resonant to one hyperfine transition. We used the following conditions: $f \approx 2859.84\,\mathrm{MHz}$ with a power of $P_{\mathrm{MW}} \approx 40\,\mathrm{mW}$ and an optical power of $P_{\mathrm{opt}} \approx 64\,\mathrm{mW}$. These parameters correspond to the magnetic resonance shown in figure 4.6. The orange curve depicts the limitation by the sampling card. The curve of the photon shot-noise limit (black line) was calculated using equation 4.5 and is proportional to $1/\sqrt{\tau}$. The data were acquired with a recording length of $100\,\mathrm{ms}$ and a sampling rate of $100\,\mathrm{MHz}$ of the 14-bit analogue-to-digital converter. This figure is based on [218].

magnetic field, which was measured by the miniaturised sensor, is B_{min} ($\tau \approx 1\,\mathrm{ms}$) $\approx 1\,\mu\mathrm{s}$. This corresponds to a sensitivity of $\eta_B \approx 31\,\mathrm{nT\,Hz^{-1/2}}$, which is roughly one order of magnitude worse than the limit of photon shot-noise.

4.4 Conclusion

In conclusion, we have demonstrated a compact and integrated magnetic field sensor based on NV centres in diamond. The device achieves sensitivities of $\eta_B \approx 31\,\mathrm{nT\,Hz^{-1/2}}$ for an integration time $\tau = 1\,\mathrm{ms}$ with a photon shot-noise limited sensitivity of roughly $3\,\mathrm{nT\,Hz^{-1/2}}$. This sensor provides a compact and portable platform for measuring both magnetic fields and temperature. Furthermore, analysis of the projection of the field on NV centre's axes allows to use the sensor for vector magnetometry [207]. We have shown that this quantum- [218]

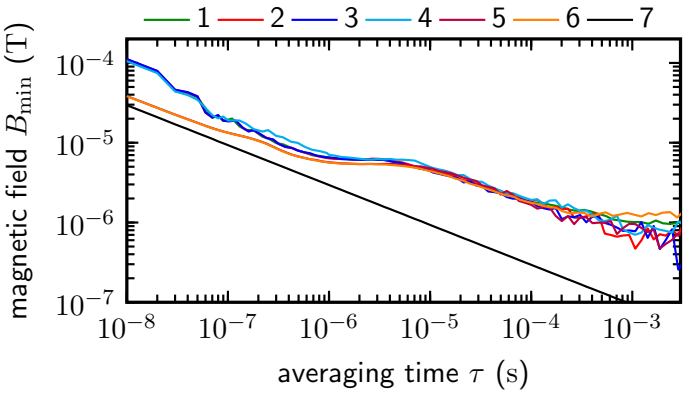

Figure 4.12: Minimum detectable magnetic field derived from the noise analysis. The dependency of the minimum detectable magnetic field $B_{\min}$ on the averaging time τ was derived from the measured Allan deviation σ_{adev} of the signal of the photodetector. Experiments were performed for different settings (curves $1-6$). Curve (7) depicts the limit of $B_{\min}$ by the photon-shot-noise of equation 4.3. This analysis shows that curve (5) and (6) have the same progression for short timescales. However, the noise level increases, as the photodetector is powered (curve 4), *i.e.* the photodetector causes the additional noise for averaging times below $1\,\mu\text{s}$. $B_{\min}$ was calculated with equation 4.13 using the fitted results of the contrast $C = 0.051\%$, the linewidth $\Delta\nu = 1.11\,\text{MHz}$, an average signal level $S = 1.845\,\text{V}$, a responsivity $Q = 0.34\,\text{A}\,\text{W}^{-1}$ and a gain factor $G = 27\,\text{kV}\,\text{A}^{-1}$. The data were acquired with a recording length of 100 ms and a sampling rate of $100\,\text{MHz}$ of the 14-bit analogue-to-digital converter. (1): Measurement, in which the data were recorded while exciting with a microwave frequency that is resonant to one hyperfine transition ($f \approx 2859.84\,\text{MHz}$ with $P_{\text{MW}} \approx 40\,\text{mW}$ and $P_{\text{opt}} \approx 64\,\text{mW}$). (2): Measurement with an applied microwave excitation, which is off-resonant to one hyperfine transition; same power settings were used as in measurement (1). (3): microwave excitation was turned off; LED and photodiode were turned on. (4): Additionally to measurement (3), the LED was turned off while recording the data. (5): Measurement of the noise level, in which microwaves, LED and photodiode were turned off. (6): Noise level caused by the sampling card; the input of the ADC was terminated by a $50\,\Omega$ resistor. This figure is based on [218].

based sensor technology can be miniaturised into a compact and integrated device with a power consumption of $\approx 1.5\,\text{W}$, see table A.4, enabling it for industrial applications.

Due to limited optical excitation intensity, the optimal operation conditions for the system were not reached in this work. Therefore, the optical power P_{opt} and microwave power P_{MW} need to be increased in order to obtain an improved contrast. Increasing the contrast C to 1% would result in a 20 times improved $\eta_B \approx 1.5\,\text{nT}\,\text{Hz}^{-1/2}$. Changing the light source from an LED-to a laser-based

system (including optical fibres) could be an option for realising higher optical excitation rates. Additionally, a remote optical excitation using a fibre-based laser system could reduce the temperature of the sensor device, which would be necessary for *e.g.* biological applications and for the detection of human brain magnetic fields [19]. Further steps in improving the performance of the sensor are linked to the limitations of the data acquisition electronics and the induced magnetic field gradient by the bond wire of the LED.

5 Fibre-Based NV Magnetometer

This chapter is based on [32] with minor edits. The taken text passages are marked by marginal notes, whereas the taken captions are not additionally highlighted. Parts of the former appendix are now included in the main text. Reprinted and modified under author rights from [32], licensed under a Creative Commons Attribution-NonCommercial-NoDerivatives License 4.0 (CC BY-NC-ND 4.0, https://creativecommons.org/licenses/by-nc-nd/4.0/). Copyright (2021) The authors.

The development of the integrated and portable NV magnetometer was conceived by Tino Fuchs, Robert Rölver, Andreas Brenneis, Thomas Buck and Felix M. Stürner in cooperation with Fedor Jelezko. The design of the 3D-printed constructions were created by Julian Kassel and the assembly of the NV sensor were performed by Julian Kassel and Felix M. Stürner. The optical filter on the photodiodes were deposited by Robert Rölver. The microwave resonator was designed and simulated by Anton Savitsky and Dieter Suter in discussion with Andreas Brenneis and Felix M. Stürner. Optical considerations of the sensor were performed by Andreas Brenneis and Felix M. Stürner. The laser module was setup by Jens Grimmel, Stefan Hengesbach and Michael Förtsch. Simulations on additional magnetic fields were performed by Tino Fuchs and Felix M. Stürner in discussion with Andreas Brenneis. The electrical circuit of the balanced photodiode circuit was designed by Thomas Buck in discussion with Andreas Brenneis and Felix M. Stürner and assembled by Julian Kassel. The diamond sample was supplied by Junichi Isoya, Shinobu Onoda, Hitoshi Sumiya and Kazuo Nakamura. The experiments were performed and analysed by Felix M. Stürner in discussion with Thomas Buck, Andreas Brenneis and Fedor Jelezko.

5.1 Introduction

[32] In this chapter, we demonstrate a fibre-integrated magnetometer based on NV centres in diamond shown in figure 5.1. The compact design of the magnetic field sensor was achieved by using a single-mode fibre for the optical initialization of the NV centres and deploying a balanced detection scheme built up by two photodiodes positioned close to the diamond. Furthermore, our integrated prototype comprises all necessary components, such as offset magnetic field, laser source, microwave generator and signal processing unit. This portable setup yields a sensitivity of $\approx 344\,\mathrm{pT\,Hz^{-1/2}}$.

One important figure of merit for magnetometers is the magnetic sensitivity characterizing the minimal magnetic field δB_{min}, which can be detected by the sensor within a given measurement time t. Due to the optical readout of the NV spin states, the sensitivity η_{PSN} is limited by photon shot-noise and is given by [120]

$$\eta_{\mathrm{PSN}} = \delta B_{\mathrm{min}}\sqrt{t} \approx \mathcal{P}_{\mathcal{F}}\frac{1}{\tilde{\gamma}_{\mathrm{NV}}}\frac{\Delta\nu}{C\sqrt{\mathcal{R}}}, \tag{5.1}$$

where $\mathcal{P}_{\mathcal{F}}$ is a numerical factor resulting from the shape of the resonance with $\mathcal{P}_{\mathcal{F}} = 4/(3\sqrt{3}) \approx 0.77$ for a Lorentzian profile, $\Delta\nu$ the linewidth, C the contrast and $\mathcal{R}$ the detected photon rate. η_{PSN} can be improved by minimising the linewidth and maximising the values of contrast and detected photon rate.

Here, the interplay between the optical pumping process and the microwave spin manipulation needs to be considered to optimise η_{PSN}. This interplay strongly depends on the used diamond material and the resulting spin-lattice relaxation time T_2^* of the NV ensembles. In general, the optical pumping rate and the microwave drive should be comparable to $1/T_2^*$ to exploit the dynamics of the NV ensembles properly [120,208]. The main extrinsic parameters limiting the sensitivity of an NV magnetometer are thus the optical power, the power of the applied microwave field and the fluorescence collection efficiency [120, 200]. Both linewidth and contrast are affected by microwave and optical power, whereas the collection efficiency results from the design of the sensor. The optical power was fixed by design but was chosen to closely fulfil an optical

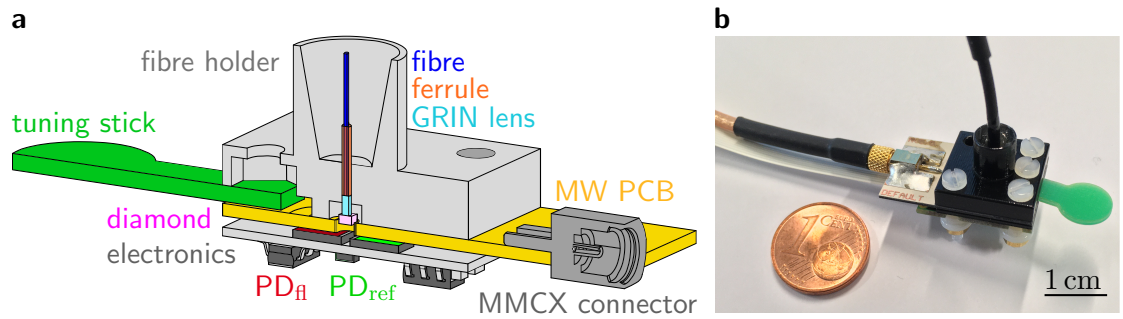

Figure 5.1: Sensor head of the fully integrated NV magnetometer. a) Schematic cross-section of the sensor head including the used components (optical fibre, GRIN rod lens, 3D-printed fibre holding construction, diamond, microwave board (MW PCB), resonator tuning stick, MMCX connector and the balanced photodetection board (PD PCB) including two photodiodes with different coating and electronic components at the back of this PCB. **b)** Photo image of the NV sensor placed next to a Euro cent coin. This figure is based on [32].

pumping rate that is comparable to $1/T_2^*$. A detailed analysis of the adjustable parameters of our NV sensor with impact on the sensitivity will be given in the experimental section.

5.2 Sensor Assembly

The sensor head of the integrated NV magnetometer is shown in figure 5.1 and the complete experimental setup can be seen in figure 5.2. The integrated sensor head includes a diamond with NV centres, which is connected to a lens and an optical single-mode fibre, a microwave circuit for providing an oscillating magnetic field necessary for the spin manipulation and a PCB containing two photodiodes for a balanced detection scheme of the emitted fluorescence and the excitation laser light. Microwave source and laser were located externally and connected to the sensor head by radiofrequency cables and an optical fibre, respectively. [32]

5.2.1 Optical Excitation

We used a fibre coupled, compact laser module from Q.ANT GmbH with an emitting wavelength of 521.9 nm providing 23.5 mW at the end of the fibre. The [32]

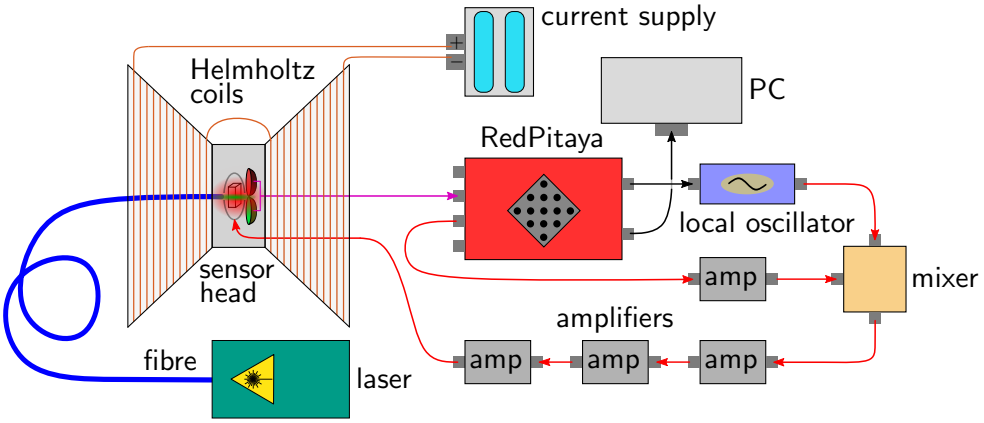

Figure 5.2: Schematic of the complete NV sensor setup. The sensor head of our NV magnetometer was placed inside a tapered pair of Helmholtz coils, which were powered by a battery. The excitation light was generated by a compact laser module and transmitted to the diamond by a single-mode fibre. A local oscillator generated microwaves in the GHz range and a mixer was used to add microwaves in the MHz range, which were generated and frequency modulated by the waveform generator module of the RedPitaya. These microwaves were further amplified by three compact low-noise amplifiers and then transmitted to the double split-ring resonator providing an oscillating field at the diamond necessary for the driving electron spin resonances. A balanced detection scheme consisting of two photodiodes and a logarithmic transimpedance amplifier was used to record both the modulated fluorescence signal and laser light. The output of the transimpedance amplifier was demodulated by the RedPitaya module and further processed by a personal computer. This figure is reprinted from [32], licensed under CC BY-NC-ND 4.0, https://creativecommons.org/licenses/by-nc-nd/4.0/.

dimensions of the laser module are $(35 \times 110 \times 115)\,\mathrm{mm}^3$. This laser is coupled to a polarization-maintaining (PM) single-mode optical fibre (Thorlabs PM-S405-XP, core diameter $3.0\,\mu\mathrm{m}$, $NA = 0.12$). A direct connection between fibre and diamond would result in an inhomogeneous optical excitation of the NV centres along the optical path, see figure 5.3c. We used therefore a GRIN rod lens (GRINTECH GT-LFRL-050-025-50-NC (670), $NA = 0.5$) to collimate the light that exits the fibre before it enters the diamond, see figure 5.3d. The GRIN rod lens and fibre were connected by an epoxy glue and inserted into a pigtailed glass ferrule to stabilise the assembly. The diamond was directly glued to the surface of the GRIN lens with a droplet of polydimethylsiloxane.

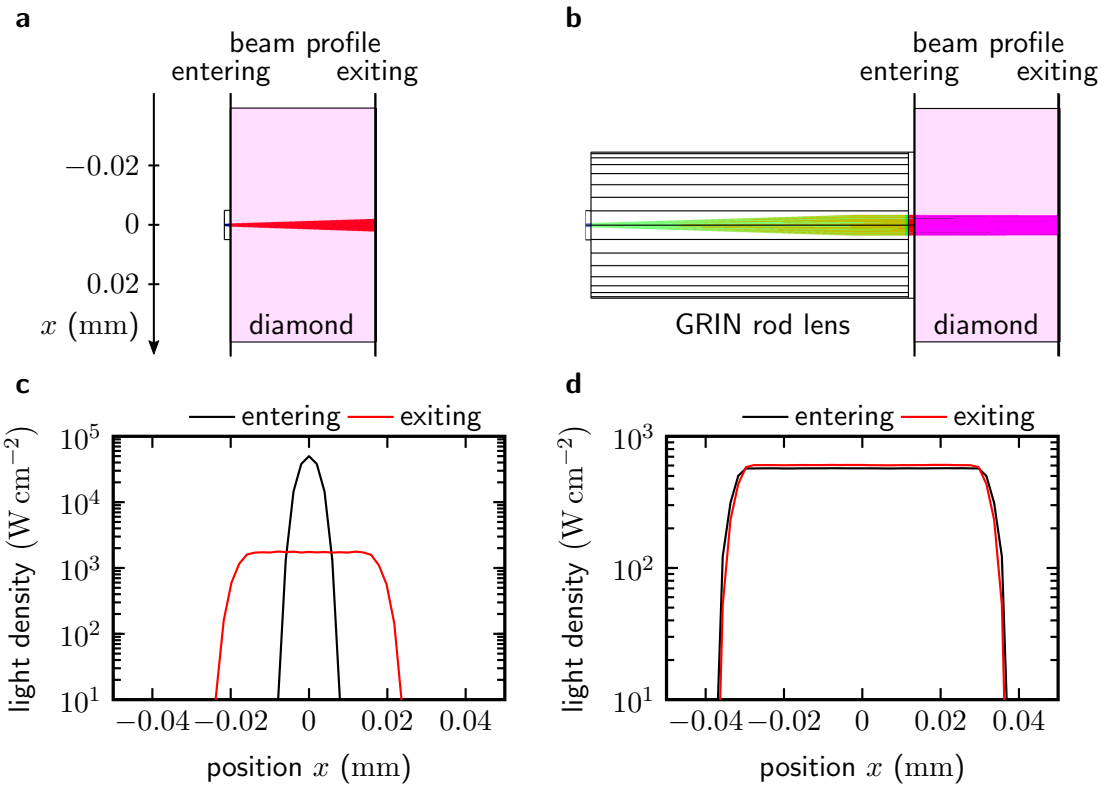

Figure 5.3: Optical ray tracing simulations for the optical excitation of the NV centres. Optical ray trace simulations were performed using Zemax OpticStudio®. We used a diamond with dimensions of $(0.8 \times 0.8 \times 0.5)\,\mathrm{mm}^3$ and modelled the optical output of a single-mode fibre with numerical aperture $NA_{\mathrm{fibre}} = 0.12$ by a radial emitting area of $2.0 \times 2.0\,\mu\mathrm{m}^2$. The emitting surface was embedded in a block of polydimethylsiloxane (PDMS) with refractive index of $n_{\mathrm{PDMS}} = 1.46$ and emitted light rays with an optical power $P_{\mathrm{out}} = 23.5\,\mathrm{mW}$ within an angle θ of $4.813°$ resulting from $\mathrm{NA}_{\mathrm{fibre}} = n_{\mathrm{PDMS}} \sin(\theta)$. We evaluated the beam profile at two positions inside the diamond: $1\,\mu\mathrm{m}$ deep from the surface of the diamond, which is connected to the fibre-GRIN compound (entering beam profile) and $499\,\mu\mathrm{m}$ deep along the optical axis (exiting beam profile). **a)** shows the graphical 2D view on the simulation settings of a direct light coupling between fibre and diamond, whereas **b)** shows the 2D view, which corresponds to the sensor head of the NV magnetometer using a GRIN rod lens inserted in the optical path between fibre output and diamond with an additional connection layer of PDMS between lens and diamond. For reasons of clarity, the axis of the position x describing the lateral distance to the centre of the fibre and used to evaluate the light distribution inside the diamond is only shown in a). Simulation results of the optical illumination evaluated at the two positions (entering and exiting the diamond) inside the diamond without using a GRIN rod lens shown in **c)** and with using a GRIN lens in **d)**. A more homogeneous illumination of the diamond is achieved for b) as the light rays leaving the fibre are parallelised by the GRIN rod lens. This figure is reprinted from [32], licensed under CC BY-NC-ND 4.0, https://creativecommons.org/licenses/by-nc-nd/4.0/.

5.2.2 Diamond Sample

[32]

We used a (111)-oriented plate with dimensions of $(0.8 \times 0.8 \times 0.5)\,\mathrm{mm}^3$ obtained by laser-cutting and polishing from a 99.97% ^{12}C enriched diamond single crystal grown by the temperature gradient method at high pressure and high temperature conditions [218]. The original crystal was irradiated with 2 MeV electrons ($2 \times 10^{18}\,\mathrm{cm}^{-2}$) at room temperature and annealed at 1000 °C for 2 h in vacuum resulting in the concentrations of $[\mathrm{NV}^-] \sim 0.4$ ppm and $[\mathrm{P1}] \sim 2.0$ ppm measured by electron spin resonance.

5.2.3 Spin Manipulation

[32]

For the microwave-based spin manipulation, we used a double split-ring resonator, see figure A.9a, formed by two inductively coupled transmission lines, which were terminated by two capacitive gaps, in order to provide a microwave field of sufficient amplitude [257]. The resonator was fabricated on a 640 µm thick Rogers RO3010™ substrate with a copper metallisation of 20 µm on both sides with PCB dimensions of $(15 \times 24.5 \times 0.72)\,\mathrm{mm}^3$. An MMCX connector was used to supply the resonator with microwave power, transferred by a 50 Ω microstrip line coupled to the double split-ring resonator. The bandwidth of the resonator is (23.48 ± 0.08) MHz and the resonance frequency can be tuned in the range from (2.8 to 3.0) GHz by putting a metallised plate (resonator tuning stick, figure 5.1) on the resonator structure. Further details of the microwave resonator will be given in appendix A.5.2.

Microwaves in the GHz range were delivered by a compact local oscillator (Windfreak Synth USB II) with an output power of 3 dBm and a fixed frequency. Additionally, we used a second source (RedPitaya STEM 125-14 V1.0) to synthesise the baseband in the MHz frequency range. The baseband signal was pre-amplified using a low noise amplifier (Mini-Circuits ZFL-1000LN+). Both signals were subsequently mixed using a low conversion loss mixer (Mini-Circuits ZFM-4212+) and amplified using three low noise microwave amplifiers (Mini-Circuits ZX60-P33ULM+) with a gain of 8.8 dB each (at a frequency of 3.0 GHz).

The frequency of the baseband signal was modulated with a modulation frequency f_{mod} and a modulation depth f_{depth}, *i.e.* $f_{\mathrm{BB}}(t) = f_{\mathrm{BB}} + f_{\mathrm{depth}} \sin(2\pi f_{\mathrm{mod}} t)$, where f_{BB} is the mean frequency of the baseband. This signal was mixed with the fixed frequency f_{LO} of the local oscillator resulting in the overall mean frequency $f_{\mathrm{c}} = f_{\mathrm{LO}} + f_{\mathrm{BB}}$ [307].

The following analysis will refer to f_{c}. For an enhancement of the magnetic sensitivity we simultaneously applied three mean frequencies f_{c}, $f_{\mathrm{c}} - f_{\mathrm{HFS}}$ and $f_{\mathrm{c}} + f_{\mathrm{HFS}}$ in order to address all three ^{14}N hyperfine resonances with a frequency splitting f_{HFS} of 2.16 MHz simultaneously [28, 271]. In the following, we will label such measurements with '3 HFS on', while '3 HFS off' means that only the mean frequency f_{c} is applied. If not explicitly mentioned, the default settings for the presented results is '3 HFS on' and the given values will refer to the total power of the three frequencies.

5.2.4 Optical Spin Readout

The fluorescence emitted by the diamond was collected by a photodiode ($\mathrm{PD_{NV}}$) located on the diamond surface opposite to the fibre and GRIN lens, see figure 5.1a. This is in contrast to previous publications, where the fibre was used both for optical excitation and fluorescence collection [308–311]. For this purpose, we used a chip photodiode (Hamamatsu S12915-33CHIP) with a photosensitive area of $(2.4 \times 2.4)\,\mathrm{mm}^2$ and a responsivity of $R_{670\,\mathrm{nm}} \approx 0.54\,\mathrm{A\,W^{-1}}$ (at 670 nm wavelength). A 1.45 µm thin DBR grown by chemical vapour deposition of several layers of amorphous silicon carbide (aSiC, $n \approx 2.6$) and silicon oxide (SiO_2, $n \approx 1.5$) was deposited on the surface of the photodiode acting as a long-pass filter to block the laser excitation light [218]. [32]

Besides the sole detection of the emitted fluorescence of the NV centres, we additionally monitored the laser intensity by a second photodiode with responsivity of $R_{522\mathrm{nm}} \approx 0.40\,\mathrm{A\,W^{-1}}$, see figure 5.4a. This photodiode was positioned next to the first photodiode on the common PCB and was coated with a customised DBR blocking the fluorescence light (shortpass filter), see figure 5.1a.

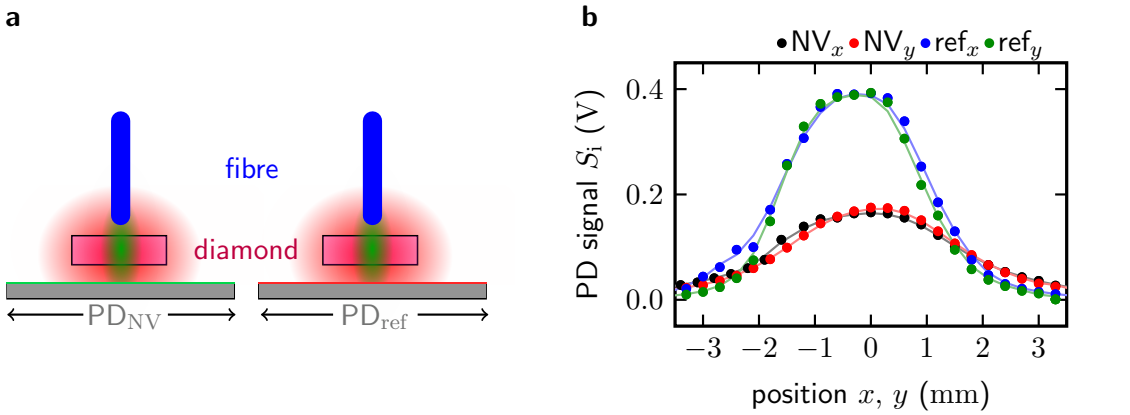

Figure 5.4: Experimental evaluation of the measured amplitude of the fluorescence and (laser) excitation signal dependent on the position of the corresponding photodiode. a) Schematic drawing of the experimental setup used to obtain information about the signal levels S_i between fluorescence and laser reference to set up a balanced detection scheme on a common board. A diamond with dimensions of $(0.68 \times 0.85 \times 0.72)\,\mathrm{mm}^3$ was glued on a $70\,\mu\mathrm{m}$ thick cover glass and connected to a single-mode fibre by a small drop of PDMS. Two different DBR filters (shortpass and longpass filter, see figure 4.2) were placed and fixed on the surface of two separate photodiodes, respectively. The distance between diamond and surface of PD was experimentally limited to $1.5\,\mathrm{mm}$. Using a micrometer translation moving stage the position of the PD relative to the diamond was varied in the xy-plane. The position information was adjusted according to the measured specific signal maximum. **b)** Experimentally measured voltages of fluorescence and laser signals dependent on the photodiode position x, y. Lines of moving mean (of three neighbouring data points) are added to the graphs.

Both photodiodes were reverse biased with a voltage of 6 V. In contrast to Kim *et al.*, the distance between the microwave circuit and the photodiodes was rather large ($\approx 1.0\,\mathrm{mm}$) such that eddy currents in the photodiodes caused by the microwave play only a minor role [103].

Implementing long cut holes on the photodetection board enabled a variable alignment of the photodiodes relative to the position of the diamond, such that the ratio of detected fluorescence and laser (reference) signal can be adjusted.

Figure 5.4b shows the measured distribution of detected signal by the corresponding PD resulting from laser and fluorescence light dependent on the relative position.

5.2.5 Signal Processing

Our design represents a compromise between full detection of the fluorescence signal and maintaining the ability of a balanced detection. For this purpose, the signals of the two photodiodes were fed to a logarithmic transimpedance amplifier (Texas Instruments LOG114), whose pre-amplified output was digitised and demodulated (according to the applied modulation frequency) by the analogue-to-digital module of the RedPitaya (14 bit, 125 MSamples s^{-1}). [32]

The demodulated signal S_{demod}, shown in figure 5.5a, indicates the peak-to-peak amplitude of a signal oscillating at the carrier frequency f_{mod}. For the experiments, we used the technique of ODMR to measure magnetic fields. Therefore, the demodulated signal output S_{demod} of the RedPitaya resembles to the derivative of the typical Lorentzian profile of the ODMR spectrum. Close to the resonance frequency, S_{demod} is proportional to the detuning Δf from the corresponding resonance frequency $f_{\pm}$ (figure 5.5a).

We extracted information about the linewidth $\Delta\nu$ and contrast C of the electron spin resonance by integrating the demodulated signal S_{demod} and fitting the resulting data S_{integ} to a Lorentzian function $g(x)$ of

$$g(x) = A\frac{(\Delta\nu/2)^2}{(x-x_0)^2+(\Delta\nu/2)^2}, \tag{5.2}$$

where A is an amplitude factor linked to spin contrast C, $\Delta\nu$ is the full width at half maximum of the resonance curve and x_0 is the resonance frequency, see figure 5.5b. Details about the signal processing, including the signal integration and the determination of the contrast, are summarised in appendix A.5.3.

5.2.6 Offset Magnetic Field

In order to spectrally separate the four NV orientations and hyperfine splittings, we used a self-constructed, current carrying Helmholtz coil, which is a necessary functional part of the sensor head. The Helmholtz coil consists of 35 windings on each side providing an offset magnetic field of $\approx 1.07\,\text{mT}$ at a current of 0.5 A. The windings were designed in a tapered shape to fulfil the Helmholtz [32]

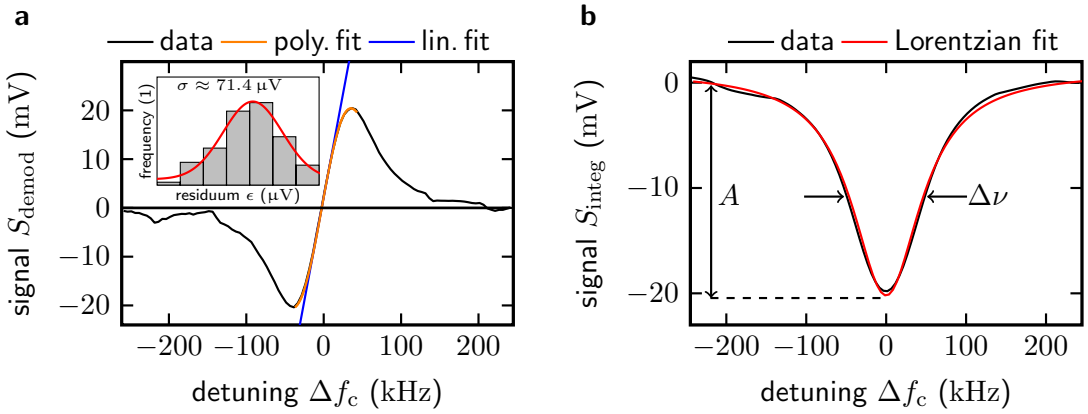

Figure 5.5: Demodulated and integrated signal of an ODMR spectrum. a) The recorded signal S_{demod} (black curve) is shown as a function of the detuning Δf_{c} from the resonance frequency, which is characterised by the zero-crossing of the signal. A polynomial of 6th order (orange curve) was applied as empirical fit to the data to determine the *slope* at the zero-crossing. The blue curve shows the linear contribution of the polynomial. The noise parameter was derived by the standard deviation σ of the residuum ε that results from subtracting the polynomial fit values from the data, which are summarised in a histogram. **b)** Integrating S_{demod} resembles the resonance curve S_{integ} (black curve) with a Lorentzian shape (fit red curve) with $\Delta\nu$ the linewidth and A the amplitude of the resonance linked to contrast C. This figure is reprinted from [32], licensed under CC BY-NC-ND 4.0, https://creativecommons.org/licenses/by-nc-nd/4.0/.

coil's condition, *i.e.* the distance between the two coils equals the radius of the coils, resulting in field deviations of less than 0.1% inside the volume of the diamond, see figure 5.6. A diameter of 22.5 mm for the smallest winding and a diameter of 36.2 mm for the largest winding were used.

5.3 Experimental Results

[32] An ODMR spectrum of the NV ensembles recorded with an offset magnetic field generated by the tapered Helmholtz coil is shown in figure 5.7a. The measured demodulated signal S_{demod} shows the spin transitions from the $m_{\mathrm{s}} = 0$ to $m_{\mathrm{s}} = +1$ states including the three sublevels that result from the hyperfine interaction with the nuclear spin of the ^{14}N isotope. All four possible orientations contribute to the spectrum depicted in figure 5.7a. The colour-coded arrows are related to the electron spin resonances of the four NV orientations. Due to the simultaneous manipulation of the three hyperfine splittings, five character-

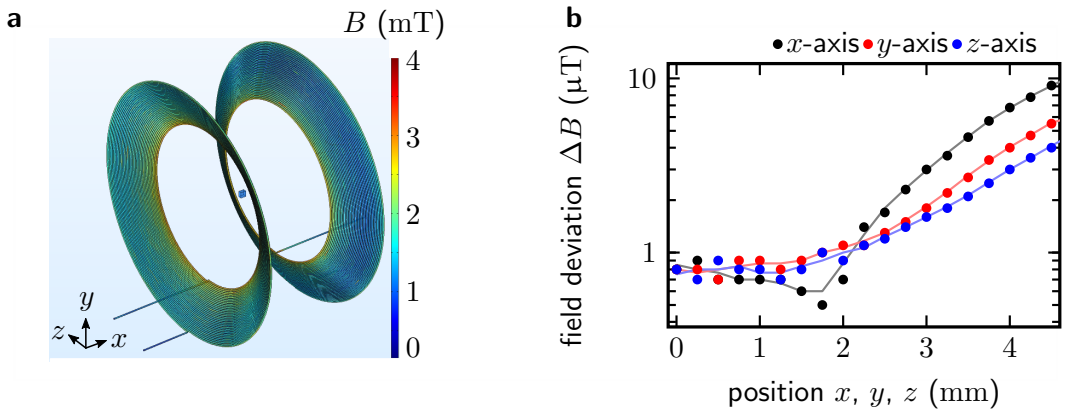

Figure 5.6: Simulative evaluation of the offset magnetic field generated by a pair of tapered Helmholtz coils. **a)** Graphical view of the simulation settings for evaluating the generated magnetic field of the tapered Helmholtz coils using COMSOL Multiphysics®. The field distribution was evaluated inside the volume of the diamond with dimensions of $(0.8 \times 0.8 \times 0.5)\,\mathrm{mm}^3$. The diamond was positioned at the centre of the two coils with its largest surface in the xz-plane. A current of $I = 500\,\mathrm{mA}$ was applied to the coils, which were electrically connected with each other. In this graphic, the generated magnetic field strength B at the surface of the coils is plotted. **b)** The position of the diamond relative to the centre of the two coils was varied along the x-, y- and z-axis and the simulated field deviation of B inside the volume of the diamond is shown, respectively. Lines of moving mean (of three neighbouring data points) are added to the graphs. This figure is reprinted from [32], licensed under CC BY-NC-ND 4.0, https://creativecommons.org/licenses/by-nc-nd/4.0/.

istic zero-crossings can be observed in figure 5.7a for each NV axis. In order to show the increase in signal amplitude due to the simultaneous hyperfine spin manipulation in comparison to a standard spin manipulation, we plotted the spectra in a common plot superimposed, see figure 5.7b. The simultaneous excitation of the three ^{14}N hyperfine split transitions should result in a threefold increase of the contrast. However, we only find a factor of approximately 2.61 larger amplitude, which may be due to an uneven power level of the combined three mean microwave frequencies, *i.e.* f_c and $f_\mathrm{c} \pm f_\mathrm{HFS}$, see figure A.11a.

As mentioned above, it is essential to evaluate the interplay between optical excitation and spin manipulation to find the optimal working point for our NV magnetometer. We used the measured curve of the ESR, which corresponds to the NV orientation with the largest field projection, as the basis for this analysis to improve the sensor's performance. As depicted in figure 5.7a, the

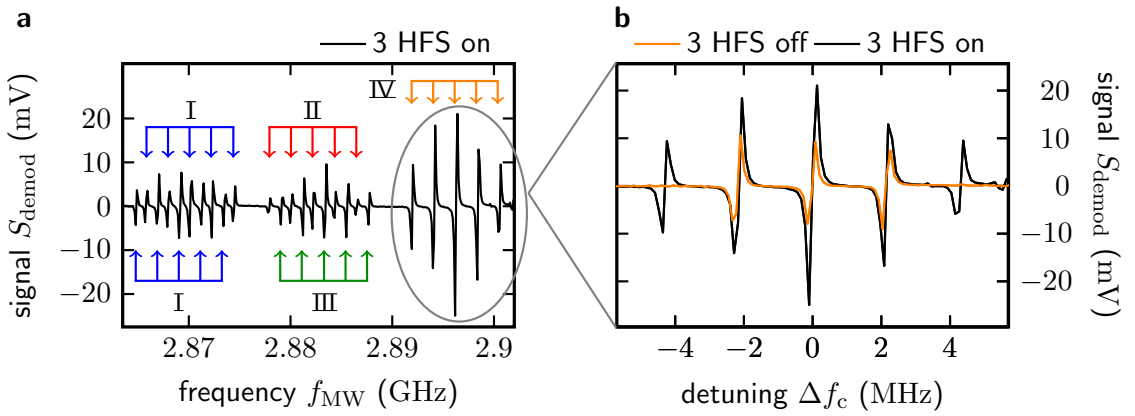

Figure 5.7: Optically detected magnetic resonance. a) Spectrum of the measured demodulated signal S_{demod} showing spin transitions from the $m_{\mathrm{s}} = 0$ to $m_{\mathrm{s}} = +1$ states including hyperfine interactions. The spectrum was recorded at a modulation frequency of $5\,\mathrm{kHz}$ and a modulation depth of $100\,\mathrm{kHz}$ with $40\,\mathrm{ms}$ integration time. The total microwave power was $0.91\,\mathrm{mW}$ with a simultaneous excitation of the three hyperfine split transitions. Each NV axis produces five characteristic zero-crossings resulting from the simultaneous manipulation of the ^{14}N hyperfine splitting, which are labelled with coloured arrows and Roman letters. An exception is orientation I, where the transitions from $m_{\mathrm{s}} = 0$ to $m_{\mathrm{s}} = \pm 1$ overlap around $D_{\mathrm{gs}} \approx 2.87\,\mathrm{GHz}$, so that 10 characteristic crossings are visible. **b)** Detailed view of the measured resonances of the NV orientation with the largest magnetic field projection with a comparison of the applied microwave manipulation: '3 HFS on' (black curve) and '3 HFS off' (orange curve). This figure is reprinted from [32], licensed under CC BY-NC-ND 4.0, https://creativecommons.org/licenses/by-nc-nd/4.0/.

mean frequency f_{c} was swept to record an ODMR spectrum of the demodulated signal S_{demod}. We applied a polynomial fit of 6th order to the measured data of S_{demod} to evaluate the linear slope m at the zero-crossing as well as to obtain information about the noise on the measured signal. The noise was calculated as the standard deviation σ of the residuum ε that results from subtracting the polynomial fit from the measured data, see figure 5.5a. Using these quantities and the gyromagnetic ratio of the NV centres, we approximated the sensitivity for a measurement time t_{int} in the linear range close to the zero-crossing point of S_{demod} with

$$\eta_B = \frac{\sigma}{\tilde{\gamma}_{\mathrm{NV}} m} \sqrt{t_{\mathrm{int}}}. \tag{5.3}$$

In the following, we evaluated the optimal working point of our NV sensor in order to improve the sensitivity η_B by varying the adjustable parameters,

i.e. modulation depth f_{depth}, microwave power P_{MW}, integration time t_{int} and modulation frequency f_{mod}, while the laser power was fixed by design in order to achieve an optimal pumping rate that is close to $1/T_2^*$. The results of this optimisation analysis are summarised in figure 5.8. The power of the laser module of 23.5 mW corresponds to an estimated average optical intensity of $I_{\text{opt}} \approx 390\,\text{W}\,\text{cm}^{-2}$ (along the optical path inside the diamond, for further details see appendix A.5.2). Based on the results by Dréau *et al.* and Levine *et al.*, this value of the optical intensity corresponds to the excitation regime where the tradeoff between high contrast and small linewidth results in an optimal value for the sensitivity [200, 208].

First, we studied the dependence of the modulation depth f_{depth} on the sensitivity, as shown in figure 5.8a. El-Ella *et al.* found an optimal modulation depth, which maximises the measured slope m, corresponding to half of the resonance linewidth [312]. The extracted slope reached a maximum at 40 kHz modulation depth, whereas the noise showed no clear trend on the modulation depths, see figure A.15c. Fitting the data of S_{integ} with the Lorentzian function from equation 5.2 a linewidth of (81.8 ± 2.4) kHz and a contrast of $(0.43 \pm 0.01)\%$ were extracted for $f_{\text{depth}} = 40$ kHz (figure A.15b), which is in good agreement to the findings of El-Ella *et al.* [312]. Therefore, $f_{\text{depth}} = 40$ kHz was chosen for the following measurements.

In a second step, the influence of the applied microwave power was evaluated. We observed an increase of the measured linewidth for microwave powers larger than 0.1 mW (figure A.16b) due to power broadening [208]. For microwave powers below 0.1 mW, the linewidth seems to be unaffected by power broadening. We extracted an inhomogeneously broadened linewidth $\Delta\nu_{\text{inh}}$ of approximately 67.47 kHz by applying a theoretical model of the linewidth of NV ensembles according to Jensen *et al.* to the measured data, see figure A.16b [223]. Regarding the measured contrast that results from the simultaneous excitation of the three hyperfine levels, a maximum value of $\approx 1.0\%$ is achieved for $P_{\text{MW}} \approx 1.45$ mW. However, for applied powers above 1.45 mW the contrast deteriorated as microwave induced power broadening dominated over the optical pumping rate and became major linewidth determining factor. We found that

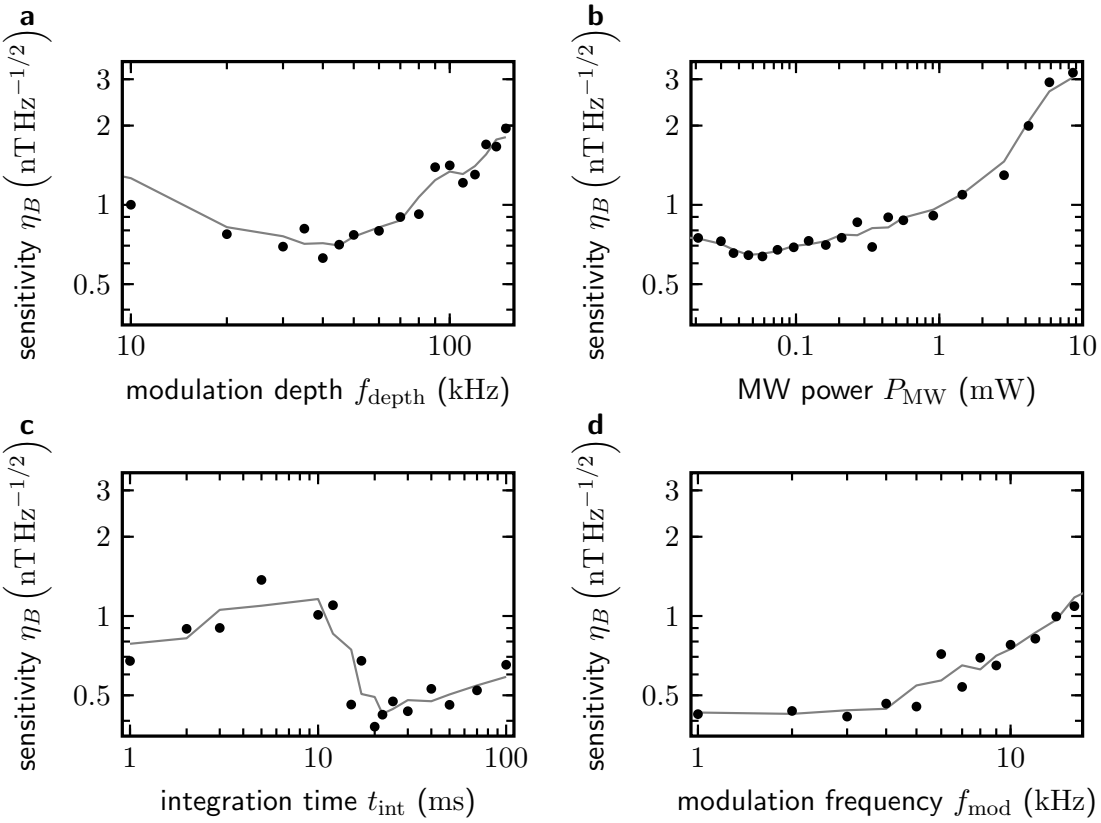

Figure 5.8: Evaluation of the magnetic field sensitivity with respect to sensor parameters. The sensitivity was evaluated on the NV orientation with the largest field projection, *i.e.* NV orientation IV in figure 5.7a. The gray line corresponds to a moving mean of three neighbouring data points and is added to the graphs as a guide to the eye. **a)** Variation of the modulation depth f_{depth} at a microwave power of $16\,\mu\mathrm{W}$, $1\,\mathrm{kHz}$ modulation frequency for an integration time of $1\,\mathrm{ms}$. **b)** Variation of the microwave power P_{MW} at $1\,\mathrm{kHz}$ modulation frequency and $40\,\mathrm{kHz}$ modulation depth for an integration time of $1\,\mathrm{ms}$. **c)** Variation of the integration time t_{int} at a microwave power of $58\,\mu\mathrm{W}$, $1\,\mathrm{kHz}$ modulation frequency and $40\,\mathrm{kHz}$ modulation depth. **d)** Variation of the modulation frequency f_{mod} at a microwave power of $58\,\mu\mathrm{W}$ and $40\,\mathrm{kHz}$ modulation depth for an integration time of $20\,\mathrm{ms}$. This figure is reprinted from [32], licensed under CC BY-NC-ND 4.0, https://creativecommons.org/licenses/by-nc-nd/4.0/.

the slope was largest for a moderate microwave power of $\approx 58\,\mu\mathrm{W}$. The noise had a similar dependence on the microwave power. As a result, the overall sensitivity showed a rather weak dependence on the evaluated power range from $0.02\,\mathrm{mW}$ to $0.2\,\mathrm{mW}$.

In the third step, we varied the integration time based on the optimal parameters to date to record slope and noise. The best value for the sensitivity was

obtained for an integration time of 20 ms, see figure 5.8c, which is linked to the 50 Hz main frequency of the European power lines. The measured values of slope and noise are shown in figure A.17a.

In the fourth step, the modulation frequency was varied under the parameters determined so far, see figure 5.8d. We found a maximum slope for $\approx 1\,\mathrm{kHz}$ modulation frequency, see figure A.12b. While the slope decreased for $f_{\mathrm{mod}} > 1\,\mathrm{kHz}$, the noise level was almost constant for all investigated values of f_{mod}, see figure A.18c. Modulation frequencies smaller than 1 kHz resulted in a decreased slope, which can be understood by the used highpass filter in our photodetection circuit, see figure A.13 and figure A.12b. The measured values of linewidth and contrast of the modulation frequency variation are summarised in figure A.18b. The contrast resembled the behaviour of the slope and decreased as the modulation frequency was increased, see figure A.18c. A maximum contrast of 0.62% was obtained for $f_{\mathrm{mod}} = 1\,\mathrm{kHz}$. The linewidth showed a slight increase up to a modulation frequency of 10 kHz; for larger f_{mod} the linewidth broadened significantly. Here, we note that the resulting shape of the measured signal significantly deviated from a Lorentzian profile for $f_{\mathrm{mod}} > 16\,\mathrm{kHz}$ such that the linewidth and contrast of the electron spin resonance cannot be extracted correctly. We will refer to this behaviour in the discussion section.

Based on the described method of slope and noise characterization the best measured sensitivity was $\approx 424\,\mathrm{pT\,Hz^{-1/2}}$, which was achieved for a frequency modulation and simultaneous excitation of the three hyperfine interactions with $f_{\mathrm{depth}} = 40\,\mathrm{kHz}$, $P_{\mathrm{MW}} = 58\,\mu\mathrm{W}$, $t_{\mathrm{int}} = 20\,\mathrm{ms}$ and $f_{\mathrm{mod}} = 1\,\mathrm{kHz}$, see figure 5.8d.

The magnetic sensitivity of the sensor device was further evaluated using a magnetic shielding. For this purpose, we put a 180 mm diameter end cap of a mu-metal shield (Twinleaf MS-2) on top of the sensor and characterised the magnetic sensitivity with the method described above. We measured a sensitivity of $369\,\mathrm{pT\,Hz^{-1/2}}$ for this partial enclosure of the NV sensor. A further reduction of the measured sensitivity was achieved by a complete enclosure of the NV sensor using two shielding end caps resulting in a sensitivity to $344\,\mathrm{pT\,Hz^{-1/2}}$. This is an improvement of factor 1.23 compared to the unshielded setting.

Besides the determination of the magnetic sensitivity by taking the measured parameters of slope and noise of the demodulated signal at the zero-crossing point, we further evaluated the sensor performance under the application of a test magnetic field. A copper wire was wound around the pair of Helmholtz coils, on which a signal with square-wave function of 2 Hz frequency and amplitude of 2.18 mA was applied by an arbitrary waveform generator (Agilent 33220A). The applied signal corresponds to an induced magnetic field of $\approx$ 333 nT with a field orientation parallel to the applied offset magnetic field; a detailed description of the generated test field is summarised in appendix A.5.5. We analysed the sensitivity by recording the demodulated signal as a time trace under the application of the test field, see figure 5.9a. Each data point of the recorded time trace corresponds to an integration time of $t_{\text{int}} = 20\,\text{ms}$. The noise on a single 1 s step was evaluated by fitting the histogram of the recorded data set with a Gaussian distribution. Indicating a standard deviation σ of $\approx 3.03\,\text{nT}$, this measurement extrapolated to a sensitivity of $\sigma\sqrt{t_{\text{int}}} \approx 424\,\text{pT}\,\text{Hz}^{-1/2}$.

The sensor performance was further analysed by recording time traces of magnetic stimuli, *i.e.* the microwave frequency was set to the zero-crossing and by calculating the Allan deviation σ_{adev} of this data. In general, the Allan deviation determines the deviation of the measured data binned to intervals with averaging length τ [306]. In contrast to the standard deviation, the Allan deviation analyses data sets depending on the averaging time τ and thus providing time dependent noise information. The Allan variance $\sigma^2_{\text{adev}}(\tau)$ is calculated by [22]

$$\sigma^2_{\text{adev}}(\tau) = \frac{1}{2}\left\langle(\overline{y}_{n+1} - \overline{y}_n)^2\right\rangle, \tag{5.4}$$

where $\overline{y}_{n+1}$ and $\overline{y}_{n+1}$ are the mean values of two consecutive intervals of length τ. The calculated values of the Allan deviation adjusted by the slope m to translate deviations in the measured signal into magnetic field deviations, see figure 5.9b. We additionally enclosed the NV sensor using the magnetic shielding of two mu-metal half-shelves, as described above, to evaluate the influence of surrounding magnetic noise sources on the achievable sensor. The noise of a magnetically

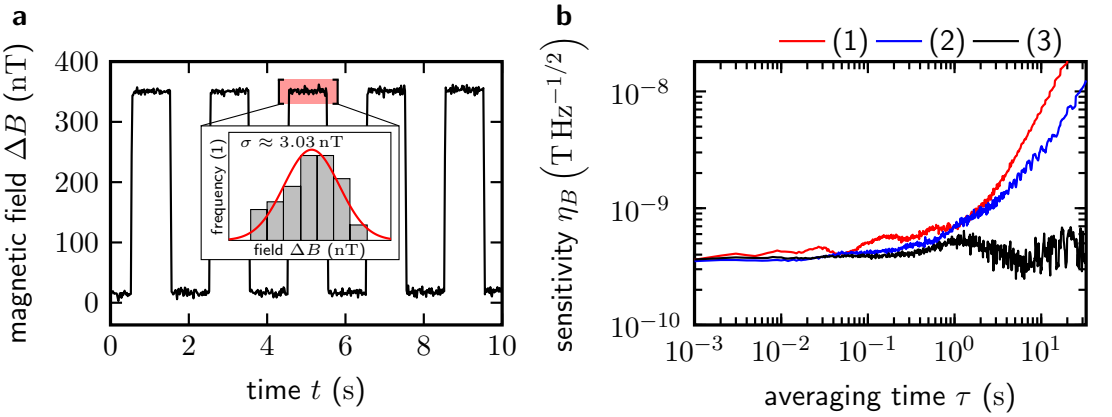

Figure 5.9: Sensitivity determination with square-wave test field using the Allan deviation. a) The demodulated signal S_{demod} was recorded for $10\,\mathrm{s}$ with an integration time of $20\,\mathrm{ms}$ per data point. A test magnetic field was applied with a square-wave function of $2\,\mathrm{Hz}$ and amplitude of $2.18\,\mathrm{mA}$ on the copper windings around the pair of Helmholtz coils corresponding to an induced magnetic field of $333\,\mathrm{nT}$ and is clearly visible in the recorded data trace (black curve). The noise on a single $1\,\mathrm{s}$ step was evaluated by the standard deviation of a Gaussian distribution ($\sigma \approx 3.03\,\mathrm{nT}$, red curve) on the recorded data and extrapolates to $429\,\mathrm{pT\,Hz^{-1/2}}$ for $20\,\mathrm{ms}$ integration time. **b)** Magnetic field sensitivity derived by analysing the Allan deviation $\sigma_{\mathrm{adev}}(\tau)$ of recorded time traces (without applying any magnetic test field). The data of (1) and (2) are based on time traces of magnetically sensitive cases, where the applied microwave field was set to the point of zero-crossing in the demodulated spectrum. In (2) the NV sensor was totally enclosed in the magnetic shielding of two half-shells made of mu-metal, for details see main text, whereas in (1) the sensor was unshielded. (3) shows the magnetically insensitive data without using any shielding. The time traces were recorded with a sampling rate of $1\,\mathrm{kHz}$ and a simultaneous manipulation of the three hyperfine states was applied in all measurements. This figure is reprinted from [32], licensed under CC BY-NC-ND 4.0, https://creativecommons.org/licenses/by-nc-nd/4.0/.

insensitive case was additionally measured without using any magnetic shielding. For this purpose, we applied a microwave frequency with 19.45 MHz detuning from the selected resonance frequency.

For short averaging times τ in the range of $(1 - 100)\,\mathrm{ms}$, the mean sensitivity level of the magnetically sensitive measurement was improved from $440\,\mathrm{pT\,Hz^{-1/2}}$ to $396\,\mathrm{pT\,Hz^{-1/2}}$ through introducing the shielding. Considering a 20 ms integration time derived by the optimisation steps, the unshielded measurements revealed a sensitivity of $436\,\mathrm{pT\,Hz^{-1/2}}$ and $356\,\mathrm{pT\,Hz^{-1/2}}$ was achieved for the shielded measurement environment. The shielded measurements showed a flat behaviour for $(1 - 100)\,\mathrm{ms}$ comparable to the magnetically

insensitive measurement, whereas the sensor in the unshielded environment varied in its sensitivity result. An increase in the measured sensitivity for both settings was observed for time scales larger than 100 ms. Here, we note that we observed fluctuations in the data from measurement to measurement for the unshielded setting, which may be due to magnetic fields that prevail in the background.

The logarithmic balancing of the two photodiodes prevented noise measurements of the detection output without laser and microwave excitation such that the contribution of electronic noise to the overall sensitivity cannot be solely analysed. A noise floor of $\approx 364\,\mathrm{pT\,Hz^{-1/2}}$ was characterised for 1 ms integration time recorded by the magnetically insensitive measurement, see figure 5.9b, indicating a lower limit of the achievable sensitivity of our device.

As an application, we used the NV sensor to measure the change in magnetic field ΔB due to the movement of an elevator, see figure 5.10. For this purpose, we positioned the NV sensor roughly 4 m away from the doors of an elevator in the third floor. The NV magnetometer recorded the movement of the elevator by tracking the resonance frequency of the selected spin transition using a feedback loop to adjust the applied microwave frequency.

From the measured change in magnetic field, shown in figure 5.10, it can be clearly identified when the elevator started with the upward movement (observed by an increase of the field change), opened its doors (by an additional increase of the field change compared to the 'standing' case at the third level) and waiting period in this upper level. The closing of the doors, the downward movement, as well as the repeated opening of the doors were detected by the sensor in the form of a decreasing change decreasing ΔB compared to the starting situation.

5.4 Discussion And Outlook

[32] For the evaluation of the achieved sensor performance, it is essential to have a look on its fundamental limit. Due to the optical readout of the spin states,

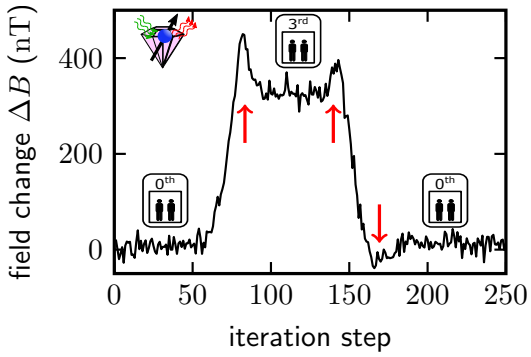

Figure 5.10: Measurement of the change in the magnetic field due to the movement of an elevator. The NV magnetometer was positioned roughly 4 m away from the doors of an elevator three floors above the ground floor. For tracking the resonance condition of the selected NV transition, the demodulated signal S_{demod} was used as an error signal for a feedback loop to adjust the applied microwave frequency. The microwave frequency was adjusted by 250 Hz corresponding to a magnetic field change of 8.92 nT. We recorded S_{demod} for 1 ms integration time (per iteration step) with the following experimental parameters: 1 Hz modulation frequency, 40 Hz modulation depth and 58 µW microwave power. In this measurement, the elevator started in the ground floor and moved to third level, opened and closed its doors and moved then down to the ground floor. The red arrows indicate the impact of opening and closing the elevator's doors. This figure is reprinted from [32], licensed under CC BY-NC-ND 4.0, https://creativecommons.org/licenses/by-nc-nd/4.0/.

the NV magnetometer is limited by photon shot-noise given by equation 5.1. To calculate η_{PSN}, we determined the photon rate from the average photocurrent $I_{\mathrm{PD_{fl}}}$ by measuring the voltage U_{shunt} drop at a $R_{\mathrm{shunt}} = 10\,\Omega$ shunt resistor. For a measured U_{shunt} of 0.40 mW the photon rate $\mathcal{R} = I_{\mathrm{PD_{fl}}}/e = U_{\mathrm{shunt}}/(R_{\mathrm{shunt}}e)$ results in $\approx 2.47 \times 10^{14}$ Hz with e being the elementary charge. Using equation 5.1 and the measured linewidth of 92.19 kHz and contrast of 0.62% the photon shot-noise limited sensitivity is $\approx 26\,\mathrm{pT\,Hz^{-1/2}}$. This value is a factor of ≈ 13 smaller than the best measured sensitivity of $\approx 344\,\mathrm{pT\,Hz^{-1/2}}$. Regarding this discrepancy a factor of $\sqrt{2} \approx 1.41$ can be explained by the usage of the balanced photodetection unit based on two single independent compared to a single-photodiode-usage. Further deviations may photodiodes arise from fluctuations of the laser and its interplay with the limited common mode rejection of the balanced photodetector module. For time scales ≥ 1 s, the observed magnetic field noise is possibly due to power fluctuations of the laser associated with temperature variations of the diamond (for further details see appendix A.5.5).

Finding the optimal working point of the NV magnetometer by optimising the relevant operation parameters is essential to obtain a highly sensitive device at efficient usage of the sensor power supply. Due to the interplay between optical and microwave excitation it may be possible that altering the applied laser power improves the sensitivity. The performed one-dimensional parameter sweeps might result in a local optimum of the sensitivity, which can be potentially further improved.

We further note that the parameter evaluation of the modulation frequency was not straight forward compared to the parameter sweeps of microwave power and modulation depth. This is mainly linked to the implemented highpass filter in the transimpedance amplification circuit of the balanced detection unit. Based on simulations of the electronic circuit using LTspice®, we expected the output of the logarithmic transimpedance amplification circuit to show a flat behaviour over a frequency range between (1 to 50) kHz, see figure A.13. However, experimental results of the contrast and slope determination revealed a maximum value at 1 kHz modulation frequency, as depicted in figure A.12b. The measured signal deteriorated for higher modulation frequencies, which can be explained by a relatively small optical pumping rate compared to the modulation frequency of the microwave. We estimated the pumping rate to be $\approx 32\,\mathrm{kHz}$ (see appendix A.5.2), so that under these conditions the pumping of the NV system is too slow to follow the fast modulation resulting in a reduced signal. In the simulation, the dynamics of the NV centres was neglected. Therefore, we assume that the discrepancy between experimental observation and simulative prediction results from the complex excitation dynamics of the NV centres.

The method of applying an additional magnetic test field to the NV sensor and measuring the noise on the demodulated signal at the point of zero-crossing, *i.e.* resonance condition, confirmed the sensitivity that was obtained from the analysis of the slope and its residuum, see figure 5.5a. For short averaging times in the range of $(1-100)\,\mathrm{ms}$ the achievable sensitivity varied, which may be due to (magnetic) noise/fluctuations in the sensor's environment. The analysis of

the Allan deviation revealed that the performance worsened for sensing times exceeding 1 s independent on the sensor's environment, *i.e.* unshielded and magnetically shielded. Observed drifts in the recorded time traces may be linked to temperature variations and need to be mitigated to improve both the sensor's sensitivity and stability on larger time scales. Recent publications have shown how to set up a sensor with temperature invariance by simultaneously addressing both transitions from the $m_s = 0$ to $m_s = \pm 1$, *i.e.* making use of double quantum magnetometry [195, 313]. A complete enclosure of the NV magnetometer in a magnetic shielding showed an improvement of the sensitivity.

The fluorescence collection efficiency could be further optimised, as we detected less than one percent of the power that was used for excitation (a calculated fluorescence power of 73.1 µW based on the detected photocurrent for a fluorescence wavelength of 670 nm and an estimated excitation output power at the GRIN lens of 18.3 mW). This low fluorescence collection efficiency originates from the small solid angle of the photodetector seen from the fluorescing diamond. While the geometric centre of the diamond was located above the photodiode used to detect the reference signal from the laser, only the share of the fluorescence that was emitted laterally to the side of the other photodetector (PD_{fl}) was detected, see figure 5.1a. The DBR filters deposited on the surface of the photodiode further reduced the detectable fluorescence intensity as these filters showed a transmission of $\approx 78\%$. An instant improvement in the fluorescence detection efficiency could be achieved by avoiding the step in refractive index between the diamond and the photodiode by filling the gap with a material having a larger refractive index than air. This could mitigate the problem of total internal reflections of the emitted fluorescence due to diamond's high refractive index.

A further improvement of sensor performance could be achieved by equalising the microwave power levels at the three hyperfine frequencies, since different power levels prevent a full exploitation of simultaneously addressing hyperfine levels.

Besides the implementation of temperature invariance of the NV sensor, an-

other possibility to enhance the achievable sensitivity could be the use of flux concentrators, as recently shown by Fescenko *et al.*, which collect the magnetic flux from a large area and direct it to the NV sensor [25]. The use of such concentrators must nevertheless be viewed critically from the point of view of the intended application, as any restrictions on the use of the sensor could be associated with the use of these concentrators, *e.g.* for a vector magnetometry application.

Setting up the sensor device as a vector magnetometer, we would need to implement a simultaneous addressing of at least three NV orientations in the microwave and signal processing circuitry [213]. Tracking fast changing magnetic signals would further require a closed loop control for tracking the NV resonance frequencies.

Further miniaturisation for mobile applications of NV magnetometers could take advantage of using the CMOS technology as shown by Kim *et al.* [103].

Regarding power consumption of the NV magnetometer, the power efficiency of the microwave resonator could be further enhanced by optimising the coupling property, *e.g.* by placing additional dielectric material on the coupling gap. This could reduce the need of amplification or the input power for the spin manipulation.

The compactness and portability of our NV magnetometer was designed to pave the way for a wide range of applications including GPS-free navigation on earth and space missions as well as the detection of biomagnetic signals, *e.g.* for magnetocardiography and magnetoencephalography [314]. By implementing the above mentioned measures, the sensor's sensitivity could be improved to the required level of $\approx 10\,\mathrm{pT\,Hz^{-1/2}}$ for magnetocardiography. In addition, our NV magnetometer could be used for the detection of electric currents, *e.g.* for battery diagnostics.

To classify our NV sensor in terms of sensitivity and level of integration, we summarised recent results both for NV diamond magnetometers as well as for OPMs in table 5.1. Some experiments with NV centres and OPMs have outperformed our work in terms of sensitivity. However, regarding these NV

Table 5.1: Comparison of magnetometer technologies. A selection of magnetometers based on NV centres in diamond and optically pumped magnetometers are summarised with regard on the level of miniaturisation and achieved magnetic field sensitivity. The classification of the maturity level distinguishes between laboratory setups, prototypes in an advanced development stage and commercially available products. This table is based on [32].

Technology	Level of miniaturisation	Magnetic field sensitivity	References
NV magnetometer	Laboratory setup	$900\,\mathrm{fT\,Hz^{-1/2}}$ to $30\,\mathrm{pT\,Hz^{-1/2}}$	[22–26]
	Integrated sensor head	$310\,\mathrm{pT\,Hz^{-1/2}}$ to $67\,\mathrm{nT\,Hz^{-1/2}}$	[28–30, 315]
	Integrated sensor head	$344\,\mathrm{pT\,Hz^{-1/2}}$	This sensor [32]
OPM	Laboratory setup	$160\,\mathrm{aT\,Hz^{-1/2}}$ to $5\,\mathrm{fT\,Hz^{-1/2}}$	[34, 35]
	Integrated sensor head	$10\,\mathrm{fT\,Hz^{-1/2}}$	[316]
	Commerical product	$10\,\mathrm{fT\,Hz^{-1/2}}$ to $20\,\mathrm{pT\,Hz^{-1/2}}$	QZFMGen-2[1], QTFM[2], microSAM[3], microSERF[4]

experiments, the results have been achieved with laboratory equipment, such as confocal microscopes, limiting their usability for portable applications. Considering OPMs, a few companies have specialised in manufacturing OPMs, which achieve sensitivities $< 20\,\mathrm{pT\,Hz^{-1/2}}$ and can be used for mobile applications.

Further comparing our work to recently demonstrated integrated NV sensors, our work shows both advances in performance with sub-$\mathrm{nT\,Hz^{-1/2}}$ sensitivity and increased level of integration. analysing the overall power consumption, our NV magnetometer consumes $\approx 5.1\,\mathrm{W}$ in operation mode (excluding the power of the computer needed to control the experiments). This value is comparable to the values given in the data sheets of commercially available OPMs, see table 5.1, ranging from $(0.7$ to $5.0)\,\mathrm{W}$.

[1] https://quspin.com/products-qzfm/ (2020/12/02)
[2] https://quspin.com/qtfm/ (2020/12/02)
[3] https://twinleaf.com/scalar/microSAM/ (2020/12/02)
[4] https://twinleaf.com/vector/microSERF/ (2020/12/02)

5.5 Conclusion

[32]

In conclusion, we have demonstrated an integrated portable prototype of a magnetometer based on the NV centres in diamond. The diamond attached to an optical fibre, the microwave resonator and a balanced detection scheme built up by two photodiodes were integrated into a compact sensor head. Our focus in setting up this prototype was put on the size and compactness of the complete sensor device while enabling high sensitivity measurements. This includes the choice of laser source, microwave equipment and signal processing such that the sensor device can be used in real world applications outside laboratory environments. Using the frequency modulation technique for measuring electron spin resonance we achieved a magnetic field sensitivity of $344\,\mathrm{pT\,Hz^{-1/2}}$. We further discussed solutions to improve the sensor performance and abilities to increase the integration level.

6 Fluorescence Lifetime-Based NV Magnetometry

This chapter is based on [317] with minor edits. The taken text passages are marked by marginal notes, whereas the taken captions are not additionally highlighted. Reprinted from [317] with the permission of AIP Publishing. Copyright (2021) The authors.

The idea of fluorescence lifetime experiments was conceived by Fedor Jelezko, Andreas Brenneis and Felix M. Stürner. The diamond sample was provided by Pierre-Olivier Colard and Matthew Markham. The experiments were planned and conducted by Felix M. Stürner and Yan Liu and the measurement data was analysed by Yan Liu and Felix M. Stürner in discussion with Fedor Jelezko. Fruitful discussions with Nicolas Staudenmaier and Timo Joas helped with the advancement of the experiments. Note that Yan Liu and Felix M. Stürner contributed equally to this work.

6.1 Introduction

[317]

> Most magnetometry experiments with NV centres in current research projects are based on the analysis of the NV centre's fluorescence intensity to measure its spin state. The simplest technique to measure magnetic fields using the spin-dependent fluorescence intensity is the optical detection of the magnetic resonance. The magnetic field sensitivity of NV magnetometers is fundamentally limited by photon shot-noise or spin projection-noise [50]. However, this bound is not always reached due to presence of technical noise involving fluctuations of the excitation laser, to which the NV centre's fluorescence emis-

sion is typically correlated [120, 200]. Methods to circumvent instabilities in laser power, polarization, or wavelength are mostly based on common mode rejection implemented in balanced detection schemes [28, 32].

Here, we demonstrate a proof-of-principle by using the excited-state lifetime of a single NV centre to measure its electron spin resonance. Conventional measurements, which make use of the fluorescence intensity, may suffer from technical noise, *e.g.* fluctuations in the optical pumping process. To overcome these limitations, we target to implement the lifetime-based analysis in sensing protocols, if technical noise impacts the sensor's performance. We used a single NV centre in bulk diamond and performed single spin state readout based on excited-state lifetime measurements on a confocal microscope setup. In addition, we compared long-term precision results derived from lifetime-based and intensity-based sensing techniques.

6.2 Materials And Methods

6.2.1 Experimental Setup

[317] The fluorescence lifetime experiments were performed on a home-made confocal microscope setup. A schematic drawing of the confocal microscope setup is shown in figure A.20 and details of the used components are summarised in appendix A.6.1. A pulsed laser (PicoQuant LDH-D-FA-530L) and an arbitrary waveform generator (AWG, Tektronix AWG70001A) were employed. The AWG was used to generate microwaves as well as to synchronise the laser and data acquisition unit consisting of an avalanche photodiode (APD, Excelitas SPCM-AQRH-13) and a fast counting device (FAST ComTec MCS6A), see figure 6.1. The laser was capable of generating laser pulses with 100 ps pulse width and spacing of 10 ns at a wavelength of 531 nm. As shown in figure 6.3, the NV spin can be polarised by a condensed train of laser pulses and then manipulated by microwave pluses generated by the AWG, which were additionally amplified (Mini-Cirucits ZHL-16W-43-S+).

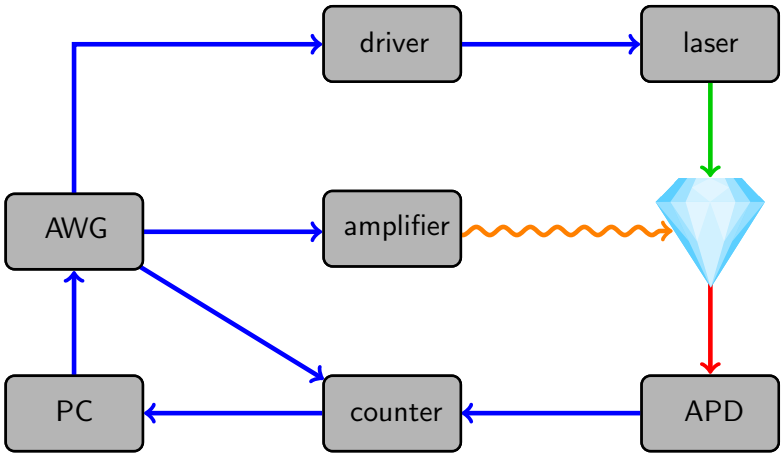

Figure 6.1: Schematic of the pulsed setup. The 'central' time clock of the pulsed setup was the AWG, which triggered both the laser and the fast counting unit by sending voltage pulses to the laser driver and to the fast counter. Additionally, the AWG further created microwave pulses necessary for the lifetime experiments, which were amplified, and then passed to the copper wire providing an oscillating magnetic field on the diamond. The laser source was set to the pulsed mode and was used to optically pumped the NV centre into its excited state, whereas the APD counted the emitted photons. Details about the confocal microscope setup are summarised in appendix A.6.1. A PC was used to control the experiment and to process the measured data.

For measuring the excited-state lifetime of the $m_s = 0$ spin state, the NV centre was first optically initialised by 100 subsequent laser pulses with a pulse width of 100 ps and a pulse spacing of 10 ns adding up to a microsecond optical excitation. The fluorescence decay data was then accumulated based on the excitation of the subsequent single probing laser pulse. Determining the lifetime decay of the $m_s = \pm 1$ states required an additional microwave π-pulse to revert the spin population from the $m_s = 0$ to $m_s = \pm 1$ states. This microwave pulse was introduced between the optical pumping pulses and the single probing pulse, see figure 6.3.

6.2.2 Diamond Sample

We used a diamond grown by the method of CVD with 99.99% ^{12}C enrichment and a nitrogen concentration of approximately < 5 ppb based on electron paramagnetic resonance measurement of samples grown with the same conditions. [317]

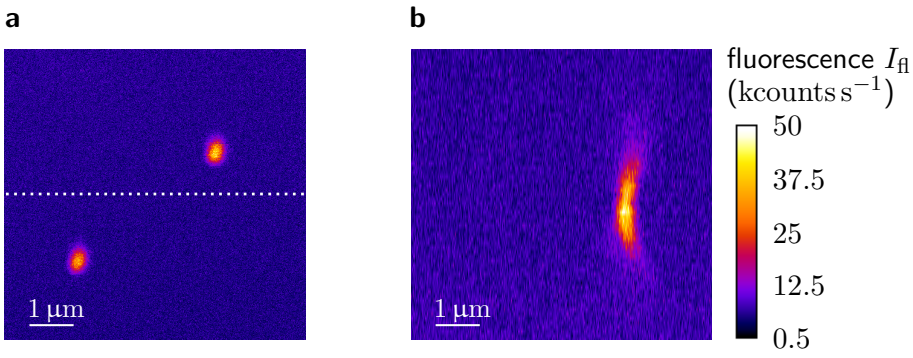

Figure 6.2: Confocal images of single NV centres. The confocal images were taken under continuous optical excitation on the confocal microscope setup described in appendix A.6.1. **a)** Confocal scan of the lateral plane of the diamond showing two single NV centres. **b)** Confocal scan of the depth at the position indicated with the white dashed line in a). A scale bar of the recorded fluorescence rate used for both confocal images is shown on the right side of this figure.

The NV centres were formed during the growth process. For the experiments, we selected a single NV centre located about 5 µm below the surface of the diamond, which was well isolated from other NV centres, see confocal scan images in figure 6.2.

6.3 Experimental Results And Discussion

[317] To extract the lifetimes of the $m_s = 0$ and $m_s = \pm 1$ states, we probed the NV system in the selected state by applying a spin-selective π-pulse between the pump and probe laser pulses and fitted the recorded fluorescence data S_{fl} with a single exponential decay function of

$$S_{fl}(t) = A_{ref,i} \exp(-t/\tau_i), \tag{6.1}$$

where $A_{ref,i}$ is an amplitude factor and τ_i the excited-state lifetime of the respective spin state with $i \in \{0; \pm 1\}$. The recorded decay curves of the $m_s = 0$ and $m_s = \pm 1$ states differed in terms of total detected photon number, but showed similar amplitudes ($A_{ref,0}$ and $A_{ref,\pm 1}$), see figure 6.3. From these decay curves, lifetimes of 12.2 ns for τ_0 and 8.6 ns for $\tau_{\pm 1}$ were extracted.

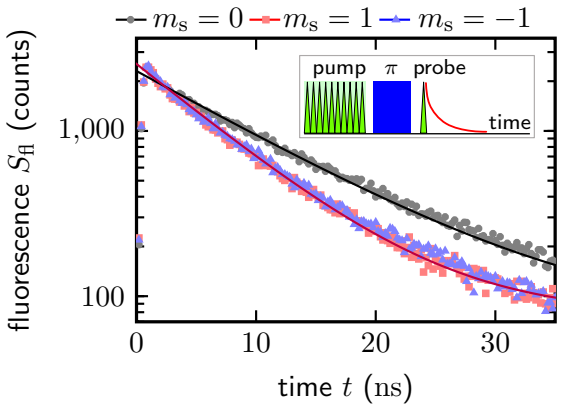

Figure 6.3: Spin-selective fluorescence decay curves. Excited-state lifetimes τ of 12.2 ns for τ_0 and 8.6 ns for $\tau_{\pm1}$ were extracted from these decay curves using equation 6.1. The inset shows the pulse sequence of the lifetime measurement. The selected single NV centre was optically polarised into the $m_s = 0$ state by a condensed laser-pulse train composed of 100 laser pulses. Depending on the addressed spin state, a spin-selective π-pulse followed the optical pumping process. After the NV centre was excited by the probe laser pulse, the fluorescence decay data was recorded, from which the corresponding lifetime can be extracted according to equation 6.1. The total length of a single measurement is 2.288 µs. This figure is reprinted from [317] with the permission of AIP Publishing.

These values are comparable to previously reported lifetimes of 12.0 ns for $m_s = 0$ and 7.8 ns for $m_s = \pm1$ [182].

In conventional intensity-based ODMR measurements, the electron spin resonance is determined by monitoring the fluorescence intensity I_{fl} dependent on the applied microwave frequency f. For the lifetime-based ODMR technique, the applied frequency of the π-pulse was analogously swept over the frequency range and the fluorescence decay data S_{fl} after the probing laser pulse was recorded, see sequence scheme in figure 6.3.

For an appropriate fitting result, we repeated this sequence and accumulated the data for 600 s at each microwave frequency. To analyse this spectral data, we applied a physical model that considers the spin population between the $m_s = 0$ and $m_s = \pm1$ states for a given microwave frequency. The model is composed of two exponential terms respective to $m_s = 0$ and $m_s = \pm1$ as the following

$$S_{fl}(t) = A_{ref}[A_0 \exp(-t/\tau_0) + (1 - A_0) \exp(-t/\tau_{\pm1})], \tag{6.2}$$

where the coefficient A_0 describes the spin population of the $m_s = 0$ state. The parameter A_{ref} is a free parameter for the fitting procedure, which takes the peak amplitude of the decay curve into account. The resulting spectrum is shown in figure 6.4a.

We further applied single exponential fits with equation 6.1 to the measured decay curves and fitted out the resulting decay times as the effective lifetimes τ, see figure 6.4b. This is a simplified way to analyse the decay data without having a justified physical model, which is in contrast to the existing model for the analysis of A_0. To compare the lifetime-based analysis with the conventional intensity-based method using the same data set, we integrated the detected photons in the decay curves recorded for different applied microwave frequencies and plotted the resulting spectrum in figure 6.4c.

The NV centre is most sensitive to changes in the magnetic field at the position of maximum *slope* of the spin resonance, *i.e.* where the derivatives $\partial I_{fl}/\partial f$, $\partial \tau/\partial f$ and $\partial A_0/\partial f$ of the spectra in figure 6.4a-c are maximised, respectively. According to Dréau *et al.*, the maximum slope of a Lorentzian shaped spin resonance is characterised by [208]

$$\max\ slope = \frac{C\,\langle I_{fl}\rangle}{\Delta\nu\mathcal{P}_F}, \tag{6.3}$$

where C is the measured contrast, $\langle I_{fl}\rangle$ the average photon rate of the $m_s = 0$ state, $\Delta\nu$ is the full width at half maximum of the spin resonance and $\mathcal{P}_F$ a numerical factor related to the resonance profile (for the Lorentzian model, $\mathcal{P}_F \approx 0.77$) [208]. Using this equation and fitting the recorded spectra with a double-dip Lorentzian model, we obtained a *slope* of $0.50\,\mathrm{MHz}^{-1}$ for the spin population based ODMR, a *slope* of $0.13\,\mathrm{ns\,MHz}^{-1}$ for lifetime based ODMR and a *slope* of $6.86\,\mathrm{counts\,s}^{-1}\,\mathrm{MHz}^{-1}$ for the intensity based ODMR. The minimal detectable magnetic field B_{min} can then be calculated by

$$B_{min} = \frac{1}{\tilde{\gamma}_{NV}}\frac{noise}{slope}, \tag{6.4}$$

where *noise* is the deviation of the magnetically sensitive signal in the respective ODMR spectrum. For this purpose, we repeatedly recorded the fluorescence

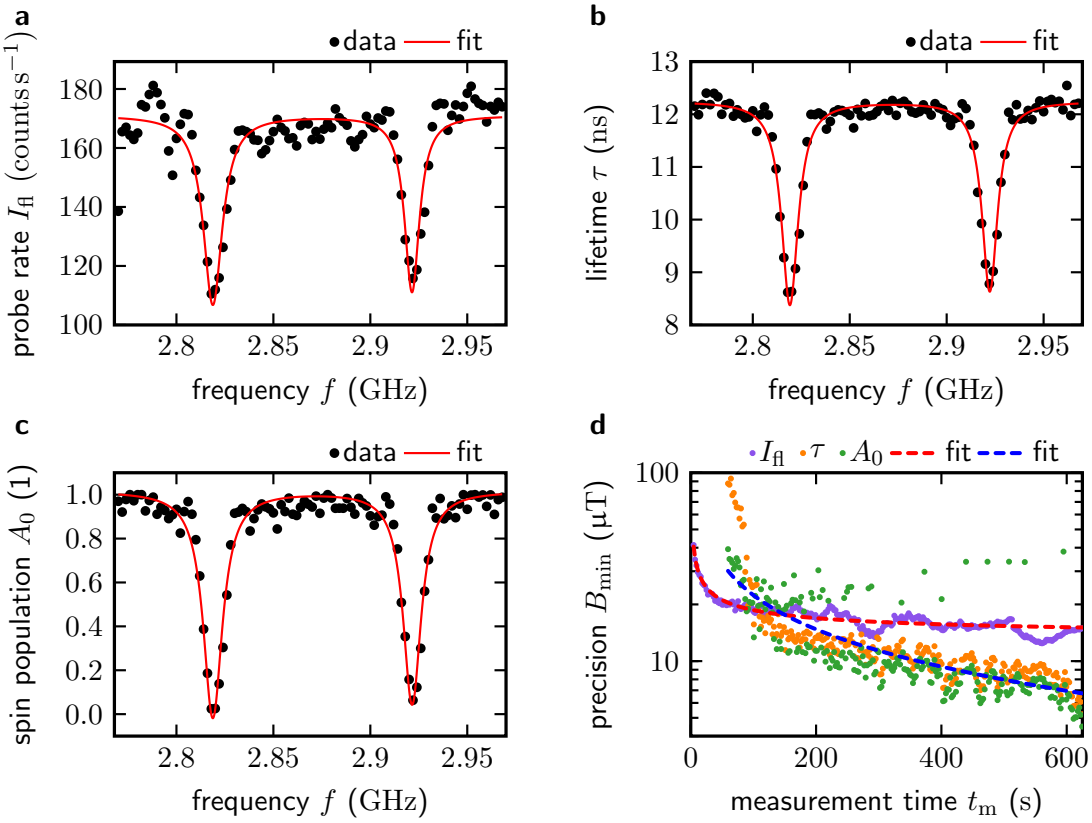

Figure 6.4: ODMR spectra based on the three different analysis methods and resulting minimal detectable magnetic field B_{min}. The shown ODMR spectra are based on the same data set. **a)** Lifetime-based ODMR spectrum showing the extracted spin population A_0. The values of A_0 were derived from fitting the decay curve of each microwave frequency with equation 6.2 using the determined lifetimes τ_0 and $\tau_{\pm1}$ from figure 6.3. **b)** Lifetime-based ODMR spectrum showing the extracted lifetimes τ. The values of τ were derived from fitting the decay curve of each microwave frequency with equation 6.1. **c)** Intensity-based ODMR spectrum showing the detected probe photon rate I_{fl}. The number of photons was derived by integrating the fluorescence decay curve of each microwave frequency. **d)** Resulting B_{min} performance dependent on the measurement time t_{m} for the three measured ODMR spectra analysing I_{fl} (purple data), τ (orange data) and A_0 (green data). To derive B_{min}, the *slope* values were derived from the respective spectrum and the signal deviation, described by the *noise* values, was characterized by equation 6.5 for the three analysis methods. A square root scaling of the inverse measurement time t_{m} is added as a guide to the eye for the plots of I_{fl} and A_0 (dashed red and blue lines), respectively. Note that several single outliers exist in the curve of A_0 as a result of a fast decaying background of $\sim 6\,\mathrm{ns}$, which is close to the excited-state lifetime of $m_{\mathrm{s}} = \pm1$. This adds up to uncertainties in determining the parameter of the spin population for $m_{\mathrm{s}} = \pm1$. This figure is adapted from [317] with the permission of AIP Publishing.

decay curve with a microwave frequency of the π-pulse corresponding to the position of maximum *slope* and a sampling length of 2.288 µs, from which the values of A_0, τ, and I_{fl} were extracted for each sampling bin. We periodically refocused the confocal microscope onto the NV centre every 600 s, as to avoid NV sample drifting off the focus of the microscope. Merging the decay data of subsequent sampling bins and extracting the desired values from the resulting data allowed a time dependent noise analysis using the Allan deviation [306]. The Allan variance σ^2_{adev} was calculated by [22]

$$\sigma^2_{\mathrm{adev}}(t_{\mathrm{m}}) = \frac{1}{2}\left\langle (y_{n+1} - y_n)^2 \right\rangle , \tag{6.5}$$

where y_n and y_{n+1} are the extracted values of A_0, τ and I_{fl} of two subsequent intervals of length t_{m}. The minimum detectable magnetic field from equation 6.4 follows to

$$B_{\mathrm{min}}(t_{\mathrm{m}}) = \frac{1}{\tilde{\gamma}_{\mathrm{NV}}} \frac{\sigma_{\mathrm{adev}}(t_{\mathrm{m}})}{slope}. \tag{6.6}$$

The corresponding graphs of B_{min} for the three analysis methods are shown in figure 6.4d. In contrast to the intensity-based analysis, which directly used the photon rate I_{fl}, we needed accumulation times longer than 60 s to conduct the exponential decay fits (both single and double exponential decay fit) for the deviation analysis of τ and A_0, see figure 6.4d. This is linked to the fact that we addressed a single NV centre located about 5 µm deep inside the diamond resulting in a relatively low detected fluorescence rate.

For measurement times shorter than 100 s, the intensity-based method outperformed the lifetime analysis (using the variables of τ and A_0) in terms of a smaller value of B_{min}. If t_{m} exceeded 100 s, both lifetime-based methods showed a better performance than the intensity-based readout of the spin state. For the majority of the analysed t_{m}, the noise analysis of τ and A_0 showed a similar behaviour for B_{min}.

However, a small set of B_{min} data points obtained from the noise analysis of A_0 deviates from this behaviour. The rare appearance of these outliers is linked to the data analysis and is caused by a fast decaying background of 6 ns after laser pulse arrival being present in the measured decay data. This background

contributed to the spin population of $m_s = \pm 1$ as it was close to the excited-state lifetime of the $m_s = \pm 1$ states. As the noise counts were dependent on fluctuations of the laser power and some random drifts of the confocal scanner also reduced the signal counts from the NV centre, the contribution from the fast decaying background was dynamic. The fitting process with the double exponential model can therefore go for some coincidences to a wrong direction leading to the spikes in the curve of A_0, see figure 6.4d. The nature of the fast background is not fully understood. It could be very specific to the used sample. Even though the single events are rare and associated with the data analysis, it indicates that our analysing method is not yet robust enough against such a dynamic signal-to-noise ratio.

In cases, where the noise ratio could be restrained, for example, NV centres embedded in nanodiamonds have much longer excited-state lifetimes than NV centres in bulk diamond [318], the fast decaying background could be minimised or even erased by removing the first few ns photon count in measured lifetime data.

In contrast, the method analysing the lifetime using a single exponential fit has taken the overall photon counts, including background and NV fluorescence counts, leading to smaller relative fluctuations, see figure 6.4d. Although this single-exponential function is not supported by any physical model, it can be used to easily derive an ODMR spectrum from the recorded decay data.

From the results of figure 6.4d, a minimal magnetic field sensitivity described by $\eta_B = B_{\min}\sqrt{t_m}$ of approximately $100.3\,\mu\mathrm{T\,Hz^{-1/2}}$ was achieved using A_0. Whereas η_B of both lifetime-based methods improved with increasing t_m for $t_m > 100\,\mathrm{s}$ and followed an inverse square root scaling of t_m (see figure 6.4d), the noise analysis of I_{fl} showed increasing values of η_B while extending the measurement time t_m.

Whereas conventional continuous-wave ODMR can achieve sensitivities of a few $\mu\mathrm{T\,Hz^{-1/2}}$ for single NV centres [49, 319], the overall sensitivity of the lifetime technique is worse, but shows an improved precision on the long-term scale. The resulting sensitivity is mainly affected by the much lower probe

photon rate compared to conventional ODMR, which is linked to the sequence protocol shown in figure 6.3. This prevents the lifetime-based ODMR to provide magnetic field information as quickly as conventional ODMR. For continuous optical excitation, the fluorescence intensity of the selected NV centre is about 80 kcounts s^{-1}, which could then provide a similar sensitivity. However, continuous-wave ODMR protocols are typically limited by the laser's stability during a measurement. Outside these limits, technical noise impacts the NV sensor's performance and thus worsens the achievable sensitivity. For cases, where technical noise is a limiting factor, the lifetime-based technique is target to be applied by making use of the intrinsic NV properties.

6.4 Conclusion And Outlook

[317] In summary, we demonstrated a proof-of-principle about a sensing technique to measure the electron spin resonance of a single NV centre. We showed that the excited-state lifetime can be used for NV magnetometry experiments and demonstrated that the lifetime-based analysis can have advantages over the conventional intensity-based sensing technique.

The sample used in this study contains single NV centres deeply located inside the diamond, which required a long measurement time to accumulate sufficient fluorescence photons for a reliable lifetime analysis. However, transferring the lifetime analysis method onto the experiments with NV nanodiamonds or NV ensembles as well as combining the fluorescence collection with advanced readout techniques can tremendously increase the data accumulation speed.

We believe that the lifetime analysis has high potential for life science experiments using NV nanodiamonds, *e.g.* NV nanodiamonds as bio-fluorescent markers, as their fluorescence intensity is strongly correlated with the environment [320]. This makes intensity-based sensing experiments vulnerable if the refractive index of the environment changes or the nanodiamond rotates during a measurement. Our method could also provide significant advantage when blinking effects are present [321], which also true for shallow NV centres often showing instabilities of the charge state.

Furthermore, a shorter data acquisition time needed for the analysis of the fluorescence decay is expected for NV nanodiamonds compared to a single NV centre in bulk diamond due to their longer excited-state lifetimes as well as a larger ratio of $\tau_{\pm1}/\tau_0$ [318]. This is related to the modulation of the refractive index of the environment affecting the excited lifetime [185], whereas the non-radiative shelving rate to singlet states is independent of the surrounding medium. A combination of lifetime-based sensing technique and NV nanodiamonds would therefore be extremely interesting.

The roll out of this technique on NV ensembles in bulk diamond can represent the next step to be tested. A larger number of emitters would result in an increased photon rate for NV ensembles in comparison to a single NV centre reducing the necessary measurement time. Using maximum likelihood estimation or artificial intelligence techniques, *e.g.* proposed by Santagati *et al.* [97], could further reduce the required time of measurement needed to determine the lifetimes compared to the described fitting procedure in our experiments.

The use of the lifetime information can also be interesting for microwave-free, as this magnetometry technique crucially relies on the precise detection of the fluorescence intensity [245]. As demonstrated, the lifetime analysis can be implemented in an ODMR protocol to measure magnetic fields. This means that the lifetime analysis can be used to measure temperature by ODMR [54, 195], especially as the excited-state lifetime has a very weak temperature dependence around 300 K [322].

7 Conclusion And Outlook

7.1 Conclusion

This thesis reports on the sensor development of high sensitive magnetometers using NV centres. To enable this technology for a wide range of mobile and novel applications, a strong integration and miniaturisation of the sensor components for an NV magnetometer is required. The chapters 4 and 5 deal with the challenges of setting up compact and high sensitive NV sensors for measuring magnetic fields. In these chapters, the design and sensor concept of two NV magnetometers with a performance characterisation are discussed. The prototypes assembled at Corporate Research and Advance Engineering Sector of Robert Bosch GmbH are depicted in figure 7.1.

Primary goal of the NV magnetometer described in chapter 4 was put on the construction volume of the sensor head using a bare LED die as compact light source. This NV sensor allowed a detection of magnetic fields with minimal field strength in the microtesla-range within an integration time of 1 s, which results in a sensitivity of roughly 31 $\mathrm{nT\,Hz^{-1/2}}$ [218]. Main limiting factor for the sensor's performance was associated with the weak optical pumping due the light emission of the LED.

To overcome these limitations in the optical pumping process, the LED was replaced by a laser for the prototype described in chapter 5. For this NV sensor, the emitted laser light was coupled into a single mode fibre, which was in turn attached to the diamond by an adhesive layer. During development, special emphasis was placed on the selection of components for the construction of a highly integrated and portable NV magnetometer. Besides the use of a compact laser module and a self-made construction for providing an offset magnetic field, this NV sensor is

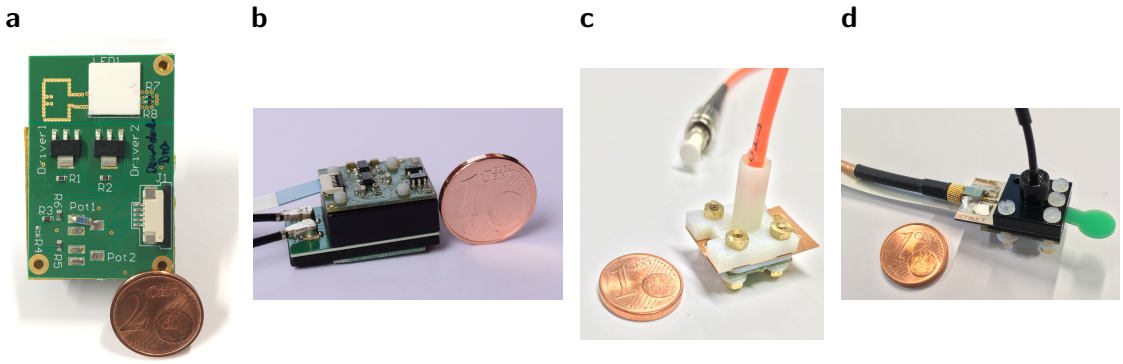

Figure 7.1: Images of the NV magnetometers assembled at the Corporate Research and Advance Engineering Sector of Robert Bosch GmbH. a) Prototype of an LED-based NV magnetometer, whose documentation is not included in this dissertation. **b)** Sugar cube-sized NV sensor from chapter 4. **c)** Fibre-based NV magnetometer, whose documentation is not included in this dissertation. **d)** Portable and integrated fibre-based NV magnetometer from chapter 5 containing a balanced detection scheme on a common PCB integrated in the sensor head.

equipped with optical and electronic off-the-shelf components. A balanced detection scheme composed of two photodiodes, which are mounted on a common PCB, is implemented in this sensor. This NV sensor is characterised with a magnetic field sensitivity of approximately $0.3\,\mathrm{nT\,Hz^{-1/2}}$ and a portability outside of laboratory environments is proven by the mobile detection of lift movement [32].

Typical ESR experiments using NV centres, like CW ODMR, make use of the fluorescence intensity in order to evaluate the electron spin state, from which the magnetic field information can be extracted. However, fluctuations in the optical excitation, *e.g.* introduced by instabilities of the laser's output power or polarisation issues, may weaken the performance of an NV magnetometer. In chapter 6, a proof-of-principle of a novel sensing method using the excited-state lifetimes of a single NV centre for the analysis of the spin states is demonstrated [317]. Comparing the lifetime-based with the conventional intensity-based method showed advantages for this new sensing technique for specific measurement conditions. Target to implement the lifetime-based sensing technique is, if technical noise impacts the performance of an NV sensor.

7.2 Outlook

While the three demonstrated prototypes can be considered as one of the first published compact and miniaturised NV magnetometers in the research community [32,218], the best sensitivity values previously demonstrated using NV centres could not be achieved with these sensors [22, 23, 25, 213]. However, the concepts of these sensors show how sensor integration can be accomplished, which is indispensable for an application-oriented sensor development.

To both achieve a higher level of integration and improve the detection performance, existing sensor concepts need to be further developed or new approaches with subsequent testing may be required. Promising approaches are for example the use of flux concentrators [25,31,33], the application of CMOS technology [103,214] and gradiometer approaches using multiple NV sensors [31,323]. In addition, the development of the necessary sensor components must be further advanced for setting up a compact and robust NV sensor system.

The intended use of the NV magnetometer also plays a crucial role in sensor development. Among other things, the following questions have to be answered: what kind of magnetic fields are to be investigated, *i.e.* temporally static or variable fields, what field information is to be obtained, *i.e.* absolute values or vector information, what dynamic field strength range the sensor is to cover and what bandwidth is to be achieved with the sensor.

Although NV centres can be for example used as thermometers [54, 55], pressure sensors [56], or electric field sensors [51–53], these colour centres are considered to have the greatest application potential as magnetometers. In particular, the detection of magnetic fields associated with neuronal activity in the brain [20,88,324] and the heartbeat [325] is of great interest and has a wide scope of application [314,326], even if it is difficult to estimate it at the moment. An NV sensor system could serve as an interface for human-machine communication, which detects the magnetic field generated by neuronal impulses, from which machine adjustments could be carried out. It would be conceivable to use it as a control aid for prostheses by reading out neuronal signals or to use it in medical diagnostics for a less intrusive examination of patients [91, 326]. Other applications of NV magnetometers may

include mobility and positioning [65, 67, 68, 327], *e.g.* for GPS-free navigation and aerospace [77, 328, 329], as supporting instruments in space exploration missions.

A Supplementary Information

A.1 Introduction

State-of-the-art magnetic field sensors are Hall sensors, induction coil magnetometers, magnetoresistance sensors (GMR, AMR and TMR), fluxgate sensors, magnetometers based on NV centres, OPMs based on alkali gases and SQUIDs. These sensing technologies differ not only in their sensitivity performance, but also in the capability to measure magnetic fields over a wide range of field strength. The sensor characteristics for a selection of magnetometers are summarised in table A.1.

Table A.1: Overview of magnetometer technologies in terms of sensing capabilities with respect to field strength and frequency range. Values of the dynamic range are taken from [22, 330, 331], whereas the measurable frequencies are extracted from [24, 330, 332].

Sensor technology	Field strength range	Frequency range
Hall	1 fT to 1 mT	DC to 1 MHz
Induction coil	1 fT to 1 mT	AC
GMR	100 pT to 10 mT	DC to GHz
AMR	1 nT to 1 mT	DC to 10 MHz
TMR	100 pT to 10 mT	DC to GHz
Fluxgate	5 pT to 100 µT	DC to 5 kHz
NV diamond	100 fT to 10 T	DC to GHz
OPM	1 fT to 1 µT	DC to GHz
SQUID	1 fT to 100 µT	DC to 100 kHz

A.2 The Nitrogen-Vacancy Centre In Diamond

A.2.1 NV Spin Hamiltonian

The spin dynamics of the NV centre's electron spin in the ground state including the corresponding spin Hamiltonian are described in section 2.2.5. Additional information for this description is given in the following.

For a spin $S = 1$ system, the spin operator $\hat{\boldsymbol{S}}$ can be defined as $\hat{\boldsymbol{S}}^\dagger = \left(\hat{S}_x, \hat{S}_y, \hat{S}_z\right)$ with

$$\hat{\boldsymbol{S}}_{\boldsymbol{x}} = \frac{h}{\sqrt{2}} \begin{pmatrix} 0 & 1 & 0 \\ 1 & 0 & 1 \\ 0 & 1 & 0 \end{pmatrix}, \quad \hat{\boldsymbol{S}}_{\boldsymbol{y}} = \frac{ih}{\sqrt{2}} \begin{pmatrix} 0 & -1 & 0 \\ 1 & 0 & -1 \\ 0 & 1 & 0 \end{pmatrix}, \quad \hat{\boldsymbol{S}}_{\boldsymbol{z}} = h \begin{pmatrix} 1 & 1 & 0 \\ 0 & 0 & 0 \\ 0 & 0 & -1 \end{pmatrix}. \tag{A.1}$$

Taking the eigenvalue frame, the electron interaction tensor $\mathbb{D}$ from equation 2.2 is diagonal and can be written as [116]

$$\mathbb{D} = \begin{pmatrix} D_x & 0 & 0 \\ 0 & D_y & 0 \\ 0 & 0 & D_z \end{pmatrix} = \begin{pmatrix} -\frac{1}{3}D + E & 0 & 0 \\ 0 & -\frac{1}{3}D - E & 0 \\ 0 & 0 & \frac{2}{3}D \end{pmatrix}, \tag{A.2}$$

where the relations of $D = \frac{3}{2}D_z$ and $E = \frac{1}{2}(D_x - D_y)$ are applied [116]. The hyperfine tensor $\mathbb{A}$ from equation 2.3 can be written as [174]

$$\mathbb{A} = \begin{pmatrix} A_{\text{gs}}^{\perp} & 0 & 0 \\ 0 & A_{\text{gs}}^{\perp} & 0 \\ 0 & 0 & A_{\text{gs}}^{\parallel} \end{pmatrix} \tag{A.3}$$

and the nuclear interaction tensor $\mathbb{Q}$ is described by

$$\mathbb{Q} = \begin{pmatrix} Q_x & 0 & 0 \\ 0 & Q_y & 0 \\ 0 & 0 & Q_z \end{pmatrix}. \tag{A.4}$$

A.3 Magnetometry Using NV Centres

A.3.1 Sensitivity Optimisation

A theoretical analysis of the spin dynamics of an NV ensemble is conducted in section 3.2, where the ESR behaviour with parameters of linewidth $\Delta\nu$, contrast C and detected photon rate $\mathcal{R}$ is evaluated dependent on the applied process parameters of optical pumping and spin manipulation. The resulting $\Delta\nu$ and C according to the equations 3.14 and 3.15 are shown in figure A.1.

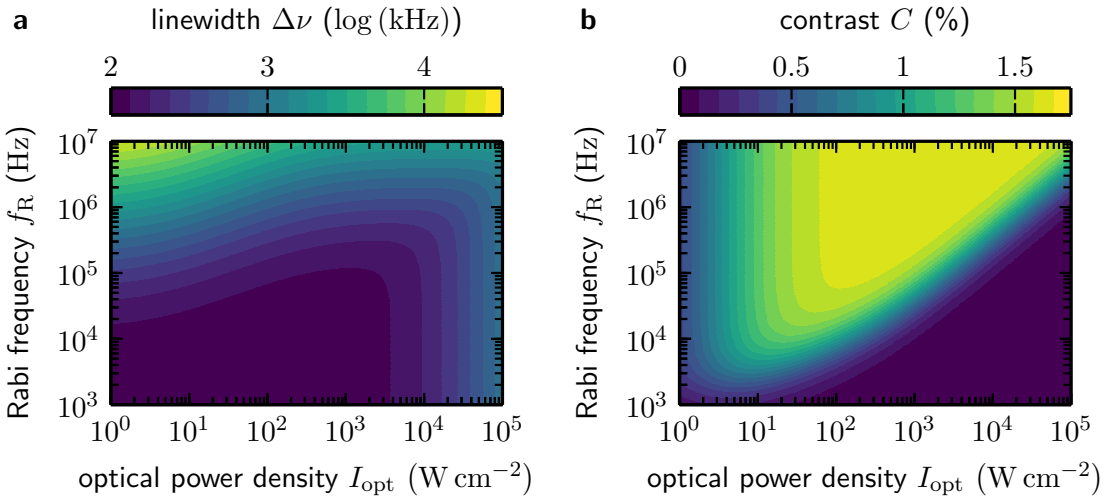

Figure A.1: Simulative analysis of the achievable linewidth and contrast for an NV ensemble magnetometer depending on the applied processes of optical pumping and spin manipulation. The achievable sensitivity for an NV magnetometer with specific properties and working parameters is evaluated in section 3.2. The corresponding input parameters for this simulation are summarised in the caption of figure 3.2. **a)** Simulation result of the linewidth $\Delta\nu$ according to equation 3.14 with dependence on the optical excitation and spin manipulation. **b)** Corresponding 2D plot of the simulated contrast result accordingt to equation 3.15.

A.4 LED-Based NV Magnetometer

Portions of this section are based on [218] with minor edits. The taken text passages are marked by marginal notes, whereas the taken captions are not additionally highlighted. Reprinted under author rights from [218]. Copyright (2019) Elsevier B.V. All rights reserved.

A.4.1 Optical Spin Readout

The optical spin readout of the LED-based NV magnetometer using the GRIN rod lens is described in section 4.2.4. A simulative analysis of the collection efficiency is shown in figure 4.5. Further results of this simulation are presented in figure A.2, which allows an analysis of the detection efficiency off the GRIN rod lens along the optical axis. The simulation shows that the GRIN rod lens collects the emitted fluorescence with an efficiency $> 15\%$. However, due to the refractive index difference between the lens and the PD, TIR reduces the fluorescence intensity detectable by the PD to 7.8%, if the detector has a distance of 200 µm to the lens. In addition, it is shown that a non-negligible proportion of the light intensity collected by the GRIN is lost along the length of the lens.

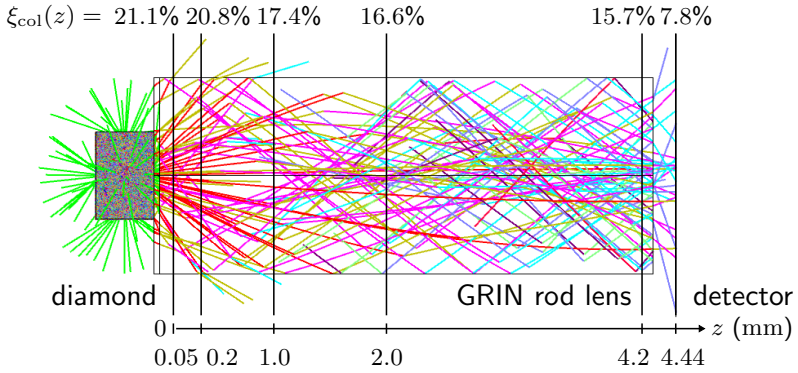

Figure A.2: Simulative analysis of the collection efficiency along the optical axis of the GRIN rod lens. Optical ray trace simulations are performed using Zemax OpticStudio® to evaluate the collection efficiency ξ_{col} of the fluorescence light by the GRIN rod lens. The simulation settings described in figure 4.5a are extended for this purpose such that the detector has the property of an absorbing surface and is positioned at different positions z along the optical axis. This allows that the collection efficiency described by $\xi_{col}(z) = P_{col}(z)/P_{out}$ can be analysed for collected light powers $P_{col}(z)$ on specific positions z. 300 rays are displayed in the graphical 2D view and the colouring of the displayed rays results from the number of interfaces interactions.

In contrast, ξ_{col} would result in 9.4%, see figure 4.5c, if the diamond is only surrounded by air for a 200 µm distance between diamond and detector. The main reason to use the GRIND rod lens in the assembly of the LED-based magnetometer is to mitigate the influence of any additional magnetic fields induced by electronic circuits linked to the PD while ensuring an optical guidance of the emitted fluorescence.

Improvement measures could include the application of reflective layers, which reflects light rays back, and the introduction of a transparent medium between the lens and the PD, which mitigates the effect of TIR. The refractive index of the transparent medium should match to the properties of the lens.

As a general remark, the input for the refractive indices of materials, which have been used in the optical ray tracing simulations to evaluate the excitation and spin readout of the NV centres using Zemax OpticStudio®, are summarised in table A.2 with specific wavelength dependence.

Table A.2: Refractive indices of different materials applied in optical ray tracing simulations using Zemax OpticStudio®. Wavelength-dependent refractive indices are based on the online page of https://refractiveindex.info/ with corresponding material search (retrieved on 13th November 2020).

Material	Wavelength λ (nm)	Refractive index $n(\lambda)$
Air	independent	1.0
Diamond	522	2.4264
Diamond	532	2.425
Diamond	700	2.4065
PDMS	522	1.4342
PDMS	532	1.4335
PDMS	700	1.426
N-BK7 (Schott)	532	1.5168

A.4.2 Experimental Results

The temperature T_{dia} of the diamond from chapter 4 is derived by extracting the two transition frequencies $\nu_{\pm}$ of the crystallographic orientation with the largest splitting from the ODMR spectrum shown in figure 4.6b. In the displayed spectrum, the resonance dips corresponding to this orientation are labelled as I. As this crystallographic orientation is almost parallel to the static magnetic field $\boldsymbol{B_0}$, the orthogonal component of $\boldsymbol{B_0}$ is lowest, *i.e.* the mixing of the electron spin states due to the orthogonal magnetic field is lowest [186]. [218]

The temperature T_{dia} inside the diamond can be calculated according to the frequency shift ΔT by

$$\Delta T = \left(\frac{\nu_+ + \nu_-}{2} - D_{\text{gs}} \right) \frac{\mathrm{d}T}{\mathrm{d}D_{\text{gs}}}, \tag{A.5}$$

where $\mathrm{d}D_{\text{gs}}/\mathrm{d}T$ is the temperature dependency of the zero-field splitting with $\mathrm{d}D_{\text{gs}}/\mathrm{d}T \approx -74.2\,\text{kHz}\,\text{K}^{-1}$ [195]. The resonance frequencies and the evaluated temperature from the measured ODMR spectrum, shown in figure 4.6b, for the four NV orientations are summarised in table A.3.

Table A.3: Temperature estimation of the diamond used in the LED-based magnetometer from chapter 4. For each NV orientation (labelled with I-IV in figure 4.6b) the temperature of the diamond is evaluated according the Zeeman splitting and shift relative to the ZFS. This table is based on [218].

NV axis	ν_- (MHz)	ν_+ (MHz)	ΔT (K)	T_{dia} (°C)
I	2813.316	2919.423	48.93	68.93
II	2833.773	2900.715	37.15	57.15
III	2850.084	2884.402	37.16	57.16
IV	2860.409	2874.839	32.02	52.02

A.4.3 Power Consumption

[218] The total power consumption of the LED-based sensor device sums to roughly 1.45 W and is based on the following functional parts of the NV sensor: optical power by the LED, microwave power by the microwave source, electrical power by the photodiode an the electronic circuits. The corresponding power values are summarised in table A.4.

Table A.4: Power consumption of the LED-based sensor. These values are based on [218].

Component	Power consumption (mW)
LED	600
Microwave source	80
Electronic control and drive circuits	540
Photodiode	230

A.5 Fibre-Based NV Magnetometer

Portions of this section are based on [32] with minor edits. The taken text passages are marked by marginal notes, whereas the taken captions are not additionally highlighted. Reprinted and modified under author rights from [32], licensed under a Creative Commons Attribution-NonCommercial-NoDerivatives License 4.0 (CC BY-NC-ND 4.0, https://creativecommons.org/licenses/by-nc-nd/4.0/). Copyright (2021) The authors.

A.5.1 Sensor Assembly

Figure A.3 shows the portable setup of the fibre-based NV magnetometer with the relevant equipment, as described in section 5.2. Selective images of the portable fibre-based NV magnetometer from chapter 5 are shown in figure A.4, including the GRIN-fibre compound connected to the diamond (figure A.4a), the balanced detection board with the different DBR filters deposited on the surfaces of the two PDs (figure A.4b) and the NV sensor head placed into the pair of tapered Helmholtz coils (figure A.4c).

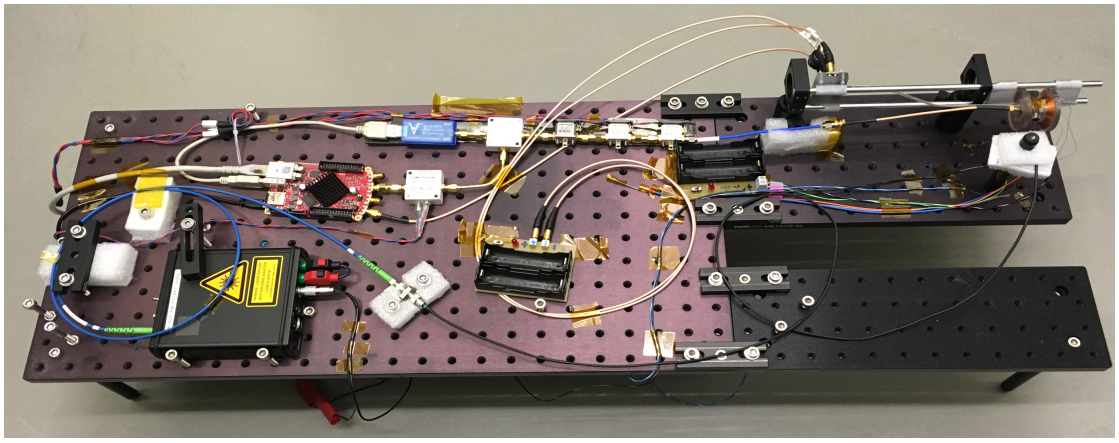

Figure A.3: Image of the portable setup of the fibre-based NV magnetometer. All relevant components (excluding a PC) are mounted on solid breadboards with total dimension of $(0.3 \times 0.9)\,\mathrm{m}^2$, which allows the NV sensor for portable measurements.

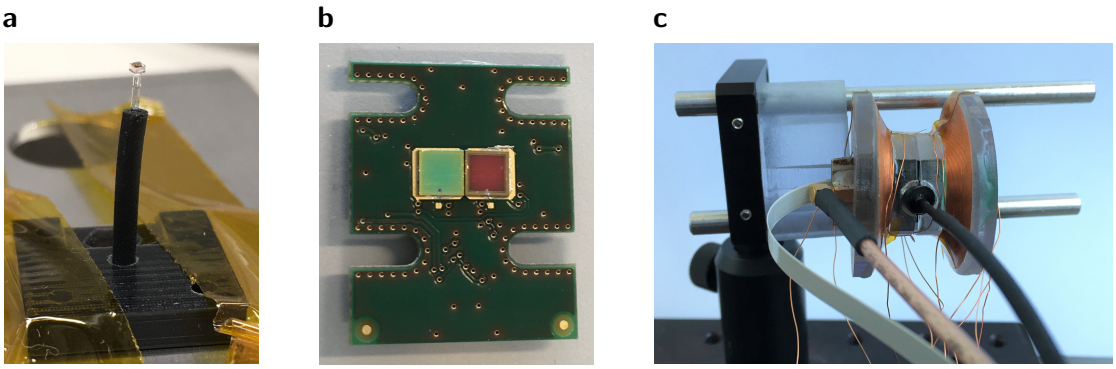

Figure A.4: Images of the integrated fibre-based NV magnetometer. a) Image of the fibre-GRIN assembly. The diamond is connected with a thin layer of PDMS on a GRIN rod lens with a lens length of $1.09\,\mathrm{mm}$. We inserted the optical fibre into pigtailed glass ferrule with length of $5.0\,\mathrm{mm}$ and connected to the GRIN rod lens by an epoxy glue. The fibre is surrounded by a black shrinkdown plastic tubing in order to protect the fibre from breakage and for an easy handling of the fibre system. As a next step, the fibre is inserted into a 3D-printed construction (fibre holder, fixed with yellow tape) and then stabilised with a two component glue. **b)** Image of the balanced detection board using two locally separated PDs with different DBR filters positioned on the PD surface. The left PD with long pass filter is responsible for the fluorescence detection, whereas the PD on the right side with short pass filter deposited on the sensitive surface measures the laser excitation light. The electronic for the balancing of the two signals (fluorescence and reference) is placed at the backside of the board. Four slotted holes are used to vary the position of this board relative to the diamond-fibre assembly, shown in a). **c)** Image of the construction of the tapered Helmholtz coils, into which the NV sensor is inserted. The fibre (black cable) is guided through a round recess in the coil geometry, whereas the ribbon cable (white cable) for the signal transport and the radio frequency cable (black-orange cable) for the microwave supply are connected to the NV sensor through the left opening of the coil geometry.

A.5.2 Spin Manipulation

[32]

As described in section 5.2.3, we used a double-split ring resonator to provide a microwave field necessary for the electron spin resonance measurements, which can be seen in figure A.5a. It consists of two circular spit-rings capacitively coupled to the feed strip line via a coupling gap. The geometrical parameters of the structure are summarised in table A.5 with corresponding scanning electron microscope images shown in figure A.6.

The resonance frequency of the empty resonator on the substrate (Rogers RO3010 with thickness $0.64\,\mathrm{mm}$, copper metallization $20\,\mu\mathrm{m}$, dielectric con-

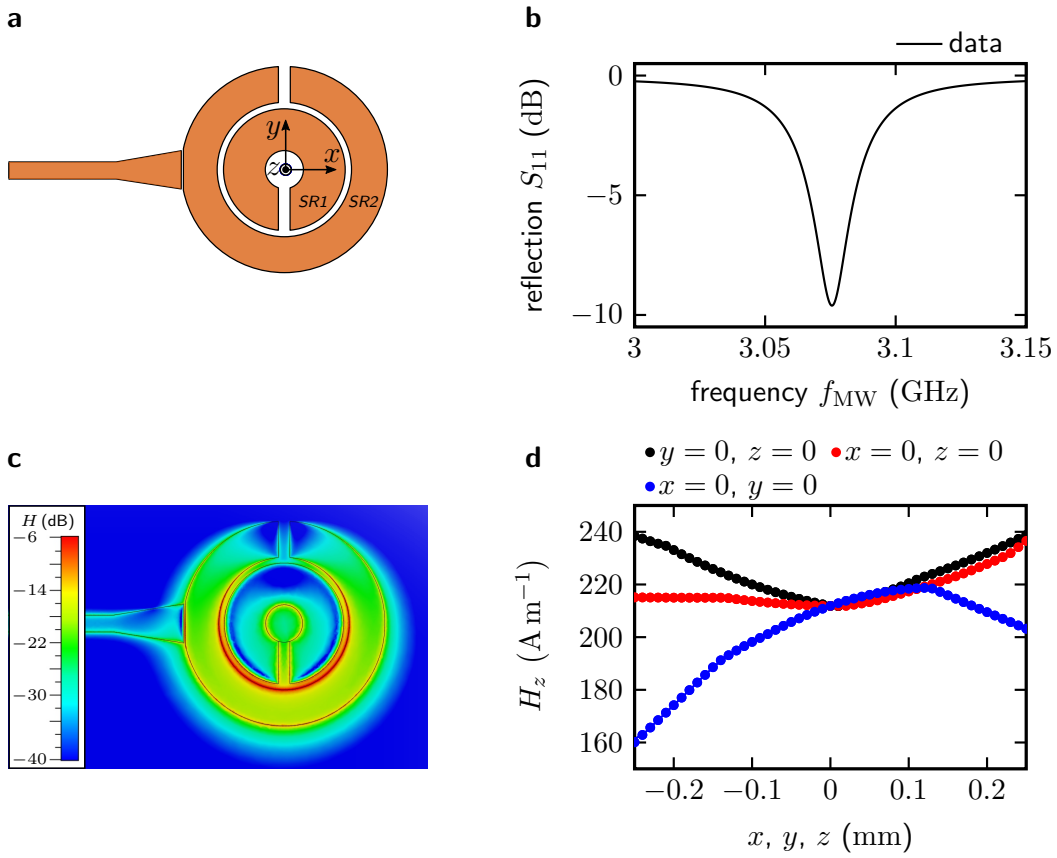

Figure A.5: Design and simulation of the double split-ring resonator. a) The double split-ring resonator with coordinate system indicated. The geometrical parameters are summarised in table A.5. **b)** Contour plot of the normalised microwave magnetic field magnitude at $z = 0\,\mathrm{mm}$ in logarithmic scale was calculated using CST Microwave Studio®. **c)** Calculated S_{11} curve for an empty resonator. **d)** The amplitude of the magnetic microwave field component H_z in dependence on x,y and z as indicated in a) for a critically coupled structure. This figure is modified as author from [32], licensed under CC BY-NC-ND 4.0, https://creativecommons.org/licenses/by-nc-nd/4.0/.

stant $\varepsilon = 10.2$, $\tan\delta = 2.2 \times 10^{-3}$) was calculated to be $f_{\mathrm{res}} = 3.073\,\mathrm{GHz}$.

The resonator was modelled to be undercoupled having an unloaded Q-value of $Q_0 = 147$ and a coupling coefficient of $\beta = 0.5$. The resonance frequency f_{res} and the coupling coefficient β of the structure are adjustable by positioning a thin metal plate above the outer split ring and a dielectric plate over the coupling gap, respectively.

Figure A.7 shows the simulation of β dependent on the position of the coupler (Rogers RO3010 with dimensions of $(0.6 \times 1.6 \times 0.3)\,\mathrm{mm}^3$) and the resulting

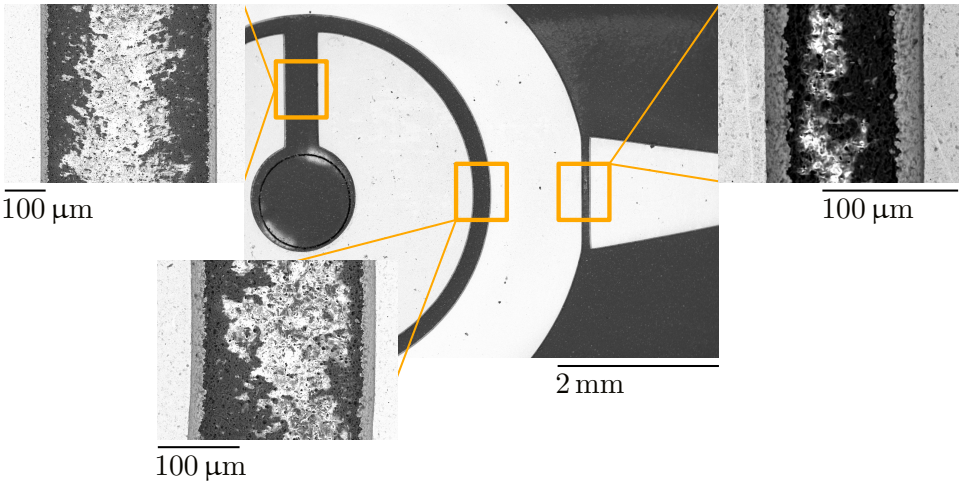

Figure A.6: Scanning electron microscope (SEM) images of the double split-ring resonator. Images of the fabricated PCB were recorded by a SEM (Hitachi TM 3000 with energy of 15 kV). The width of the coupling gap was measured to be $(120.7 \pm 5.5)\,\mu\text{m}$, the width of the gap between the inner and outer ring to be $(226.7 \pm 3.8)\,\mu\text{m}$ and the width of the inner gap to be $(430.0 \pm 2.0)\,\mu\text{m}$. The data was obtained by analysing three fabricated PCBs, from which the values of mean and standard deviation were calculated. This figure is reprinted from [32], licensed under CC BY-NC-ND 4.0, https://creativecommons.org/licenses/by-nc-nd/4.0/.

f_{res} dependent on the position of the tuner, which is a copper plate with dimensions of $(3.0 \times 1.2 \times 0.02)\,\text{mm}^3$, on the outer split-ring.

Based on simulations using CST Microwave Studio®, an amplitude H_z of the linearly polarised magnetic field along the z-axis of $310\,\text{A}\,\text{m}^{-1}$ was calculated

Table A.5: Geometrical parameters of the double split-ring resonator. A schematic drawing of the resonator is shown in figure A.5a. This table is based on [32].

Parameter	Dimension (mm)
Inner radius (SR1)	1.3
Outer radius (SR1)	4.2
Inner radius (SR2)	4.6
Outer radius (SR2)	7.1
Gap width (SR1, SR2)	0.4
Gap width (coupling)	0.1
Gap length (coupling)	1.45

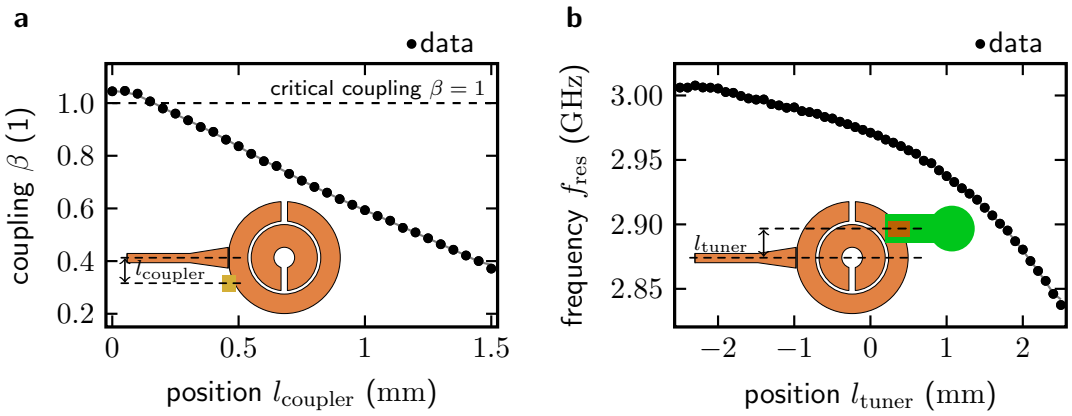

Figure A.7: Adjustments of the properties of the double split-ring resonator. a) Adjustment of the coupling parameter. Calculated coupling coefficient in dependence on coupler (Rogers RO3010, $(0.6 \times 1.6 \times 0.3)\,\text{mm}^3$) position above the coupling gap of $0.1\,\text{mm}$. **b)** Adjustment of the resonance frequency. Calculated resonance frequency in dependence on the position of the frequency tuner (copper, $(3.0 \times 1.2 \times 0.02)\,\text{mm}^3$), which is placed on top of the surface of the outer split-ring. This figure is based on [32].

at the resonator centre for the critically coupled structure and 1 W incident microwave power. Over the sample volume of $(0.8 \times 0.8 \times 0.5)\,\text{mm}^3$ an average amplitude of the z-component of the magnetic field with $H_z = 335\,\text{A}\,\text{m}^{-1}$ was simulated for 1 W, see figure A.5d and figure A.8.

The fabricated structure is shown in figure A.9a. Figure A.9b depicts the reflection curve S_{11} of the resonator recorded by a network analyser (Hewlett Packard 8753D) in the assembled NV sensor. The experimental curve was analysed using a general expression for the reflection coefficient by the following equation

$$S_{11} = 10 \log_{10} \left(|\Gamma|^2 \right), \tag{A.6}$$

where the reflection coefficient Γ is given by

$$\Gamma = \frac{1 - \beta - i\xi}{1 + \beta - i\xi}, \tag{A.7}$$

where β is the coupling coefficient and $\xi = 2Q_0 \left(\frac{f}{f_{\text{res}}} - \frac{f_{\text{res}}}{f} \right)$ an offset parameter.

The numerical fit yields an unloaded Q-value of $Q_0 = 117.12$ and a coupling coefficient of $\beta = 0.3$, which are in a good agreement with the calculated values. The small deviation between calculated and experimental values is explained

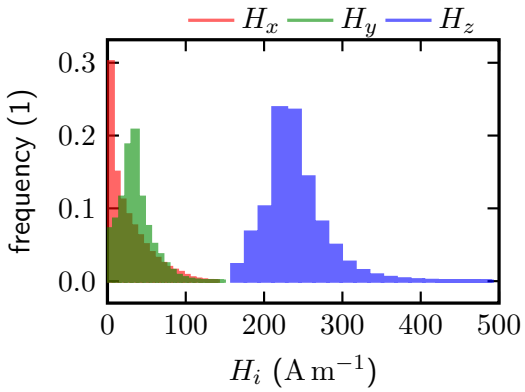

Figure A.8: Simulative result of the field distribution of the double split-ring resonator. Amplitude distributions of the microwave magnetic field components H_x, H_y and H_z over the sample volume of $(0.8 \times 0.8 \times 0.5)\,\mathrm{mm}^3$. This figure is based on [32].

by the roughness of the substrate surface, imperfections of metallization from the fabrication process as well as the discrepancy of real dielectric parameters of substrate material, which are not considered in the simulation.

The experimentally determined resonator bandwidth of 32.26 MHz is in good agreement with the predicted value of 30 MHz using

$$\Delta f = (1+\beta)\frac{f_{\mathrm{res}}}{Q_0}. \tag{A.8}$$

Figure A.9c depicts the measured contrast of the optically detected electron spin resonance. For these measurements, the applied offset magnetic field was varied resulting in a change of the resonance frequency of the selected electron spin transition.

As the spin resonance signal described by the contrast C depends on the applied microwave field B_1, we compared the measured contrast with the induced B_1 by the following approximation

$$C \propto B_1 \propto \sqrt{\frac{P_{\mathrm{abs}}}{P_0}} = \sqrt{1-\frac{P_{\mathrm{refl}}}{P_0}} = \sqrt{1-|\Gamma|^2} = \sqrt{1-10^{S_{11}/10}}. \tag{A.9}$$

The curves of C and B_1 in figure A.9c show a similar behaviour, which can be attributed to the characteristics of the double split-ring resonator.

We further analysed the resonator structure by considering the extracted ODMR linewidths for different microwave powers P_{MW}, see figure A.9d. This

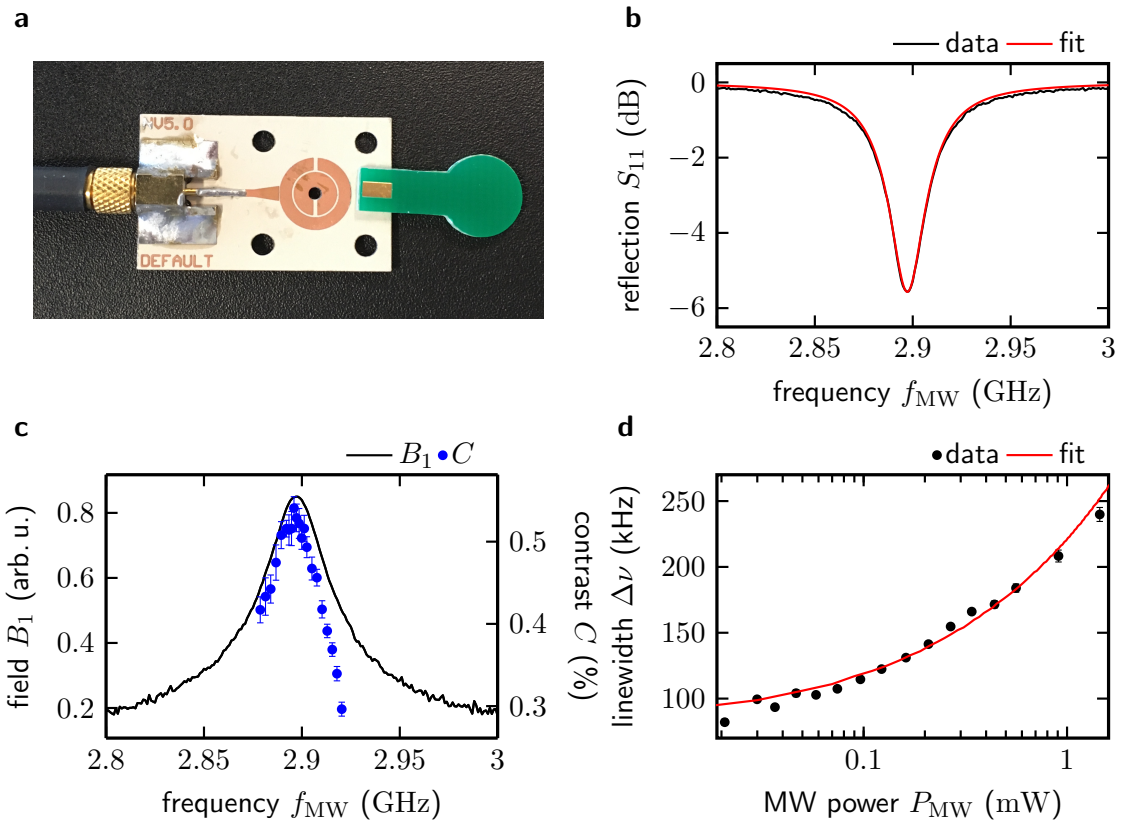

Figure A.9: Microwave double-split ring resonator. **a)** Photo of the double split-ring resonator with the additional metallised plate to tune the resonance frequency. **b)** The S_{11} coefficient data (black curve) measured by a network analyser (Hewlett Packard 8753D) was used to determine the quality factor Q_0 and the coupling property of the microwave resonator by fitting the data. From a Lorentzian fit, we extracted a resonance dip of $(-5.44 \pm 0.01)\,\mathrm{dB}$ and a width of $(32.25 \pm 0.11)\,\mathrm{MHz}$ (red curve) resulting in $Q_0 = 117.12$ and $\beta = 0.3$. The structure was modelled to be undercoupled without a dielectric coupler resulting in $Q_0 = 185$ and $\beta = 0.31$. **c)** Measured contrast C (blue dots) for different strengths of the offset magnetic field generated by the tapered Helmholtz coils. For the experiments, the resonator was tuned to a resonance frequency $f_{\mathrm{res}} = 2.898\,\mathrm{GHz}$ by adjusting the position of a metallised plate on the resonator structure that varied the capacitance of the split ring resonator. A microwave power of $36\,\mu\mathrm{W}$ was used. Based on the measured S_{11} data shown in b) the B_1 field strength (black curve) according to equation A.9 is added to this graph. **d)** Measured linewidth $\Delta\nu$ (black dots) depending on the applied microwave power P_{MW} (data from figure A.16b). The values of the linewidth were extracted from fitting the recorded spectra using the Lorentzian function of equation 5.2. We applied the model of the NV linewidth by Jensen *et al.*- summarised in equation A.10 - to the data (red curve), from which the Rabi frequency Ω_{R} can be derived using $\Omega_{\mathrm{R}} \propto \sqrt{P_{\mathrm{MW}}}$. This figure is reprinted from [32], licensed under CC BY-NC-ND 4.0, https://creativecommons.org/licenses/by-nc-nd/4.0/.

data corresponds to the second optimization step regarding the sensor's performance, where we evaluated the magnetic field sensitivity with respect to the applied microwave power, see section 5.3.

Typically, the NV linewidth broadens for an increased microwave field strength compared to the natural linewidth described by the inhomogeneously broadened linewidth $\Delta\nu_{\mathrm{inh}}$ in a low power regime [208]. We therefore considered the measured ODMR linewidth to be the sum of $\Delta\nu_{\mathrm{inh}}$ and a power induced linewidth $\Delta\nu_{\mathrm{power}}$. This is in accordance with the linewidth model for NV ensembles described by Jensen *et al.* [223]. We used this model to fit the measured linewidth by using the following equation

$$\Delta\nu = \Delta\nu_{\mathrm{inh}} + \Delta\nu_{\mathrm{power}} = \frac{\gamma_2^*}{\pi} + \sqrt{\left(\frac{\gamma_2^{\mathrm{eff}}}{\pi}\right)^2 + \frac{4\gamma_1^{\mathrm{eff}}}{\gamma_2^{\mathrm{eff}}}\left(\frac{\Omega_{\mathrm{R}}}{2\pi}\right)^2}, \tag{A.10}$$

where γ_2^* is the inhomogeneous dephasing rate with $\gamma_2^* = 1/T_2^*$, γ_1^{eff} and γ_2^{eff} are the effective relaxation rates described by $\gamma_1^{\mathrm{eff}} = 1/T_1 + \Gamma_{\mathrm{P}}$ and by $\gamma_2^{\mathrm{eff}} = 1/T_2 + \Gamma_{\mathrm{P}}/2$ with T_1 the longitudinal and T_2 the transverse relaxation times, Γ_{P} the optical pumping rate and Ω_{R} the Rabi frequency in units of rad/s.

The Rabi frequency is directly proportional to the microwave field, *i.e.* $\Omega_{\mathrm{R}} \propto B_1 \propto \sqrt{P_{\mathrm{MW}}}$. For the optical pumping rate, we considered the following relationship

$$\Gamma_{\mathrm{P}} = \sigma\frac{I_{\mathrm{opt}}}{E_{\mathrm{ph}}}, \tag{A.11}$$

where σ is the absorption cross-section with $0.31 \times 10^{-16}\,\mathrm{cm}^2$, [219] I_{opt} the optical excitation intensity and E_{ph} the photon energy of the 521.9 nm laser wavelength with $E_{\mathrm{ph}} \approx 2.38\,\mathrm{eV}$. We estimated an average optical power at the output of the GRIN lens of 18.3 mW with a diameter of 75.2 µm for a laser output power of 23.0 mW due to losses in the optical path. We used relaxation times of $T_1 = 5.89\,\mathrm{ms}$ and $T_2 = 96.49\,\mu\mathrm{s}$, which have been evaluated for this diamond on a confocal microscope setup. For an NV concentration of 0.4 ppm, we calculated an average intensity along the optical path over diamond's thickness of $I_{\mathrm{opt}} \approx 390.19\,\mathrm{W\,cm^{-2}}$ resulting in a pumping rate of $\Gamma_{\mathrm{P}} \approx 31.78\,\mathrm{kHz}$.

The fit of the model from equation A.10 revealed an inhomogeneously broad-

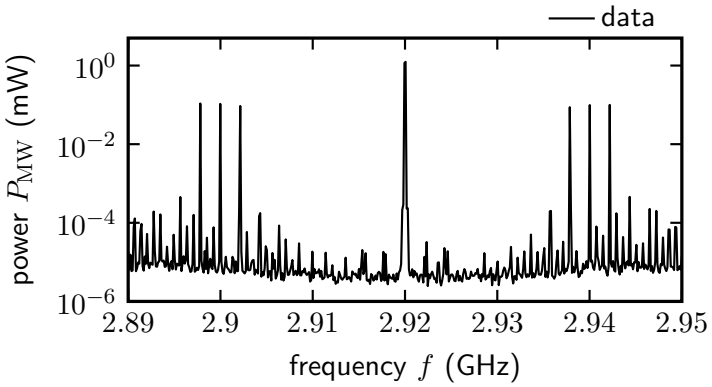

Figure A.10: Measured spectral power output of the spin manipulation equipment. The frequency of the local oscillator f_{LO} is set to 2.92 GHz and f_{BB} to 30 MHz. A simultaneous excitation of the three hyperfine features with a splitting of 2.16 MHz is applied. The spectral power P_{MW} is measured by a spectrum analyser (Rhode&Schwarz FSEA 30) with a bandwidth of 10 kHz for a selected setting of the two combined and amplified microwave sources (for details see section 5.2.3).

ened linewidth of $\Delta\nu_{\mathrm{inh}} = (68.67 \pm 2.99)$ kHz, which is in good agreement with the minimal measured linewidth of (68.79 ± 3.30) kHz, see figure A.16b. Concerning the power broadening we extracted $\Delta\nu_{\mathrm{power}}$ to be 86.6 kHz for a microwave input power of 1 mW, which is also in good agreement with the measured linewidth.

The combined and amplified output of the two used microwave sources, see section 5.2.3, is analysed by a spectrum analyser. The resulting power spectrum is shown in figure A.10. Besides the peak at the frequency of the local oscillator, two sets of three peaks each are symmetrically distributed around f_{LO}. These three peaks are separated by a frequency difference of 2.16 MHz corresponding to f_{HFS} and have a slightly power level compared to f_{LO}. Additional power spikes can be observed in the recorded power spectrum of figure A.10. However, these spikes have a power difference of larger than two orders of magnitude compared to the peaks used for the simultaneous spin manipulation of the hyperfine splittings.

Figure A.11a shows the measured shows the measured power level of these three peaks in comparison to the set power value. This measurement indicates that power levels of the two peaks corresponding to $f_{\mathrm{c}} \pm f_{\mathrm{HFS}}$ have are slightly higher than the central peak of f_{c}.

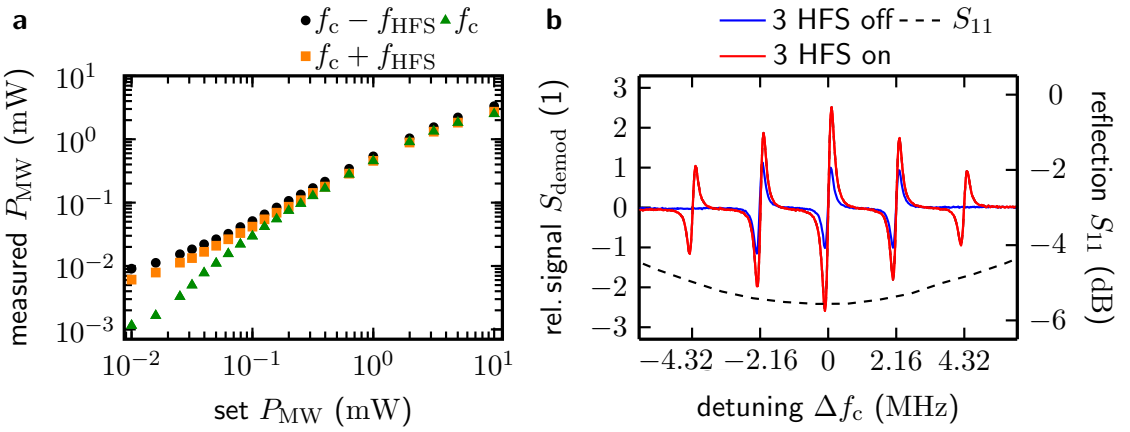

Figure A.11: Spin manipulation and ODMR spectrum for one NV orientation. a) Power level of the applied frequencies for a spin manipulation with simultaneous spin manipulation measured by a spectrum analyser (Rhode&Schwarz FSEA 30). The frequency of the local oscillator f_{LO} was set to 2.92 GHz, the baseband frequency f_{BB} to 30 MHz and a hyperfine splitting frequency f_{HFS} of 2.16 MHz was used. The power levels were measured with a resolution bandwidth of 10 kHz. **b)** Comparison of the recorded ODMR spectra for a '3 HFS on' (red curve) and a '3 HFS off' (blue curve) spin manipulation. The spectra were recorded with a modulation frequency of 10 kHz and a modulation depth of 100 kHz with 1 ms integration time (data points were 200 times averaged). The microwave power was set to 0.91 mW. The measured signals S_{demod} were normalised to the peak amplitude of the central resonance around f_c of the '3 HFS off' measurement. Data of the reflection parameter S_{11} of the double split-ring resonator measured by a network analyser (Hewlett Packard 8753D) is added to this plot (black dotted curve). This figure is reprinted from [32], licensed under CC BY-NC-ND 4.0, https://creativecommons.org/licenses/by-nc-nd/4.0/.

Figure A.11b shows a comparison of the ODMR spectra, which were recorded with and without a simultaneous manipulation of the three hyperfine splittings. In addition, the spectral reflection S_{11} data of the double split-ring resonator is added to this graph.

Figure A.12 shows the dependence of measured slope m and noise σ of the recorded signals S_{demod} on the applied hyperfine splitting frequency f_{HFS} and modulation frequency f_{mod}.

A.5.3 Signal Recording And Processing

[32] As described in the main text of section 5.2.5, we used a balanced detection

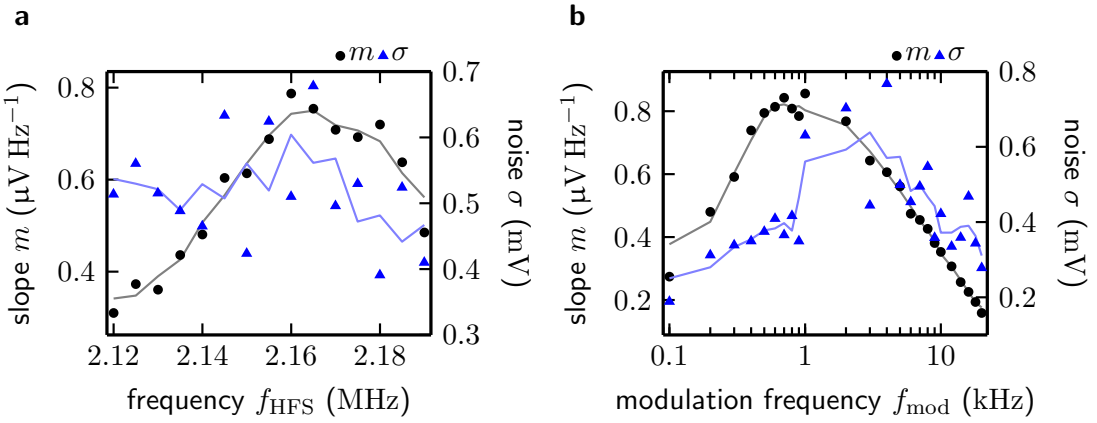

Figure A.12: Slope and noise dependence on the applied hyperfine splitting frequency f_{HFS} and on the modulation frequency f_{mod}. **a)** Slope m (black dots) and noise σ (blue triangles) parameters were extracted from a 6th order polynomial fit to the recorded signals S_{demod} (see main text) for different hyperfine splitting frequencies f_{HFS}. These signals were recorded for an integration time of 20 ms, a modulation depth of 40 kHz, a modulation frequency of 1 kHz and a simultaneous manipulation of the three hyperfine splittings with microwave power of 58 µW. A line of moving mean (of three neighbouring data points) is added to the graphs. **b)** Slope (black dots) and noise (blue triangles) values were analysed based on the used modulation frequency. The data was recorded for an integration time of 20 ms, a modulation depth f_{depth} of 40 kHz and a simultaneous manipulation of the three hyperfine splittings with microwave power of 1.45 mW. Lines of moving mean (of three neighbouring data points) are added to the graphs. This figure is reprinted from [32], licensed under CC BY-NC-ND 4.0, https://creativecommons.org/licenses/by-nc-nd/4.0/.

scheme consisting of two photodiodes and a logarithmic transimpedance amplifier to record both the modulated fluorescence signal and laser light. The output voltage V_{out} of the transimpedance amplifier is given by

$$V_{\mathrm{out}} = GK \log_{10}\left(\frac{I_{\mathrm{sig}} + \Delta I_{\mathrm{sig}}}{I_{\mathrm{ref}}}\right), \tag{A.12}$$

where G is a gain factor with $G = 20.66\,\mathrm{A}^{-1}$, K the logarithmic scale factor with $K = 0.375\,\mathrm{V}$, I_{sig} the measured photocurrent that corresponds to the background of the fluorescence, ΔI_{sig} the change of the photocurrent that corresponds to the drop of the fluorescence under resonant excitation and is caused by the modulation of the microwave frequency. I_{ref} is the measured photocurrent of the reference photodiode.

Applying a Taylor expansion on equation A.12, the output voltage V_{out} can

be approximated to

$$V_{\text{out}} \approx GK \left[\log_{10}\left(\frac{I_{\text{sig}}}{I_{\text{ref}}}\right) + \frac{\Delta I_{\text{sig}}}{I_{\text{sig}}} \frac{1}{\ln(10)} - \frac{1}{2}\left(\frac{\Delta I_{\text{sig}}}{I_{\text{sig}}}\right)^2 \frac{1}{\ln(10)} \right] \tag{A.13}$$

$$\approx GK \log_{10}\left(\frac{\Delta I_{\text{sig}}}{I_{\text{ref}}}\right) + GK \frac{\Delta I_{\text{sig}}}{I_{\text{sig}}} \frac{1}{\ln(10)} + \mathcal{O}(n^2). \tag{A.14}$$

From this equation, the modulated fluorescence signal of the NV centres can be extracted and corresponds to the voltage difference ΔV_{out} with

$$\Delta V_{\text{out}} \approx GK \frac{\Delta I_{\text{sig}}}{I_{\text{sig}}} \frac{1}{\ln(10)}. \tag{A.15}$$

In order to obtain the electron spin resonance of a standard ODMR measurement, we integrated the demodulated signal $S_{\text{demod},i}$ of the i applied microwave frequencies (with $i \in \mathcal{N}$ and step size of Δf_{step}) over the measured spectral range by

$$S_{\text{integ}} = \sum_i \frac{S_{\text{demod},i}}{2 f_{\text{depth}}} \Delta f_{\text{step}}. \tag{A.16}$$

Here, the division factor of two times the modulation depth f_{depth} takes the applied frequency modulation into account. We extracted information about the linewidth $\Delta\nu$ and contrast C of the electron spin resonance by fitting the resulting data S_{integ} with equation 5.2.

With the knowledge of the photocurrent I_{sig} corresponding to the background of the fluorescence, the contrast C of the spin resonance can be expressed by the ratio of ΔI_{sig} and I_{sig}.

A simulative analysis of the common mode suppression and the differential mode of the logarithmic transimpedance amplification circuit using the two photodiodes, PD_{sig} and PD_{ref}, dependent on the applied modulation frequency f_{mod} is shown in figure A.13.

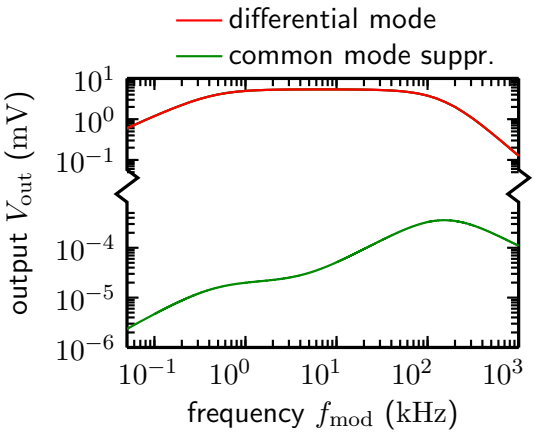

Figure A.13: Simulative analysis of the logarithmic transimpedance amplification circuit. LTspice® was used to model the transimpedance amplification circuit including the utilised logarithmic transimpedance amplifier (Texas Instruments LOG114) and to simulate the output voltage V_{out} depending on the applied modulation frequency f_{mod} and the input currents on the two photodiodes (signal photodiode $\mathrm{PD_{sig}}$ used for detecting the fluorescence light and photodiode $\mathrm{PD_{ref}}$ for referencing the laser light). In order to analyse the performance of the differential mode of this circuit, V_{out} was evaluated for an input current I_{sig} on $\mathrm{PD_{sig}}$ with a sine-wave function (1 mA DC offset, 1 µA amplitude and 100 kHz frequency) and a constant input current I_{ref} (1 mA DC offset) on $\mathrm{PD_{ref}}$ (red curve). The simulated 3 dB cut-off frequencies were at 430 Hz and at 103 kHz. For f_{mod} in the range of (1 to 50) kHz a flat curve of V_{out} with an average value of approximately 5.25 mV was obtained. The drop of the output voltage in the low frequency range around the lower cut-off frequency is mainly due to the implemented high-pass filter, whereas the drop of V_{out} above the upper cut-off frequency is linked to the internal electronic characteristics of the transimpedance amplifier. The response V_{out} was further evaluated for the common mode suppression by applying I_{ref} on $\mathrm{PD_{ref}}$ with a sine-wave function (1 mA DC offset, 1 µA amplitude and 100 kHz frequency), whereas I_{sig} was kept constant with 1 mA DC offset (green curve). This figure is reprinted from [32], licensed under CC BY-NC-ND 4.0, https://creativecommons.org/licenses/by-nc-nd/4.0/.

A.5.4 Experimental Results

An ODMR spectrum of the demodulated signal recorded by the fibre-integrated NV magnetometer is shown in figure 5.7a. Further ODMR spectra with different measurement settings are shown in figure A.14, where the applied offset magnetic field generated by the tapered Helmholtz coil and the applied spin manipulation are varied.

The evaluation of the optimal working point of the NV sensor with respect to the applied measurement parameters, *i.e.* modulation depth and frequency, microwave

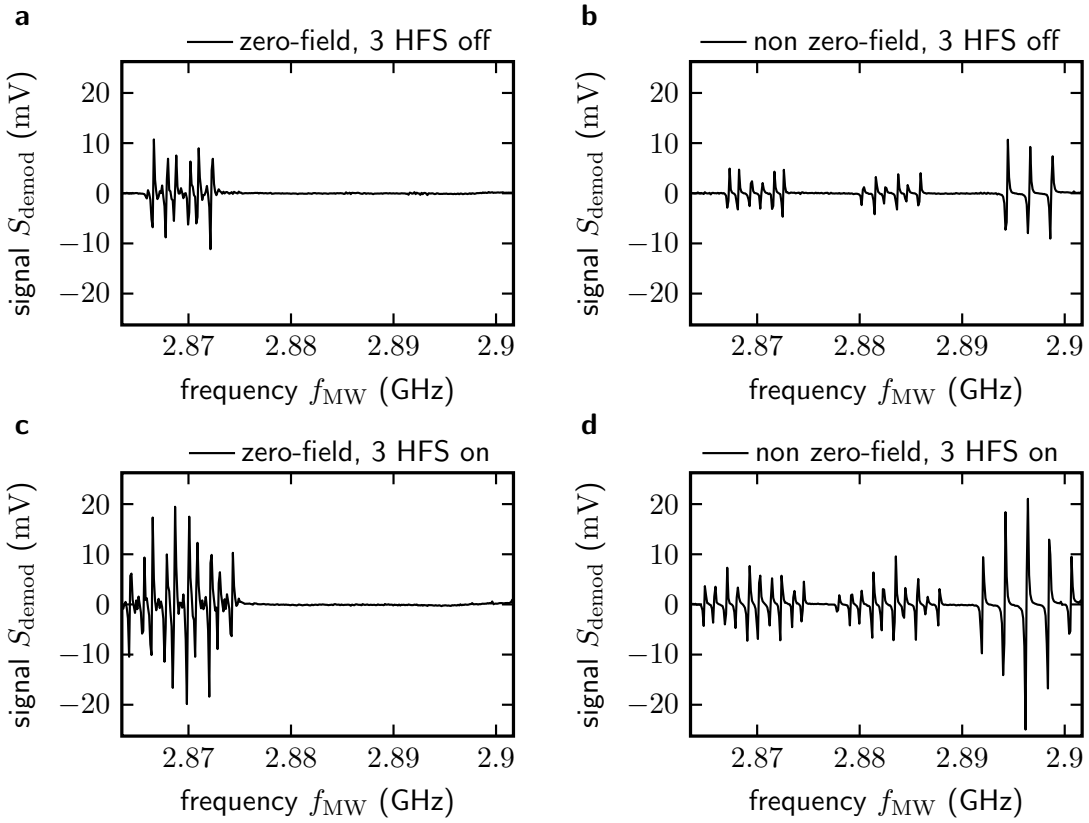

Figure A.14: Optically detected magnetic resonance. Spectra of the demodulated signal S_{demod} were recorded for an integration time of 40 ms, a modulation depth f_{depth} of 100 kHz, a modulation frequency f_{mod} of 5 kHz and a microwave power of 0.91 mW. **a)** shows the recorded spectra at zero-field with an applied microwave power of W for single resonance manipulation. **b)** shows the corresponding recorded spectrum, where an offset magnetic field generated by the pair of tapered Helmholtz coils is applied to the sensor. **c)** is the recorded spectrum for zero-field with simultaneous manipulation of the three hyperfine splittings. **d)** shows the spectrum for non zero-field and simultaneous spin manipulation. The subfigures c) and d) are modified as author from [32], licensed under CC BY-NC-ND 4.0, https://creativecommons.org/licenses/by-nc-nd/4.0/.

power and integration time, is summarised in figure 5.8. As stated in the main text of section 5.3, the laser output power is fixed. The experimental results of the variation study, where a modulation depth f_{depth} of $(5 - 150)$ kHz was applied, are shown figure A.15. Figure A.16 shows the data of the variation study for the applied microwave power P_{MW} in the range of $(0.02 - 8.56)$ mW. Time-dependent influence of noise sources on the sensor performance is analysed by changing the integration time t_{integ} with $(1 - 100)$ ms shown in figure A.17. Results of the variation of the modulation frequency f_{mod} is shown in figure A.18, where f_{mod} is analysed for

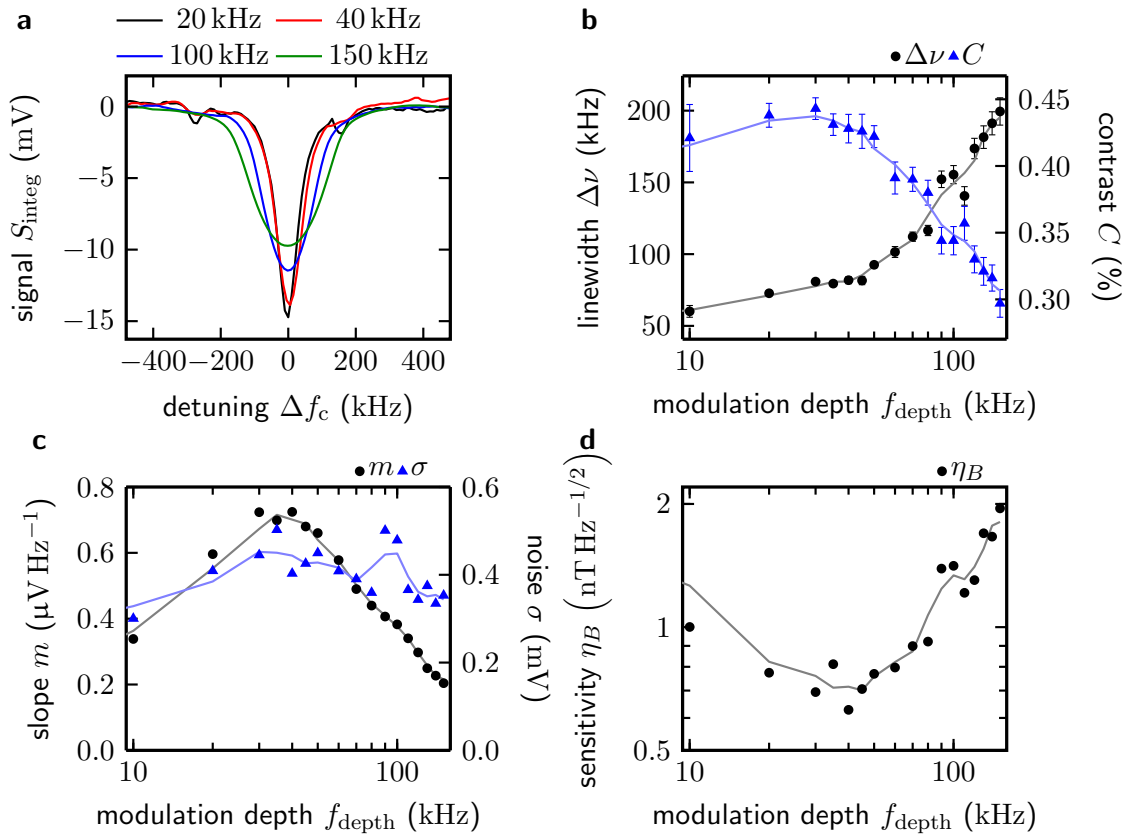

Figure A.15: Variation of the modulation depth to optimise the magnetic field sensitivity. The data of this parameter variation was recorded with an integration time of 1 ms, a modulation frequency of 1 kHz and a simultaneous manipulation of the three hyperfine splittings with a microwave power of 16 µW. Lines of moving mean (of three neighbouring data points) are added to the graphs shown in b) to d). **a)** Plots of the integrated demodulated signal S_{integ} for four applied modulation depths. **b)** Resulting linewidth $\Delta\nu$ (black dots) and contrast C (blue triangles) depending on the modulation depth. **c)** Resulting slope m (black dots) and noise σ (blue triangles) depending on the modulation depth. **d)** Based on the measured slope and noise, the sensitivity η_B (black dots) dependence on the modulation depth is shown. This figure is reprinted from [32], licensed under CC BY-NC-ND 4.0, https://creativecommons.org/licenses/by-nc-nd/4.0/.

$(1 - 30)$ kHz. A detailed description and classification of the measurement results of this parameter study can be found in section 5.3.

> Besides the determination of the magnetic sensitivity by taking the measured parameters of slope and noise of the zero-crossing point (figure 5.8), we further evaluated the sensor performance under the application of an additional mag- [32]

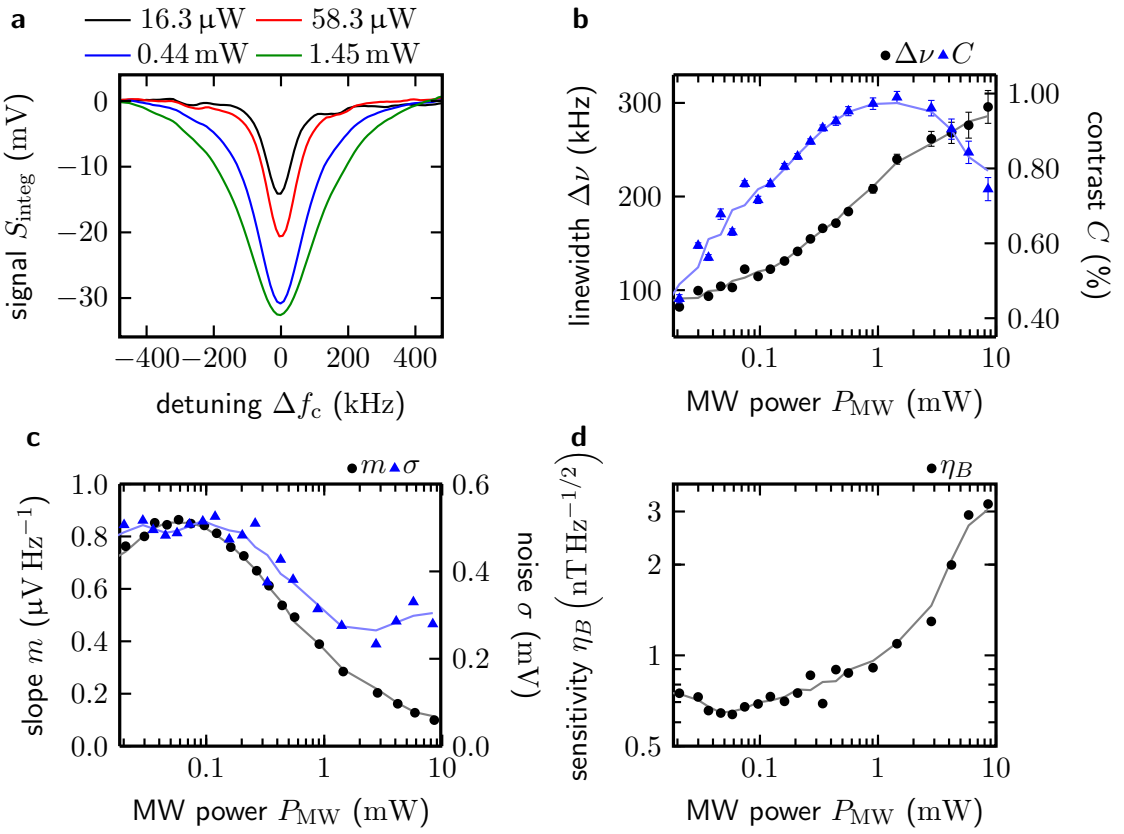

Figure A.16: Variation of the microwave power to optimise the magnetic field sensitivity. The data of this parameter variation was recorded with an integration time of 1 ms, a modulation frequency of 1 kHz, 40 kHz modulation depth and a simultaneous manipulation of the three hyperfine splittings. Lines of moving mean (of three neighbouring data points) are added to the graphs shown in b) to d). **a)** Plots of the integrated demodulated signal S_{integ} for four applied microwave powers. **b)** Resulting linewidth $\Delta\nu$ (black dots) and contrast C (blue triangles) depending on the microwave power. **c)** Resulting slope m (black dots) and noise σ (blue triangles) depending on the microwave power. **d)** Based on the measured slope and noise, the sensitivity η_B (black dots) dependence on the microwave power is shown. This figure is reprinted from [32], licensed under CC BY-NC-ND 4.0, https://creativecommons.org/licenses/by-nc-nd/4.0/.

netic field B_{test}. A copper wire was wound around the pair of Helmholtz coils and we applied a DC field to the wire by an arbitrary waveform generator (Agilent 33220A).

The generated flux density at the centre of the Helmholtz coil pair (with a coil radius r and N turns on each side) corresponds to the superposition of two circular currents and can be calculated according to Biot-Savart's law by [333]

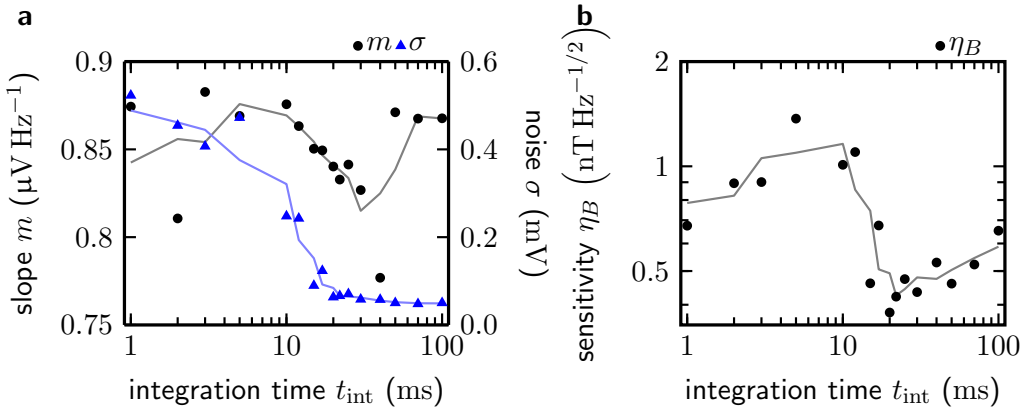

Figure A.17: Variation of the integration time to optimise the magnetic field sensitivity. The data of this parameter variation was recorded with a modulation frequency of 1 kHz, a modulation depth of 40 kHz and a simultaneous manipulation of the three hyperfine splittings with a microwave power of 58 µW. Lines of moving mean (of three neighbouring data points) are added to the graphs shown in a) and b). **a)** Resulting slope m (black dots) and noise σ (blue triangles) depending on the integration time. **b)** Based on the measured slope and noise, the sensitivity η_B (black dots) dependence on the integration time is shown. This figure is reprinted from [32], licensed under CC BY-NC-ND 4.0, https://creativecommons.org/licenses/by-nc-nd/4.0/.

$$B_{\mathrm{test}} = \frac{8}{\sqrt{125}} \frac{\mu_0 N}{r} \frac{U}{R}, \tag{A.17}$$

where μ_0 is the vacuum permeability with $\mu_0 = 4\pi \times 10^{-7}\,\mathrm{N\,A^{-2}}$, U the applied voltage and R the resistance of the coil wires.

For a generated output with an amplitude of 10 mV and a resistance of 229.8 Ω, we expected a magnetic field of $B_{\mathrm{test}} \approx 6.52$ nT at the centre of the Helmholtz coils.

To experimentally verify this induced magnetic field, we applied a DC field with voltage of 500 mV and recorded the ODMR spectrum. A shift of the resonance frequency of 9.34 kHz was observed for the NV orientation with the largest splitting, which was selected for this analysis. This resonance shift corresponds to an additional magnetic field of approximately 333 nT. Here, we neglected temperature effects as the measurements have been carried out in close succession. Assuming a linear scaling of the field strength and the applied voltage, the projected strength of the test field would be 6.66 nT on the selected NV orientation for 10 mV. The calculated value from equation A.17 is in good

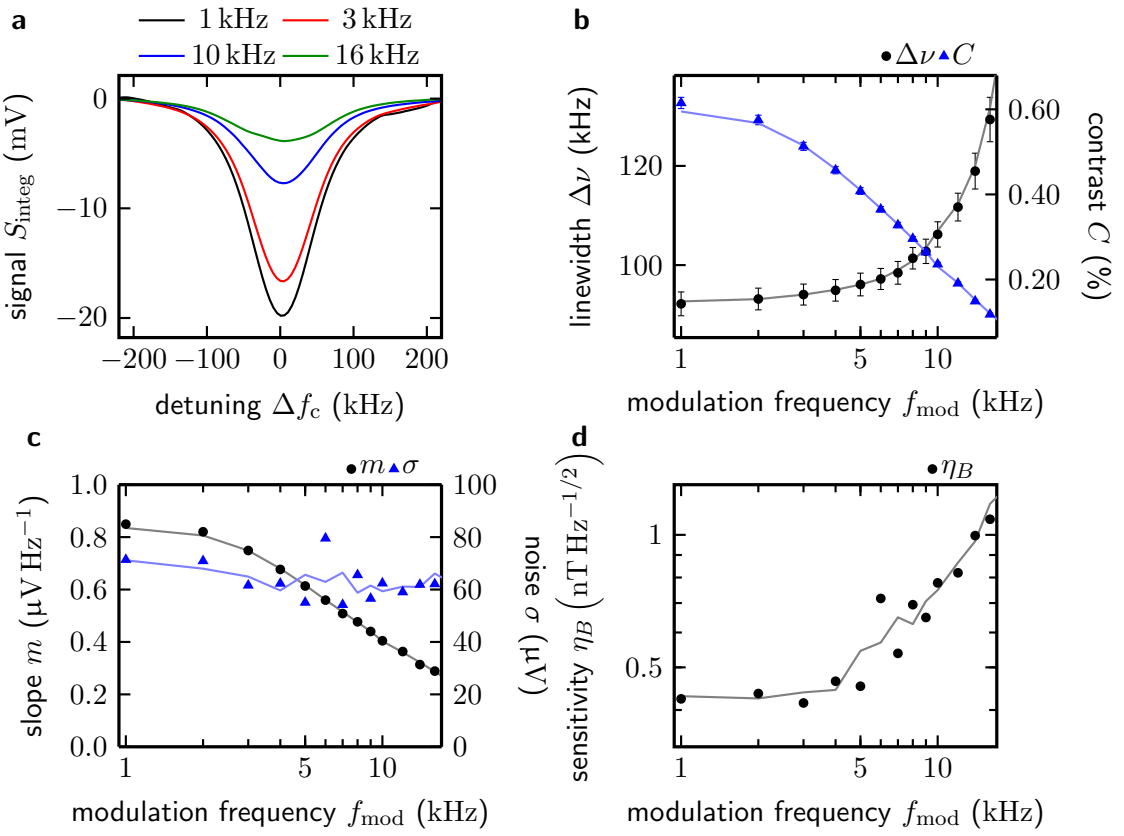

Figure A.18: Variation of the modulation frequency to optimise the magnetic field sensitivity. The data of this parameter variation was recorded with an integration time of 20 ms, a modulation depth of 40 kHz and a simultaneous manipulation of the three hyperfine splittings with a microwave power of 58 µW. Lines of moving mean (of three neighbouring data points) are added to the graphs shown in b) to d). **a)** Plots of the integrated demodulated signal S_{integ} for four applied modulation frequencies. **b)** Resulting linewidth $\Delta\nu$ (black dots) and contrast C (blue triangles) depending on the modulation depth. **c)** Resulting slope m (black dots) and noise σ (blue triangles) depending on the modulation depth. **d)** Based on the measured slope and noise, the sensitivity η_B (black dots) dependence on the modulation frequency is shown. This figure is reprinted from [32], licensed under CC BY-NC-ND 4.0, https://creativecommons.org/licenses/by-nc-nd/4.0/.

agreement with the experimentally verified frequency shift observed in the ODMR measurement.

A.5.5 Laser Power Stability

[32] We used the following simplified model to assess temperature fluctuations of the diamond induced by intensity fluctuations of the laser, see figure A.19. These

temperature fluctuations possibly lead to the observed long term variations of the magnetic field depicted in the Allan deviation in figure 5.9b.

The following ordinary differential equation was used to evaluate laser induced temperature fluctuations

$$C_{\mathrm{th}} \frac{\mathrm{d}T}{\mathrm{d}t} = P_{\mathrm{heat}} - (T - T_0)\,\lambda^*, \tag{A.18}$$

where T is the temperature of the diamond and C_{th} its thermal capacity using the following quantities: $C_{\mathrm{th}} = C^*_{\mathrm{th}}\rho V = 0.57\,\mu\mathrm{K\,J^{-1}}$, $C^*_{\mathrm{th}} = 0.502\,\mathrm{J\,kg^{-1}\,K}$, $\rho = 3520\,\mathrm{kg\,m^{-3}}$, $V = (0.8 \times 0.8 \times 0.5)\,\mathrm{mm^3}$. P_{heat} is the laser induced heating power, which we model with $P_{\mathrm{heat}} = P_0\,(1 + 10^{-4}\sin(2\pi f t))$ and $P_0 = 5\,\mathrm{mW}$. The relative modulation of 10^{-4} corresponds to the observed relative power fluctuation of the laser, see figure A.19b. T_0 is the constant temperature of the reservoir. λ^* is the thermal resistance of the glue connecting the diamond to the GRIN lens. We assume a thermal conductivity of the glue of $\lambda = 0.5\,\mathrm{W\,m^{-1}\,K^{-1}}$, a thickness of the glue of $d = 50\,\mu\mathrm{m}$ and an interface A of $(0.8 \times 0.8)\,\mathrm{mm^2}$ corresponding to the footprint of the diamond: $\lambda^* = \lambda A/d \approx 6\,\mathrm{mW\,K^{-1}}$. The AC share of the solution of the ordinary differential equation is given by

$$T_{\mathrm{AC}} = \frac{P_0 \cdot 10^{-4}}{C_{\mathrm{th}}\,(2\pi f)^2 + \frac{\lambda^{*2}}{C}} \left(\frac{\lambda^*}{C_{\mathrm{th}}} \sin(2\pi f t) - 2\pi f \cos(2\pi f t) \right) \tag{A.19}$$

$$\approx \frac{P_0 \cdot 10^{-4}}{(2\pi f C_{\mathrm{th}})^2 + \lambda^{*2}} \lambda^* \sin(2\pi f t). \tag{A.20}$$

The magnitude of the cosine term is negligible compared to the sinus term for $f \approx 0.1\,\mathrm{Hz}$. Consequently, the expected amplitude of the temperature fluctuation occurring at a frequency of 0.1 Hz is $\Delta T = \frac{P_0 \cdot 10^{-4}}{(2\pi f C_{\mathrm{th}})^2 + \lambda^{*2}} \approx 0.16\,\mathrm{mK}$. This temperature variation leads to a shift of the zero field splitting and thus to a variation of the detected magnetic field which corresponds to $\Delta B = \beta/\tilde{\gamma}_{\mathrm{NV}} \Delta T \approx 0.43\,\mathrm{pT}$, with the temperature dependence of the zero-field splitting $\beta \approx 75\,\mathrm{kHz\,K^{-1}}$ [195] and the gyromagnetic ratio $\tilde{\gamma}_{\mathrm{NV}} \approx 28.024\,\mathrm{MHz\,T^{-1}}$ [204]. This simplified model can thus explain the observed temperature drift for $t > 1\,\mathrm{s}$ in figure A.19b.

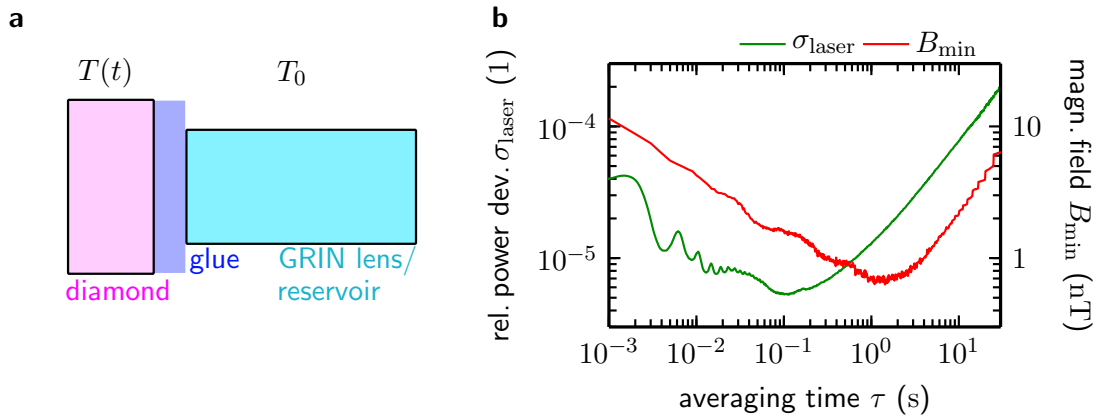

Figure A.19: Analysis of the laser stability on the performance of the magnetic field detection. **a)** Schematic of the simplified model to assess temperature fluctuations of the diamond induced by intensity fluctuations of the laser. **b)** Laser stability in terms of relative power fluctuations σ_{laser} was derived by calculating the Allan deviation of a recorded time trace of the direct laser power output. In an analogous manner, the minimum detectable magnetic field B_{min} by the NV magnetometer was analysed for a magnetically sensitive case (without using any magnetic shielding). This data corresponds to the graph shown in figure 5.9b of the main text. This figure is reprinted from [32], licensed under CC BY-NC-ND 4.0, https://creativecommons.org/licenses/by-nc-nd/4.0/.

A.5.6 Power Consumption

The total power consumption of the fibre-based NV sensor sumps to roughly 5.1 W [32], which is summarised in table A.4. Main contributions are linked to the following functional parts of the NV sensor: the optical excitation by the laser source, the spin manipulation using microwaves including amplification, the electrical power for the offset magnetic field provided by the pair of Helmholtz coils, for the balanced detection circuit, for the RedPitaya control and ADC module.

Table A.6: Power consumption of the fibre-based NV sensor.

Component	Power consumption (mW)
Laser	2.35×10^{1}
Microwaves total	5.80×10^{-2}
Helmholtz coils	1.30×10^{3}
Photodetection circuit	7.20×10^{1}
RedPitaya module	3.70×10^{3}

A.6 Fluorescence Lifetime-Based NV Magnetometry

A.6.1 Experimental Setup

The fluorescence lifetime experiments from chapter 6 were performed on a confocal microscope setup. A schematic of the main components of the setup can be found in figure 6.1.

For the optical excitation of the NV centres, we used a 531 nm wavelength laser (PicoQuant LDH-D-FA-530L). Using the laser driver module (PicoQuant PDL 800-D), this laser generates pulses with 100 ps length. As the output of the laser was fibre-coupled, a fibre collimator (Thorlabs F220APC-532) outcoupled the light. Two broadband mirrors (Thorlabs PF10-03-P01) helped to adjust the height and angle of the outcoming laser beam, which passed then a $\lambda/2$-wave plate (Thorlabs WPH10M-532). This optical element enabled adjustments of the light polarisation to align the light polarisation with the orientation of the optical dipoles of the selected NV centre such that the emitted fluorescence emission is maximised. Two lenses with focus lengths of 50 mm (Thorlabs AC254-050-A-ML) and of 300 mm (Thorlabs AC254-300-A-ML) followed the optical path, which were used to further modify the shape of the laser beam. An iris (Thorlabs ID15/M) behind the lens blocked any stray light. Two additional mirrors (Thorlabs PF10-03-P01) guided then the beam on the optical table towards a beam-sampler (Thorlabs WG12012-B). This glass contains an anti-reflection coating for wavelengths of (650 to 1050) nm on its surfaces making it transparent for the red fluorescence, but reflecting *e.g.* the excitation light. Due to the arrangement of the optical elements, the laser light was then reflected towards an immersion oil objective objective (Olympus UPLXAPO40XO) with a working distance of 0.13 mm, a numerical aperture of 1.40 and a fourtyfold magnification. The objective fulfilled two tasks to run single NV centre experiments. First, it focused the excitation beam down to the diamond sample providing the required excitation intensity. Second, the objective collected the photons emitted by the illuminated NV centre and guided this red fluorescence towards the beam-sampler.

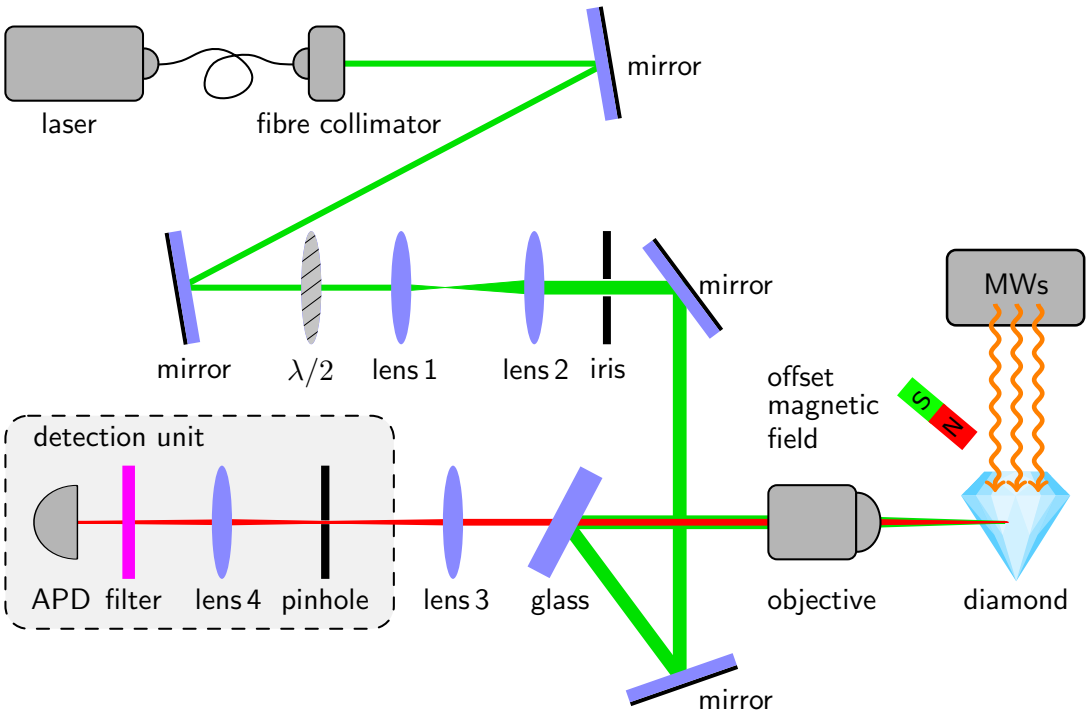

Figure A.20: Schematic of the confocal microscope setup. Laser light from a pulsed laser module was coupled out by a fibre collimator. Optical elements, such as mirrors $\lambda/2$-plate and lenses guided the laser beam towards a beam-sampler. This glass had the property of reflecting light in the green wavelength range, whereas it was transparent for light with wavelengths in range of $(650 \text{ to } 1050)\,\mathrm{nm}$. From the beam-sampler, the excitation light was guided towards an immersion oil objective, which focussed the laser beam onto the diamond. The same objective collected the emitted fluorescence from the selected NV centre and passed them to the beam-sampler. An APD counted the arriving fluorescence photons and transferred the measured signal to a fast counting device after having passed two lenses, a pinhole and an optical filter. To minimise contributions of stray light to the measured signal, the 'detection unit' was surrounded by a light shielded box. Besides the optical elements, the setup further contained microwave equipment including a $20\,\mu\mathrm{m}$ thin copper wire on top of diamond's surface used for the spin manipulation as well as a permanent magnet mounted on a rotatable stage for providing an offset magnetic field.

After having passed the beam-sampling glass, a lens (Thorlabs AC254-075-B-ML) with focus length of 75 mm focused the fluorescence light onto a 25 µm gold-plated copper pinhole (Thorlabs P25C). This pinhole enabled only light from the focal plane to pass through this element and suppressed all other light rays. To minimise the influence of stray light on the detection of the fluorescence light, we placed the pinhole and the following optical elements in a stray light shielded box, labelled as

'detection unit' in figure A.20. After having passed the pinhole, the fluorescence light was then focused by a lens (Thorlabs AC508-100-B-ML) with focus length of 100 mm onto an avalanche photodiode (Excelitas SPCM-AQRH-13) used to detect the incoming photons. Additionally, a 590 nm longpass filter (Chroma Technology ET590LP) was placed in front of the APD in the optical path to filter out any laser light.

Regarding the mounting of the diamond, the sample was glued with a superglue (ergo 5950) on a self-constructed PCB sample holder. This sample holder was screwed on a 3D piezo stage (nPoint NPXY200Z100-271), which was located (along the optical path) above the immersion oil objective, see text above. This piezo stage enabled lateral scans with an area of $(200 \times 200)\,\mathrm{mm}^2$ and depths of 100 µm and was controlled by a 3D piezo controller (Physik Instrumente E-727.3CDA). It was therefore possible to scan large areas of the diamond looking for single NV centres as well as to perform depth scan changing the focal point inside the diamond, see figure 6.2.

Besides the optical pumping and the detection of the emitted fluorescence, equipment for the spin manipulation was further set up. A copper wire (GoodFellow CU005171) with 20 µm diameter was stretched over the diamond and soldered to specially provided soldering slots on the sample holder PCB. Microwave pluses were generated by an AWG (Tektronix AWG70001A), additionally amplified by a 16 W high power amplifier (Mini-Cirucits ZHL-16W-43-S+) and then passed to the copper wire to provide an oscillating field in the proximity of the diamond. For the transport of the microwave pluses, we used various radio frequency suitable cables. A small permanent magnet of cubic size was mounted on a self-constructed rotatable stage in order to provide a bias magnetic field aligned to the axis of the selected NV centre.

Controlling the experiments, we used the AWG as the 'master clock' to trigger both the laser and the data acquisition unit composed of the APD and a fast counting device (FAST ComTec MCS6A). A personal computer (PC) was used to communicate with the AWG in terms of measurement settings and store and analyse the recorded data.

B Abbreviations And Symbols

B.1 List Of Abbreviations

The following list contains the used abbreviations of this thesis:

2D, 3D	**two-d**imensional, **three-d**imensional
AC	**A**lternating **C**urrent
ADC	**A**nalgoue-to-**D**igital **C**onverter
AI	**A**rtificial **I**ntelligence
AMR	**A**nisotropic **M**angeto**R**esistance
APD	**A**valanche **P**hoto**D**iode
arb. u.	**arb**itray **u**nit
AWG	**A**rbitrary **W**ave **G**enerator
C	**C**arbon
CAD	**C**omputer-**A**ided **D**esign
CMOS	**C**omplementary **M**etal-**O**xide-**S**emidconductor
CVD	**C**hemical **V**apour **D**eposition
CW-ODMR	**C**ontinous **W**ave-**O**ptically **D**etected **M**agnetic **R**esonance
DBR	**D**istributed **B**ragg **R**eflector
DC	**D**irect **C**urrent
e. g.	**e**xempli **g**ratia (Latin: for example)
ESR	**E**lectron **S**pin **R**esonance
et al.	**e**t **a**lia (Latin: and others)
EU	**E**uropean **U**nion
fcc	**f**ace-**c**entered-**c**ubic
FWHM	**F**ull **W**idth at **H**alf **M**aximum

GeV	**G**ermanium **V**acancy
GMR	**G**iant **M**angeto**R**esistance
GRIN	**G**radient **R**efractive **IN**dex
HFS	**H**yper**F**ine **S**plitting
HPHT	**H**igh **P**ressure, **H**igh **T**emperature
i. a.	**i**nter **a**lia (Latin: among others)
i. e.	**i**d **e**st (Latin: that)
IP	**I**ntellectual **P**roperty
ISC	**I**nter**S**ystem **C**rossing
LAC	**L**evel **A**nti-**C**rossing
LED	**L**ight-**E**mitting **D**iode
LP	**L**ong**P**ass
MCG	**M**agneto**C**ardio**G**raphy
MEG	**M**agneto**E**ncephalo**G**raphy
MNG	**M**agneto**N**euro**G**raphy
MW	**M**icro**W**ave
N	**N**itrogen
N/A	**N**ot **A**vailable
NDE	**N**on-**D**estructive **E**valuation
NMR	**N**uclear **M**agnetic **R**esonance
no.	**n**umer**o** (Latin: number)
NV	**N**itrogen-**V**acancy
ODMR	**O**ptically **D**etected **M**agnetic **R**esonance
OPM	**O**ptically **P**umped **M**agnetometer
PC	**P**ersonal **C**omputer
PCB	**P**rinted **C**ircuit **B**oard
PD	**P**hoto**D**iode
PDMS	**P**oly**D**i**M**ethyl**S**iloxane
pH	**p**otential of **H**ydrogen
RF	**R**adio **F**requency
SEM	**S**canning **E**lectron **M**icroscope
SERF	**Spin**-**E**xchange **R**elaxation **F**ree

SiV	**Si**licon **V**acancy
SM	**S**ingle-**M**ode
SMA	**S**ub**M**iniature version **A**
SNR	**S**ignal-to-**N**oise **R**atio
SnV	Tin **V**acancy
SP	**S**hort**P**ass
SQUID	**S**uperconducting **QU**antum **I**nterference **D**evice
TIR	**T**otal **I**nternal **R**eflection
TMR	**T**unnel **M**angeto**R**esistance
USA	**U**nited **S**tates of **A**merica
ZFS	**Z**ero-**F**ield **S**plitting
ZPL	**Z**ero **P**honon **L**ine

B.2 List Of Symbols

The following list contains the frequently used symbols of this thesis:

A	amplitude factor linked to the contrast
$\mathbb{A}$	hyperfine interaction tensor
A_0	spin population coefficient
$A_{\mathrm{gs}}^{\parallel}$	parallel hyperfine coupling constant
$A_{\mathrm{gs}}^{\perp}$	perpendicular hyperfine coupling constant
A_{ref}	amplitude fitting parameter
B	magnetic field strength
$\boldsymbol{B}$	magnetic field vector
$\boldsymbol{B_0}$	static bias magnetic field vector
$\boldsymbol{B_1}$	spin manipulation field vector
B_{NV}	magnetic field strength projected on an NV axis
β	temperature dependence of the zero-field splitting
C	contrast

d	distance
D	axial zero-field splitting parameter
$\mathbb{D}$	electron interaction tensor
D_{es}	zero-field splitting in the excited state
D_{gs}	zero-field splitting in the ground state
d_{laser}	laser beam diameter
δB	magnetic field noise
δB_{min}	minimal detectable magnetic field
$\Delta\nu$	linewidth (full width at half maximum)
$\Delta\nu_{\mathrm{inh}}$	inhomogeneously broadened linewidth
$\Delta\nu_{\mathrm{power}}$	power broadened linewidth
ΔT	temperature difference
E	axial zero-field splitting parameter
E_{ph}	photon energy
ε	residuum
η_B	magnetic field sensitivity
η_{PSN}	photon shot-noise limited magnetic field sensitivity
f	frequency
$\mathcal{F}$	function of the lineshape
$f_{\pm}$	resonance frequency
f_{BB}	baseband frequency
f_{c}	mean mixed frequency
f_{depth}	modulation depth
f_{HFS}	hyperfine splitting frequency
f_{LO}	local oscillator frequency
f_{mod}	modulation frequency
f_{MW}	microwave frequency
f_{R}	Rabi frequency in Hz
G	amplification / gain factor
g_{e}	Landé-factor of an electron spin
γ_{n}	gyromagnetic ratio of the nuclear spin
$\tilde{\gamma}_{\mathrm{n}}$	reduced gyromagnetic ratio of the nuclear spin

γ_{NV}	gyromagnetic ratio of the electron spin
$\tilde{\gamma}_{\mathrm{NV}}$	reduced gyromagnetic ratio of the electron spin
Γ_{P}	re-polarisation rate
h	Planck constant
$\hbar$	reduced Planck constant
$\mathcal{H}$	Hamiltonian
I	nuclear spin
$\mathcal{I}$	intensity
$\hat{\boldsymbol{I}}$	nuclear spin operator
I_{fl}	fluorescence intensity
I_{opt}	optical power density
l_{abs}	absorption length
λ	wavelength
m	slope
m_{I}	nuclear spin quantum number
m_{s}	electron spin quantum number
μ_{B}	Bohr magneton
n	refractive index
NA	numerical aperture
n_{dia}	diamond refractive index
[N]	concentration of nitrogen
[NV^{-}]	concentration of NV centres
ν	frequency
Ω_{R}	Rabi frequency
$\mathcal{P}_{\mathcal{F}}$	numerical parameter related to the specific resonance profile
P_{MW}	microwave power
P_{opt}	optical power
Q	nuclear quadrupole splitting parameter
$\mathbb{Q}$	quadrupole interaction tensor
R	responsivity
$\mathcal{R}$	fluorescence rate
S	electron spin

S	signal
$\hat{\boldsymbol{S}}$	electron spin operator
S_{11}	reflection parameter
S_{demod}	demodulated signal output
S_{fl}	fluorescence signal
S_{integ}	integrated demodulated signal output
σ	absorption cross-section
σ_{adev}	Allan deviation
t	measurement time
T	temperature
T_1	spin-lattice relaxation time
T_2	homogeneous decoherence time
T_2^*	inhomogeneously broadened transverse spin relaxation time
T_{dia}	diamond temperature
t_{int}	integration time
t_{m}	measurement time
τ	excited-state lifetime
θ	overall contrast constant
θ_{TIR}	TIR angle
ξ_{col}	collection efficiency
ξ_{det}	detection efficiency
z_{dia}	diamond thickness

Bibliography

[1] J. Jezný and M. Čurilla, *Position measurement with Hall effect sensors*, American Journal of Mechanical Engineering 1, 231 (2013),
URL: https://dx.doi.org/10.12691/ajme-1-7-16

[2] A. Ajbl, M. Pastre, and M. Kayal, *A Fully Integrated Hall Sensor Microsystem for Contactless Current Measurement*, IEEE Sensors Journal 13, 2271 (2013),
URL: https://dx.doi.org/10.1109/JSEN.2013.2251971

[3] G. Boero, M. Demierre, P.-A. Besse, and R. Popovic, *Micro-Hall devices: performance, technologies and applications*, Sensors and Actuators A: Physical 106, 314 (2003),
URL: https://dx.doi.org/10.1016/S0924-4247(03)00192-4

[4] F. Primdahl, *The fluxgate mechanism, part I: The gating curves of parallel and orthogonal fluxgates*, IEEE Transactions on Magnetics 6, 376 (1970),
URL: https://dx.doi.org/10.1109/TMAG.1970.1066795

[5] P. M. Vetoshko, N. A. Gusev, D. A. Chepurnova, E. V. Samoilova, I. I. Syvorotka, I. M. Syvorotka, A. K. Zvezdin, A. A. Korotaeva, and V. I. Belotelov, *Flux-gate magnetic field sensor based on yttrium iron garnet films for magnetocardiography investigations*, Technical Physics Letters 42, 860 (2016),
URL: https://dx.doi.org/10.1134/S1063785016080289

[6] L. Schulz, P. Heinisch, and I. Richter, *Calibration of Off-the-Shelf Anisotropic Magnetoresistance Magnetometers*, Sensors 19 (2019),
URL: https://dx.doi.org/10.3390/s19081850

[7] V. S. Luong, *High-Resolution Pinning GMR Sensors for Extremely Low Frequencies Powered by a Simple Alternating Current-Biased Scheme*, Journal of

Superconductivity and Novel Magnetism (2020),
URL: https://dx.doi.org/10.1007/s10948-020-05695-9

[8] D. Robbes, *Highly sensitive magnetometers - a review*, Sensors and Actuators A: Physical 129, 86 (2006),
URL: https://dx.doi.org/10.1016/j.sna.2005.11.023

[9] M. Wang, Y. Wang, L. Peng, and C. Ye, *Measurement of Triaxial Magnetocardiography Using High Sensitivity Tunnel Magnetoresistance Sensor*, IEEE Sensors Journal 19, 9610 (2019),
URL: https://dx.doi.org/10.1109/JSEN.2019.2927086

[10] S. Yuasa and D. D. Djayaprawira, *Giant tunnel magnetoresistance in magnetic tunnel junctions with a crystalline MgO(0 0 1) barrier*, Journal of Physics D: Applied Physics 40, R337 (2007),
URL: https://dx.doi.org/10.1088/0022-3727/40/21/r01

[11] S. Tumanski, *Induction coil sensors: a review*, Measurement Science and Technology 18, R31 (2007),
URL: https://dx.doi.org/10.1088/0957-0233/18/3/R01

[12] D. Drung, C. Abmann, J. Beyer, A. Kirste, M. Peters, F. Ruede, and T. Schurig, *Highly sensitive and easy-to-use SQUID sensors*, IEEE Transactions on Applied Superconductivity 17, 699 (2007),
URL: https://dx.doi.org/10.1109/TASC.2007.897403

[13] J. Wang, K. Yang, R. Yang, X. Kong, and W. Chen, *SQUID Gradiometer Module for Fetal Magnetocardiography Measurements Inside a Thin Magnetically Shielded Room*, IEEE Transactions on Applied Superconductivity 29, 1 (2019),
URL: https://dx.doi.org/10.1109/TASC.2018.2889865

[14] R. L. Fagaly, *Superconducting quantum interference device instruments and applications*, Review of Scientific Instruments 77, 101101 (2006),
URL: https://dx.doi.org/10.1063/1.2354545

[15] D. Budker and M. Romalis, *Optical magnetometry*, Nature Physics 3, 227 (2007),
URL: https://dx.doi.org/10.1038/nphys566

[16] S. Knappe, O. Alem, D. Sheng, and J. Kitching, *Microfabricated Optically-Pumped Magnetometers for Biomagnetic Applications*, Journal of Physics: Conference Series 723, 012055 (2016),
URL: https://dx.doi.org/10.1088/1742-6596/723/1/012055

[17] J. Allred, R. Lyman, T. Kornack, and M. Romalis, *High-sensitivity atomic magnetometer unaffected by spin-exchange relaxation*, Physical Review Letters 89, 1308011 (2002),
URL: https://dx.doi.org/10.1103/PhysRevLett.89.130801

[18] I. K. Kominis, T. W. Kornack, J. C. Allred, and M. V. Romalis, *A sub-femtotesla multichannel atomic magnetometer*, Nature 422, 596 (2003),
URL: https://dx.doi.org/10.1038/nature01484

[19] E. Boto, S. S. Meyer, V. Shah, O. Alem, S. Knappe, P. Kruger, T. M. Fromhold, M. Lim, P. M. Glover, P. G. Morris, R. Bowtell, G. R. Barnes, and M. J. Brookes, *A new generation of magnetoencephalography: Room temperature measurements using optically-pumped magnetometers*, NeuroImage 149, 404 (2017),
URL: https://dx.doi.org/10.1016/j.neuroimage.2017.01.034

[20] M. Karadas, A. M. Wojciechowski, A. Huck, N. O. Dalby, U. L. Andersen, and A. Thielscher, *Feasibility and resolution limits of opto-magnetic imaging of neural network activity in brain slices using color centers in diamond*, Scientific Reports 8, 4503 (2018),
URL: https://dx.doi.org/10.1038/s41598-018-22793-w

[21] R. Zhang, W. Xiao, Y. Ding, Y. Feng, X. Peng, L. Shen, C. Sun, T. Wu, Y. Wu, Y. Yang, Z. Zheng, X. Zhang, J. Chen, and H. Guo, *Recording brain activities in unshielded Earth's field with optically pumped atomic magneto-*

meters, Science Advances 6 (2020),
URL: https://dx.doi.org/10.1126/sciadv.aba8792

[22] T. Wolf, P. Neumann, K. Nakamura, H. Sumiya, T. Ohshima, J. Isoya, and J. Wrachtrup, *Subpicotesla Diamond Magnetometry*, Physical Review X 5, 041001 (2015),
URL: https://dx.doi.org/10.1103/PhysRevX.5.041001

[23] J. F. Barry, M. J. Turner, J. M. Schloss, D. R. Glenn, Y. Song, M. D. Lukin, H. Park, and R. L. Walsworth, *Optical magnetic detection of single-neuron action potentials using quantum defects in diamond*, Proceedings of the National Academy of Sciences 113, 14133 (2016),
URL: https://dx.doi.org/10.1073/pnas.1601513113

[24] Y. Masuyama, K. Mizuno, H. Ozawa, H. Ishiwata, Y. Hatano, T. Ohshima, T. Iwasaki, and M. Hatano, *Extending coherence time of macro-scale diamond magnetometer by dynamical decoupling with coplanar waveguide resonator*, Review of Scientific Instruments 89, 125007 (2018),
URL: https://dx.doi.org/10.1063/1.5047078

[25] I. Fescenko, A. Jarmola, I. Savukov, P. Kehayias, J. Smits, J. Damron, N. Ristoff, N. Mosavian, and V. M. Acosta, *Diamond magnetometer enhanced by ferrite flux concentrators*, Physical Review Research 2, 023394 (2020),
URL: https://dx.doi.org/10.1103/PhysRevResearch.2.023394

[26] G. Chatzidrosos, A. Wickenbrock, L. Bougas, N. Leefer, T. Wu, K. Jensen, Y. Dumeige, and D. Budker, *Miniature Cavity-Enhanced Diamond Magnetometer*, Physical Review Applied 8, 044019 (2017),
URL: https://dx.doi.org/10.1103/PhysRevApplied.8.044019

[27] B. Zhao, H. Guo, R. Zhao, F. Du, Z. Li, L. Wang, D. Wu, Y. Chen, J. Tang, and J. Liu, *High-sensitivity three-axis vector magnetometry using the electron spin ensembles in single diamond*, IEEE Magnetics Letters 10, 1 (2019),
URL: https://dx.doi.org/10.1109/LMAG.2019.2891616

[28] J. L. Webb, J. D. Clement, L. Troise, S. Ahmadi, G. J. Johansen, A. Huck, and U. L. Andersen, *Nanotesla sensitivity magnetic field sensing using a compact diamond nitrogen-vacancy magnetometer*, Applied Physics Letters 114, 231103 (2019),
URL: https://dx.doi.org/10.1063/1.5095241

[29] D. Zheng, Z. Ma, W. Guo, L. Niu, J. Wang, X. Chai, Y. Li, Y. Sugawara, C. Yu, Y. Shi, X. Zhang, J. Tang, H. Guo, and J. Liu, *A hand-held magnetometer based on an ensemble of nitrogen-vacancy centers in diamond*, Journal of Physics D: Applied Physics 53, 155004 (2020),
URL: https://dx.doi.org/10.1088/1361-6463/ab6af2

[30] R. Patel, L. Zhou, A. Frangeskou, G. Stimpson, B. Breeze, A. Nikitin, M. Dale, E. Nichols, W. Thornley, B. Green, M. Newton, A. Edmonds, M. Markham, D. Twitchen, and G. Morley, *Subnanotesla Magnetometry with a Fiber-Coupled Diamond Sensor*, Physical Review Applied 14, 044058 (2020),
URL: https://dx.doi.org/10.1103/PhysRevApplied.14.044058

[31] C. Zhang, F. Shagieva, M. Widmann, M. Kübler, V. Vorobyov, P. Kapitanova, E. Nenasheva, R. Corkill, O. Rhrle, K. Nakamura, H. Sumiya, S. Onoda, J. Isoya, and J. Wrachtrup, *Diamond Magnetometry and Gradiometry Towards Subpicotesla dc Field Measurement*, Physical Review Applied 15, 064075 (2021),
URL: https://dx.doi.org/10.1103/PhysRevApplied.15.064075

[32] F. M. Stürner, A. Brenneis, T. Buck, J. Kassel, R. Rölver, T. Fuchs, A. Savitsky, D. Suter, J. Grimmel, S. Hengesbach, M. Förtsch, K. Nakamura, H. Sumiya, S. Onoda, J. Isoya, and F. Jelezko, *Integrated and Portable Magnetometer Based on Nitrogen-Vacancy Ensembles in Diamond*, Advanced Quantum Technologies 4, 2000111 (2021),
URL: https://dx.doi.org/10.1002/qute.202000111

[33] Y. Xie, H. Yu, Y. Zhu, X. Qin, X. Rong, C.-K. Duan, and J. Du, *A hybrid magnetometer towards femtotesla sensitivity under ambient conditions*, Sci-

ence Bulletin 66, 127 (2021),
URL: https://dx.doi.org/10.1016/j.scib.2020.08.001

[34] H. B. Dang, A. C. Maloof, and M. V. Romalis, *Ultrahigh sensitivity magnetic field and magnetization measurements with an atomic magnetometer*, Applied Physics Letters 97, 151110 (2010),
URL: https://dx.doi.org/10.1063/1.3491215

[35] W. C. Griffith, S. Knappe, and J. Kitching, *Femtotesla atomic magnetometry in a microfabricated vapor cell*, Optics Express 18, 27167 (2010),
URL: https://dx.doi.org/10.1364/OE.18.027167

[36] J. Osborne, J. Orton, O. Alem, and V. Shah, *Fully integrated standalone zero field optically pumped magnetometer for biomagnetism*, in Steep dispersion engineering and opto-atomic precision metrology XI 10548, pp. 89–95, Society of Photo-Optical Instrumentation Engineers (SPIE), (2018),
URL: https://dx.doi.org/10.1117/12.2299197

[37] QuSpin Inc., *QTFM, Total Field Magnetometer*, Spec Sheet, (2016),
URL: https://quspin.com/wp-content/uploads/2016/09/QMAG-TF-Spec-Sheet.pdf,
(retrieved on 28th December 2020)

[38] M. Schmelz, R. Stolz, V. Zakosarenko, T. Schönau, S. Anders, L. Fritzsch, M. Mück, and H.-G. Meyer, *Field-stable SQUID magnetometer with sub-fT $Hz^{-1/2}$ resolution based on sub-micrometer cross-type Josephson tunnel junctions*, Superconductor Science and Technology 24, 065009 (2011),
URL: https://dx.doi.org/10.1088/0953-2048/24/6/065009

[39] J.-H. Storm, P. Hömmen, D. Drung, and R. Körber, *An ultra-sensitive and wideband magnetometer based on a superconducting quantum interference device*, Applied Physics Letters 110, 072603 (2017),
URL: https://dx.doi.org/10.1063/1.4976823

[40] C.-C. Lu, J. Huang, P.-K. Chiu, S.-L. Chiu, and J.-T. Jeng, *High-sensitivity low-noise miniature fluxgate magnetometers using a flip chip conceptual*

design, Sensors 14, 13815 (2014),
URL: https://dx.doi.org/10.3390/s140813815

[41] E. Paperno, *Suppression of magnetic noise in the fundamental-mode orthogonal fluxgate*, Sensors and Actuators A: Physical 116, 405 (2004),
URL: https://dx.doi.org/10.1016/j.sna.2004.05.011

[42] Asahi Kasei Microdevices Corp., *AK09940: Ultrahigh precision 3-axis Electronic Magnetometer*, Spec Sheet, (2018),
URL: https://akm.com/us/en/products/tri-axis-magnetic-sensor/ak09940/,
(retrieved on 28th December 2020)

[43] A. Guedes, R. Macedo, G. Jaramillo, S. Cardoso, P. P. Freitas, and D. A. Horsley, *Hybrid GMR Sensor Detecting 950 pT/sqrt(Hz) at 1 Hz and Room Temperature*, Sensors 18 (2018),
URL: https://dx.doi.org/10.3390/s18030790

[44] K. Sternickel and A. I. Braginski, *Biomagnetism using SQUIDs: status and perspectives*, Superconductor Science and Technology 19, S160 (2006),
URL: https://dx.doi.org/10.1088/0953-2048/19/3/024

[45] C. Granata and A. Vettoliere, *Nano Superconducting Quantum Interference device: A powerful tool for nanoscale investigations*, Physics Reports 614, 1 (2016),
URL: https://dx.doi.org/10.1016/j.physrep.2015.12.001

[46] V. Jacques, P. Neumann, J. Beck, M. Markham, D. Twitchen, J. Meijer, F. Kaiser, G. Balasubramanian, F. Jelezko, and J. Wrachtrup, *Dynamic Polarization of Single Nuclear Spins by Optical Pumping of Nitrogen-Vacancy Color Centers in Diamond at Room Temperature*, Physical Review Letters 102, 057403 (2009),
URL: https://dx.doi.org/10.1103/PhysRevLett.102.057403

[47] G. Balasubramanian, P. Neumann, D. Twitchen, M. Markham, R. Kolesov, N. Mizuochi, J. Isoya, J. Achard, J. Beck, J. Tissler, V. Jacques, P. R. Hemmer, F. Jelezko, and J. Wrachtrup, *Ultralong spin coherence time in isotopically*

engineered diamond, Nature Materials 8, 383 (2009),
URL: https://dx.doi.org/10.1038/nmat2420

[48] G. Waldherr, J. Beck, P. Neumann, S. R. S., M. Nitsche, M. L. Markham, D. J. Twitchen, J. Twamley, F. Jelezko, and J. Wrachtrup, *High-dynamic-range magnetometry with a single nuclear spin in diamond*, Nature Nanotechology 7, 105 (2012),
URL: https://dx.doi.org/10.1038/nnano.2011.224

[49] J. R. Maze, P. L. Stanwix, J. S. Hodges, S. Hong, J. M. Taylor, P. Cappellaro, L. Jiang, M. V. G. Dutt, E. Togan, A. S. Zibrov, A. Yacoby, R. L. Walsworth, and M. D. Lukin, *Nanoscale magnetic sensing with an individual electronic spin in diamond*, Nature 455, 644 (2008),
URL: https://dx.doi.org/10.1038/nature07279

[50] J. M. Taylor, P. Cappellaro, L. Childress, L. Jiang, D. Budker, P. R. Hemmer, A. Yacoby, R. Walsworth, and M. D. Lukin, *High-sensitivity diamond magnetometer with nanoscale resolution*, Nature Physics 4, 810 (2008),
URL: https://dx.doi.org/10.1038/nphys1075

[51] F. Dolde, H. Fedder, M. W. Doherty, T. Nöbauer, F. Rempp, G. Balasubramanian, T. Wolf, F. Reinhard, L. C. L. Hollenberg, F. Jelezko, and J. Wrachtrup, *Electric-field sensing using single diamond spins*, Nature Physics 7, 459 (2011),
URL: https://dx.doi.org/10.1038/nphys1969

[52] E. H. Chen, H. A. Clevenson, K. A. Johnson, L. M. Pham, D. R. Englund, P. R. Hemmer, and D. A. Braje, *High-sensitivity spin-based electrometry with an ensemble of nitrogen-vacancy centers in diamond*, Physical Review A 95, 053417 (2017),
URL: https://dx.doi.org/10.1103/PhysRevA.95.053417

[53] J. Michl, J. Steiner, A. Denisenko, A. Bülau, A. Zimmermann, K. Nakamura, H. Sumiya, S. Onoda, P. Neumann, J. Isoya, and J. Wrachtrup, *Robust and Accurate Electric Field Sensing with Solid State Spin Ensembles*, Nano Letters

19, 4904 (2019),
URL: https://dx.doi.org/10.1021/acs.nanolett.9b00900

[54] P. Neumann, I. Jakobi, F. Dolde, C. Burk, R. Reuter, G. Waldherr, J. Honert, T. Wolf, A. Brunner, J. H. Shim, D. Suter, H. Sumiya, J. Isoya, and J. Wrachtrup, *High-Precision Nanoscale Temperature Sensing Using Single Defects in Diamond*, Nano Letters 13, 2738 (2013),
URL: https://dx.doi.org/10.1021/nl401216y

[55] I. V. Fedotov, S. Blakley, E. E. Serebryannikov, N. A. Safronov, V. L. Velichansky, M. O. Scully, and A. M. Zheltikov, *Fiber-based thermometry using optically detected magnetic resonance*, Applied Physics Letters 105, 261109 (2014),
URL: https://dx.doi.org/10.1063/1.4904798

[56] M. W. Doherty, V. V. Struzhkin, D. A. Simpson, L. P. McGuinness, Y. Meng, A. Stacey, T. J. Karle, R. J. Hemley, N. B. Manson, L. C. L. Hollenberg, and S. Prawer, *Electronic Properties and Metrology Applications of the Diamond* NV^- *Center under Pressure*, Physical Review Letters 112, 047601 (2014),
URL: https://dx.doi.org/10.1103/PhysRevLett.112.047601

[57] M. E. Trusheim and D. Englund, *Wide-field strain imaging with preferentially aligned nitrogen-vacancy centers in polycrystalline diamond*, New Journal of Physics 18, 123023 (2016),
URL: https://dx.doi.org/10.1088/1367-2630/aa5040

[58] F. Grazioso, B. R. Patton, P. Delaney, M. L. Markham, D. J. Twitchen, and J. M. Smith, *Measurement of the full stress tensor in a crystal using photoluminescence from point defects: The example of nitrogen vacancy centers in diamond*, Applied Physics Letters 103, 101905 (2013),
URL: https://dx.doi.org/10.1063/1.4819834

[59] T. Fujisaku, R. Tanabe, S. Onoda, R. Kubota, T. F. Segawa, F. T.-K. So, T. Ohshima, I. Hamachi, M. Shirakawa, and R. Igarashi, *pH Nanosensor*

Using Electronic Spins in Diamond, ACS nano 13, 11726 (2019),
URL: https://dx.doi.org/10.1021/acsnano.9b05342

[60] C. Müller, X. Kong, J.-M. Cai, K. Melentijević, A. Stacey, M. Markham, D. Twitchen, J. Isoya, S. Pezzagna, J. Meijer, J. F. Du, M. B. Plenio, B. Naydenov, L. P. McGuinness, and F. Jelezko, *Nuclear magnetic resonance spectroscopy with single spin sensitivity*, Nature Communications 5, 4703 (2014),
URL: https://dx.doi.org/10.1038/ncomms5703

[61] H. J. Mamin, M. Kim, M. H. Sherwood, C. T. Rettner, K. Ohno, D. D. Awschalom, and D. Rugar, *Nanoscale Nuclear Magnetic Resonance with a Nitrogen-Vacancy Spin Sensor*, Science 339, 557 (2013),
URL: https://dx.doi.org/10.1126/science.1231540

[62] N. Aslam, M. Pfender, P. Neumann, R. Reuter, A. Zappe, F. Fávaro de Oliveira, A. Denisenko, H. Sumiya, S. Onoda, J. Isoya, and J. Wrachtrup, *Nanoscale nuclear magnetic resonance with chemical resolution*, Science 357, 67 (2017),
URL: https://dx.doi.org/10.1126/science.aam8697

[63] J. Smits, J. T. Damron, P. Kehayias, A. F. McDowell, N. Mosavian, I. Fescenko, N. Ristoff, A. Laraoui, A. Jarmola, and V. M. Acosta, *Two-dimensional nuclear magnetic resonance spectroscopy with a microfluidic diamond quantum sensor*, Science Advances 5 (2019),
URL: https://dx.doi.org/10.1126/sciadv.aaw7895

[64] L. Q. Zhou, R. L. Patel, A. C. Frangeskou, A. Nikitin, B. L. Green, B. G. Breeze, S. Onoda, J. Isoya, and G. W. Morley, *Imaging Damage in Steel Using a Diamond Magnetometer*, Physical Review Applied 15, 024015 (2021),
URL: https://dx.doi.org/10.1103/PhysRevApplied.15.024015

[65] A. Ajoy and P. Cappellaro, *Stable three-axis nuclear-spin gyroscope in diamond*, Physical Review A 86, 062104 (2012),
URL: https://dx.doi.org/10.1103/PhysRevA.86.062104

[66] M. P. Ledbetter, K. Jensen, R. Fischer, A. Jarmola, and D. Budker, *Gyroscopes based on nitrogen-vacancy centers in diamond*, Physical Review A 86, 052116 (2012),
URL: https://dx.doi.org/10.1103/PhysRevA.86.052116

[67] J.-C. Jaskula, K. Saha, A. Ajoy, D. Twitchen, M. Markham, and P. Cappellaro, *Cross-Sensor Feedback Stabilization of an Emulated Quantum Spin Gyroscope*, Physical Review Applied 11, 054010 (2019),
URL: https://dx.doi.org/10.1103/PhysRevApplied.11.054010

[68] V. V. Soshenko, S. V. Bolshedvorskii, O. Rubinas, V. N. Sorokin, A. N. Smolyaninov, V. V. Vorobyov, and A. V. Akimov, *Nuclear Spin Gyroscope based on the Nitrogen Vacancy Center in Diamond*, Physical Review Letters 126, 197702 (2021),
URL: https://dx.doi.org/10.1103/PhysRevLett.126.197702

[69] A. Jarmola, S. Lourette, V. M. Acosta, A. G. Birdwell, P. Blümler, D. Budker, T. Ivanov, and V. S. Malinovsky, *Demonstration of diamond nuclear spin gyroscope*, Science Advances 7 (2021),
URL: https://dx.doi.org/10.1126/sciadv.abl3840

[70] F. Casola, T. van der Sar, and A. Yacoby, *Probing condensed matter physics with magnetometry based on nitrogen-vacancy centres in diamond*, Nature Reviews Materials 3, 17088 (2018),
URL: https://dx.doi.org/10.1038/natrevmats.2017.88

[71] M. C. Marshall, M. J. Turner, M. J. H. Ku, D. F. Phillips, and R. L. Walsworth, *Directional detection of dark matter with diamond*, Quantum Science and Technology 6, 024011 (2021),
URL: https://dx.doi.org/10.1088/2058-9565/abe5ed

[72] T. D. Ladd, F. Jelezko, R. Laflamme, Y. Nakamura, C. Monroe, and J. L. O'Brien, *Quantum computers*, Nature 464, 45 (2010),
URL: https://dx.doi.org/10.1038/nature08812

[73] J. Cai, A. Retzker, F. Jelezko, and M. B. Plenio, *A large-scale quantum simulator on a diamond surface at room temperature*, Nature Physics 9, 168 (2013),
URL: https://dx.doi.org/10.1038/nphys2519

[74] C. Ju, C. Lei, X. Xu, D. Culcer, Z. Zhang, and J. Du, *NV-center-based digital quantum simulation of a quantum phase transition in topological insulators*, Physical Review B 89, 045432 (2014),
URL: https://dx.doi.org/10.1103/PhysRevB.89.045432

[75] M. W. Doherty, C. A. Meriles, A. Alkauskas, H. Fedder, M. J. Sellars, and N. B. Manson, *Towards a Room-Temperature Spin Quantum Bus in Diamond via Electron Photoionization, Transport, and Capture*, Physical Review X 6, 041035 (2016),
URL: https://dx.doi.org/10.1103/PhysRevX.6.041035

[76] M. V. G. Dutt, L. Childress, L. Jiang, E. Togan, J. Maze, F. Jelezko, A. S. Zibrov, P. R. Hemmer, and M. D. Lukin, *Quantum Register Based on Individual Electronic and Nuclear Spin Qubits in Diamond*, Science 316, 1312 (2007),
URL: https://dx.doi.org/10.1126/science.1139831

[77] J. S. Bennett, B. E. Vyhnalek, H. Greenall, E. M. Bridge, F. Gotardo, S. Forstner, G. I. Harris, F. A. Miranda, and W. P. Bowen, *Precision Magnetometers for Aerospace Applications: A Review*, Sensors 21 (2021),
URL: https://dx.doi.org/10.3390/s21165568

[78] R. R. Fu, B. P. Weiss, E. A. Lima, R. J. Harrison, X.-N. Bai, S. J. Desch, D. S. Ebel, C. Suavet, H. Wang, D. Glenn, D. Le Sage, T. Kasama, R. L. Walsworth, and A. T. Kuan, *Solar nebula magnetic fields recorded in the Semarkona meteorite*, Science 346, 1089 (2014),
URL: https://dx.doi.org/10.1126/science.1258022

[79] D. R. Glenn, R. R. Fu, P. Kehayias, D. Le Sage, E. A. Lima, B. P. Weiss, and R. L. Walsworth, *Micrometer-scale magnetic imaging of geological samples*

using a quantum diamond microscope, Geochemistry, Geophysics, Geosystems 18, 3254 (2017),
URL: https://dx.doi.org/10.1002/2017GC006946

[80] S. E. Crawford, R. A. Shugayev, H. P. Paudel, P. Lu, M. Syamlal, P. R. Ohodnicki, B. Chorpening, R. Gentry, and Y. Duan, *Quantum Sensing for Energy Applications: Review and Perspective*, Advanced Quantum Technologies 4, 2100049 (2021),
URL: https://dx.doi.org/10.1002/qute.202100049

[81] J.-P. Tetienne, N. Dontschuk, D. A. Broadway, A. Stacey, D. A. Simpson, and L. C. L. Hollenberg, *Quantum imaging of current flow in graphene*, Science Advances 3 (2017),
URL: https://dx.doi.org/10.1126/sciadv.1602429

[82] M. J. Turner, N. Langellier, R. Bainbridge, D. Walters, S. Meesala, T. M. Babinec, P. Kehayias, A. Yacoby, E. Hu, M. Lončar, R. L. Walsworth, and E. V. Levine, *Magnetic Field Fingerprinting of Integrated-Circuit Activity with a Quantum Diamond Microscope*, Physical Review Applied 14, 014097 (2020),
URL: https://dx.doi.org/10.1103/PhysRevApplied.14.014097

[83] A. Nowodzinski, M. Chipaux, L. Toraille, V. Jacques, J.-F. Roch, and T. Debuisschert, *Nitrogen-Vacancy centers in diamond for current imaging at the redistributive layer level of Integrated Circuits*, Microelectronics Reliability 55, 1549 (2015),
URL: https://dx.doi.org/10.1016/j.microrel.2015.06.069

[84] S. Bodenstedt, I. Jakobi, J. Michl, I. Gerhardt, P. Neumann, and J. Wrachtrup, *Nanoscale spin manipulation with pulsed magnetic gradient fields from a hard disc drive writer*, Nano letters 18, 5389 (2018),
URL: https://dx.doi.org/10.1021/acs.nanolett.8b01387

[85] G. Chatzidrosos, A. Wickenbrock, L. Bougas, H. Zheng, O. Tretiak, Y. Yang, and D. Budker, *Eddy-Current Imaging with Nitrogen-Vacancy Centers in Dia-*

mond, Physical Review Applied 11, 014060 (2019),
URL: https://dx.doi.org/10.1103/PhysRevApplied.11.014060

[86] X. Zhang, G. Chatzidrosos, Y. Hu, H. Zheng, A. Wickenbrock, A. Jerschow, and D. Budker, *Battery Characterization via Eddy-Current Imaging with Nitrogen-Vacancy Centers in Diamond*, Applied Sciences 11 (2021),
URL: https://dx.doi.org/10.3390/app11073069

[87] G. Petrini, E. Moreva, E. Bernardi, P. Traina, G. Tomagra, V. Carabelli, I. P. Degiovanni, and M. Genovese, *Is a Quantum Biosensing Revolution Approaching? Perspectives in NV-Assisted Current and Thermal Biosensing in Living Cells*, Advanced Quantum Technologies 3, 2000066 (2020),
URL: https://dx.doi.org/10.1002/qute.202000066

[88] M. Karadas, C. Olsson, N. Winther Hansen, J.-F. Perrier, J. L. Webb, A. Huck, U. L. Andersen, and A. Thielscher, *In-vitro Recordings of Neural Magnetic Activity From the Auditory Brainstem Using Color Centers in Diamond: A Simulation Study*, Frontiers in Neuroscience 15, 516 (2021),
URL: https://dx.doi.org/10.3389/fnins.2021.643614

[89] D. Le Sage, K. Arai, D. R. Glenn, S. J. Devience, L. M. Pham, L. Rahn-Lee, M. D. Lukin, A. Yacoby, A. Komeili, and R. L. Walsworth, *Optical magnetic imaging of living cells*, Nature 496, 486 (2013),
URL: https://dx.doi.org/10.1038/nature12072

[90] K. Arai, A. Kuwahata, D. Nishitani, I. Fujisaki, R. Matsuki, Z. Xin, Y. Nishio, X. Cao, Y. Hatano, S. Onoda, C. Shinei, M. Miyakawa, T. Taniguchi, M. Yamazaki, T. Teraji, T. Ohshima, M. Hatano, M. Sekino, and T. Iwasaki, *Millimetre-scale magnetocardiography of living rats using a solid-state quantum sensor*, arXiv preprint, arXiv:2105.11676 (2021),
URL: https://arxiv.org/abs/2105.11676

[91] M. Sekino, A. Kuwahata, T. Ookubo, M. Shiozawa, K. Ohashi, M. Kaneko, I. Saito, Y. Inoue, H. Ohsaki, H. Takei, et al., *Handheld magnetic probe with permanent magnet and Hall sensor for identifying sentinel lymph nodes in*

breast cancer patients, Scientific Reports 8, 1195 (2018),
URL: https://dx.doi.org/10.1038/s41598-018-19480-1

[92] A. Kuwahata, T. Kitaizumi, K. Saichi, T. Sato, R. Igarashi, T. Ohshima, Y. Masuyama, T. Iwasaki, M. Hatano, F. Jelezko, M. Kusakabe, T. Yatsui, and M. Sekino, *Magnetometer with nitrogen-vacancy center in a bulk diamond for detecting magnetic nanoparticles in biomedical applications*, Scientific Reports 10, 2483 (2020),
URL: https://dx.doi.org/10.1038/s41598-020-59064-6

[93] T. Kitaizumi, A. Kuwahata, K. Saichi, T. Sato, R. Igarashi, T. Ohshima, Y. Masuyama, T. Iwasaki, M. Hatano, F. Jelezko, M. Kusakabe, T. Yatsui, and M. Sekino, *Magnetic Field Generation System of the Magnetic Probe With Diamond Quantum Sensor and Ferromagnetic Materials for the Detection of Sentinel Lymph Nodes With Magnetic Nanoparticles*, IEEE Transactions on Magnetics 57, 1 (2021),
URL: https://dx.doi.org/10.1109/TMAG.2020.3009334

[94] F. Gorrini, R. Giri, C. E. Avalos, S. Tambalo, S. Mannucci, L. Basso, N. Bazzanella, C. Dorigoni, M. Cazzanelli, P. Marzola, A. Miotello, and A. Bifone, *Fast and Sensitive Detection of Paramagnetic Species Using Coupled Charge and Spin Dynamics in Strongly Fluorescent Nanodiamonds*, ACS Applied Materials & Interfaces 11, 24412 (2019),
URL: https://dx.doi.org/10.1021/acsami.9b05779

[95] A. Ermakova, G. Pramanik, J. M. Cai, G. Algara-Siller, U. Kaiser, T. Weil, Y. K. Tzeng, H. C. Chang, L. P. McGuinness, M. B. Plenio, B. Naydenov, and F. Jelezko, *Detection of a Few Metallo-Protein Molecules Using Color Centers in Nanodiamonds*, Nano Letters 13, 3305 (2013),
URL: https://dx.doi.org/10.1021/nl4015233

[96] A. A. Gentile, B. Flynn, S. Knauer, N. Wiebe, S. Paesani, C. E. Granade, J. G. Rarity, R. Santagati, and A. Laing, *Learning models of quantum systems from experiments*, Nature Physics 17 (2021),
URL: https://dx.doi.org/10.1038/s41567-021-01201-7

[97] R. Santagati, A. A. Gentile, S. Knauer, S. Schmitt, S. Paesani, C. Granade, N. Wiebe, C. Osterkamp, L. P. McGuinness, J. Wang, M. G. Thompson, J. G. Rarity, F. Jelezko, and A. Laing, *Magnetic-Field Learning Using a Single Electronic Spin in Diamond with One-Photon Readout at Room Temperature*, Physical Review X 9, 021019 (2019),
URL: https://dx.doi.org/10.1103/PhysRevX.9.021019

[98] A. A. Gentile, R. Santagati, S. Knauer, S. Schmitt, S. Paesani, C. Granade, N. Wiebe, C. Osterkamp, L. P. McGuinness, J. Wang, M. G. Thompson, J. G. Rarity, F. Jelezko, and A. Laing, *High-sensitivity magnetometry at room temperature with post-processed optical readout of single NV-centres*, in 2019 Conference on Lasers and Electro-Optics (CLEO) SM2F.2, Optical Society of America, (2019),
URL: https://dx.doi.org/10.1364/CLEO_SI.2019.SM2F.2

[99] J. Mackeprang, D. Bhaktavatsala Rao Dasari, and J. Wrachtrup, *A Reinforcement Learning approach for Quantum State Engineering*, arXiv preprint, arXiv:1908.05981 (2019),
URL: https://arxiv.org/abs/1908.05981

[100] K. Craigie, E. M. Gauger, Y. Altmann, and C. Bonato, *Resource-efficient adaptive Bayesian tracking of magnetic fields with a quantum sensor*, Journal of Physics: Condensed Matter 33, 195801 (2021),
URL: https://dx.doi.org/10.1088/1361-648x/abe34f

[101] L. Bougas, A. Wilzewski, Y. Dumeige, D. Antypas, A. Wu, T.and Wickenbrock, E. Bourgeois, M. Nesladek, H. Clevenson, D. Braje, D. Englund, and D. Budker, *On the Possibility of Miniature Diamond-Based Magnetometers Using Waveguide Geometries*, Micromachines 9 (2018),
URL: https://dx.doi.org/10.3390/mi9060276

[102] M. I. Ibrahim, C. Foy, D. Kim, D. R. Englund, and R. Han, Room-temperature quantum sensing in cmos: On-chip detection of electronic spin states in diamond color centers for magnetometry, in 2018 IEEE Symposium on VLSI

Circuits, pp. 249–250, (2018),
URL: https://dx.doi.org/10.1109/VLSIC.2018.8502329

[103] D. Kim, M. I. Ibrahim, C. Foy, M. E. Trusheim, R. Han, and D. R. Englund, *A CMOS-integrated quantum sensor based on nitrogen–vacancy centres*, Nature Electronics 2, 284 (2019),
URL: https://dx.doi.org/10.1038/s41928-019-0275-5

[104] T. Oeckinghaus, R. Stöhr, R. Kolesov, J. Tisler, F. Reinhard, and J. Wrachtrup, *A compact, diode laser based excitation system for microscopy of NV centers*, Review of Scientific Instruments 85, 073101 (2014),
URL: https://dx.doi.org/10.1063/1.4885469

[105] N. Zhang, H. Yuan, C. Zhang, L. Xu, J. Zhang, G. Bian, P. Fan, H. Yuan, and J. Fang, *Microwave Field Uniformity Impact on DC Magnetic Sensing With NV Ensembles in Diamond*, IEEE Sensors Journal 19, 451 (2019),
URL: https://dx.doi.org/10.1109/JSEN.2018.2878220

[106] R. Staacke, R. John, R. Wunderlich, L. Horsthemke, W. Knolle, C. Laube, P. Glösekötter, B. Burchard, B. Abel, and J. Meijer, *Isotropic Scalar Quantum Sensing of Magnetic Fields for Industrial Application*, Advanced Quantum Technologies 3, 2000037 (2020),
URL: https://dx.doi.org/10.1002/qute.202000037

[107] I. Aharonovich, S. Castelletto, D. Simpson, C. Su, A. Greentree, and S. Prawer, *Diamond-based single-photon emitters*, Reports on progress in Physics 74, 076501 (2011),
URL: https://dx.doi.org/10.1088/0034-4885/74/7/076501

[108] F. Jelezko and J. Wrachtrup, *Single defect centres in diamond: a review*, physica status solidi (a) 203, 3207 (2006),
URL: https://dx.doi.org/10.1002/pssa.200671403

[109] M. W. Doherty, N. B. Manson, P. Delaney, F. Jelezko, J. Wrachtrup, and L. C. Hollenberg, *The nitrogen-vacancy colour centre in diamond*, Physics Reports

528, 1 (2013),
URL: https://dx.doi.org/10.1016/j.physrep.2013.02.001

[110] L. J. Rogers, K. D. Jahnke, M. W. Doherty, A. Dietrich, L. P. McGuinness, C. Müller, T. Teraji, H. Sumiya, J. Isoya, N. B. Manson, and F. Jelezko, *Electronic structure of the negatively charged silicon-vacancy center in diamond*, Physical Review B 89, 235101 (2014),
URL: https://dx.doi.org/10.1103/PhysRevB.89.235101

[111] C. Hepp, T. Müller, V. Waselowski, J. N. Becker, B. Pingault, H. Sternschulte, D. Steinmüller-Nethl, A. Gali, J. R. Maze, M. Atatüre, and C. Becher, *Electronic Structure of the Silicon Vacancy Color Center in Diamond*, Physical Review Letters 112, 036405 (2014),
URL: https://dx.doi.org/10.1103/PhysRevLett.112.036405

[112] T. Iwasaki, F. Ishibashi, Y. Miyamoto, Y. Doi, S. Kobayashi, T. Miyazaki, K. Tahara, K. D. Jahnke, L. J. Rogers, B. Naydenov, et al., *Germanium-vacancy single color centers in diamond*, Scientific Reports 5 (2015),
URL: https://dx.doi.org/10.1038/srep12882

[113] P. Siyushev, M. H. Metsch, A. Ijaz, J. M. Binder, M. K. Bhaskar, D. D. Sukachev, A. Sipahigil, R. E. Evans, C. T. Nguyen, M. D. Lukin, P. R. Hemmer, Y. N. Palyanov, I. N. Kupriyanov, Y. M. Borzdov, L. J. Rogers, and F. Jelezko, *Optical and microwave control of germanium-vacancy center spins in diamond*, Physical Review 96, 081201 (2017),
URL: https://dx.doi.org/10.1103/PhysRevB.96.081201

[114] T. Iwasaki, Y. Miyamoto, T. Taniguchi, P. Siyushev, M. H. Metsch, F. Jelezko, and M. Hatano, *Tin-Vacancy Quantum Emitters in Diamond*, Physical Review Letters 119, 253601 (2017),
URL: https://dx.doi.org/10.1103/PhysRevLett.119.253601

[115] F. Bitter, *The Optical Detection of Radiofrequency Resonance*, Physica Review 76, 833 (1949),
URL: https://dx.doi.org/10.1103/PhysRev.76.833

[116] J. H. N. Loubser and J. A. van Wyk, *Electron spin resonance in the study of diamond*, Reports on Progress in Physics 41, 1201 (1978),
URL: https://dx.doi.org/10.1088/0034-4885/41/8/002

[117] N. Reddy, N. Manson, and E. Krausz, *Two-laser spectral hole burning in a colour centre in diamond*, Journal of Luminescence 38, 46 (1987),
URL: https://dx.doi.org/10.1016/0022-2313(87)90057-3

[118] E. van Oort, N. B. Manson, and M. Glasbeek, *Optically detected spin coherence of the diamond N-V centre in its triplet ground state*, Journal of Physics C: Solid State Physics 21, 4385 (1988),
URL: https://dx.doi.org/10.1088/0022-3719/21/23/020

[119] A. Gruber, A. Dräbenstedt, C. Tietz, L. Fleury, J. Wrachtrup, and C. v. Borczyskowski, *Scanning Confocal Optical Microscopy and Magnetic Resonance on Single Defect Centers*, Science 276, 2012 (1997),
URL: https://dx.doi.org/10.1126/science.276.5321.2012

[120] J. F. Barry, J. M. Schloss, E. Bauch, M. J. Turner, C. A. Hart, L. M. Pham, and R. L. Walsworth, *Sensitivity optimization for NV-diamond magnetometry*, Reviews of Modern Physics 92, 015004 (2020),
URL: https://dx.doi.org/10.1103/RevModPhys.92.015004

[121] R. Schirhagl, K. Chang, M. Loretz, and C. L. Degen, *Nitrogen-Vacancy Centers in Diamond: Nanoscale Sensors for Physics and Biology*, Annual Review of Physical Chemistry 65, 83 (2013),
URL: https://dx.doi.org/10.1146/annurev-physchem-040513-103659

[122] R. S. Balmer, J. R. Brandon, S. L. Clewes, H. K. Dhillon, J. M. Dodson, I. Friel, P. N. Inglis, T. D. Madgwick, M. L. Markham, T. P. Mollart, N. Perkins, G. A. Scarsbrook, D. J. Twitchen, A. J. Whitehead, J. J. Wilman, and S. M. Woollard, *Chemical vapour deposition synthetic diamond: materials, technology and applications*, Journal of Physics: Condensed Matter 21, 364221 (2009),
URL: https://dx.doi.org/10.1088/0953-8984/21/36/364221

[123] C. Kittel, *Einführung in die Festkörperphysik*, Oldenburg Verlag, (2006)

[124] N. Savvides and T. J. Bell, *Microhardness and Young's modulus of diamond and diamondlike carbon films*, Journal of Applied Physics 72, 2791 (1992), URL: https://dx.doi.org/10.1063/1.351530

[125] C. Bandis and B. B. Pate, *Simultaneous field emission and photoemission from diamond*, Applied Physics Letters 69, 366 (1996), URL: https://dx.doi.org/10.1063/1.118062

[126] L. Wei, P. K. Kuo, R. L. Thomas, T. R. Anthony, and W. F. Banholzer, *Thermal conductivity of isotopically modified single crystal diamond*, Physical Review Letters 70, 3764 (1993), URL: https://dx.doi.org/10.1103/PhysRevLett.70.3764

[127] K. E. Spear and J. P. Dismukes, *Synthetic diamond: emerging CVD science and technology*, volume 25, John Wiley & Sons, (1994)

[128] R. P. Mildren and J. R. Rabeau, *Optical engineering of diamond*, Wiley-VCH, Weinheim, (2013)

[129] S. Coe and R. Sussmann, *Optical, thermal and mechanical properties of CVD diamond*, Diamond and Related Materials 9, 1726 (2000), URL: https://dx.doi.org/10.1016/S0925-9635(00)00298-3

[130] M. Schwander and K. Partes, *A review of diamond synthesis by CVD processes*, Diamond and Related Materials 20, 1287 (2011), URL: https://dx.doi.org/10.1016/j.diamond.2011.08.005

[131] P. Jacobson and S. Stoupin, *Thermal expansion coefficient of diamond in a wide temperature range*, Diamond and Related Materials 97, 107469 (2019), URL: https://dx.doi.org/10.1016/j.diamond.2019.107469

[132] M. Radtke, E. Bernardi, A. Slablab, R. Nelz, and E. Neu, *Nanoscale sensing based on nitrogen vacancy centers in single crystal diamond and nanodiamonds: achievements and challenges*, Nano Futures 3, 042004 (2019), URL: https://dx.doi.org/10.1088/2399-1984/ab5f9b

[133] F. Bundy, H. Hall, H. Strong, and R. H. Wentorf, *Man-Made Diamonds*, Nature 176, 51 (1955),
URL: https://dx.doi.org/10.1038/176051a0

[134] J. E. Butler and H. Windischmann, *Developments in CVD-Diamond Synthesis During the Past Decade*, MRS Bulletin 23 (1998),
URL: https://dx.doi.org/10.1557/S0883769400029316

[135] J. Achard, V. Jacques, and A. Tallaire, *Chemical vapour deposition diamond single crystals with nitrogen-vacancy centres: a review of material synthesis and technology for quantum sensing applications*, Journal of Physics D: Applied Physics 53, 313001 (2020),
URL: https://dx.doi.org/10.1088/1361-6463/ab81d1

[136] F. P. Bundy, *Direct Conversion of Graphite to Diamond in Static Pressure Apparatus*, The Journal of Chemical Physics 38, 631 (1963),
URL: https://dx.doi.org/10.1063/1.1733716

[137] P. M. Martineau, M. P. Gaukroger, K. B. Guy, S. C. Lawson, D. J. Twitchen, I. Friel, J. O. Hansen, G. C. Summerton, T. P. G. Addison, and R. Burns, *High crystalline quality single crystal chemical vapour deposition diamond*, Journal of Physics: Condensed Matter 21, 364205 (2009),
URL: https://dx.doi.org/10.1088/0953-8984/21/36/364205

[138] R. C. Burns, A. I. Chumakov, S. H. Connell, D. Dube, H. P. Godfried, J. O. Hansen, J. Härtwig, J. Hoszowska, F. Masiello, L. Mkhonza, M. Rebak, A. Rommevaux, R. Setshedi, and P. Van Vaerenbergh, *HPHT growth and x-ray characterization of high-quality type IIa diamond*, Journal of Physics Condensed Matter 21, 364224 (2009),
URL: https://dx.doi.org/10.1088/0953-8984/21/36/364224

[139] A. Tallaire, V. Mille, O. Brinza, T. N. Tran Thi, J. Brom, Y. Loguinov, A. Katrusha, A. Koliadin, and J. Achard, *Thick CVD diamond films grown on high-quality type IIa HPHT diamond substrates from New Diamond Tech-*

nology, Diamond and Related Materials 77, 146 (2017),
URL: https://dx.doi.org/10.1016/j.diamond.2017.07.002

[140] A. M. Zaitsev, *Optical Properties of Diamond: A Data Handbook*, Springer-Verlag, (2001)

[141] J. C. Angus, H. A. Will, and W. S. Stanko, *Growth of Diamond Seed Crystals by Vapor Deposition*, Journal of Applied Physics 39, 2915 (1968),
URL: https://dx.doi.org/10.1063/1.1656693

[142] J. E. Butler, Y. A. Mankelevich, A. Cheesman, J. Ma, and M. N. R. Ashfold, *Understanding the chemical vapor deposition of diamond: recent progress*, Journal of Physics: Condensed Matter 21, 364201 (2009),
URL: https://dx.doi.org/10.1088/0953-8984/21/36/364201

[143] M. Gaukroger, P. Martineau, M. Crowder, I. Friel, S. Williams, and D. Twitchen, *X-ray topography studies of dislocations in single crystal CVD diamond*, Diamond and Related Materials 17, 262 (2008),
URL: https://dx.doi.org/10.1016/j.diamond.2007.12.036

[144] A. Lenef and S. C. Rand, *Electronic structure of the N-V center in diamond: Theory*, Physical Review B 53, 13441 (1996),
URL: https://dx.doi.org/10.1103/PhysRevB.53.13441

[145] R. J. Epstein, F. M. Mendoza, Y. K. Kato, and D. D. Awschalom, *Anisotropic interactions of a single spin and dark-spin spectroscopy in diamond*, Nature Physics 1, 94 (2005),
URL: https://dx.doi.org/10.1038/nphys141

[146] J. Michl, T. Teraji, S. Zaiser, I. Jakobi, G. Waldherr, F. Dolde, P. Neumann, M. W. Doherty, N. B. Manson, J. Isoya, et al., *Perfect alignment and preferential orientation of nitrogen-vacancy centers during chemical vapor deposition diamond growth on (111) surfaces*, Applied Physics Letters 104, 102407 (2014),
URL: https://dx.doi.org/10.1063/1.4868128

[147] K. Ohno, F. Joseph Heremans, L. C. Bassett, B. A. Myers, D. M. Toyli, A. C. Bleszynski Jayich, C. J. Palmstrøm, and D. D. Awschalom, *Engineering shallow spins in diamond with nitrogen delta-doping*, Applied Physics Letters 101, 082413 (2012),
URL: https://dx.doi.org/10.1063/1.4748280

[148] C. Osterkamp, J. Lang, J. Scharpf, C. Müller, L. P. McGuinness, T. Diemant, R. J. Behm, B. Naydenov, and F. Jelezko, *Stabilizing shallow color centers in diamond created by nitrogen delta-doping using SF6 plasma treatment*, Applied Physics Letters 106, 113109 (2015),
URL: https://dx.doi.org/10.1063/1.4915305

[149] H. Ishiwata, M. Nakajima, K. Tahara, H. Ozawa, T. Iwasaki, and M. Hatano, *Perfectly aligned shallow ensemble nitrogen-vacancy centers in (111) diamond*, Applied Physics Letters 111, 043103 (2017),
URL: https://dx.doi.org/10.1063/1.4993160

[150] T. Fukui, Y. Doi, T. Miyazaki, Y. Miyamoto, H. Kato, T. Matsumoto, T. Makino, S. Yamasaki, R. Morimoto, N. Tokuda, M. Hatano, Y. Sakagawa, H. Morishita, T. Tashima, S. Miwa, Y. Suzuki, and N. Mizuochi, *Perfect selective alignment of nitrogen-vacancy centers in diamond*, Applied Physics Express 7, 055201 (2014),
URL: https://dx.doi.org/10.7567/APEX.7.055201

[151] J. M. Smith, S. A. Meynell, A. C. Bleszynski Jayich, and J. Meijer, *Colour centre generation in diamond for quantum technologies*, Nanophotonics 8, 196 (2019),
URL: https://dx.doi.org/10.1515/nanoph-2019-0196

[152] J.-P. Tetienne, R. W. de Gille, D. A. Broadway, T. Teraji, S. E. Lillie, J. M. McCoey, N. Dontschuk, L. T. Hall, A. Stacey, D. A. Simpson, and L. C. L. Hollenberg, *Spin properties of dense near-surface ensembles of nitrogen-vacancy centers in diamond*, Physical Review B 97, 085402 (2018),
URL: https://dx.doi.org/10.1103/PhysRevB.97.085402

[153] J. Meijer, B. Burchard, M. Domhan, C. Wittmann, T. Gaebel, I. Popa, F. Jelezko, and J. Wrachtrup, *Generation of single color centers by focused nitrogen implantation*, Applied Physics Letters 87, (2005),
URL: https://dx.doi.org/10.1063/1.2103389

[154] C. A. McLellan, B. A. Myers, S. Kraemer, K. Ohno, D. D. Awschalom, and A. C. Bleszynski Jayich, *Patterned Formation of Highly Coherent Nitrogen-Vacancy Centers Using a Focused Electron Irradiation Technique*, Nano Letters 16, 2450 (2016),
URL: https://dx.doi.org/10.1021/acs.nanolett.5b05304

[155] F. Fávaro de Oliveira, D. Antonov, Y. Wang, P. Neumann, S. A. Momenzadeh, T. Häußermann, A. Pasquarelli, A. Denisenko, and J. Wrachtrup, *Tailoring spin defects in diamond by lattice charging*, Nature Communications 8, 15409 (2017),
URL: https://dx.doi.org/10.1038/ncomms15409

[156] M. Ruf, M. IJspeert, S. van Dam, N. de Jong, H. van den Berg, G. Evers, and R. Hanson, *Optically Coherent Nitrogen-Vacancy Centers in Micrometer-Thin Etched Diamond Membranes*, Nano Letters 19, 3987 (2019),
URL: https://dx.doi.org/10.1021/acs.nanolett.9b01316

[157] T. Nöbauer, K. Buczak, A. Angerer, S. Putz, G. Steinhauser, J. Akbarzadeh, H. Peterlik, J. Majer, J. Schmiedmayer, and M. Trupke, *Creation of ensembles of nitrogen-vacancy centers in diamond by neutron and electron irradiation*, arXiv preprint, arXiv:1309.0453 (2013),
URL: https://arxiv.org/abs/1309.0453

[158] Y.-C. Chen, B. Griffiths, L. Weng, S. S. Nicley, S. N. Ishmael, Y. Lekhai, S. Johnson, C. J. Stephen, B. L. Green, G. W. Morley, M. E. Newton, M. J. Booth, P. S. Salter, and J. M. Smith, *Laser writing of individual nitrogen-vacancy defects in diamond with near-unity yield*, Optica 6, 662 (2019),
URL: https://dx.doi.org/10.1364/OPTICA.6.000662

[159] S. B. van Dam, M. Walsh, M. J. Degen, E. Bersin, S. L. Mouradian, A. Galiullin, M. Ruf, M. IJspeert, T. H. Taminiau, R. Hanson, and D. R. Englund, *Optical coherence of diamond nitrogen-vacancy centers formed by ion implantation and annealing*, Physical Review B 99, 161203 (2019),
URL: https://dx.doi.org/10.1103/PhysRevB.99.161203

[160] S. Felton, A. M. Edmonds, M. E. Newton, P. M. Martineau, D. Fisher, and D. J. Twitchen, *Electron paramagnetic resonance studies of the neutral nitrogen vacancy in diamond*, Physical Review B 77, 081201 (2008),
URL: https://dx.doi.org/10.1103/PhysRevB.77.081201

[161] N. Aslam, G. Waldherr, P. Neumann, F. Jelezko, and J. Wrachtrup, *Photo-induced ionization dynamics of the nitrogen vacancy defect in diamond investigated by single-shot charge state detection*, New Journal of Physics 15, 013064 (2013),
URL: https://dx.doi.org/10.1088/1367-2630/15/1/013064

[162] M. Pfender, N. Aslam, P. Simon, D. Antonov, G. Thiering, S. Burk, F. Fávaro de Oliveira, A. Denisenko, H. Fedder, J. Meijer, J. A. Garrido, A. Gali, T. Teraji, J. Isoya, M. W. Doherty, A. Alkauskas, A. Gallo, A. Grüneis, P. Neumann, and J. Wrachtrup, *Protecting a Diamond Quantum Memory by Charge State Control*, Nano Letters 17, 5931 (2017),
URL: https://dx.doi.org/10.1021/acs.nanolett.7b01796

[163] R. Hanson, O. Gywat, and D. D. Awschalom, *Room-temperature manipulation and decoherence of a single spin in diamond*, Physical Review B 74, 161203 (2006),
URL: https://dx.doi.org/10.1103/PhysRevB.74.161203

[164] D. A. Redman, S. Brown, R. H. Sands, and S. C. Rand, *Spin dynamics and electronic states of N-V centers in diamond by EPR and four-wave-mixing spectroscopy*, Physical Review Letters 67, 3420 (1991),
URL: https://dx.doi.org/10.1103/PhysRevLett.67.3420

[165] C. J. Meara, M. J. Rayson, P. R. Briddon, and J. P. Goss, *Density functional theory study on magnetically detecting positively charged nitrogen-vacancy center in diamond*, Physical Review B 100, 104108 (2019),
URL: https://dx.doi.org/10.1103/PhysRevB.100.104108

[166] B. Grotz, M. V. Hauf, M. Dankerl, B. Naydenov, S. Pezzagna, J. Meijer, F. Jelezko, J. Wrachtrup, M. Stutzmann, F. Reinhard, et al., *Charge state manipulation of qubits in diamond*, Nature Communications 3, 729 (2012),
URL: https://dx.doi.org/10.1038/ncomms1729

[167] G. Davies and M. Hamer, *Optical studies of the 1.945 eV vibronic band in diamond*, 348, 285 (1976),
URL: https://dx.doi.org/10.1098/rspa.1976.0039

[168] J. R. Maze, A. Gali, E. Togan, Y. Chu, A. Trifonov, E. Kaxiras, and M. D. Lukin, *Properties of nitrogen-vacancy centers in diamond: the group theoretic approach*, New Journal of Physics 13, 025025 (2011),
URL: https://dx.doi.org/10.1088/1367-2630/13/2/025025

[169] M. W. Doherty, N. B. Manson, P. Delaney, and L. C. L. Hollenberg, *The negatively charged nitrogen-vacancy centre in diamond: the electronic solution*, New Journal of Physics 13, 025019 (2011),
URL: https://dx.doi.org/10.1088/1367-2630/13/2/025019

[170] Y. Chu and M. D. Lukin, *Quantum optics with nitrogen-vacancy centers in diamond*, arXiv preprint, arXiv:1504.05990 (2015),
URL: https://arxiv.org/abs/1504.05990

[171] A. Gali, M. Fyta, and E. Kaxiras, *Ab initio supercell calculations on nitrogen-vacancy center in diamond: Electronic structure and hyperfine tensors*, Physical Review B 77, 155206 (2008),
URL: https://dx.doi.org/10.1103/PhysRevB.77.155206

[172] V. M. Acosta, A. Jarmola, E. Bauch, and D. Budker, *Optical properties of the nitrogen-vacancy singlet levels in diamond*, Physical Review B 82, 201202

(2010),
URL: https://dx.doi.org/10.1103/PhysRevB.82.201202

[173] S. Hong, M. S. Grinolds, L. M. Pham, D. Le Sage, L. Luan, R. L. Walsworth, and A. Yacoby, *Nanoscale magnetometry with NV centers in diamond*, MRS Bulletin 38, 155 (2013),
URL: https://dx.doi.org/10.1557/mrs.2013.23

[174] M. W. Doherty, F. Dolde, H. Fedder, F. Jelezko, J. Wrachtrup, N. B. Manson, and L. C. L. Hollenberg, *Theory of the ground state spin of the NV- center in diamond: I. Fine structure, hyperfine structure, and interactions with electric, magnetic and strain fields*, Physical Review B 85, 205203 (2012),
URL: https://dx.doi.org/10.1103/PhysRevB.85.205203

[175] L. J. Rogers, R. L. McMurtrie, M. J. Sellars, and N. B. Manson, *Time-averaging within the excited state of the nitrogen-vacancy centre in diamond*, New Journal of Physics 11, 063007 (2009),
URL: https://dx.doi.org/10.1088/1367-2630/11/6/063007

[176] V. A. Acosta, *Optical Magnetometry with Nitrogen-Vacancy Centers in Diamond*, PhD thesis, University of California, Berkeley, (2011)

[177] K. Beha, A. Batalov, N. B. Manson, R. Bratschitsch, and A. Leitenstorfer, *Optimum Photoluminescence Excitation and Recharging Cycle of Single Nitrogen-Vacancy Centers in Ultrapure Diamond*, Physical Review Letters 109, 097404 (2012),
URL: https://dx.doi.org/10.1103/PhysRevLett.109.097404

[178] Y. Dumeige, R. Alléaume, P. Grangier, F. Treussart, and J.-F. Roch, *Controlling the single-diamond nitrogen-vacancy color center photoluminescence spectrum with a Fabry-Perot microcavity*, New Journal of Physics 13, 025015 (2011),
URL: https://dx.doi.org/10.1088/1367-2630/13/2/025015

[179] C. Santori, D. Fattal, and Y. Yamamoto, *Single-photon devices and applications*, Wiley-VCH, (2010)

[180] A. Batalov, V. Jacques, F. Kaiser, P. Siyushev, P. Neumann, L. J. Rogers, R. L. McMurtrie, N. B. Manson, F. Jelezko, and J. Wrachtrup, *Low Temperature Studies of the Excited-State Structure of Negatively Charged Nitrogen-Vacancy Color Centers in Diamond*, Physical Review Letters 102, 195506 (2009),
URL: https://dx.doi.org/10.1103/PhysRevLett.102.195506

[181] R. Ulbricht, S. Dong, A. Gali, S. Meng, and Z.-H. Loh, *Vibrational relaxation dynamics of the nitrogen-vacancy center in diamond*, Physical Review B 97, 220302 (2018),
URL: https://dx.doi.org/10.1103/PhysRevB.97.220302

[182] A. Batalov, C. Zierl, T. Gaebel, P. Neumann, I.-Y. Chan, G. Balasubramanian, P. R. Hemmer, F. Jelezko, and J. Wrachtrup, *Temporal Coherence of Photons Emitted by Single Nitrogen-Vacancy Defect Centers in Diamond Using Optical Rabi-Oscillations*, Physical Review Letters 100, 077401 (2008),
URL: https://dx.doi.org/10.1103/PhysRevLett.100.077401

[183] L. Robledo, H. Bernien, T. van der Sar, and R. Hanson, *Spin dynamics in the optical cycle of single nitrogen-vacancy centres in diamond*, New Journal of Physics 13, 025013 (2011),
URL: https://dx.doi.org/10.1088/1367-2630/13/2/025013

[184] R. Ulbricht and Z.-H. Loh, *Excited-state lifetime of the* NV^- *infrared transition in diamond*, Physical Review B 98, 094309 (2018),
URL: https://dx.doi.org/10.1103/PhysRevB.98.094309

[185] Ádám Gali, *Ab initio theory of the nitrogen-vacancy center in diamond*, Nanophotonics 8, 1907 (2019),
URL: https://dx.doi.org/10.1515/nanoph-2019-0154

[186] J.-P. Tetienne, L. Rondin, P. Spinicelli, M. Chipaux, T. Debuisschert, J.-F. Roch, and V. Jacques, *Magnetic-field-dependent photodynamics of single NV defects in diamond: an application to qualitative all-optical magnetic imaging*,

New Journal of Physics 14, 103033 (2012),
URL: https://dx.doi.org/10.1088/1367-2630/14/10/103033

[187] L. J. Rogers, M. W. Doherty, M. S. J. Barson, S. Onoda, T. Ohshima, and N. B. Manson, *Singlet levels of the NV-centre in diamond*, New Journal of Physics 17, 013048 (2015),
URL: https://dx.doi.org/10.1088/1367-2630/17/1/013048

[188] L. J. Rogers, S. Armstrong, M. J. Sellars, and N. B. Manson, *Infrared emission of the NV centre in diamond: Zeeman and uniaxial stress studies*, New Journal of Physics 10, 103024 (2008),
URL: https://dx.doi.org/10.1088/1367-2630/10/10/103024

[189] J. Harrison, M. Sellars, and N. Manson, *Measurement of the optically induced spin polarisation of NV centres in diamond*, Diamond and Related Materials 15, 586 (2006),
URL: https://dx.doi.org/10.1016/j.diamond.2005.12.027

[190] V. M. Acosta, E. Bauch, M. P. Ledbetter, C. Santori, K.-M. C. Fu, P. E. Barclay, R. G. Beausoleil, H. Linget, J. F. Roch, F. Treussart, S. Chemerisov, W. Gawlik, and D. Budker, *Diamonds with a high density of nitrogen-vacancy centers for magnetometry applications*, Physical Review B 80, 115202 (2009),
URL: https://dx.doi.org/10.1103/PhysRevB.80.115202

[191] F. Jelezko, I. Popa, A. Gruber, C. Tietz, J. Wrachtrup, A. Nizovtsev, and S. Kilin, *Single spin states in a defect center resolved by optical spectroscopy*, Applied Physics Letters 81, 2160 (2002),
URL: https://dx.doi.org/10.1063/1.1507838

[192] P. Neumann, *Towards a room temperature solid state quantum processor - The nitrogen-vacancy center in diamond*, PhD thesis, University of Stuttgart, (2011)

[193] L. Rondin, J.-P. Tetienne, T. Hingant, J.-F. Roch, P. Maletinsky, and V. Jacques, *Magnetometry with nitrogen-vacancy defects in diamond*, Re-

ports on Progress in Physics 77, 056503 (2014),
URL: https://dx.doi.org/10.1088/0034-4885/77/5/056503

[194] B. Rose, C. Weis, A. Tyryshkin, T. Schenkel, and S. Lyon, *Spin coherence and ^{14}N ESEEM effects of nitrogen-vacancy centers in diamond with X-band pulsed ESR*, Diamond and Related Materials 72, 32 (2017),
URL: https://dx.doi.org/10.1016/j.diamond.2016.12.009

[195] V. M. Acosta, E. Bauch, M. P. Ledbetter, A. Waxman, L.-S. Bouchard, and D. Budker, *Temperature Dependence of the Nitrogen-Vacancy Magnetic Resonance in Diamond*, Physical Review Letters 104, 070801 (2010),
URL: https://dx.doi.org/10.1103/PhysRevLett.104.070801

[196] B. Smeltzer, L. Childress, and A. Gali, *13 C hyperfine interactions in the nitrogen-vacancy centre in diamond*, New Journal of Physics 13, 025021 (2011),
URL: https://dx.doi.org/10.1088/1367-2630/13/2/025021

[197] S. Felton, A. M. Edmonds, M. E. Newton, P. M. Martineau, D. Fisher, D. J. Twitchen, and J. M. Baker, *Hyperfine interaction in the ground state of the negatively charged nitrogen vacancy center in diamond*, Physical Review B 79, 075203 (2009),
URL: https://dx.doi.org/10.1103/PhysRevB.79.075203

[198] C. S. Shin, M. C. Butler, H.-J. Wang, C. E. Avalos, S. J. Seltzer, R.-B. Liu, A. Pines, and V. S. Bajaj, *Optically detected nuclear quadrupolar interaction of ^{14}N in nitrogen-vacancy centers in diamond*, Physical Review B 89, 205202 (2014),
URL: https://dx.doi.org/10.1103/PhysRevB.89.205202

[199] M. Steiner, P. Neumann, J. Beck, F. Jelezko, and J. Wrachtrup, *Universal enhancement of the optical readout fidelity of single electron spins at nitrogen-vacancy centers in diamond*, Physical Review B 81, 035205 (2010),
URL: https://dx.doi.org/10.1103/PhysRevB.81.035205

[200] E. V. Levine, M. J. Turner, P. Kehayias, C. A. Hart, N. Langellier, R. Trubko, D. R. Glenn, R. R. Fu, and R. L. Walsworth, *Principles and techniques of the*

quantum diamond microscope, Nanophotonics 8, 209 (2019),
URL: https://dx.doi.org/10.1515/nanoph-2019-0209

[201] J. R. Rabeau, P. Reichart, G. Tamanyan, D. N. Jamieson, S. Prawer, F. Jelezko, T. Gaebel, I. Popa, M. Domhan, and J. Wrachtrup, *Implantation of labelled single nitrogen vacancy centers in diamond using N15*, Applied Physics Letters 88, (2006),
URL: https://dx.doi.org/10.1063/1.2158700

[202] H. Zheng, J. Xu, G. Z. Iwata, T. Lenz, J. Michl, B. Yavkin, K. Nakamura, H. Sumiya, T. Ohshima, J. Isoya, J. Wrachtrup, A. Wickenbrock, and D. Budker, *Zero-Field Magnetometry Based on Nitrogen-Vacancy Ensembles in Diamond*, Physical Review Applied 11, 064068 (2019),
URL: https://dx.doi.org/10.1103/PhysRevApplied.11.064068

[203] E. Abe and K. Sasaki, *Tutorial: Magnetic resonance with nitrogen-vacancy centers in diamond-microwave engineering, materials science, and magnetometry*, Journal of Applied Physics 123, 161101 (2018),
URL: https://dx.doi.org/10.1063/1.5011231

[204] T. Plakhotnik, *Diamonds for quantum nano sensing*, Current Opinion in Solid State and Materials Science 21, 25 (2017),
URL: https://dx.doi.org/10.1016/j.cossms.2016.08.001

[205] H. Zheng, Z. Sun, G. Chatzidrosos, C. Zhang, K. Nakamura, H. Sumiya, T. Ohshima, J. Isoya, J. Wrachtrup, A. Wickenbrock, and D. Budker, *Microwave-Free Vector Magnetometry with Nitrogen-Vacancy Centers along a Single Axis in Diamond*, Physical Review Applied 13, 044023 (2020),
URL: https://dx.doi.org/10.1103/PhysRevApplied.13.044023

[206] G. Chatzidrosos, J. S. Rebeirro, H. Zheng, M. Omar, A. Brenneis, F. M. Stürner, T. Fuchs, T. Buck, R. Rölver, T. Schneemann, P. Blümler, D. Budker, and A. Wickenbrock, *Fiberized Diamond-Based Vector Magnetometers*, Frontiers in Photonics 2, 4 (2021),
URL: https://dx.doi.org/10.3389/fphot.2021.732748

[207] G. Balasubramanian, I. Y. Chan, R. Kolesov, M. Al-Hmoud, J. Tisler, C. Shin, C. Kim, A. Wojcik, P. R. Hemmer, A. Krueger, T. Hanke, A. Leitenstorfer, R. Bratschitsch, F. Jelezko, and J. Wrachtrup, *Nanoscale imaging magnetometry with diamond spins under ambient conditions*, Nature 455, 648 (2008), URL: https://dx.doi.org/10.1038/nature07278

[208] A. Dréau, M. Lesik, L. Rondin, P. Spinicelli, O. Arcizet, J.-F. Roch, and V. Jacques, *Avoiding power broadening in optically detected magnetic resonance of single NV defects for enhanced dc magnetic field sensitivity*, Physical Review B 84, 195204 (2011), URL: https://dx.doi.org/10.1103/PhysRevB.84.195204

[209] N. Aslam, M. Pfender, R. Stöhr, P. Neumann, M. Scheffler, H. Sumiya, H. Abe, S. Onoda, T. Ohshima, J. Isoya, and J. Wrachtrup, *Single spin optically detected magnetic resonance with 60-90 GHz (E-band) microwave resonators*, Review of Scientific Instruments 86 (2015), URL: https://dx.doi.org/10.1063/1.4922664

[210] N. F. Ramsey, *A Molecular Beam Resonance Method with Separated Oscillating Fields*, Physical Review 78, 695 (1950), URL: https://dx.doi.org/10.1103/PhysRev.78.695

[211] J. Webb, L. Troise, N. W. Hansen, J. Achard, O. Brinza, R. Staacke, M. Kieschnick, J. Meijer, J.-F. Perrier, K. Berg Sørensen, A. Huck, and U. L. Andersen, *Sensing of magnetic fields from biological signals using diamond nitrogen vacancy centres*, arXiv preprint, arXiv:2004.02279 (2020), URL: https://arxiv.org/abs/2004.02279v1

[212] E. Bourgeois, A. Jarmola, P. Siyushev, M. Gulka, J. Hruby, F. Jelezko, D. Budker, and M. Nesladek, *Photoelectric detection of electron spin resonance of nitrogen-vacancy centres in diamond*, Nature Communications 6, 8577 (2015), URL: https://dx.doi.org/10.1038/ncomms9577

[213] J. M. Schloss, J. F. Barry, M. J. Turner, and R. L. Walsworth, *Simultaneous Broadband Vector Magnetometry Using Solid-State Spins*, Physical Review Applied 10, 034044 (2018),
URL: https://dx.doi.org/10.1103/PhysRevApplied.10.034044

[214] M. I. Ibrahim, C. Foy, D. R. Englund, and R. Han, *29.2 A Scalable Quantum Magnetometer in 65nm CMOS with Vector-Field Detection Capability*, in IEEE International Solid- State Circuits Conference (ISSCC), pp. 458–461, (2019),
URL: https://dx.doi.org/10.1109/ISSCC.2019.8662434

[215] P. Maletinsky and V. Jacques, *Diamond magnetic sensors*, in Quantum Information Processing with Diamond, pp. 240–263, Elsevier, (2014),

[216] L. M. Pham, *Magnetic Field Sensing with Nitrogen-Vacancy Color Centers in Diamond*, PhD thesis, Harvard University, (2013)

[217] K. Jensen, P. Kehayias, and D. Budker, *Magnetometry with Nitrogen-Vacancy Centers in Diamond*, in High sensitivity magnetometers, volume 19, pp. 553–576, Springer International Publishing, (2017)

[218] F. M. Stürner, A. Brenneis, J. Kassel, U. Wostradowski, R. Rölver, T. Fuchs, K. Nakamura, H. Sumiya, S. Onoda, J. Isoya, and F. Jelezko, *Compact integrated magnetometer based on nitrogen-vacancy centres in diamond*, Diamond and Related Materials 93, 59 (2019),
URL: https://dx.doi.org/10.1016/j.diamond.2019.01.008

[219] T.-L. Wee, Y.-K. Tzeng, C.-C. Han, H.-C. Chang, W. Fann, J.-H. Hsu, K.-M. Chen, and Y.-C. Yu, *Two-photon Excited Fluorescence of Nitrogen-Vacancy Centers in Proton-Irradiated Type Ib Diamond*, The Journal of Physical Chemistry A 111, 9379 (2007),
URL: https://dx.doi.org/10.1021/jp073938o

[220] J. Zheng, A. C. Liapis, E. H. Chen, C. T. Black, and D. Englund, *Chirped circular dielectric gratings for near-unity collection efficiency from quantum*

emitters in bulk diamond, Optics Express 25, 32420 (2017),
URL: https://dx.doi.org/10.1364/OE.25.032420

[221] G. Waldherr, J. Beck, M. Steiner, P. Neumann, A. Gali, T. Frauenheim, F. Jelezko, and J. Wrachtrup, *Dark States of Single Nitrogen-Vacancy Centers in Diamond Unraveled by Single Shot NMR*, Physical Review Letters 106, 157601 (2011),
URL: https://dx.doi.org/10.1103/PhysRevLett.106.157601

[222] I. P. Radko, M. Boll, N. M. Israelsen, N. Raatz, J. Meijer, F. Jelezko, U. L. Andersen, and A. Huck, *Determining the internal quantum efficiency of shallow-implanted nitrogen-vacancy defects in bulk diamond*, Optics Express 24, 27715 (2016),
URL: https://dx.doi.org/10.1364/OE.24.027715

[223] K. Jensen, V. M. Acosta, A. Jarmola, and D. Budker, *Light narrowing of magnetic resonances in ensembles of nitrogen-vacancy centers in diamond*, Physical Review B 87, 014115 (2013),
URL: https://dx.doi.org/10.1103/PhysRevB.87.014115

[224] K. Fang, V. M. Acosta, C. Santori, Z. Huang, K. M. Itoh, H. Watanabe, S. Shikata, and R. G. Beausoleil, *High-Sensitivity Magnetometry Based on Quantum Beats in Diamond Nitrogen-Vacancy Centers*, Physical Review Letters 110, 130802 (2013),
URL: https://dx.doi.org/10.1103/PhysRevLett.110.130802

[225] A. M. Edmonds, C. A. Hart, M. J. Turner, P.-O. Colard, J. M. Schloss, K. Olsson, R. Trubko, M. L. Markham, A. Rathmill, B. Horne-Smith, et al., *Generation of nitrogen-vacancy ensembles in diamond for quantum sensors: Optimization and scalability of CVD processes*, arXiv preprint, arXiv:2004.01746 (2020),
URL: https://arxiv.org/abs/2004.01746

[226] P. Jamonneau, M. Lesik, J. P. Tetienne, I. Alvizu, L. Mayer, A. Dréau, S. Kosen, J.-F. Roch, S. Pezzagna, J. Meijer, T. Teraji, Y. Kubo, P. Bertet,

J. R. Maze, and V. Jacques, *Competition between electric field and magnetic field noise in the decoherence of a single spin in diamond*, Physical Review B 93, 024305 (2016),
URL: https://dx.doi.org/10.1103/PhysRevB.93.024305

[227] S. Eaton−Magaña, J. E Shigley, and C. M Breeding, *Observations on HPHT-Grown Synthetic Diamonds: A Review*, Gems and Gemology 53 (2017),
URL: https://dx.doi.org/10.5741/GEMS.53.3.262

[228] N. Mizuochi, P. Neumann, F. Rempp, J. Beck, V. Jacques, P. Siyushev, K. Nakamura, D. J. Twitchen, H. Watanabe, S. Yamasaki, F. Jelezko, and J. Wrachtrup, *Coherence of single spins coupled to a nuclear spin bath of varying density*, Physical Review B 80, 041201 (2009),
URL: https://dx.doi.org/10.1103/PhysRevB.80.041201

[229] C. Grezes, B. Julsgaard, Y. Kubo, W. L. Ma, M. Stern, A. Bienfait, K. Nakamura, J. Isoya, S. Onoda, T. Ohshima, V. Jacques, D. Vion, D. Esteve, R. B. Liu, K. Mølmer, and P. Bertet, *Storage and retrieval of microwave fields at the single-photon level in a spin ensemble*, Physical Review A 92, 020301 (2015),
URL: https://dx.doi.org/10.1103/PhysRevA.92.020301

[230] V. M. Acosta, K. Jensen, C. Santori, D. Budker, and R. G. Beausoleil, *Electromagnetically Induced Transparency in a Diamond Spin Ensemble Enables All-Optical Electromagnetic Field Sensing*, Physical Review Letters 110, 213605 (2013),
URL: https://dx.doi.org/10.1103/PhysRevLett.110.213605

[231] P. Kehayias, M. Mrózek, V. M. Acosta, A. Jarmola, D. S. Rudnicki, R. Folman, W. Gawlik, and D. Budker, *Microwave saturation spectroscopy of nitrogen-vacancy ensembles in diamond*, Physical Review B 89, 245202 (2014),
URL: https://dx.doi.org/10.1103/PhysRevB.89.245202

[232] R. Rubinas, V. V. Vorobyov, V. V. Soshenko, S. V. Bolshedvorskii, V. N. Sorokin, A. N. Smolyaninov, V. G. Vins, A. P. Yelisseyev, and A. V. Akimov,

Spin properties of NV centers in high-pressure, high-temperature grown diamond, Journal of Physics Communications 2, 115003 (2018),
URL: https://dx.doi.org/10.1088/2399-6528/aae992

[233] B. Naydenov, F. Reinhard, A. Lämmle, V. Richter, R. Kalish, U. F. S. D'Haenens-Johansson, M. Newton, F. Jelezko, and J. Wrachtrup, *Increasing the coherence time of single electron spins in diamond by high temperature annealing*, Applied Physics Letters 97, 242511 (2010),
URL: https://dx.doi.org/10.1063/1.3527975

[234] E. E. Kleinsasser, M. M. Stanfield, J. K. Q. Banks, Z. Zhu, W.-D. Li, V. M. Acosta, H. Watanabe, K. M. Itoh, and K.-M. C. Fu, *High density nitrogen-vacancy sensing surface created via He+ ion implantation of 12C diamond*, Applied Physics Letters 108, 202401 (2016),
URL: https://dx.doi.org/10.1063/1.4949357

[235] H. Clevenson, M. E. Trusheim, C. Teale, T. Schröder, D. Braje, and D. Englund, *Broadband magnetometry and temperature sensing with a light-trapping diamond waveguide*, Nature Physics 11, 393 (2015),
URL: https://dx.doi.org/10.1038/nphys3291

[236] L. Xie, T. X. Zhou, R. J. Stöhr, and A. Yacoby, *Crystallographic Orientation Dependent Reactive Ion Etching in Single Crystal Diamond*, Advanced Materials 30, 1705501 (2018),
URL: https://dx.doi.org/10.1002/adma.201705501

[237] P. Appel, E. Neu, M. Ganzhorn, A. Barfuss, M. Batzer, M. Gratz, A. Tschöpe, and P. Maletinsky, *Fabrication of all diamond scanning probes for nanoscale magnetometry*, Review of Scientific Instruments 87, 063703 (2016),
URL: https://dx.doi.org/10.1063/1.4952953

[238] H. A. Atikian, A. Eftekharian, A. Jafari Salim, M. J. Burek, J. T. Choy, A. Hamed Majedi, and M. Lončar, *Superconducting nanowire single photon detector on diamond*, Applied Physics Letters 104, 122602 (2014),
URL: https://dx.doi.org/10.1063/1.4869574

[239] H. Ozawa, K. Tahara, H. Ishiwata, M. Hatano, and T. Iwasaki, *Formation of perfectly aligned nitrogen-vacancy-center ensembles in chemical-vapor-deposition-grown diamond (111)*, Applied Physics Express 10, 045501 (2017), URL: https://dx.doi.org/10.7567/APEX.10.045501

[240] C. Osterkamp, M. Mangold, J. Lang, P. Balasubramanian, T. Teraji, B. Naydenov, and F. Jelezko, *Engineering preferentially-aligned nitrogen-vacancy centre ensembles in CVD grown diamond*, Scientific Reports 9, 5786 (2019), URL: https://dx.doi.org/10.1038/s41598-019-42314-7

[241] D. Duan, V. K. Kavatamane, S. R. Arumugam, G. Rahane, G.-X. Du, Y.-K. Tzeng, H.-C. Chang, and G. Balasubramanian, *Laser-induced heating in a high-density ensemble of nitrogen-vacancy centers in diamond and its effects on quantum sensing*, Optics Letters 44, 2851 (2019), URL: https://dx.doi.org/10.1364/OL.44.002851

[242] C.-K. Lin, Y.-H. Wang, H.-C. Chang, M. Hayashi, and S. H. Lin, *One- and two-photon absorption properties of diamond nitrogen-vacancy defect centers: A theoretical study*, The Journal of Chemical Physics 129, 124714 (2008), URL: https://dx.doi.org/10.1063/1.2987717

[243] N. B. Manson, M. Hedges, M. S. J. Barson, R. Ahlefeldt, M. W. Doherty, H. Abe, T. Ohshima, and M. J. Sellars, *NV^-–N^+ pair centre in 1b diamond*, New Journal of Physics 20, 113037 (2018), URL: https://dx.doi.org/10.1088/1367-2630/aaec58

[244] M. Mrózek, D. Rudnicki, P. Kehayias, A. Jarmola, D. Budker, and W. Gawlik, *Longitudinal spin relaxation in nitrogen-vacancy ensembles in diamond*, EPJ Quantum Technology 2, 22 (2015), URL: https://dx.doi.org/10.1140/epjqt/s40507-015-0035-z

[245] A. Wickenbrock, H. Zheng, L. Bougas, N. Leefer, S. Afach, A. Jarmola, V. M. Acosta, and D. Budker, *Microwave-free magnetometry with nitrogen-vacancy centers in diamond*, Applied Physics Letters 109, 053505 (2016), URL: https://dx.doi.org/10.1063/1.4960171

[246] N. Sadzak, M. Héritier, and O. Benson, *Coupling a Single Nitrogen-Vacancy Center in Nanodiamond to Superparamagnetic Nanoparticles*, Scientific Reports 8, 8430 (2018),
URL: https://dx.doi.org/10.1038/s41598-018-26633-9

[247] H. Raich and P. Blümler, *Design and construction of a dipolar Halbach array with a homogeneous field from identical bar magnets: NMR Mandhalas*, Concepts in Magnetic Resonance Part B: Magnetic Resonance Engineering 23B, 16 (2004),
URL: https://dx.doi.org/10.1002/cmr.b.20018

[248] A. Wickenbrock, H. Zheng, G. Chatzidrosos, J. Shaji Rebeirro, T. Schneemann, and P. Blümler, *High homogeneity permanent magnet for diamond magnetometry*, Journal of Magnetic Resonance 322, 106867 (2021),
URL: https://dx.doi.org/10.1016/j.jmr.2020.106867

[249] J. Mu, Z. Qu, Z. Ma, S. Zhang, Y. Shi, J. Gao, X. Zhang, H. Cao, li Qin, J. Liu, and Y. Li, *Ensemble spin fabrication and manipulation of NV centres for magnetic sensing in diamond*, Sensor Review 37, 419 (2017),
URL: https://dx.doi.org/10.1108/SR-09-2016-0163

[250] T. Watanabe, T. Taniuchi, S. Takano, T. Aoki, and K. Fukami, *Permanent magnet based dipole magnets for next generation light sources*, Physical Review Accelerators and Beams 20, 072401 (2017),
URL: https://dx.doi.org/10.1103/PhysRevAccelBeams.20.072401

[251] J. Herrmann, M. A. Appleton, K. Sasaki, Y. Monnai, T. Teraji, K. M. Itoh, and E. Abe, *Polarization- and frequency-tunable microwave circuit for selective excitation of nitrogen-vacancy spins in diamond*, Applied Physics Letters 109, 183111 (2016),
URL: https://dx.doi.org/10.1063/1.4967378

[252] M. Mrozek, J. Mlynarczyk, D. S. Rudnicki, and W. Gawlik, *Circularly polarized microwaves for magnetic resonance study in the GHz range: Application*

to nitrogen-vacancy in diamonds, Applied Physics Letters 107, 013505 (2015), URL: https://dx.doi.org/10.1063/1.4923252

[253] X. Yang, N. Zhang, H. Yuan, G. Bian, P. Fan, and M. Li, *Microstrip-line resonator with broadband, circularly polarized, uniform microwave field for nitrogen vacancy center ensembles in diamond*, AIP Advances 9, 075213 (2019), URL: https://dx.doi.org/10.1063/1.5099651

[254] M. I. Ibrahim, C. Foy, D. R. Englund, and R. Han, *High-Scalability CMOS Quantum Magnetometer With Spin-State Excitation and Detection of Diamond Color Centers*, IEEE Journal of Solid-State Circuits 56, 1001 (2021), URL: https://dx.doi.org/10.1109/JSSC.2020.3027056

[255] P. Kapitanova, V. V. Soshenko, V. V. Vorobyov, D. Dobrykh, S. V. Bolshedvorskii, V. N. Sorokin, and A. V. Akimov, *3D Uniform Manipulation of NV Centers in Diamond Using Dielectric Resonator Antenna*, JETP Letters 108, 588 (2018), URL: https://dx.doi.org/10.1134/S0021364018210014

[256] E. R. Eisenach, J. F. Barry, L. M. Pham, R. G. Rojas, D. R. Englund, and D. A. Braje, *Broadband loop gap resonator for nitrogen vacancy centers in diamond*, Review of Scientific Instruments 89, 094705 (2018), URL: https://dx.doi.org/10.1063/1.5037465

[257] K. Bayat, J. Choy, M. Farrokh Baroughi, S. Meesala, and M. Lončar, *Efficient, Uniform, and Large Area Microwave Magnetic Coupling to NV Centers in Diamond Using Double Split-Ring Resonators*, Nano Letters 14, 1208 (2014), URL: https://dx.doi.org/10.1021/nl404072s

[258] W. Jia, Z. Shi, X. Qin, X. Rong, and J. Du, *Ultra-broadband coplanar waveguide for optically detected magnetic resonance of nitrogen-vacancy centers in diamond*, Review of Scientific Instruments 89, 064705 (2018), URL: https://dx.doi.org/10.1063/1.5028335

[259] K. Sasaki, Y. Monnai, S. Saijo, R. Fujita, H. Watanabe, J. Ishi-Hayase, K. M. Itoh, and E. Abe, *Broadband, large-area microwave antenna for optically*

detected magnetic resonance of nitrogen-vacancy centers in diamond, Review of Scientific Instruments 87, 053904 (2016),
URL: https://dx.doi.org/10.1063/1.4952418

[260] N. Zhang, H. Yuan, C. Zhang, L. Xu, J. Zhang, G. Bian, B. Li, and J. Fang, *Robust frequency calibration of a large-area high-Q resonator in magnetic imaging with spin ensembles in diamond*, Applied Physics Express 11, 086602 (2018),
URL: https://dx.doi.org/10.7567/apex.11.086602

[261] N. Zhang, C. Zhang, L. Xu, M. Ding, W. Quan, Z. Tang, and H. Yuan, *Microwave magnetic field coupling with nitrogen-vacancy center ensembles in diamond with high homogeneity*, Applied Magnetic Resonance 47, 589 (2016),
URL: https://dx.doi.org/10.1007/s00723-016-0777-5

[262] P. Andrich, C. F. de las Casas, X. Liu, H. L. Bretscher, J. R. Berman, F. J. Heremans, P. F. Nealey, and D. D. Awschalom, *Long-range spin wave mediated control of defect qubits in nanodiamonds*, npj Quantum Information 3, 28 (2017),
URL: https://dx.doi.org/10.1038/s41534-017-0029-z

[263] C. Zhang, H. Yuan, N. Zhang, L. Xu, J. Zhang, B. Li, and J. Fang, *Vector magnetometer based on synchronous manipulation of nitrogen-vacancy centers in all crystal directions*, Journal of Physics D: Applied Physics 51, 155102 (2018),
URL: https://dx.doi.org/10.1088/1361-6463/aab2d0

[264] Y. Twig, E. Suhovoy, and A. Blank, *Sensitive surface loop-gap microresonators for electron spin resonance*, Review of Scientific Instruments 81, 104703 (2010),
URL: https://dx.doi.org/10.1063/1.3488365

[265] N. Zhang, H. Yuan, C. Zhang, L. Xu, J. Zhang, G. Bian, P. Fan, H. Yuan, and J. Fang, *Microwave Field Uniformity Impact on DC Magnetic Sensing With NV Ensembles in Diamond*, IEEE Sensors Journal 19, 451 (2019),
URL: https://dx.doi.org/10.1109/JSEN.2018.2878220

[266] A. Horsley, P. Appel, J. Wolters, J. Achard, A. Tallaire, P. Maletinsky, and P. Treutlein, *Microwave Device Characterization Using a Widefield Diamond Microscope*, Physical Review Applied 10, 044039 (2018),
URL: https://dx.doi.org/10.1103/PhysRevApplied.10.044039

[267] D. A. Simpson, R. G. Ryan, L. T. Hall, E. Panchenko, S. C. Drew, S. Petrou, P. S. Donnelly, P. Mulvaney, and L. C. L. Hollenberg, *Electron paramagnetic resonance microscopy using spins in diamond under ambient conditions*, Nature Communications 8, 458 (2017),
URL: https://dx.doi.org/10.1038/s41467-017-00466-y

[268] B. S. Miller, L. Bezinge, H. D. Gliddon, D. Huang, G. Dold, E. R. Gray, J. Heaney, P. J. Dobson, E. Nastouli, J. J. L. Morton, and R. A. McKendry, *Spin-enhanced nanodiamond biosensing for ultrasensitive diagnostics*, Nature 587, 588 (2020),
URL: https://dx.doi.org/10.1038/s41586-020-2917-1

[269] V. R. Horowitz, B. J. Alemán, D. J. Christle, A. N. Cleland, and D. D. Awschalom, *Electron spin resonance of nitrogen-vacancy centers in optically trapped nanodiamonds*, 109, 13493 (2012),
URL: https://dx.doi.org/10.1073/pnas.1211311109

[270] V. Yaroshenko, A. Zalogina, D. Zuev, P. Kapitanova, and I. Shadrivov, *Circularly polarized antenna for coherent manipulation of NV-centers in diamond*, Journal of Physics: Conference Series 1092, 012168 (2018),
URL: https://dx.doi.org/10.1088/1742-6596/1092/1/012168

[271] S. Ahmadi, H. A. R. El-Ella, J. O. B. Hansen, A. Huck, and U. L. Andersen, *Pump-Enhanced Continuous-Wave Magnetometry Using Nitrogen-Vacancy Ensembles*, Physical Review Applied 8, 034001 (2017),
URL: https://dx.doi.org/10.1103/PhysRevApplied.8.034001

[272] H. Zheng, G. Chatzidrosos, A. Wickenbrock, L. Bougas, R. Lazda, A. Berzins, F. H. Gahbauer, M. Auzinsh, R. Ferber, and D. Budker, *Level anti-crossing magnetometry with color centers in diamond*, in Society of Photo-Optical

Instrumentation Engineers (SPIE) Conference Series, volume 10119 of *Society of Photo-Optical Instrumentation Engineers (SPIE) Conference Series*, p. 101190X, (2017),
URL: https://dx.doi.org/10.1117/12.2261160

[273] D. A. Hopper, H. J. Shulevitz, and L. C. Bassett, *Spin Readout Techniques of the Nitrogen-Vacancy Center in Diamond*, Micromachines 9 (2018),
URL: https://dx.doi.org/10.3390/mi9090437

[274] D. Le Sage, L. M. Pham, N. Bar-Gill, C. Belthangady, M. D. Lukin, A. Yacoby, and R. L. Walsworth, *Efficient photon detection from color centers in a diamond optical waveguide*, Physical Review B 85, 121202 (2012),
URL: https://dx.doi.org/10.1103/PhysRevB.85.121202

[275] R. N. Patel, T. Schröder, N. Wan, L. Li, S. L. Mouradian, E. H. Chen, and D. R. Englund, *Efficient photon coupling from a diamond nitrogen vacancy center by integration with silica fiber*, Light: Science & Applications 5, e16032 (2016),
URL: https://dx.doi.org/10.1038/lsa.2016.32

[276] N. M. Israelsen, S. Kumar, M. Tawfieq, J. S. Neergaard-Nielsen, A. Huck, and U. L. Andersen, *Increasing the photon collection rate from a single NV center with a silver mirror*, Journal of Optics 16, 114017 (2014),
URL: https://dx.doi.org/10.1088/2040-8978/16/11/114017

[277] L. Marseglia, J. P. Hadden, A. C. Stanley-Clarke, J. P. Harrison, B. Patton, Y.-L. D. Ho, B. Naydenov, F. Jelezko, J. Meijer, P. R. Dolan, J. M. Smith, J. G. Rarity, and J. L. O'Brien, *Nanofabricated solid immersion lenses registered to single emitters in diamond*, Applied Physics Letters 98, 133107 (2011),
URL: https://dx.doi.org/10.1063/1.3573870

[278] J. Hadden, J. Harrison, A. Stanley-Clarke, L. Marseglia, Y.-L. Ho, B. Patton, J. O'Brien, and J. Rarity, *Strongly enhanced photon collection from diamond defect centers under microfabricated integrated solid immersion lenses*, Ap-

plied Physics Letters 97, 241901 (2010),
URL: https://dx.doi.org/10.1063/1.3519847

[279] A. W. Schell, T. Neumer, Q. Shi, J. Kaschke, J. Fischer, M. Wegener, and O. Benson, *Laser-written parabolic micro-antennas for efficient photon collection*, Applied Physics Letters 105, 231117 (2014),
URL: https://dx.doi.org/10.1063/1.4903804

[280] N. H. Wan, B. J. Shields, D. Kim, S. Mouradian, B. Lienhard, M. Walsh, H. Bakhru, T. Schröder, and D. Englund, *Efficient Extraction of Light from a Nitrogen-Vacancy Center in a Diamond Parabolic Reflector*, Nano Letters 18, 2787 (2018),
URL: https://dx.doi.org/10.1021/acs.nanolett.7b04684

[281] D. Riedel, D. Rohner, M. Ganzhorn, T. Kaldewey, P. Appel, E. Neu, R. J. Warburton, and P. Maletinsky, *Low-Loss Broadband Antenna for Efficient Photon Collection from a Coherent Spin in Diamond*, Physical Review Applied 2, 064011 (2014),
URL: https://dx.doi.org/10.1103/PhysRevApplied.2.064011

[282] L. Xu, J. Zhang, G. Bian, P. Fan, M. Li, Y. Liu, N. Zhang, and H. Yuan, *Enhancement of fluorescence from nitrogen-vacancy center ensemble in bulk diamond with broadband antireflection coatings*, AIP Advances 10, 085124 (2020),
URL: https://dx.doi.org/10.1063/5.0018433

[283] S. A. Momenzadeh, R. J. Stöhr, F. F. de Oliveira, A. Brunner, A. Denisenko, S. Yang, F. Reinhard, and J. Wrachtrup, *Nanoengineered Diamond Waveguide as a Robust Bright Platform for Nanomagnetometry Using Shallow Nitrogen Vacancy Centers*, Nano Letters 15, 165 (2015),
URL: https://dx.doi.org/10.1021/nl503326t

[284] J. T. Choy, I. Bulu, B. J. M. Hausmann, E. Janitz, I.-C. Huang, and M. Lončar, *Spontaneous emission and collection efficiency enhancement of single emitters in diamond via plasmonic cavities and gratings*, Applied Physics Letters 103,

161101 (2013),
URL: https://dx.doi.org/10.1063/1.4817397

[285] L. Li, E. H. Chen, J. Zheng, S. L. Mouradian, F. Dolde, T. Schröder, S. Karaveli, M. L. Markham, D. J. Twitchen, and D. Englund, *Efficient Photon Collection from a Nitrogen Vacancy Center in a Circular Bullseye Grating*, Nano Letters 15, 1493 (2015),
URL: https://dx.doi.org/10.1021/nl503451j

[286] L. Xu, H. Yuan, N. Zhang, J. Zhang, G. Bian, P. Fan, M. Li, C. Zhang, Y. Zhai, and J. Fang, *High-efficiency fluorescence collection for NV- center ensembles in diamond*, Optics Express 27, 10787 (2019),
URL: https://dx.doi.org/10.1364/OE.27.010787

[287] R. Nelz, P. Fuchs, O. Opaluch, S. Sonusen, N. Savenko, V. Podgursky, and E. Neu, *Color center fluorescence and spin manipulation in single crystal, pyramidal diamond tips*, Applied Physics Letters 109, 193105 (2016),
URL: https://dx.doi.org/10.1063/1.4967189

[288] B. J. Shields, Q. P. Unterreithmeier, N. P. de Leon, H. Park, and M. D. Lukin, *Efficient Readout of a Single Spin State in Diamond via Spin-to-Charge Conversion*, Physical Review Letters 114, 136402 (2015),
URL: https://dx.doi.org/10.1103/PhysRevLett.114.136402

[289] H. Jayakumar, S. Dhomkar, J. Henshaw, and C. A. Meriles, *Spin readout via spin-to-charge conversion in bulk diamond nitrogen-vacancy ensembles*, Applied Physics Letters 113, 122404 (2018),
URL: https://dx.doi.org/10.1063/1.5040261

[290] M. Gulka, E. Bourgeois, J. Hruby, P. Siyushev, G. Wachter, F. Aumayr, P. R. Hemmer, A. Gali, F. Jelezko, M. Trupke, and M. Nesladek, *Pulsed Photoelectric Coherent Manipulation and Detection of* N$-V$ *Center Spins in Diamond*, Physical Review Applied 7, 044032 (2017),
URL: https://dx.doi.org/10.1103/PhysRevApplied.7.044032

[291] F. M. Hrubesch, G. Braunbeck, M. Stutzmann, F. Reinhard, and M. S. Brandt, *Efficient Electrical Spin Readout of* NV^- *Centers in Diamond*, Physical Review Letters 118, 037601 (2017),
URL: https://dx.doi.org/10.1103/PhysRevLett.118.037601

[292] L. Jiang, J. S. Hodges, J. R. Maze, P. Maurer, J. M. Taylor, D. G. Cory, P. R. Hemmer, R. L. Walsworth, A. Yacoby, A. S. Zibrov, and M. D. Lukin, *Repetitive Readout of a Single Electronic Spin via Quantum Logic with Nuclear Spin Ancillae*, Science 326, 267 (2009),
URL: https://dx.doi.org/10.1126/science.1176496

[293] P. Neumann, J. Beck, M. Steiner, F. Rempp, H. Fedder, P. R. Hemmer, J. Wrachtrup, and F. Jelezko, *Single-Shot Readout of a Single Nuclear Spin*, Science 329, 542 (2010),
URL: https://dx.doi.org/10.1126/science.1189075

[294] Y. Dumeige, M. Chipaux, V. Jacques, F. Treussart, J.-F. Roch, T. Debuisschert, V. M. Acosta, A. Jarmola, K. Jensen, P. Kehayias, and D. Budker, *Magnetometry with nitrogen-vacancy ensembles in diamond based on infrared absorption in a doubly resonant optical cavity*, Physical Review B 87, 155202 (2013),
URL: https://dx.doi.org/10.1103/PhysRevB.87.155202

[295] V. M. Acosta, E. Bauch, A. Jarmola, L. J. Zipp, M. P. Ledbetter, and D. Budker, *Broadband magnetometry by infrared-absorption detection of nitrogen-vacancy ensembles in diamond*, Applied Physics Letters 97, 174104 (2010),
URL: https://dx.doi.org/10.1063/1.3507884

[296] J. Zhang, L. Xu, T. Shi, G. Bian, P. Fan, M. Li, P. Chen, C. Xu, N. Zhang, and H. Yuan, *An improved spin readout for nitrogen vacancy center ensemble based on a maximum likelihood estimation method*, Journal of Physics D: Applied Physics 53, 455305 (2020),
URL: https://dx.doi.org/10.1088/1361-6463/aba7de

[297] J. Jeske, J. H. Cole, and A. D. Greentree, *Laser threshold magnetometry*, New Journal of Physics 18, 013015 (2016),
URL: https://dx.doi.org/10.1088/1367-2630/18/1/013015

[298] J. Jeske, D. W. M. Lau, X. Vidal, L. P. McGuinness, P. Reineck, B. C. Johnson, M. W. Doherty, J. C. McCallum, S. Onoda, F. Jelezko, T. Ohshima, T. Volz, J. H. Cole, B. C. Gibson, and A. D. Greentree, *Stimulated emission from nitrogen-vacancy centres in diamond*, Nature Communications 8, 14000 (2017),
URL: https://dx.doi.org/10.1038/ncomms14000

[299] V. G. Savitski, *Optical gain in NV-colour centres for highly-sensitive magnetometry: a theoretical study*, Journal of Physics D: Applied Physics 50, 475602 (2017),
URL: https://dx.doi.org/10.1088/1361-6463/aa8e8e

[300] J. A. van Wyk, E. C. Reynhardt, G. L. High, and I. Kiflawi, *The dependences of ESR line widths and spin - spin relaxation times of single nitrogen defects on the concentration of nitrogen defects in diamond*, Journal of Physics D: Applied Physics 30, 1790 (1997),
URL: https://dx.doi.org/10.1088/0022-3727/30/12/016

[301] A. O. Levchenko, V. V. Vasil'ev, S. A. Zibrov, A. S. Zibrov, A. V. Sivak, and I. V. Fedotov, *Inhomogeneous broadening of optically detected magnetic resonance of the ensembles of nitrogen-vacancy centers in diamond by interstitial carbon atoms*, Applied Physics Letters 106, 102402 (2015),
URL: https://dx.doi.org/10.1063/1.4913428

[302] I. Moreno, M. Avendaño-Alejo, and R. I. Tzonchev, *Designing light-emitting diode arrays for uniform near-field irradiance*, Applied Optics 45, 2265 (2006),
URL: https://dx.doi.org/10.1364/AO.45.002265

[303] R. Chapman and T. Plakhotnik, *Quantitative luminescence microscopy on Nitrogen-Vacancy Centres in diamond: Saturation effects under pulsed excit-*

ation, Chemical Physics Letters 507, 190 (2011),
URL: https://dx.doi.org/10.1016/j.cplett.2011.03.057

[304] K. Sasaki, E. E. Kleinsasser, Z. Zhu, W.-D. Li, H. Watanabe, K.-M. C. Fu, K. M. Itoh, and E. Abe, *Dynamic nuclear polarization enhanced magnetic field sensitivity and decoherence spectroscopy of an ensemble of near-surface nitrogen-vacancy centers in diamond*, Applied Physics Letters 110, 192407 (2017),
URL: https://dx.doi.org/10.1063/1.4983350

[305] A. Jarmola, V. M. Acosta, K. Jensen, S. Chemerisov, and D. Budker, *Temperature- and Magnetic-Field-Dependent Longitudinal Spin Relaxation in Nitrogen-Vacancy Ensembles in Diamond*, Physical Review Letters 108, 197601 (2012),
URL: https://dx.doi.org/10.1103/PhysRevLett.108.197601

[306] D. W. Allan, *Should the classical variance be used as a basic measure in standards metrology?*, IEEE Transactions on Instrumentation and Measurement 36, 646 (1987),
URL: https://dx.doi.org/10.1109/TIM.1987.6312761

[307] Z. Ma, S. Zhang, Y. Fu, H. Yuan, Y. Shi, J. Gao, L. Qin, J. Tang, J. Liu, and Y. Li, *Magnetometry for precision measurement using frequency-modulation microwave combined efficient photon-collection technique on an ensemble of nitrogen-vacancy centers in diamond*, Optics Express 26, 382 (2018),
URL: https://dx.doi.org/10.1364/OE.26.000382

[308] D. Duan, V. K. Kavatamane, S. R. Arumugam, G. Rahane, Y.-K. Tzeng, H.-C. Chang, H. Sumiya, S. Onoda, J. Isoya, and G. Balasubramanian, *Enhancing fluorescence excitation and collection from the nitrogen-vacancy center in diamond through a micro-concave mirror*, Applied Physics Letters 113, 041107 (2018),
URL: https://dx.doi.org/10.1063/1.5037807

[309] I. V. Fedotov, L. V. Doronina-Amitonova, A. A. Voronin, A. O. Levchenko, S. A. Zibrov, D. A. Sidorov-Biryukov, A. B. Fedotov, V. L. Velichansky, and A. M. Zheltikov, *Electron spin manipulation and readout through an optical fiber*, Scientific Reports 4, 5362 (2014),
URL: https://dx.doi.org/10.1038/srep05362

[310] A. K. Dmitriev and A. K. Vershovskii, *Concept of a microscale vector magnetic field sensor based on nitrogen-vacancy centers in diamond*, Journal of the Optical Society of America B 33, B1 (2016),
URL: https://dx.doi.org/10.1364/JOSAB.33.0000B1

[311] L. Mayer and T. Debuisschert, *Direct optical interfacing of CVD diamond for deported sensing experiments involving nitrogen-vacancy centres*, physica status solidi (a) 213, 2608 (2016),
URL: https://dx.doi.org/10.1002/pssa.201600220

[312] H. A. R. El-Ella, S. Ahmadi, A. M. Wojciechowski, A. Huck, and U. L. Andersen, *Optimised frequency modulation for continuous-wave optical magnetic resonance sensing using nitrogen-vacancy ensembles*, Optics Express 25, 14809 (2017),
URL: https://dx.doi.org/10.1364/OE.25.014809

[313] H. J. Mamin, M. H. Sherwood, M. Kim, C. T. Rettner, K. Ohno, D. D. Awschalom, and D. Rugar, *Multipulse Double-Quantum Magnetometry with Near-Surface Nitrogen-Vacancy Centers*, Physical Review Letters 113, 030803 (2014),
URL: https://dx.doi.org/10.1103/PhysRevLett.113.030803

[314] M. W. Dale and G. W. Morley, *Medical applications of diamond magnetometry: commercial viability*, arXiv preprint, arXiv:1705.01994 (2017),
URL: https://arxiv.org/abs/1705.01994

[315] S. Maayani, C. Foy, D. Englund, and Y. Fink, *Distributed Quantum Fiber Magnetometry*, Laser & Photonics Reviews 13, 1900075 (2019),
URL: https://dx.doi.org/10.1002/lpor.201900075

[316] V. K. Shah and R. T. Wakai, *A compact, high performance atomic magnetometer for biomedical applications*, Physics in Medicine & Biology 58, 8153 (2013),
URL: https://dx.doi.org/10.1088/0031-9155/58/22/8153

[317] F. M. Stürner, Y. Liu, P.-O. Colard, M. Markham, and F. Jelezko, *Magnetometry based on the excited-state lifetimes of a single nitrogen-vacancy center in diamond*, Applied Physics Letters 119, 134001 (2021),
URL: https://dx.doi.org/10.1063/5.0070639

[318] P. Neumann, R. Kolesov, V. Jacques, J. Beck, J. Tisler, A. Batalov, L. Rogers, N. B. Manson, G. Balasubramanian, F. Jelezko, and J. Wrachtrup, *Excited-state spectroscopy of single NV defects in diamond using optically detected magnetic resonance*, New Journal of Physics 11, 013017 (2009),
URL: https://dx.doi.org/10.1088/1367-2630/11/1/013017

[319] R. S. Schoenfeld and W. Harneit, *Real Time Magnetic Field Sensing and Imaging Using a Single Spin in Diamond*, Physical Review Letters 106, 030802 (2011),
URL: https://dx.doi.org/10.1103/PhysRevLett.106.030802

[320] J. Storteboom, P. Dolan, S. Castelletto, X. Li, and M. Gu, *Lifetime investigation of single nitrogen vacancy centres in nanodiamonds*, Optics Express 23, 11327 (2015),
URL: https://dx.doi.org/10.1364/OE.23.011327

[321] C. Bradac, T. Gaebel, N. Naidoo, M. J. Sellars, J. Twamley, L. J. Brown, A. S. Barnard, T. Plakhotnik, A. V. Zvyagin, and J. R. Rabeau, *Observation and control of blinking nitrogen-vacancy centres in discrete nanodiamonds*, Nature Nanotechnology 5, 345 (2010),
URL: https://dx.doi.org/10.1038/nnano.2010.56

[322] D. M. Toyli, D. J. Christle, A. Alkauskas, B. B. Buckley, C. G. Van de Walle, and D. D. Awschalom, *Measurement and Control of Single Nitrogen-Vacancy*

Center Spins above 600 K, Physical Review X 2, 031001 (2012),
URL: https://dx.doi.org/10.1103/PhysRevX.2.031001

[323] Y. Masuyama, K. Suzuki, A. Hekizono, M. Iwanami, M. Hatano, T. Iwasaki, and T. Ohshima, *Gradiometer Using Separated Diamond Quantum Magnetometers*, Sensors 21 (2021),
URL: https://dx.doi.org/10.3390/s21030977

[324] E. Boto, N. Holmes, J. Leggett, G. Roberts, V. Shah, S. Meyer, L. Muñoz, K. Mullinger, T. Tierney, S. Bestmann, G. Barnes, R. Bowtell, and M. Brookes, *Moving magnetoencephalography towards real-world applications with a wearable system*, Nature 555, 657 (2018),
URL: https://dx.doi.org/10.1038/nature26147

[325] L. Marmugi and F. Renzoni, *Optical Magnetic Induction Tomography of the Heart*, Scientific Reports 6, 23962 (2016),
URL: https://dx.doi.org/10.1038/srep23962

[326] D. Murzin, D. J. Mapps, K. Levada, V. Belyaev, A. Omelyanchik, L. Panina, and V. Rodionova, *Ultrasensitive Magnetic Field Sensors for Biomedical Applications*, Sensors 20 (2020),
URL: https://dx.doi.org/10.3390/s20061569

[327] A. A. Wood, L. C. L. Hollenberg, R. E. Scholten, and A. M. Martin, *Observation of a Quantum Phase from Classical Rotation of a Single Spin*, Physical Review Letters 124, 020401 (2020),
URL: https://dx.doi.org/10.1103/PhysRevLett.124.020401

[328] A. Balogh, *Planetary Magnetic Field Measurements: Missions and Instrumentation*, Space Science Reviews 152, 23 (2010),
URL: https://dx.doi.org/10.1007/s11214-010-9643-1

[329] M. Díaz-Michelena, *Small Magnetic Sensors for Space Applications*, Sensors 9, 2271 (2009),
URL: https://dx.doi.org/10.3390/s90402271

[330] C. Fermon, *Introduction on Magnetic Sensing and Spin Electronics*, chapter 1, pp. 1–18, John Wiley & Sons, Ltd, (2017)

[331] V. Stepanov, F. H. Cho, C. Abeywardana, and S. Takahashi, *High-frequency and high-field optically detected magnetic resonance of nitrogen-vacancy centers in diamond*, Applied Physics Letters 106, 063111 (2015),
URL: https://dx.doi.org/10.1063/1.4908528

[332] C. L. Degen, F. Reinhard, and P. Cappellaro, *Quantum sensing*, Reviews of Modern Physics 89, 035002 (2017),
URL: https://dx.doi.org/10.1103/RevModPhys.89.035002

[333] V. E. Baranova and P. F. Baranov, The helmholtz coils simulating and improved in comsol, *2014 Dynamics of Systems, Mechanisms and Machines (Dynamics)*, (2014),
URL: https://dx.doi.org/10.1109/Dynamics.2014.7005634

Acknowledgements

The acknowledgements have been removed for data protection reasons.

The acknowledgements have been removed for data protection reasons.

The acknowledgements have been removed for data protection reasons.

List Of Publications

Regular Articles

[1] S. Schmitt, T. Gefen, F. M. Stürner, T. Unden, G. Wolff, C. Müller, J. Scheuer, B. Naydenov, M. Markham, S. Pezzagna, J. Meijer, I. Schwarz, M. Plenio, A. Retzker, L. P. McGuinness, and F. Jelezko, *Submillihertz magnetic spectroscopy performed with a nanoscale quantum sensor*, Science 356, 832 (2017), URL: http://dx.doi.org/10.1126/science.aam5532

[2] R. Fukuda†, P. Balasubramanian†, I. Higashimata, G. Koike, T. Okada, R. Kagami, T. Teraji, S. Onoda, M. Haruyama, K. Yamada, M. Inaba, H. Yamano, F. M. Stürner, S. Schmitt, L. P. McGuinness, F. Jelezko, T. Ohshima, T. Shinada, H. Kawarada, W. Kada, O. Hanaizumi, T. Tanii, and J. Isoya, *Lithographically engineered shallow nitrogen-vacancy centers in diamond for external nuclear spin sensing,* New Journal of Physics 20, 083029 (2018), URL: http://dx.doi.org/10.1088/1367-2630/aad997

[3] F. M. Stürner, A. Brenneis, J. Kassel, U. Wostradowski, R. Rölver, T. Fuchs, K. Nakamura, H. Sumiya, S. Onoda, J. Isoya, and F. Jelezko, *Compact integrated magnetometer based on nitrogen-vacancy centres in diamond*, Diamond and Related Materials 93, 59 (2019), URL: http://dx.doi.org/10.1016/j.diamond.2019.01.008

[4] F. M. Stürner, A. Brenneis, T. Buck, J. Kassel, R. Rölver, T. Fuchs, A. Savitsky, D. Suter, J. Grimmel, S. Hengesbach, M. Förtsch, K. Nakamura, H. Sumiya, S. Onoda, J. Isoya, and F. Jelezko, *Integrated and Portable Magnetometer Based on Nitrogen-Vacancy Ensembles in Diamond*, Advanced Quantum Tech-

nologies 4, 2000111 (2021),
URL: http://dx.doi.org/10.1002/qute.202000111

[5] G. Chatzidrosos, J. S. Rebeirro, H. Zheng, M. Omar, A. Brenneis, F. M. Stürner, T. Fuchs, T. Buck, R. Rölver, T. Schneemann, P. Blümler, D. Budker, and A. Wickenbrock, *Fiberized Diamond-Based Vector Magnetometers*, Frontiers in Photonics 2, 4 (2021),
URL: http://dx.doi.org/10.3389/fphot.2021.732748

[6] F. M. Stürner†, Y. Liu†, P.-O. Colard, M. Markham, and F. Jelezko, *Magnetometry based on the excited-state lifetimes of a single nitrogen-vacancy center in diamond*, Applied Physics Letters 119, 134001 (2021),
URL: http://dx.doi.org/10.1063/5.0070639

† These authors contributed equally to the work.

Conference Contributions

[1] F. M. Stürner, A. Brenneis, R. Rölver, U. Wostradowski, J. Kassel, T. Fuchs, and F. Jelezko, *A miniaturised magnetic field sensor based on nitrogen-vacancy centres in diamond*, Talk, 29th International Conference on Diamond and Carbon Materials, Dubrovnik, Croatia (2018)

[2] F. M. Stürner, A. Brenneis, J. Kassel, U. Wostradowski, R. Rölver, T. Fuchs, and F. Jelezko, *A miniaturised magnetic field sensor based on nitrogen-vacancy centres in diamond*,
Talk, microTEC Südwest Clusterkonferenz 2019, Freiburg, Germany (2019)

[3] F. M. Stürner, A. Brenneis, J. Kassel, U. Wostradowski, R. Rölver, T. Fuchs, and F. Jelezko, *Fibre-optical integrated magnetic field sensor based on nitrogen-vacancy centres in diamond*, Talk, 30th International Conference on Diamond and Carbon Materials, Seville, Spain (2019)

[4] F. M. Stürner, *GMM-Preis 2021: Integrated and Portable Magnetometer Based on Nitrogen-Vacancy Ensembles in Diamond*, Talk, MikroSystemTechnik Kongress 2021, Ludwigsburg, Germany (2021)

Additionally, the author contributed to more than 25 patent applications, which partially have been disclosed.

Curriculum Vitae

The curriculum vitae has been removed for data protection reasons.

The curriculum vitae has been removed for data protection reasons.

Erklärung

Ich erkläre hiermit, dass die vorliegende Arbeit selbständig von mir angefertigt worden ist. Weiter versichere ich, dass ich keine anderen als die angegebenen Quellen und Hilfsmittel benutzt und wörtlich und inhaltlich übernommene Stellen als solche kenntlich gemacht habe.

Weiterhin erkläre ich, dass die vorliegende Arbeit weder vollständig noch in Auszügen einer anderen Fakultät mit dem Ziel einen akademischen Titel zu erwerben vorgelegt worden ist. Ich bewerbe mich hiermit erstmalig um den Doktorgrad der Naturwissenschaften der Universität Ulm.

Ulm, den 1. Juli 2023

Felix M. Stürner